1/23/91

A PRECISION MEASUREMENT OF THE A-DEPENDENCE OF DIMUON PRODUCTION IN PROTON-NUCLEUS COLLISIONS AT 800 GEV/C

by

MING-JER WANG

Submitted in partial fulfillment of the requirements
for the Degree of Doctor of Philosophy

Thesis Adviser: **Professor HELMUT W. BAER**

Department of Physics
CASE WESTERN RESERVE UNIVERSITY
January, 1991

ABSTRACT

Precision measurements of the A-dependence of the reaction $p+A \rightarrow \mu^+\mu^- + X$ at 800 GeV/c are reported in this thesis. Data were taken at Fermilab (E772) using a modified version of the large dimuon spectrometer in the Meson-East beamline. A total of 6×10^5 muon pairs were recorded for targets of D, C, Ca, Fe, and W. The kinematic region spanned by the data corresponds to a dimuon invariant mass of $3 \leq M_{\mu^+\mu^-} \leq 14$ GeV, a Feynman-x of $-0.1 \leq x_F \leq 0.7$, and a target parton momentum fraction of $0.03 \leq x_2 \leq 0.30$. Accurate relative target normalizations were achieved by careful monitoring of beam intensity and position, cyclic interchanges of targets, maintaining nearly 100% electronic livetime, and by use of precisely fabricated targets. The systematic errors in the relative yields are less than 2% for all targets.

Results are presented on the ratios of cross sections for nuclear targets relative to deuterium for the Drell-Yan process and for the production of the J/ψ, ψ', and Υ quarkonia. These ratios are presented as functions of variables P_T and x_F, and *versus* x_1 and x_2 for the Drell-Yan process. Nuclear depletion at low-x_2 is observed for the first time in the Drell-Yan process. No nuclear enhancement of the antiquark distribution is observed in the region $x_2 \geq 0.1$. The data give tight constraints on models developed to explain nuclear medium effects in deep inelastic lepton scattering (EMC effect). Specifically, published models that have postulated a pion excess and 6-quark clusters are ruled out. The A-dependent behaviors on x_F and P_T for J/ψ, ψ', and Υ production are also reported and compared with previous experiments. Substantial nuclear depletions are observed in both the x_F and P_T dependence. These depletions increase with increasing x_F, and decrease with increasing P_T.

ACKNOWLEDGEMENTS

I would like to show my sincere appreciation to my adviser Professor H.W. Baer. During the last four months, he frequently advised me on this thesis, even in the period of his illness. I am more than happy to see his amazing and rapid recovery. Throughout last four years, he has been providing me constant encouragement, warm caring, and stimulating discussion. Most of all, he kindly induces my motivation to think deeply about physics problems, and also shows me the spirit of dedication.

I would like to express my deep appreciation to Professor W.L. Gordon, Professor W.J. Fickinger, and Professor R.W. Brown, who introduced me to this excellent research program. I also would like to show my thanks to their encouragement and supports over the last five years.

I like to thank all the members of E772 collaboration group. It was the good work by each individual to make this experiment possible and successful.

I specially thank Dr. C.N. Brown for giving me an orientation to the spectrometer, the Meson-East beam line, and other basic skills for a beginning experimentalist. Dr. Y.B. Hsiung introduced me the concepts of data acquisition and Nevis transport system. I really enjoyed and appreciated the hospitality of his family. With their kindness, the life at Fermilab was joyful.

Professor K.B. Luk taught me how to maintain a proportional-wire chamber and provided me several assistance at Fermilab. I also want to thank Professor R.L. McCarthy for his advise on the work of hodoscope calibration. Special thank goes to Mr. D. Shieh for his many helps on technical issues.

Many thanks to Dr. J.C. Peng for many enlightening discussions and stimulating ideals on this thesis subject. The hospitality of his family brought me lots of joy, while at Los Alamos. I greatly enjoyed working with Dr. P.L. Mc-

Gaughey on data analysis and MC simulation. Under his guiding, I learned how to deal with a complicated task and break it down to several solvable items. I would like to acknowledge Dr. J.M. Moss, Dr. M.J. Leitch, Dr. T.A. Carey, and Dr. C.S. Mishra for their constant helps and advice during the experiment and data analysis.

I would like to thank Dr. D.H. White for his support on my work at LAMPF. Many warm thanks to my terrific officemate Dr. Mario E. Schillaci and his wife Barbara for their caring and advises throughout last three years. Especially, I would like to express my sincere appreciation to Mario's effort on the corrections of my thesis. Many thanks to Dr. C.L. Morris for his kind assistance on the peak-fitting program NEWFIT that was used to extract J/ψ , ψ' , and Υ peak areas from mass spectra. A special thank goes to Dr. M.K. Jones for his helps on MAPPER and LATEX with which I was able to present this thesis in this format.

Discussions with one of my fellow graduate students R. Guo are very helpful and joyful.

Here, I would like to express my sympathy and memory to a fellow graduate student J. Mills, who passed away in early 1990 and did not have a chance to read our publications. The Drell-Yan part of this thesis is, specially, dedicated to her.

Contents

List of Figures

List of Tables

Chapter 1

Introduction and Physics Background

1.1 Lepton-pair Production in Hadron-Nucleus Collisions

Lepton-pair production in *hadron-hadron* collisions is a powerful tool to probe *parton distributions* in hadrons for both nuclear and particle physics. Figure 1.1 shows the dimuon mass spectrum in proton-nucleus collisions measured at Fermilab[5]. The J/ψ , ψ' , and Υ resonances ride on top of a dimuon continuum, which falls rapidly with invariant mass. The underlying mechanism for producing this $\mu^+\mu^-$ continuum is the *Drell-Yan Process*[1], shown schematically in figure 1.2. In this process, a quark annihilates with an antiquark to form a virtual time-like photon which subsequently decays into a pair of leptons. The mass and momentum of the lepton pair directly reflects the momentum distributions, of quarks and antiquarks in the interacting hadrons. Current knowledge[11] of these momentum distributions comes essentially from

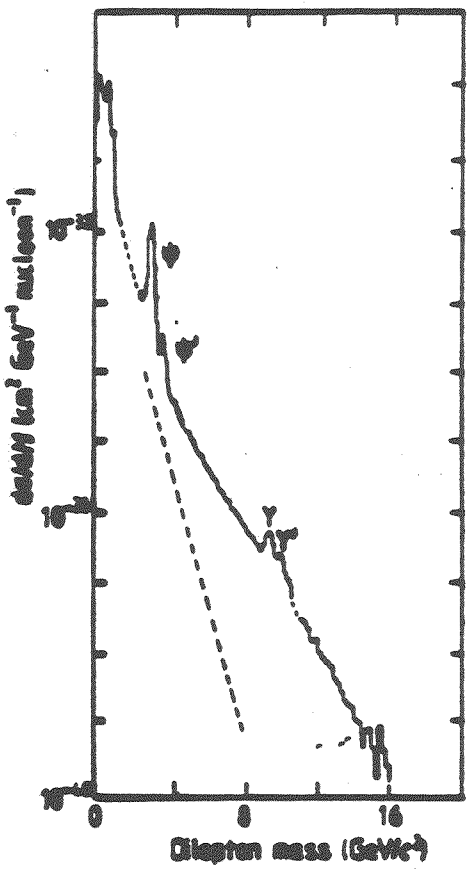

Figure 1.1: Dimuon mass spectra for 400 GeV/c protons incident on a Pt target. measured at Fermilab[5].

measurements of deep-inelastic lepton scattering (DIS) and the Drell-Yan process [1].

Lepton-pair production is also a powerful technique to search for new particles. Indeed the charmonium J/ψ ($c\bar{c}$) state was discovered in 1974 in a dilepton experiment[61] at Brookhaven National Laboratory. The reaction employed was $p + Be \longrightarrow e^+e^-X$ with a 28-GeV proton beam. Three years later, a similar experiment E288[60] at Fermi National Accelerator Laboratory led to the discovery of bound states of heavier bottom [2] quarks with charge -1/3, and generically named Υ ($b\bar{b}$). This experiment used the reaction $p + Be, Cu, Pt \longrightarrow \mu^+\mu^-X$ with a 400-GeV proton beam. It is quite conceivable that the top quark could also be discovered through the detection of dilepton decay of toponium states, provided their widths are sufficiently narrow. Also, the intermediate vector boson, Z^0, couple to lepton pairs. The discovery of the Z^0 at UA1[7] and UA2 was through lepton-pair detection.

Recently, great interest has been focused on the A-dependent behavior of the Drell-Yan process and heavy quarkonium production cross sections. In 1983, the European Muon Collaboration (EMC)[36] discovered that parton distribution functions were modified in the nuclear medium. Experiments between 1983 and 1990[32,33,34,35,30] have confirmed and extended the EMC results. This A-dependent behavior of quark distribution was not expected [3] for hard scattering processes. A similar effect on antiquark distributions might now be expected. Among different hard scattering processes, only the Drell-Yan process can probe nuclear medium effects on antiquark distribution to a high accuracy.

[1] The Drell-Yan process is also a unique method to determine structure functions of π, K, and $\bar{p}$ when they are used as beams.

[2] Also called beauty quark.

[3] Because the quark distribution dominates the antiquark distribution in most kinematic regions.

Measurement of the nuclear-medium effects on antiquark distributions was the main research goal of our experiment E772[66] and of this thesis.

In this thesis, the Drell-Yan models are discussed from section 1.2 to 1.4 and various A-dependent behaviors are discussed in section 1.5. The unique role of the Drell-Yan process in the study of A-dependence of antiquark distributions is explained in section 1.5.3.

Because heavy quarkonium production is also a hard process, one may naively expect it not to be affected by the nuclear medium. However, several experiments [96,97] have measured a definite A-dependent behavior of J/ψ production. This raises a question about the formation time from a $c\bar{c}$ state to the bound state of J/ψ . If the laboratory momentum of the produced $c\bar{c}$ is small, it would be expected to evolve into the J/ψ , while still in the nucleus. One, therefore, might expect the J/ψ to scatter with the nuclear medium, and a nuclear dependence of the production cross section would be observed. A recent experiment E537[57] at Fermilab observed a significant suppression of the J/ψ with large momentum in nuclear medium. This observation could not be fully understood by the rescattering picture mentioned above. Therefore, it is interesting to study the A-dependence of both the J/ψ and a similar, but heavier, quarkonium system Υ . Comparison between these two A-dependence studies can shed some light on the observed suppression in the large-momentum region. Our E772 data includes both J/ψ and Υ data with good statistics. It provides unique information on this question of abnormal suppression in the large-momentum region.

The production mechanism of quarkonium is sketched in section 1.6, and its A-dependence is described in section 1.7. In section 1.8, the physics goals and the requirements of E772 are explained. Principal physics results are given in chapter 7.

1.2 The Naive Drell-Yan Model

The study of continuum-dilepton production in hadronic collisions at Q^2 $(=M^2_{\mu^+\mu^-}) \geq 16$ GeV^2,

$$h_A + h_B \longrightarrow \mu^+\mu^- + X, \tag{1.1}$$

can be used to determine the structure of hadrons in a way that is complementary to DIS, $l + h \longrightarrow l' + X$. In the early 1970's, Drell and Yan[1] suggested that the quarks in the initial-hadron states, h_A and h_B, can be regarded as instantaneously *free* fermions during the violent interaction (i.e., Q^2 , S$\rightarrow \infty$ but Q^2 /S $\rightarrow$ constant). This is just the subnucleon analogue of the impulse approximation of nuclear physics. The Drell-Yan parton model treated the dynamics of the dominant subprocess [4] ,

$$q_A + \bar{q}_B \longrightarrow \gamma^* \longrightarrow \mu^+\mu^- \ . \tag{1.2}$$

as a point-like *electromagnetic annihilation* process. The *final state interactions* confining the quarks were irrelevant to this subprocess because they act at space-time distances of the order of the hadron size, which is much larger than the parton size and timescale of the interaction.

It is generally believed that the gauge field theory known as Quantum Chromodynamics (QCD) is the right candidate to describe strong interactions among quarks. We should expect QCD to give a field-theoretic justification for the quark-parton model. Indeed, in QCD the running (effective) coupling constant of the color force tends to go to zero as the space-time scale of the interaction approaches zero. This is known as asymptotic freedom[8,9]. This is the characteristic feature of non-Abelian gauge field theories. QCD gives the quark-parton

[4] According to the uncertainty principle, interactions at very large Q^2 and s imply small space-time scale, and the point-like(in space-time) electromagnetic annihilation might dominate the violent interaction.

model a theoretical grounding within the principles of relativistic quantum field theory[20].

1.2.1 Kinematics

Figure 1.2 illustrates the kinematics of the Drell-Yan process in the hadron-hadron center-of-mass frame at three stages. First of all, we define a property of each active quark-parton: x_1 is the fraction of beam hadron momentum carried by the active beam quark/antiquark and x_2 is the fraction of target hadron momentum for active target antiquark/quark. Here x is called Bjorken x and is defined as $-q^2/2p\cdot q$ in DIS processes (p and q are 4-momenta for the hadron and the space-like virtual photon). The second stage of this process involves the virtual photon(dilepton). The kinematic variables associated with it are: the mass M_γ represents the virtuality of the photon, x_F is the fraction of the maximum possible longitudinal momentum carried by the virtual photon in the beam direction, P_T is its transverse momentum, and ϕ_γ is its azimuthal production angle. At the third stage, the virtual photon decays into a lepton pair. In the virtual photon rest frame, θ_{μ^+} and ϕ_{μ^+} are the polar and azimuthal decay angles, respectively, of one of the leptons. In principle, θ_{μ^+} and ϕ_{μ^+} should be specified with respect to the quark-antiquark annihilation axis, but in practice this is impossible because the individual transverse momenta of the quarks are unknown from measurements. The Collins-Soper frame (CS)[13], where the reference axis is the bisector of the angle between the directions of interacting hadrons in the muon-pair rest frame, is used in our off-line analysis program to define θ_{μ^+} and ϕ_{μ^+}. In total, we have introduced the eight kinematic variables x_1 , x_2 , M_γ, x_F , P_T , ϕ_γ, θ_{μ^+}, and ϕ_{μ^+}.

Experimentally, we measure six *independent* variables, viz., the vector momenta of each lepton. This is sufficient because the above eight variables are

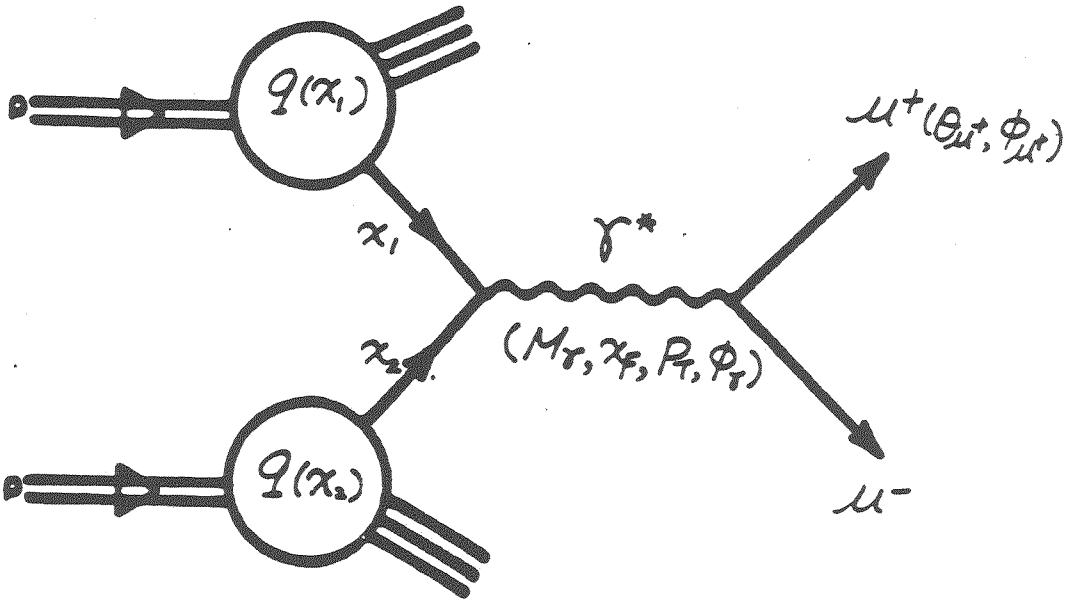

Figure 1.2: Schematic diagram for the Drell-Yan process[20]. It shows three stages of this process: 1) quarks at initial states; 2) virtual photon at intermediate state; and 3) muon pair at final states.

not independent. Two pairs of variables (mass, x_F) and (x_1 , x_2) are correlated by the equations expressing the annihilation kinematics:

$$x_F \equiv P_l/(\frac{\sqrt{s}}{2}) = x_1 - x_2 \tag{1.3}$$

$$M^2 \equiv E^2 - P_l^2 = s x_1 x_2 \tag{1.4}$$

where

$$E = (x_1 + x_2)\sqrt{s}/2, P_l = (x_1 - x_2)\sqrt{s}/2$$

In these equations, we have ignored the *quark masses* and the *transverse momentum*. Therefore, in the hadron-hadron c.m. frame, the longitudinal momenta of the annihilating quarks are $x_1\sqrt{s}/2$ and $-x_2\sqrt{s}/2$, respectively with $\sqrt{s}$ denoting the total energy. The energies of the quarks are $x_1\sqrt{s}/2$ and $x_2\sqrt{s}/2$.

In this approximation, the measured 3-momenta of μ^+ and μ^-, are sufficient to calculate the quantities (M, x_F , P_T , ϕ_γ , θ_{μ^+}, ϕ_{μ^+}) or equivalently, (x_1, x_2, P_T , ϕ_γ, θ_{μ^+}, ϕ_{μ^+}).

1.2.2 Dynamics

The impulse approximation of the Drell-Yan model assumes the annihilating quarks and antiquarks are free within each hadron during the time scale of a hard interaction. Therefore, there are no correlations between the probability distribution functions of the annihilating particles. In addition, these distributions are also assumed to be independent of the annihilation subprocess. Within this simple picture, the Drell-Yan cross section can be resolved into two *independent parts*: the probability functions to find the active partons in each interacting hadron and the cross section of this electromagnetic subprocess. In other words, we can separate long-distance effects (probability functions) from

short-distance effects (hard scattering). Now we can formulate the Drell-Yan cross section item by item according to the annihilation diagram in figure 1.2. At the quark-photon vertex, the conservation of color quantum number leads to a color factor [5] of 1/3. The conservation of flavor quantum number and the quark structure of hadrons A and B, lead to the product $q_f^A(x_1)\overline{q}_f^B(x_2)$ of quark and antiquark probability distribution functions, which describes the joint probability of finding partons with opposite flavors in hadrons. The next step is to find out the unpolarized cross section of the Drell-Yan subprocess. Because this process is analogous to the $e+\overline{e} \longrightarrow \mu^+\mu^-$ process, its cross section is given by the QED formula[20],

$$\sigma = 4\pi\alpha^2 e_f^2/3M^2, \tag{1.5}$$

where α is the electromagnetic fine structure constant, e_f is the number of charge units carried by quark of flavor f in the initial-state (either $\pm$ 1/3 or $\pm$ 2/3) and M is the dilepton mass. Because hadrons A and B contain both quarks and antiquarks, the particle-antiparticle exchange symmetry must be imposed on this cross section. The product of these three factors gives the expression for the *hadron-hadron* Drell-Yan cross section[1],

$$\frac{d^2\sigma}{dx_1 dx_2} = (\frac{1}{3})(\frac{4\pi\alpha^2}{3M^2})\sum_f e_f^2[q_f^A(x_1)\overline{q}_f^B(x_2) + q_f^B(x_1)\overline{q}_f^A(x_2)], \tag{1.6}$$

where the sum is over all flavors of quark. Re-expressing this in terms of the measurable dilepton parameters M and x_F gives (using equation 1.3 and 1.4)

$$M^2\frac{d^2\sigma}{dM^2 dx_F} = (\frac{1}{3})(\frac{4\pi\alpha^2}{3M^2})(\frac{x_1 x_2}{x_1 + x_2})\sum_f e_f^2[q_f^A(x_1)\overline{q}_f^B(x_2) + q_f^B(x_1)\overline{q}_f^A(x_2)], \tag{1.7}$$

where

$$x_1 = \tfrac{1}{2}[(x_F^2 + 4\tau)^{1/2} + x_F]\ ,\ x_2 = \tfrac{1}{2}[(x_F^2 + 4\tau)^{1/2} - x_F]\ ^{6}\ ;\ \tau = M^2/s.$$

[5] Only $q\overline{q}$ of opposite color can annihilate into a colorless virtual photon. There are three possibilities $R\overline{R}$, $B\overline{B}$, and $G\overline{G}$ out of 3×3 cases.

[6] These formulas are valid while masses and transverse momenta of quarks are negligible.

The cross section can be written in terms of dimensionless variables to give a *scaling* form,

$$s\frac{d^2\sigma}{d\sqrt{\tau}dy} = (\frac{1}{3})(\frac{4\pi\alpha^2}{3})\sum_f e_f^2[q_f^A(x_1)\overline{q}_f^B(x_2) + q_f^B(x_1)\overline{q}_f^A(x_2)]. \qquad (1.8)$$

Here,

$$x_1 = \sqrt{\tau}e^y \ , \ x_2 = \sqrt{\tau}e^{-y},$$

where y is the usual rapidity variable defined $= \frac{1}{2}\ln(x_1/x_2)$.

This scale-independent form of equation 1.6 implies that data taken at different values of M and s, but at the same y, should have the same differential cross section as a function of τ. This is called the *scaling* behavior.

In equations 1.6, 1.7, and 1.8, we notice that these cross sections are factorized into two factors: one subprocess cross section and one term that is dependent only on quark distribution functions. This factorization picture is the main ingredient of the quark-parton model. It assumes that the Drell-Yan cross section is factorized and the $q_f(x)$ and $\overline{q}_f(x)$are universal, i.e., they do not depend on the particular process used to probe the constituents inside hadrons. In addition, the summation over different flavors in those equations implies that each parton-parton cross section contributes incoherently to the total hadron-hadron cross section. This is the parton incoherence picture within a single hadron. The question addressed in this thesis is whether this picture can be strictly applied to the nuclear case.

1.2.3 Parton Distribution Functions

The parton distributions $q_f(x)$ and $\overline{q}_f(x)$ within nucleons are mostly measured in DIS experiments. The current status of the experimental determination of these distributions is given by S.R. Mishra and F. Sciulli in Annual

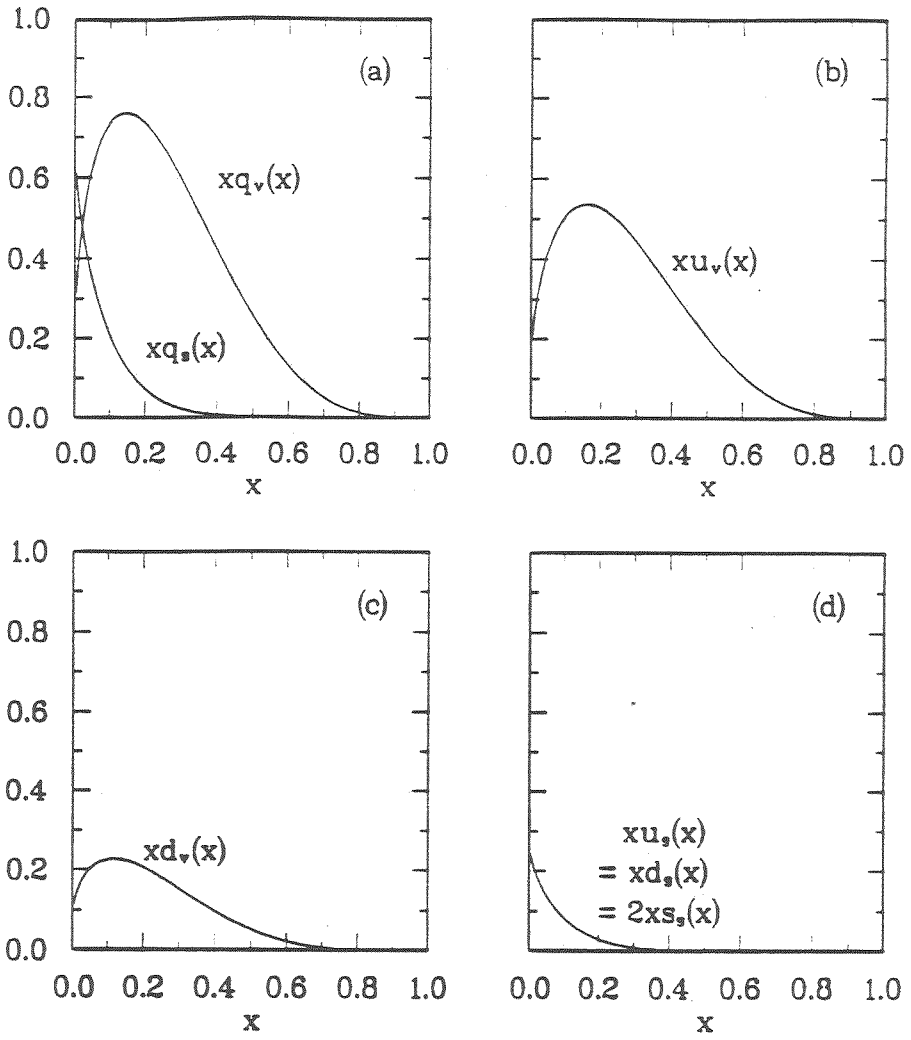

Figure 1.3: Valence-quark and sea-quark distributions calculated from EHLQ parametrization[73], at $Q^2 = 36$ GeV^2. Diagram (a) shows the valence and sea quark distributions; (b) the valence-up quark distribution; (c) the valence-down quark distribution; and (d) the sea-quark distribution for each flavor.

Review of Nuclear and Particle Science, 1989. To date, the data from DIS with electrons, muons, and neutrinos [11] have been used to extract parton distributions. More recently, Drell-Yan data also have been used as a constraint in a parton-distribution parametrization[12].

Because the virtual photon mediating the DIS process interacts with a single quark within the nucleon, the scattering data allow a determination of the momentum fraction distribution of the quarks. In fact, it is the structure function (F_2 or νW_2) that is measured in DIS, not the quark distributions, individually. These structure functions can be written in terms of q_f and $\overline{q}_f$:

$$F_2(x) = \nu W_2(x) = \sum_f e_f^2 x[q_f(x) + \overline{q}_f(x)] \tag{1.9}$$

Graphs of valence-quark and sea-quark distributions are shown in figure 1.3. These were calculated using the EHLQ parametrization[73]. One sees that the valence-quark distribution is peaked at $x \approx 0.2$, and sea-quark distribution has a maximum at $x = 0.0$, but decreases rapidly with increasing x. In the region of $x \geq 0.2$, the valence-quark distribution clearly dominates the sea-quark distribution.

1.3 Tests of the Naive Drell-Yan Model

Because the Drell-Yan process can be described within the framework of QCD, it provides not only an ideal place for testing the quark-parton model but also a QCD testing ground. The procedure of testing QCD naturally follows a sequence of steps. First, one has to establish the approximate validity of the naive quark-parton model. Once the *quark-parton picture* is really found to be dominant in this process, then the next step is to study in detail the deviations from the naive quark-parton dynamics and to compare these with the QCD predictions.

The Drell-Yan process has offered very clean signatures for the underlying parton picture. We discuss some of the experimental confirmation bearing on the validity of the quark-parton picture. It should be noted that these experiments were performed using nuclear targets in order to increase the dimuon event rate. The cross sections per nucleon were obtained by dividing the nuclear cross section by target nucleon number A. It was simply assumed that nuclear effects were negligible. This was a good approximation at $\pm$ 20% level, which was the experimental uncertainty. It may not hold at the $\pm$ 1% level of accuracy, which was the aimed-for experimental accuracy of E772.

The Point-Like Quark

One of the main predictions based on the quark-parton picture is the scaling behavior of cross sections or distribution functions in equation 1.8. Fermilab experiments E288[77] and E605[78] have tested scaling in proton-nucleus collisions by comparing the dimuon cross section measured at four beam energies: 200, 300, 400, and 800 GeV, corresponding to $\sqrt{s}$ = 19.4, 23.8, 27.4, and 38.8 GeV, respectively. For values of $\tau < 0.33$, the agreement among the data is good to the 20% level in this comparison.

The scaling property of parton distributions (Q^2 independent) implies that the parton never shows the further layer of its structure, no matter what level of spatial resolution is used to probe it. Here, we could regard Q^2 as the inverse of the spatial resolution. Therefore, this scaling observation lent support to the validity of a point-like parton description. This was an important feature of the naive Drell-Yan model.

The Quark Charge

The Drell-Yan process initiated with high energy π^+ and π^- beams played an important role for verifying that the up quarks have charge of $e_u = 2/3$ and the down quarks have charge of $e_u = \mid -1/3 \mid$. In these reactions, at $\tau > 0.6$, annihilation of valence antiquarks in the pion beam with valence quarks in the target dominate the Drell-Yan process. The cross section ratio for incident π^- relative to π^- approaches e_d^2/e_u^2. The data of E444 with a 225 GeV pion beam and data of OMEGA with a 40 GeV pion beam measured a value of 1/4 for this ratio[3,16]. The fractional charges of 2/3 and -1/3 for up and down quarks, respectively, were revealed in these beam-dependent cross sections.

The Quark Spin

Because the virtual photon decays into a lepton pair in the Drell-Yan process, the angular distribution of these leptons is determined by the type of photon polarization. According to the naive Drell-Yan model, the virtual photon will be predominantly transversely polarized if it is formed by annihilation of spin-1/2 parton-antiparton pairs. This means that the angular distribution in the dimuon rest frame has $(1+\cos^2\theta)$ dependence.

Several groups (NA3, ABCS, and CHFMNP[5,3]) have measured the decay angular distribution for dileptons, and have fitted their data by an expression of the form:

$$dN/d\theta = 1 + \lambda \cos^2\theta$$

Within the errors, the global data are all consistent with the simple Drell-Yan prediction that λ should equal unity [7].

[7] A deviation from this value has been observed for large x_1 [14], which suggests that the higher-twist effect[6,15] becomes important in this kinematic region.

It is important to *refine* and *extend* the experimental analysis in order to precisely determine the domain of validity and the accuracy of the naive quark-parton approximation. The next step is to ask whether or not the additional QCD effects deviating from the naive quark-parton model are visible in the data. Indeed, scaling violations, a K-factor greater than unity, and large transverse momentum were observed, indicating that QCD effects must be taken into account.

1.3.1 Scaling Violation

High sensitivity experiments studying pion-induced dileptons have shown scaling violations. Fermilab experiment E326[3,17] favors the inclusion of scaling violation in the mass distribution. CERN experiment NA10[3.18] has reported the observation of scaling violation in the x_F distribution for high-mass dimuons. E605[78] has also seen this effect in the region of large values of τ.

1.3.2 K-Factor

The Drell-Yan model predicts the shape of the proton-nucleus cross section quite well. The magnitude of the measurements is, however, a factor of two to three larger than the prediction. This discrepancy has been observed both in pN and πN lepton-pair production and has been the object of extensive theoretical and experimental investigations. It is usually referred to as the K-factor and defined in the following equation,

$$d\sigma/dQ^2 \mid_{exp.} = K_{exp.} \cdot d\sigma/dQ^2 \mid_{lowest-order} \tag{1.10}$$

The experimental values of K-factor are listed in table 1.1[3].

Although these results are all in the range 1.5-3, there are significant variations within that range. One source of this discrepancy is the use of different

Group	Beam/Target	Momentum:[$\sqrt{s}$](GeV)	K
NA3	$(\overline{p}-p)$/Pt	150	2.3±0.4
E537	$\overline{p}$/W	125	2.45±0.12±0.20
E288	p/Pt	300/400	~1.7
E439	p/W	400	1.6±0.3
NA3	p/Pt	400	3.1±0.5±0.3
CHFMNP	pp	[44.63]	1.6±0.2
A^{2}BCSY	pp	[44.63]	~1.7
OMEGA	$\pi^{\pm}$/W	30.5	~2.4
NA3	$\pi^{\pm}$Pt	200	2.3±0.5
	π^-/Pt	150	2.49±0.37
	π^-/Pt	280	2.22±0.33
NA10	π^-/W	194	2.77±0.12
E326	π^-/W	225	2.70±0.08±0.40

Table 1.1: Experimental K-factors.

parametrizations of the quark momentum distribution functions. Also, there are differences in the assumed momentum fraction carried by gluons within the nucleon.

1.3.3 Transverse Momentum

According to the quark-parton picture, the partons inside the hadron carry only the intrinsic transverse momenta of order ~ 400 MeV [8] . This value is proportional to the inverse of the hadron dimension, and is also measured from the mean transverse momentum for secondary hadrons. However, the measured mean P_T in Drell-Yan experiments is larger than this expectation and increases with dilepton mass in the compiled data of CFS, CIP, and NA3[5]. The Omega collaboration[5] has shown the $\sqrt{s}$ dependence of mean P_T at a fixed value of

[8]This can be obtained by taking the Fourier transform of the spatial charge distribution of hadrons measured in elastic electron scattering. The value of r.m.s. radius for the proton is 0.83 fm.

τ. The data are fitted with the form:

$$< P_T > = 0.45 + 0.025\sqrt{s}$$
$$< P_T > = 0.54 + 0.029\sqrt{s},$$

where the former is for the proton-induced reaction, and the latter is for the pion-induced reaction. The constant term is interpreted to result from the intrinsic parton P_T distributions.

1.4 QCD-improved Drell-Yan Model

From the discussion in the last section, we know that the scaling violation, the large K-factor, and the large transverse momentum phenomena could not be explained by the naive Drell-Yan model. It then becomes necessary to improve the naive Drell-Yan model by including the QCD effects, i.e., the gluon interactions. Furthermore, in QCD, the universality property of the distribution functions may not hold, due to the differences in gluon radiation processes in Drell-Yan and DIS. In order to maintain the predictive power of the QCD improved Drell-Yan model, the factorization picture must be the guideline of this calculation.

Consider the effects of interactions among the partons within one hadron, for example, the radiation of a *soft* gluon from the active quark that is going to participate in the annihilation. In the parton model, one says that all such internal reactions are slowed by time dilation in the fast moving hadron, and therefore happen long before the hard interaction. These reactions affect the parton distribution $q_f(x)$ but do not alter the factorized structure of the Drell-Yan cross section.

On the other hand, the gluon emission can happen on very short time scales, of order $\Delta t \sim 1/Q$ before the annihilation, if the gluon is *hard*. In this case, the gluon emission is counted as part of the hard scattering subprocess. Therefore, the naive Drell-Yan subprocess cross section is expected to be modified by some hard-gluon emission diagrams.

Figure 1.4 shows the six gluon-emission diagrams for a complete $first-order$ perturbative QCD calculation. The annihilation correction graphs are shown in (a) and (b). Diagrams (c) and (d) are the "Compton" diagrams, in which lepton pairs are produced through the interaction of a quark and a gluon rather than by quark-antiquark annihilation. Note that in these four diagrams (a-d) the virtual photon recoils against an outgoing quark or gluon. Thus, here is a natural mechanism for producing lepton pairs with non-negligible transverse momentum. The two final diagrams, (e) and (f), represent virtual and real emission of soft gluons. These processes can alter the magnitude of the cross section because of the analytic continuation from $q^2 < 0$ to $q^2 > 0$. The results of this first-order correction is to give scale-dependent parton distributions as discussed in section 1.4.2, a K-factor of ~ 2 as discussed in section 1.4.3, and an s dependence of $< P_T^2 >$ as discussed in section 1.4.4.

1.4.1 The Leading-Log and Next-to-Leading-Log Approximations

In the calculation of the cross section for dilepton production, the contributions from all the relevant graphs must be added. Each strong interaction vertex in a graph introduces into the cross section a factor of α_s, the strong interaction fine structure constant.

These QCD corrections are introduced to the naive Drell-Yan cross section in two ways. First, the amplitudes of figure 1.4 (c) and (d), would lead to a

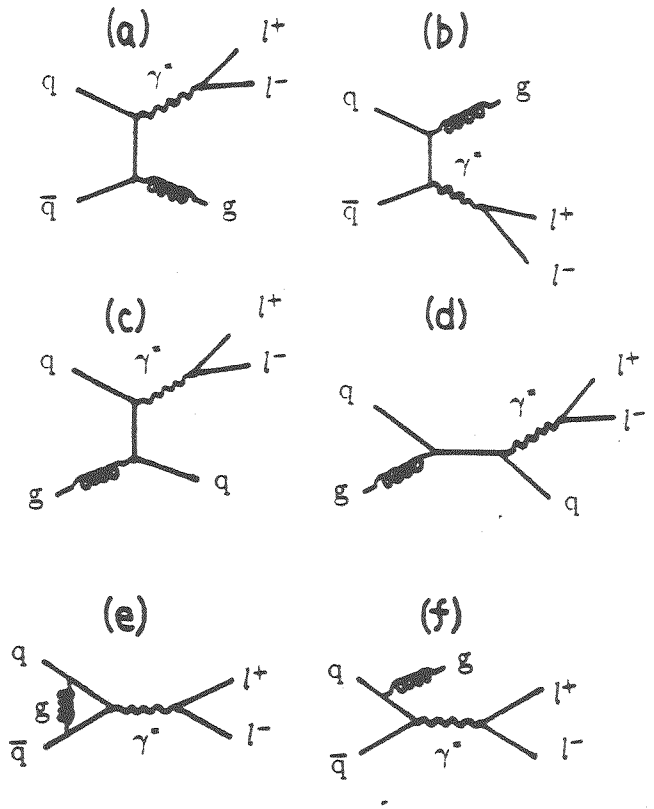

Figure 1.4: QCD corrections to the naive Drell-Yan model process[3,5]. Diagram (a) and (b) represent annihilation correction terms, (c) and (d) "Compton" scattering terms, (e) vertex correction term, and (f) soft gluon radiation term.

collinear singularity, where a collinear massless gluon is emitted by a massless quark. For the specifics of the Drell-Yan picture to be self-consistent, we must require the collinear singularity factors to be absorbed into the distribution functions q_f and $\overline{q}_f$ of the annihilating partons. And, finally, for the parton distribution functions to be the same functions encountered in the DIS process, the collinear singularity terms must be the same for the two processes[10].

Secondly, the emission of hard and soft gluons gives rise to finite perturbative corrections. These corrections are different for the two processes and the QCD-corrected Drell-Yan subprocess formula would include extra terms with increasing order of α_s.

The contribution to the Drell-Yan cross section from all of the graphs to order n can be expanded in two parameters, α_s and $\ln Q^2/\Lambda^2$. The QCD perturbative expansion[2] is represented as follows:

$$
\begin{aligned}
Q^2 d\sigma/dx_1 dx_2 = & \\
& \alpha_s^0 F_{00}(x_1,x_2) \\
& + \alpha_s^1[F_{11}(x_1,x_2)\ln^1\tfrac{Q^2}{\Lambda^2} + F_{10}(x_1,x_2)\ln^0\tfrac{Q^2}{\Lambda^2}] \\
& + \alpha_s^2[F_{22}(x_1,x_2)\ln^2\tfrac{Q^2}{\Lambda^2} + F_{21}(x_1,x_2)\ln^1\tfrac{Q^2}{\Lambda^2} + F_{20}(x_1,x_2)\ln^0\tfrac{Q^2}{\Lambda^2}] \\
& + \vdots \\
& + \alpha_s^n[F_{nn}(x_1,x_2)\ln^n\tfrac{Q^2}{\Lambda^2} + \cdots\cdots\cdots\cdots + F_{n0}(x_1,x_2)\ln^0\tfrac{Q^2}{\Lambda^2}].
\end{aligned}
$$

where Λ is the QCD scale parameter introduced to control the collinear singularity and the logarithms come from integrating over the transverse momenta of the quarks and gluons produced in the interaction[10]. In QCD, α_s is not a constant but rather depends on the scale of the interaction. Its Q^2 dependence[20]

is given by

$$\alpha_s(Q^2) = 12\pi/[(33 - 2n_f)\ln(Q^2/\Lambda^2)] \quad (1.11)$$

where n_f is the number of flavors and Λ is the renormalization or reference momentum. The latter has a value of the order of a typical hadronic mass. It can be regarded as a marker of the boundary between a world of quasi-free quarks and gluons, and the world of mesons and baryons.

For each order n, the term containing the highest power of the logarithm, i.e., (*leading logarithm*) can be quite large because the factor $\ln^n(Q^2/\Lambda^2)$ just cancels the logarithmic dependence on Q^2 in α_s. Therefore, it is not useful to calculate these leading terms only to the first few orders. The next-to-leading-log terms make contributions to the cross section proportional to $\ln^{-1}(Q^2/\Lambda^2)$. Practically, it is not necessary to perform the calculation to all orders. Taking only the highest power of the log at each order in α_s gives us the *leading-log approximation* (LLA). Including the next-highest power of the log gives the *next-to-leading-log approximation* (NLLA).

The α_s^0 term in the first line of the perturbative expansion, is the naive Drell-Yan cross section formula given in section 1.2.2. At the first order of α_s, the next-to-leading-log term is so-called a constant term , i.e., $\ln^0$. The LLA results in the same Q^2-dependent parton distributions as those in DIS. The NLLA, to the first order of α_s, modifies the subprocess cross section by multiplying the LLA cross section by a factor of K.

1.4.2 Q^2-Dependence of Parton Distribution Functions

In the LLA, it has been shown that $d^2\sigma/dx_1dx_2$ has the same factorization form as that of the naive Drell-Yan cross section, except that the distribution functions become Q^2-Dependent[20,21], i.e.,

$$q_f(x) \longrightarrow q_f(x,Q^2)$$
$$\overline{q}_f(x) \longrightarrow \overline{q}_f(x,Q^2)$$

These distribution functions, which have a weak logarithmic dependence on Q^2, are just the scale-violation distribution functions measured in deep inelastic lepton-nucleon scattering. Therefore, the cross sections in the form of equation 1.8 at different $\sqrt{s}$ and M, but the same y, would have slightly different shape as a function of τ.

Because of the "renormalized" distribution functions, the point-like picture of the parton ($Q^2 \to \infty$) must be modified to include the soft-gluon radiation into its structure. In other words, the presence of these scale violation distribution functions is the natural result of this new parton definition (Q^2 is finite). The Q^2 dependence of the distribution functions is governed by the Altarelli-Parisi Q^2 evolution equation[20,37,87]. For the valence quark distribution in hadron h, this equation is

$$dq_v^h(x,t)/dt = \alpha_s(Q^2)/\pi \int_x^1 (dy/y) q_v^h(y,t) p_{qq}(x/y), \qquad (1.12)$$

where $t = \ln(Q^2/\Lambda^2)$ and α_s is the strong coupling constant describing the qqg vertex. Because the integral over the transverse momentum of the radiated gluon is formally divergent, the scale Λ^2 which is contained in the running coupling constant, is introduced as a lower momentum "confinement" cutoff. Its value is unspecified in QCD perturbation theory, but is determined from experiment. The probability (or splitting) function $p_{qq}(x/y)$ is universal[87], i.e., independent of the type of hadron under discussion. The only place where the hadron properties are introduced is through the parton distribution function $q_v^h(y,t)$ and possibly the scale Λ [9].

[9] As what the rescaling model suggests in 1.5.2.

Equation 1.12 expresses the fact that the valence quark distribution at x is determined by its value in the range of x<y<1, and by the probability $p_{qq}(x/y)$ for the transition $q(y) \rightarrow q(x)$ via gluon radiation.

From the viewpoint of the resolution power of Q^2, $p_{qq}(x/y)$ could be regarded as the sub-parton distribution probed at higher Q^2 within the parton probed at lower Q^2. With the convolution concept, the sub-parton distribution within a hadron is obtained by integrating the joint probability $q_v^h(y,t)p_{qq}(x/y)$ from x to 1, where x is the minimum allowed momentum fraction for y, and x/y is the momentum fraction of the sub-parton with respect to the momentum of the parton. Using the above picture, the distribution function of the parton at higher Q^2 will be softer than that at lower Q^2, therefore the cross section at higher Q^2 will be larger in small x region and smaller in large x region. Although the main feature of the data of EMC, BCDMS and SLAC[19] is that the structure function is approximately independent of Q^2 at fixed x, the weak Q^2 dependence outlined above is clearly revealed at $x = 0.05$ and $x = 0.65$.

This Q^2 dependence tells us there is a parton structure following a continue scaling violation way. Because this logarithmic dependence is not in the usual dipole form of the form factor, it is not interpreted as the usual constitutional structure of a particle but the revelation of gluon-radiation processes that occur constantly inside the hadron.

1.4.3 Calculation of the K-Factor

In the LLA, the Drell-Yan cross section of equation 1.6 is modified by replacing $q(x)$ with $q(x, Q^2)$. In this approximation, one still has K=1. In other words, the subprocess cross section has not been modified yet.

The next-to-leading-log approximation (NLLA) corrections include, in addition, all first-order α_s terms. This leads to an overall cross section approxi-

mately 1.7 times[3] larger than that of the LLA. This excess factor arises primarily because the DIS functions are measured with space-like photons while the Drell-Yan process involves time-like photons. From the viewpoint of the first-order correction, this K-factor is defined as,

$$d\sigma/dQ^2 \mid_{o(\alpha_s)} \approx K \cdot d\sigma/dQ^2 \mid_{LLA} \tag{1.13}$$

In the NLLA, up to first order in α_s, the calculation becomes more complicated than that in the LLA, with the cross-section acquiring several additional terms. Thus the K-factor also has additional corresponding terms[22], as shown below:

$$K(\tau, Q^2) = 1 + \frac{\alpha_s(Q^2)}{2\pi}(R_\delta + \overline{R}_{q\bar{q}} + R_{qG}) \tag{1.14}$$

where R_δ, $\overline{R}_{q\bar{q}}$, and R_{qG} result from the vertex correction, annihilation corrections, and Compton corrections, respectively. R_δ is a constant term. $\overline{R}_{q\bar{q}}$ is a function of τ and has singular behavior in the limit of $\tau \rightarrow 1$, due to the emission of soft gluons. R_{qG} is nearly constant in the region of $\tau < 0.2$.

Fortunately, for most of the experimentally accessible kinematic region($\tau < 0.5$), the correction is dominated by one such term, the vertex correction. This results in the LLA cross section being multiplied by a nearly constant K factor.

$$K \simeq 1 + 2\pi\alpha_s/3 \tag{1.15}$$

It appears that this one correction term, when calculated to *all orders*, gives a convergent exponential series for K[3]:

$$K \simeq exp(2\pi\alpha_s/3), \tag{1.16}$$

which is $\simeq$1.87 for $\alpha_s = 0.3$.

The QCD first-order corrections to the Drell-Yan formula are finite, calculable and are not affected by spectator interactions[22]. These corrections are

large and approximately independent of τ, for small τ. They produce qualitative agreement with experiment.

Recently, there has been a calculation of σ_{DY} up to second order in α_s. Matsuura, van der Marck, and van Neerven[23] found that at $\sqrt{s} = 10.1$ GeV the second-order correction to the K-factor is about 62% of the zeroth order cross section at $M_{\mu\mu} = 10$ GeV. The first-order correction was about 83% of the zeroth order cross section. They also found that the correction of the *vertex term* up to second order almost exponentiates in the numerical sense, with a deviation of about 9% .

1.4.4 Transverse Momentum

The Compton and annihilation diagrams (a), (b), (c), and (d) provide mechanisms for producing dileptons with large transverse momentum. The average transverse momentum of the lepton pair is expected to have the form $< P_T^2 > = sf(x_F, \tau)$. The dynamics are contained within the dimensionless function f. If we also allow for the intrinsic P_T of the initial-state partons due to their confinement within the hadron, a small constant should be added to the above relation. Thus we expect a growth in the average momentum as a function of center-of-mass energy:

$$< P_T^2 > = a + bs \text{ , at fixed } \tau$$

The available data are in agreement with this equation.

1.4.5 Initial-State-Interaction Effects in Hadron-Hadron Collisions

The validity of the factorization picture of the Drell-Yan model in the presence of initial-state interactions has been questioned. In 1981, Bodwin, Brodsky, and Lepage (BBL) showed that in QCD there is a contribution to the Drell-Yan

process due to exchange of a gluon between an active quark and a spectator quark (called the leading twist effect) in another hadron that persists even in the limit $Q^2 \rightarrow \infty$. Such interactions could destroy the ability to factorize the Drell-Yan cross section into a product of two factors. The equality of the $q_f(x)$ from the DIS and Drell-Yan processes can not be established without factorization.

Bodwin, Brodsky, and Lepage[29] argued that the elastic and inelastic collisions of a hadron propagating in a nuclear target might be expected to alter its constituents' transverse momentum distribution ($d\sigma/dQ^2dP_T^2$) and longitudinal momentum distributions ($d\sigma/dQ^2dx_F$) as well as their color quantum number correlations. These kinds of initial-state interactions indicated that soft-gluon exchange effects do not cancel and might destroy the universality property of the parton distribution, i.e., the factorization picture. Later Mueller[28] showed that the color-enhancement effect on $d\sigma/dQ^2dx_F$ that BBL considered, is suppressed by the Sudakov effects[28] with a factor proportional to $1/exp[C\ln^2 Q^2]$[28]. However the smearing effect on transverse momentum distribution is still valid.

Later, a more complete theoretical work showed that a cancellation of amplitudes results in factorization being maintained. In other words, the initial-state interactions are ***cancelled out*** in the hadron-hadron Drell-Yan process. Collin, Soper, and Sterman[25] proved this factorization picture at leading twist level and Bodwin[26] implemented this program to all orders in perturbation theory. They showed the Drell-Yan distribution functions contain all the collinear singularities and spectator interactions, and these functions are simply related to those in DIS. Finally, the $q_f(x)$ and $\overline{q}_f(x)$ measured in DIS can *really* be used in analyzing Drell-Yan data, i.e., the factorization picture does survive the gluon radiation and the leading twist effects.

1.5 Motivation for the Study of the Drell-Yan Process in Nuclei

The dependence of cross section on the nucleon number A of the nuclear target (A-dependence) has generally been assumed to be *linear* in the parton regime. This assumption, i.e. ,

$$\sigma_A(x, Q^2) = A^\alpha \sigma_N(x, Q^2) \tag{1.17}$$

with $\alpha = 1$, is called the incoherence assumption for the nucleus. This is an extension to the parton level of the incoherence picture of single nucleons in the case of a nucleus. The purpose of an A-dependence study is to find out whether the nuclear medium would invalidate this incoherence picture. Based on the discussion in section 1.4.5, if it does invalidate this picture, we would expect deviations from $\alpha = 1$ in the Drell-Yan process to result from changes in the quark distribution functions due to the long-distance effect of the nuclear medium, rather than from the modification of the form of the subprocess cross section equation. In addition to the factorized form of the Drell-Yan cross section, the incoherence assumption of cross section implied in equation 1.17 can be reduced to an incoherence assumption of parton distribution functions.

The general view of nuclear structure before 1983 was that, at large Q^2 , nucleons contribute incoherently to the structure function $F_2(x, Q^2)$ (defined in equation 1.9), which is probed by DIS experiments, at least for $0.05 \leq x \leq 0.7$. For quark distributions, this statement may be expressed in the form

$$A * q_f^A(x, Q^2) = Z * q_f^p(x, Q^2) + (A - Z) * q_f^n(x, Q^2). \tag{1.18}$$

At small enough x, the *shadowing effect*[48] was expected to invalidate equation 1.18. Because the virtual photon in that kinematic region could not resolve individual nucleons within the nucleus, the cross section would not grow linearly

with A. For large enough x, Fermi smearing[72] of the nucleon's momentum distribution also invalidates equation 1.18.

Except for the shadowing effect at very small x and Fermi smearing at large x, it was generally believed that equation 1.18 would hold to a good approximation. Moreover, prior to 1983, experiments were usually not of sufficient statistical or systematic precision to reveal more than gross deviations from equation 1.18.

The experimental results published in 1983 by the European Muon Collaboration showed that there were deviations from this expectation, and this phenomenon is now referred to as the "EMC effect".

1.5.1 EMC Effect

The first precise "test" of the incoherence assumption was published by the European Muon Collaboration (EMC) [36] in 1983. It was a DIS experiment using $\mu + A \rightarrow \mu' + A$ to probe the nuclear structure. Because it is known that the x dependence of up and down quark distributions differ, it would be inappropriate to compare heavy-target data with hydrogen data. The best comparison is for an $N = Z$ nucleus, such as ^{40}Ca, to be compared with an unbound deuterium target. As the latter is not available, comparison is made to real deuterium, which is a loosely bound $n - p$ system ($E_{bind} = 2.2$ MeV). The EMC group[36] compared data from iron with data from deuterium. The fact that there is a slight neutron excess in Fe leads to only a small correction. The data were published in the form of a ratio:

$$R_{EMC}(x) \equiv \frac{F_2^{Fe}(x)}{F_2^{D}(x)} \tag{1.19}$$

A compilation of data is presented in figure 1.5[30]. The data of the EMC[36] and BCDMS[32,33] collaborations are taken at "large Q^2 " in the sense that

$Q^2 \geq 10$ GeV^2 for all x. On the other hand, in the SLAC data sample[34,35], Q^2 becomes rather small at small x (i.e., $Q^2 \simeq 1$ GeV^2). Except in the small x region ($x < 0.1$), all data are consistent with each other. Thus, this indicates that no marked Q^2 dependence of $R_{EMC}(x,Q^2)$ is observed. In addition, within either the CERN or SLAC data samples, there is no observed Q^2 dependence either. In the small x region, SLAC iron and EMC copper data reveal the shadowing effect. For $0.1 < x < 0.2$, all data show an indication of enhancement. In the region of intermediate x ($0.2 < x < 0.7$), all data consistently show the depletion. SLAC data, which starts to rise in the region of larger x, shows an indication of the Fermi smearing effect.

The "naive" expectation expressed in equation 1.18 implies that $R_{EMC}(x,Q^2) \simeq 1$, for $0.05 \leq x \leq 0.7$. However, the data in figure 1.5 show a definite deviation from this expectation.

DIS from atomic nuclei has revealed a depletion and a moderate enhancement of the sum of valence and sea quark distribution functions, i.e., $F_2^A(x,Q^2)$, in the region of parton momentum fraction, $0.3 \leq x \leq 0.6$ and $0.1 \leq x \leq 0.2$ respectively. There have been numerous experimental confirmations[30,32,33,34,35] of the original EMC effect in the intermediate x region. Recently, the region $x \leq 0.10$, often referred to as the shadowing region, has become an interesting experimental and theoretical topic. We shall postpone the discussion of this topic until section 1.5.4.

1.5.2 Models for the EMC Effect

Many of the theoretical attempts to calculate the EMC effect fall into two general categories: QCD and conventional Nuclear Physics approaches. Q^2 rescaling models belong to the former, while pion-excess models and quark-

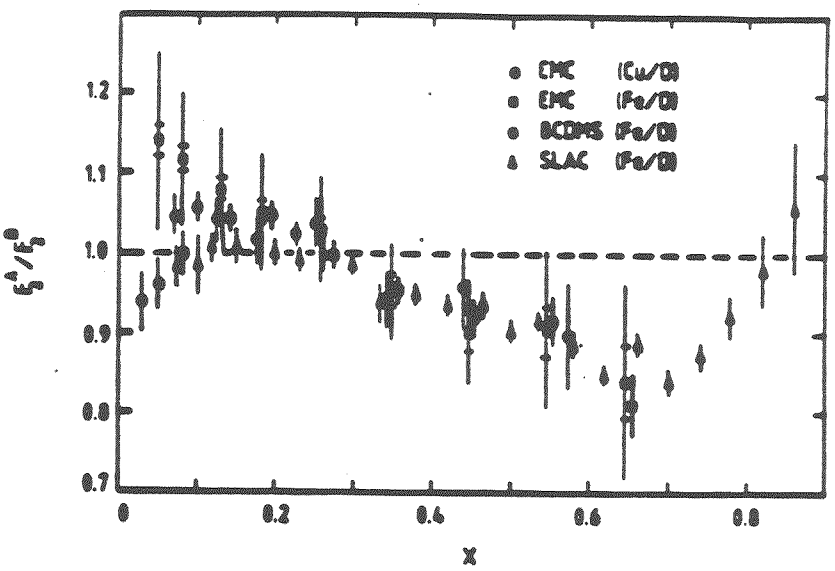

Figure 1.5: Ratios of the nucleon structure functions $F_2^{Cu,Fe}/F_2^D$; 1988 compilation taken from Ref. [30].

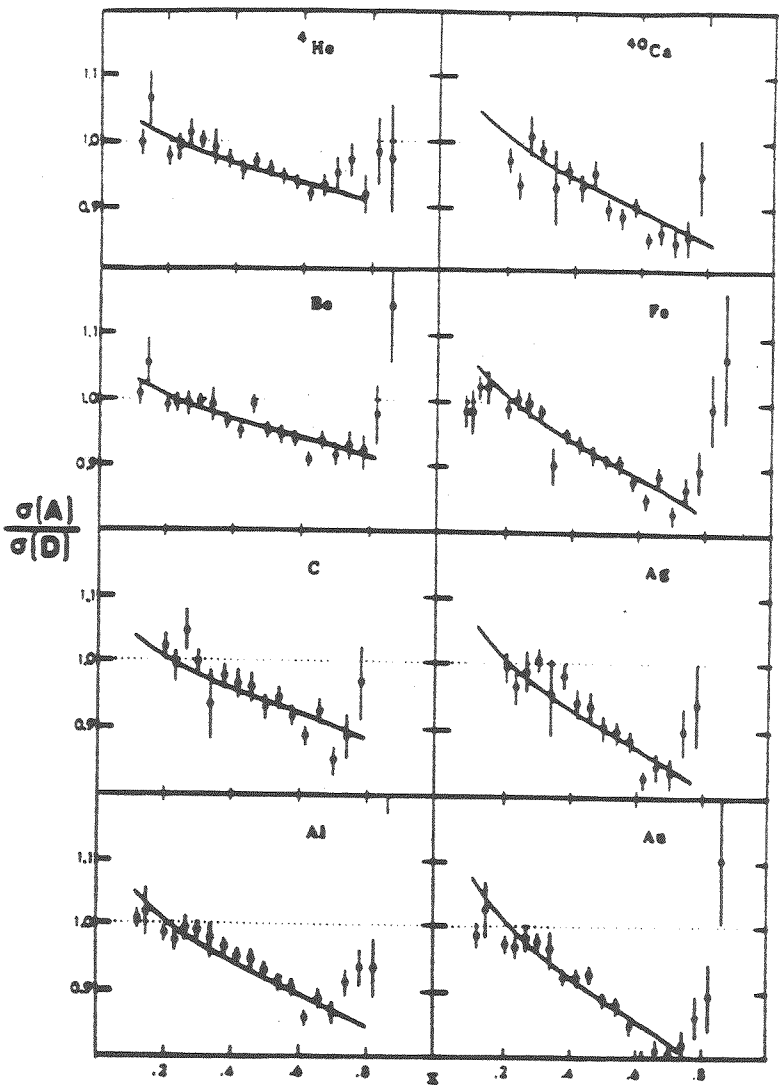

Figure 1.6: Comparison of the measured x-dependence of the ratio of electroproduction cross sections, $\sigma(A)/\sigma(D)$, with descriptions of the rescaling model (indicated by solid curves)[42]. The data are from SLAC and are averaged over Q^2. The eight nuclei correspond to A = 4, 9, 12, 27, 40, 56, 107, and 197.

cluster models are of the latter [10].

In the context of the Q^2 evolution equation, one may suppose two reasons for the EMC effect, $q^A(x,Q^2) \neq q^N(x,Q^2)$: either $\Lambda_A^2 \neq \Lambda_N^2$, or $q^A(x,\Lambda^2) \neq q^N(x,\Lambda^2)$. In other words, the lower momentum confinement cutoff Λ^2 may be different for a quark in a nucleus, or the initial (non-perturbative) distributions from which one begins the QCD evolution may be different. The QCD approach is to assume the confinement sizes of free and bound nucleons are different. The conventional approach is to assert that the initial boundary conditions, $q^A(x,\Lambda^2)$ and $q^N(x,\Lambda^2)$ are different.

Within the uncertainty of the data, the rescaling model describes fairly well the A-dependence of the F_2 structure functions in the region of $0.2 < x < 0.7$. The other class of models describes the A-dependent behavior of F_2 structure functions equally well in the region of $0.2 < x < 0.8$. However, they make significantly different predictions on the A-dependence of the antiquark distribution.

Rescaling Model

The rescaling model[42] assumes that nuclear binding generates EMC effect in a way similar to the Q^2 dependence of the structure function. It is based on the observation that data measured with a particular target at various values of Q^2 show essentially the same phenomenon as data measured at the same Q^2 but with different targets.

[10] Quark cluster model is not discussed here because of four reasons: 1) Its usage of counting rules, which determine the quark distributions in multiquark clusters, has been questioned. The counting rules can only be applied properly near the edge of phase space; however the EMC effect is in the region of $0.1 < x < 0.7$. 2) Even in the three-quark case, this model only works qualitatively. 3) It is very sensitive to the details of the six-quark cluster and nucleon distributions. 4) After incorporating Fermi smearing into this model, it gives a rise in the A-dependent ratio at considerably smaller values of x than in the EMC data[39].

The main idea is that, in a nucleus, the hadron scale Λ_h is smaller than that in the free nucleon, i.e., the confinement size increases, but the exact mechanism is not specified in the model. Therefore, the value of Q^2/Λ_h^2 in nuclear structure functions per nucleon is larger than that in the nucleon structure functions, while compared at the same value of Q^2.

The Bjorken-x dependence of the ratio $\frac{F_2^A(x,Q_0^2/\Lambda^2)}{F_2^D(x,Q_0^2/\Lambda^2)}$ can be described by an equivalent ratio $\frac{F_2^D(x,Q_0^2/\Lambda_A^2)}{F_2^D(x,Q_0^2/\Lambda_D^2)}$, where Λ_D is larger than Λ_A. The discussion of the Q^2-dependent distribution function in the section 1.4.2 tells us that the latter ratio would give a value greater than unity in smaller-x regions, but a value less than unity in larger-x regions. This is just the qualitative shape of the EMC effect. This model predicts characteristic enhancements at low x and depletion at medium x in *both* the valence- and sea-quark distributions. One thing to bear in mind is that this is a phenomenological model, i.e., it does not have a mechanism to calculate the A-dependence of the EMC effect. It has its own free parameter to be adjusted in order to fit the experimental data.

Figure 1.6 shows the fit of this model to the DIS data. It gives a fair fit between 0.2 and 0.7. In order to describe the rise of ratio between 0.7 and 0.9 (Fermi smearing effect), one needs a detailed model of the A-dependence of Λ_h, which is not contained in this model. Because this model does not incorporate shadowing and Fermi smearing mechanisms, it is not applicable in the regions of $x < 0.2$ and $x > 0.7$.

Pion-Excess Model

The pion-excess model assumes that the structure functions of nucleons and pions, $F_2^N(x,Q^2)$ and $F_2^\pi(x,Q^2)$, are not affected by the nuclear medium, and each hadron in a nucleus contributes incoherently in DIS. The reason for the EMC effect is attributed to the excess of pions in the nucleus, which determines

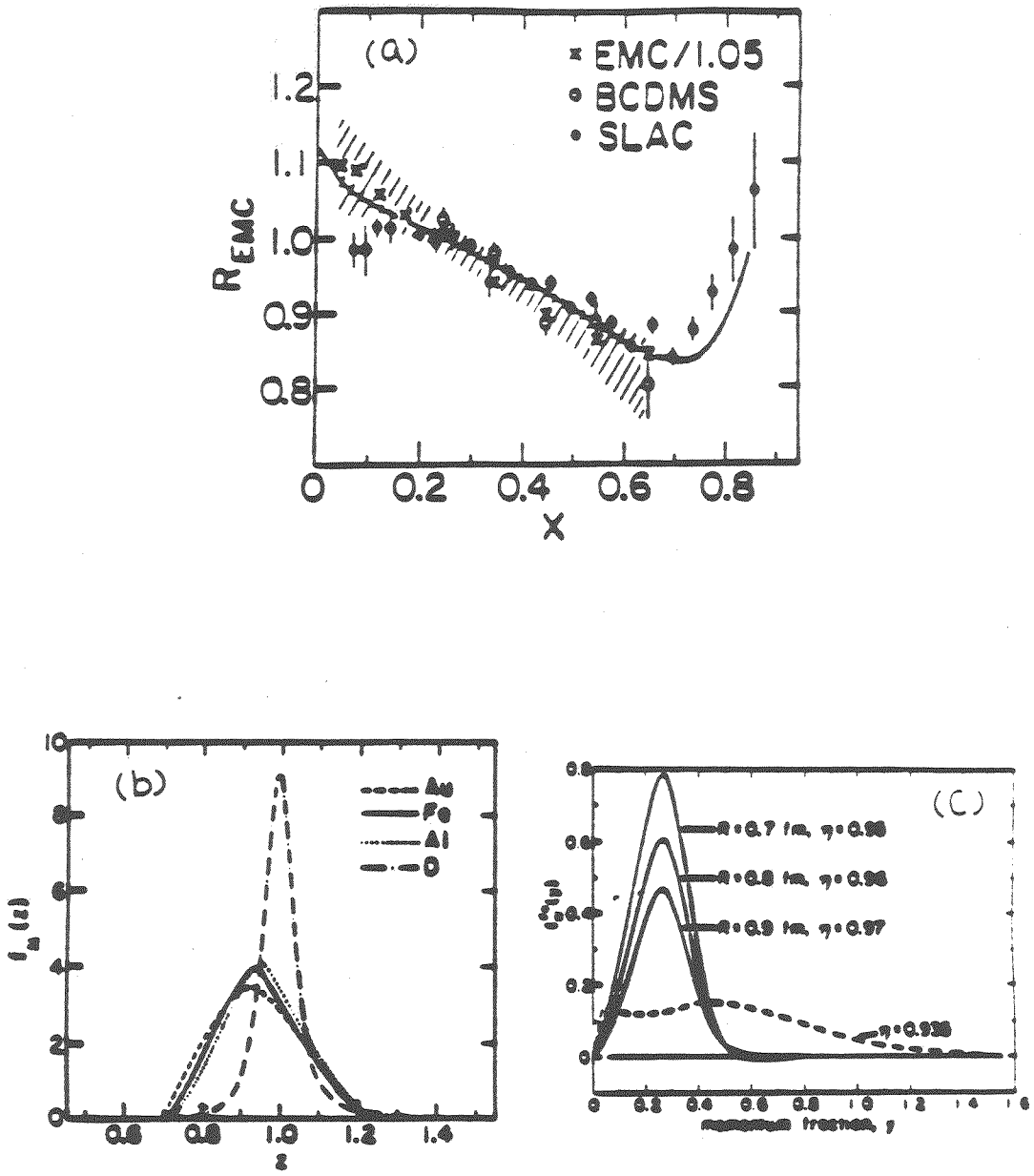

Figure 1.7: Comparison between DIS data and pion-excess model description is shown in the upper panel where EMC data is normalized downward by 5% : Computed nucleon and pion distributions in nuclear medium are shown in the lower two panels[39,43].

the initial boundary condition, i.e., the nuclear structure function at Q_0.

We start with the momentum conservation of a nucleus,

$$\int_0^A z f_N(z) dz + \int_0^A y f_\pi(y) dy = 1. \qquad (1.20)$$

where z and y are momentum fractions per nucleon carried by nucleons and pions in a nucleus. The number distributions $f_N(z)$ and $f_\pi(y)$ are for nucleons and pions. With this condition, one may derive a convolution formula [11] for the structure function $F_2^A(x, Q^2)$ as,

$$F_2^A(x, Q^2) = \int_{z>x}^A f_N^A(z) F_2^N(x/z, Q^2) dz + \int_{y>x}^A f_\pi^A(y) F_2^\pi(x/y, Q^2) dy \qquad (1.21)$$

where x is the momentum fraction per nucleon carried by the struck parton inside a nucleus. The structure function of a nucleus, per nucleon, $F_2^A(x, Q^2)$ is expressed in terms of the structure functions $F_2^N(x, Q^2)$ and $F_2^\pi(x, Q^2)$, which have been measured by the DIS and Drell-Yan processes on free nucleons and pions, respectively. These two structure functions serve as the inputs to the pion-excess models and the magnitude of excess pions is controlled by a parameter η. The distribution functions that are needed to be calculated in this model are $f_N(z)$ and $f_\pi(y)$. Because the bound state wave function of a nucleus is known, at least in principle, the distributions $f_N(z)$ and $f_\pi(y)$ in a nucleus are calculable.

The distribution $f_N(z)$, which is calculated with the shell model and a Fermi-gas distribution[43], has a peak at z slightly less than unity. Figure 1.7(b) shows $f_N(z)$ distributions calculated for nuclear targets. It is clear that the rise at large x in the EMC data can be described by the smearing effect of nuclear $f_N(z)$ distributions.

[11] This is not quite the same situation encountered in the Q^2 evolution equation because it convolutes two different space-scale descriptions, quark and nucleon distributions, to give a quark distribution in a nucleus.

The one-pion-exchange (OPE) process leads to a contribution

$$\delta^{OPE} F_2^N(x, Q^2) = \int_x^1 f_\pi^N(y) F_2^\pi(x/y, Q^2) dy, \tag{1.22}$$

to the intrinsic structure function of the nucleon. The distribution function $f_\pi^N(y)$ in a free nucleon is simply calculated with the elastic form factor at the πNN vertex[39]. The distribution function in a nucleus is calculable by the conventional approaches[39]. The net result of this calculation is that there is an *excess* distribution of pions, which contributes to the DIS process for a nucleon in a nucleus. Thus, the distribution function $f_\pi^A(y)$ in the second term of equation 1.21 is identified as the excess-pion distribution in a nucleus. Because of the requirement of momentum conservation (equation 1.20), both the enhancement of the valence-quark distribution at large x and the excess-pion distribution produced in nuclear targets, result in a decrease of the valence-quark distribution[43] in the region of intermediate x. This decrease consequently accounts for the depletion in the region of intermediate x where valence-quarks dominate. The enhancement of the data at small x clearly is attributed to the excess-pion distributions, which peak at small x.

The shell-model binding energies are not known precisely and computations of $f_\pi^A(y)$ are model dependent. Therefore, different nuclear models essentially have their own way to compute these two distribution functions. The nucleon distribution used by Berger, Coester, and Wiringa[44] has a slightly narrower width than that of Llewellyn-Smith and of Ericson, and Thomas [46,47], but the difference has no substantial effect[39] on the prediction of Fermi motion at large x. Because valence quarks dominate in the regions of intermediate and large x, the nuclear structure function F_2^A is not particularly sensitive to the shape of f_π^A; both models give similar descriptions of the EMC data in the intermediate region of x. Llewellyn-Smith[46] calculated a pion-excess

distribution (as shown in figure 1.7(c)) with a peak at $y \approx 0.3$, which is very different from that calculated by Berger et al.[43,44], as the latter distribution extends to large y. Thus the former one causes the sea distribution to be enhanced at low x and depleted at large x, but the latter one results in an enhancement of the sea distribution over a wider range of x.

Comparison with the data (figure 1.7(a)) indicates that the pion-excess model successfully accounts for the EMC data in the region of $0.2 < x < 0.8$. These models do not incorporate the shadowing mechanism; therefore, they could not describe the ratio below $x = 0.1$.

1.5.3 The Unique Role of the Drell-Yan Process in the Study of the Antiquark Sea

There are two different proposals to explain the EMC effect: the QCD and pion-excess approaches. They make very different predictions of the A-dependence on antiquark sea, as seen in figure 1.8. Therefore, a decisive measurement on antiquark sea is needed to resolve different models.

Natural processes to consider are neutrino and antineutrino DIS on nuclei, which enable one to extract separate valence and sea distributions. Because most models make similar predictions for the A-dependence of structure function in the x region where valence distributions dominate, a measurement of separate valence distributions could not help in resolving models. In contrast , there are significant differences between various predictions for the sea at intermediate x (> 0.3). However, the sea is dying out in this region and the uncertainty of neutrino flux is large; previous neutrino data shown in figure 1.8 had over 30% uncertainty within which all predictions are consistent. A precision measurement of the tail of the sea distribution using antineutrinos seems unreachable.

The process of J/ψ production in muon-nucleus collisions is also a possibility for determining the nuclear gluon distribution. However, there are uncertainties in the free-nucleon gluon distribution function, as well as in the knowledge of the production mechanism for J/ψ formation. The data are also limited to very low values of x. Therefore, this process is not very useful in separating the models.

Bickerstaff, Birse, and Miller[39] proposed that these models can be distinguished by the proton-nucleus Drell-Yan experiments, which measure lepton pairs in certain kinematic regions. Because the factorization picture of the Drell-Yan process holds and the K-factor does not depend on target or projectile, nuclear cross sections probed by the Drell-Yan process at large x_F can reveal the modification of the antiquark sea in the nuclear medium. For the experimentally accessible kinematic regions ($x_F > 0$) in which the annihilation of a projectile quark and a target antiquark dominate, the A-dependent ratio of the Drell-Yan cross sections leads to the A-dependent ratio of antiquark distributions[38]. This can be seen from the following sequence of equations. We define R_{DY} to be the ratio of Drell-Yan cross sections.

$$R_{DY} \equiv [(d^2\sigma_A/dx_1dx_2)/(d^2\sigma_N/dx_1dx_2)] \cdot [2/A].$$

For the kinematic condition $x_F \geq 0.3$, one can see from equation 1.6 and the fact that $\bar{q} \approx 0$ for $x \geq 0.3$ that the ratio reduces to,

$$R_{DY} \approx \sum_f e_f^2 \cdot q_f^{beam}(x_1)\bar{q}_f^A(x_2) / \sum_f e_f^2 \cdot q_f^{beam}(x_1)\bar{q}_f^N(x_2).$$

The sum over quark flavors, $\sum e_f^2 q_f^2$, is dominated by the up quark term because: 1) the charge-squared ratio of up quark to down quark is four; 2) there are two up quarks to one down quark in the proton beam; and 3) the up quark

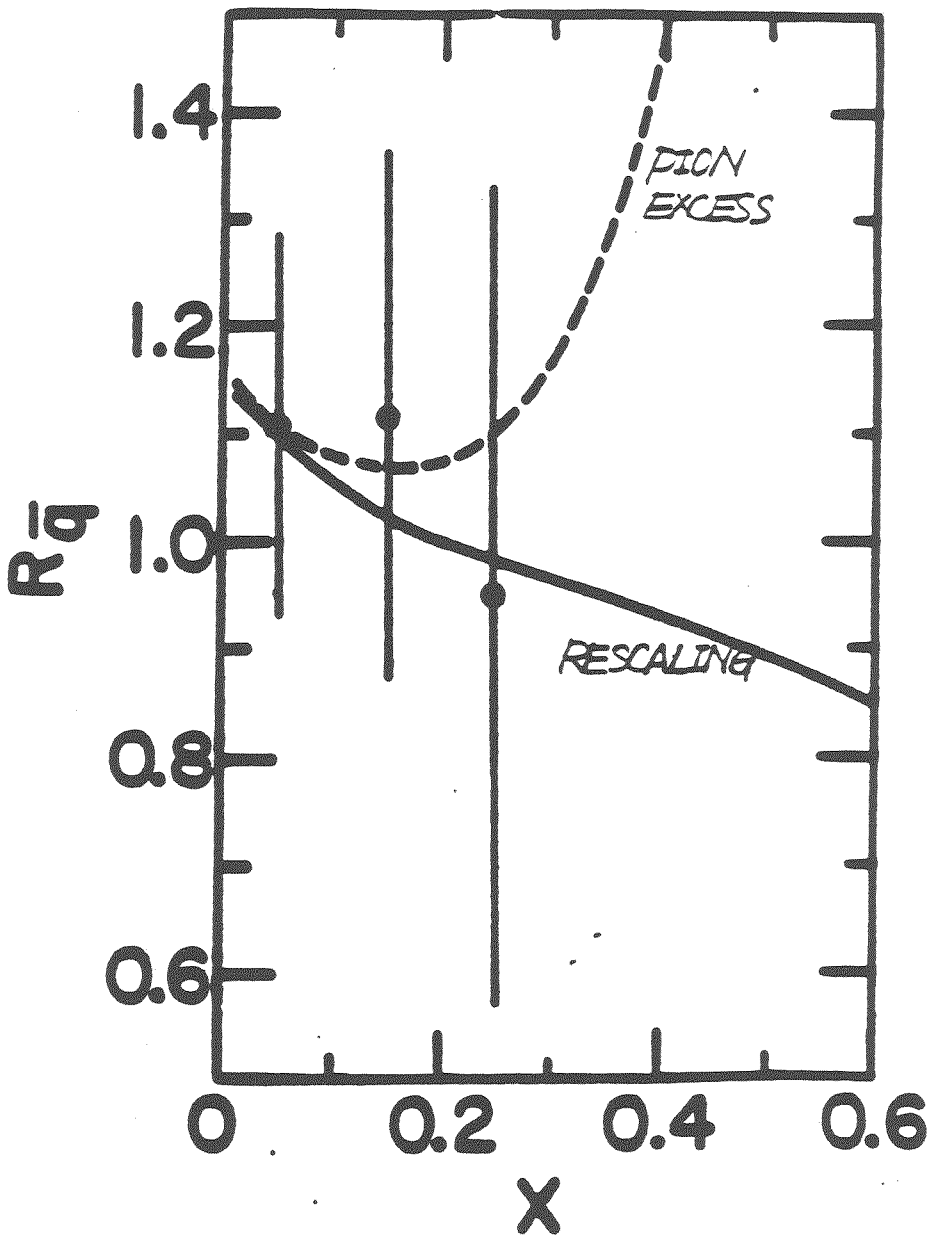

Figure 1.8: Comparison of the rescaling and pion excess prescriptions with Fe data. The solid curve shows Q^2 rescaling result and dashed curve shows pion excess result on the ratio of antiquark distributions[43].

distribution is stiffer than that of down quark. Thus, the previous equation reduces to

$$\begin{aligned} R_{DY} &\approx e_u^2 \cdot q_u^{beam}(x_1)\overline{q}_u^A(x_2)/e_u^2 \cdot q_u^{beam}(x_1)\overline{q}_u^N(x_2) \\ &= \overline{q}_u^A(x_2)/\overline{q}_u^N(x_2). \end{aligned}$$

Thus, a measurement of R_{DY} for proton-nucleus compared to proton-deuterium collisions with $x_F \approx 0.3$ is a direct measure of the nuclear medium modification of the up antiquark distributions. The requirements of such a dedicated Drell-Yan experiment will be high statistics data at $x_F > 0.3$ (large rapidity) with very good control of systematic errors.

1.5.4 The Shadowing Effect

Shadowing is a term used to describe the situation in which the cross section of a particular physical process is observed to increase less rapidly than linearly with nuclear baryon number A. In other words, the parameter α is less than 1.

Recently, the EMC group[30,31] has extended their measurements into the region of $x \leq 0.1$. Shadowing is a notable feature of the new results, which are shown in figure 1.9. One sees that the ratio of structure functions $F_2^A(x, Q^2)$ / $F_2^D(x, Q^2)$ drops below unity for $x \leq 0.1$. It begins to occur at larger values of Bjorken x as A increases. Also, the magnitude of the deviation from unity grows with increasing A.

The kinematic range of the data in figure 1.9 is $< Q^2 > \geq 4$ GeV^2 at $x \simeq 0.03$, increasing to greater values as x increases. Thus, the shadowing effect in these data seems to be a large-Q^2 phenomenon.

The notion of incoherence in the parton model, extended from simple hadrons to nuclei, leads one to expect that, to first approximation, cross sections for

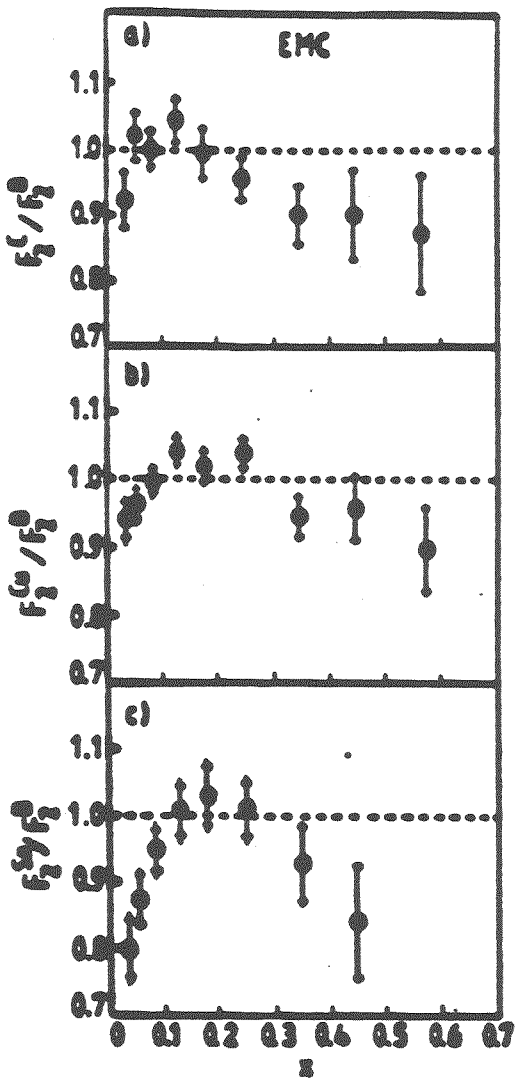

Figure 1.9: Ratios of the nucleon functions (a)F_2^C/F_2^D, (b)$F_2^{C_u}/F_2^D$, and (c)$F_2^{S_n}/F_2^D$ as a function of x. The errors shown are the total errors. obtained by adding the statistical and systematical errors in quadrature. The inner error bars show the statistical errors only[30].

short-distance or "hard-scattering" processes should grow linearly with A in the small x regime. The parton model predicts neither shadowing nor anti-shadowing.

This feature is not dealt with in either the nuclear-bound-state or QCD-rescaling models of the EMC effect. Moreover, these and other data indicate weak dependence of shadowing on Q^2. The observed weak dependence on Q^2 is not consistent with the nuclear shadowing model of Brodsky, Close, and Gunion[106], nor is it easy to reconcile with conventional hadron dominance or vector-meson dominance models of shadowing.

The parton-recombination model of Berger and Qiu[51] is consistent with not only the existence of shadowing, but also the qualitative features of the data.

Parton Recombination Explanation

A parton-recombination idea was proposed by Nicolaev and Zakharov[49] in 1975 to account for the low x depletion effect. The recombination model assumes that at sufficiently small x, the constituent quarks and/or gluons from different nucleons (and mesons) in a nucleus are not independent. Instead, in contrast with the simplest assumption in the parton model, these constituents overlap spatially, interact, and recombine so as to reduce the effective parton number per nucleon.

Partons in a large nucleus are overcrowded in the small x region due to two reasons: 1) QCD evolution requires the number of small-x partons grows significantly with Q^2; and 2) if the nucleus incoherence assumption is valid, the effective nuclear parton number at any fixed impact parameter would be proportional to $A^{1/3}$.

Partons from different nucleons could overlap spatially at a given impact

parameter. In the nuclear infinite momentum frame, the nucleus occupies a Lorentz contracted longitudinal size $\Delta z_A \simeq 2RM/P$, where R, M, and P are the nuclear radius, mass and momentum respectively; $M \simeq mA$, where m is the mass of a nucleon, and we define $p = P/A$ to be the per-nucleon momentum. The longitudinal size of a sea quark or gluon of momentum of $k_z = xp$ is about $\Delta z \approx 1/k_z$. When $\Delta z > \Delta z_A$, or $x < 1/2mR$, all sea quarks and gluons having such x values, and having the same impact parameter, overlap spatially. As $R \approx r_0 A^{1/3}$, with $r_0 \approx 1$fm, this occurs at values of $x \simeq 0.1A^{-1/3}$; for ^{12}C, $x \simeq 0.04$, for ^{184}W, $x \simeq 0.02$. On the other hand, *onset* of shadowing could begin at larger values of x, where the partons from neighboring nucleons first begin to overlap partially. This occurs at $R = r_0$ or $x \simeq 0.1$.

Because of the large number of overlapping partons in the small-x region, one would expect to have interactions among the partons from different nucleons and, consequently, changes in the effective parton number distribution per nucleon. The net effect of parton recombination is to decrease the effective parton number per nucleon in the small-x region. This model predicts shadowing effect in the small-x region, where parton recombination is the dominant effect.

Q^2 Dependence of Shadowing

Because parton recombination would produce the opposite effect on the sea distribution against that of the gluon radiation while Q^2 is increasing, the Altarelli-Parisi evolution equation was expected to be modified to include the parton-recombination mechanism in order to describe the weak Q^2-Dependent behavior shown in the data. Indeed, Mueller and Qiu[50] formulated a modified, nonlinear Altarelli-Parisi evolution equation by adding two small terms. These terms determine recombination probabilities for gluons to go into gluons or into quarks in a low-density limit. The nuclear radius and mean density in

these two terms enable one to characterize the nuclear medium. A factor of $1/Q^2$ is compensated with the Q^2 dependence of $q(x,Q^2)$ to produce a weak Q^2-dependent shadowing effect. Their description is consistent with the new EMC data in the region of low x.

x Dependence of Shadowing

In order to have a precise prediction of shadowing at a given Q^2, a set of well-measured nuclear parton distributions at a reference starting value, Q_0^2, is needed. In principle, these parton distributions with low x depletion at low-Q^2 can be calculated with the leading twist-4 contribution[52]. The x dependence of shadowing effect is also interpreted as a consequence of an antiquark-nucleus multiscattering process[53]. In a way to describe the shadowing effect, Berger and Qiu parametrize the x-Dependent ratio of shadowing as

$$\begin{aligned} & = 1, x_c < x < 1 \\ R_s(x,Q_0^2,A) & = 1 - K_s\cdot(A^{1/3}-1)\cdot\tfrac{\Delta x-\Delta x_c}{\Delta x_A-\Delta x_c}, x_A \le x \le x_c \\ & = 1 - K_s\cdot(A^{1/3}-1), 0 < x < x_A \end{aligned}$$

where K_s is a recombination constant, $x_A = 1/2mR$, and x_c is a critical value below which parton recombination starts to occur.

Combined with the parametrization of the EMC effect, they made a theoretical estimate, not a prediction, that is consistent with the data for the full range of x, with $K_s = 0.1$ and $x_c(Fe) = 0.18$.

A-Dependence of Onset of Shadowing

Berger and Qiu[51] argued that, qualitatively, the observed A-dependence of the onset of shadowing should show the following behavior: 1) $x_c \sim 0.2$ for a

"large enough" nucleus; 2)x_c is between 0.1 and 0.2 for smaller nuclei; and 3)x_c is larger for the bigger nucleus because the bigger nucleus has more non-surface nucleons. They averaged over the recombination effect of partons from both surface and non-surface nucleons and derived the A-dependence of x_c as,

$$x_c = 1/mr(1 + 3(\frac{2}{A^{1/3}}) - 3(\frac{2}{A^{1/3}})^2 + (\frac{2}{A^{1/3}})^3),$$

where $A^{1/3} \geq 2$, m is the nucleon mass, and r is the nucleon radius.

This recombination picture explains the low-x depletion effect in the new EMC data fairly well. Here, we want to ask whether the same effect exists in the antiquark content probed by the Drell-Yan process, i.e., is it a process-independent effect?. Further, if it exists for the Drell-Yan process, can parton-recombination make a fair description of it? An A-dependence Drell-Yan experiment that covers the x region below 0.1 can provide an answer to the first question and a motivation for the second one.

1.5.5 Initial-State-Interaction Effects in Hadron-Nucleus Collisions

According to the discussion in section 1.4.5, the factorization theorem was proved by Collin and Soper in the case of hadron-hadron collisions. The natural question to be asked next is "whether it will hold in the hadron-nucleus collision ?". If it does hold in the hadron-nucleus case, a problem discussed below would occur. Bodwin, Brodsky, and Lepage[27] pointed out that according to the factorization theorem, when the mass of the lepton pair is large, the cross section for the Drell-Yan process can be written in the parton-model form as shown in equation 1.6. This equation implies that the beam quark does not interact with spectator partons in the target hadron. If a nuclear target such as ^{238}U is used, this expression suggests that the quark is unaffected by its passage

through the nucleus enroute to annihilation on, say, the back face of the nucleus. Consequently, all nucleons in the nucleus participate equally in the process and there is no nuclear-induced energy loss for the incoming parton. However, nuclear-induced energy loss phenomenon is familiar to experimentalists who routinely deal with the consequences of thick-target radiation.

BBL presented the analysis in terms of a nonrelativistic QED model and argued that the principal conclusions are valid in QCD as well[27]. The analysis showed that the effects of initial-state interactions lead to an increase in the average of the square of the transverse momentum of the lepton pair that is proportional to the length of the target, and the factorized form of the Drell-Yan cross section can be invalidated unless the beam energy is greater than a scale that grows with the length of the target. In other words, the factorization picture is valid provided a target-length condition is satisfied.

Target-Length Condition and Q^2-Dependent cross section

This target-length condition can be understood in terms of the uncertainty principle, which is applicable for both elastic interactions and inelastic interactions induced by gluon-exchange. This argument can be illustrated by the inelastic interaction shown in figure 1.10, where s is the invariant mass square of interacting proton and nucleus A, and s_a is the invariant mass square of beam active quark and nucleus A. The transverse mass square caused by the soft-gluon exchange from nucleus A is given by

$$\begin{aligned} \Delta m^2 &= (P_a + P_g)^2 - P_a^2 \\ &\approx -2E_a P_{gz}, \end{aligned}$$

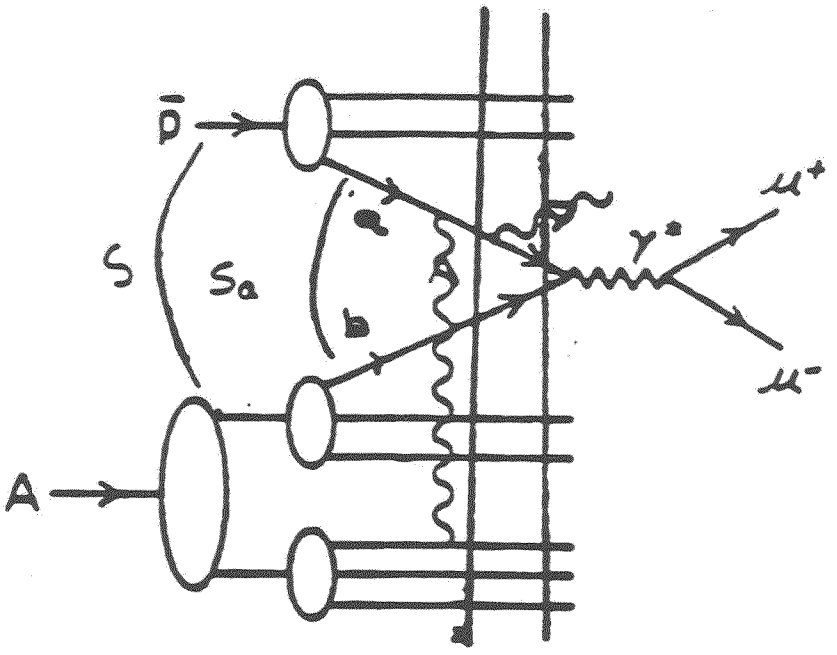

Figure 1.10: Inelastic interaction induced by soft gluon exchange.

where P_a and E_a are the momentum and energy of active parton a, and P_g is the momentum of the gluon exchanged by parton a with a spectator parton in nucleus A. Thus, the magnitude of longitudinal momentum of this soft gluon is $\Delta m^2/2E_a$. According to the uncertainty principle, the off-shell active quark must radiate a gluon after traveling a length greater than $L_{coh.}$ in order to recover from the virtual state before the annihilation process. The coherence length $L_{coh.}$ is given by,

$$\Delta P_{az} \cdot L_{coh.} \approx 1,$$

with $\Delta P_{az} = P_{gz} = \Delta m^2/2E_a$. Because of $s_a \approx 2E_a M$ and $s_a = x_a s$, the target-length condition can be expressed as,

$$L_A(\text{thickness of nucleus}) \quad < L_{coh.} \approx x_a s/M\Delta m^2 < s/M\Delta m^2,$$

where M is the nucleon mass and x_a is the momentum fraction of proton beam carried by the active parton a. In the case of elastic scattering, the same target-length condition is obtained with a similar argument. For an 800 GeV proton beam, this condition is clearly satisfied, provided $M \approx 1$ GeV, $\Delta m^2 \approx 1$ GeV^2, and $L_A \approx 5$ fm (25 GeV^{-1}).

If a target length is greater than the coherence length, the beam active quark would radiate a gluon before annihilating an active antiquark in the target. In other words, the energy of the beam quark is depleted, and the cross section $d\sigma/dM^2$ is affected by the soft-gluon exchange. Therefore, the coherent cancellation of soft-gluon interactions is not valid and the factorization picture breaks down.

On the other hand, if it is satisfied, the elastic active-spectator initial-state interactions would have a negligible effect on the beam parton's longitudinal

momentum, and the copious radiation induced by these interactions would not occur. Thus, the factorization picture in hadron-nucleus holds under the target-length condition.

When the target-length condition is satisfied, then one must look beyond $d\sigma/dQ^2dx_F$ in order to see the effects or signatures of active-spectator initial-state interactions. A sensitive quantity is the P_T distribution of the lepton pair, which is broadened by initial-state interactions.

Smearing of P_T Distribution

The P_T distribution of the Drell-Yan pair for a nuclear target is a result of three different contributions: 1) the intrinsic transverse momentum fluctuations of the constituents of the interacting hadrons, as predicted in the naive Drell-Yan model; 2) the transverse momentum gained by one of the active quarks through the gluon radiation process, as discussed in section 1.4; and 3) the transverse momentum kicks accumulated by the beam active quark going through the nuclear medium via initial-state interactions. The P_T distribution of a nucleon is the net result of the first two contributions, and the third factor will smear or broaden this distribution in the case of a nuclear target.

Michael and Wilk[54] investigated this P_T broadening effect about the time other people were studying the effect of gluon radiation. They made a simple but rather model-independent analysis. Their main conclusions are: 1) the nuclear cross section per nucleon after integration over P_T , is the same as that of the nucleon, i.e., there is no A-dependence of the total cross section; 2) the difference $\delta < P_T^2 >$ between the average values $< P_T^2 >_A$ and $< P_T^2 >_{A=1}$ depends on the rescattering factor and the absorption coefficients only, not the P_T distribution caused by the gluon radiation correction term. Because the P_T dependence of the nuclear enhancement parameter α depends on a term

that is the convolution of gluon-radiation and rescattering factors, as is the A-dependent ratio of cross sections, one could not separate these two effects cleanly. However, $\delta < P_T^2 >$, which depends on the rescattering effect only, is a more sensitive quantity to reveal the A-dependent behavior of the initial-state interaction effects. They compared the prediction on α as a function of P_T with the result of an A-dependence experiment E288[77] at Fermilab. The prediction is consistent with E288 data, but the over 5% error on α is too large to make a decisive comparison. BBL[29] used another approach to get a similar result on the increment of P_T , which is shown below:

$$\Delta < P_T^2 > \propto L \propto A^{1/3}, \tag{1.23}$$

where L is the length of target.

This transverse momentum smearing effect was further confirmed by the Drell-Yan A-dependence experiment NA10[55] using π^- beams at energies of 140 and 286 GeV with tungsten and deuterium targets. They found the differences of $< P_T^2 >$ between tungsten and deuterium targets are $0.16 \pm 0.03 \pm 0.03$ GeV^2 at 140 GeV and $0.15 \pm 0.03 \pm 0.03$ GeV^2 at 286 GeV.

1.6 The Production Mechanism of Heavy Quarkonia

Because charmonium and bottomonium are composed of *heavy* quarks, perturbative QCD in combination with the nonrelativistic quarkonium model provide a description of their production mechanisms. The lowest order QCD cross sections are initiated by gluons and light quarks. To order α_s^2, the quark and gluon fusion processes contribute to the cross section in the low-P_T region with a mean P_T determined by the intrinsic transverse momentum carried by active

gluons. The inclusive cross section is expressed as

$$d\sigma(hN \to QX) \approx \sum_{A,B} \int dx_1 dx_2 f_a(x_1, Q^2) f_b(x_2, Q^2) d\sigma(ab \to Q\overline{Q}), \qquad (1.24)$$

where x_1 and x_2 now stand for gluon momentum fractions. It is similar to the formula for the naive Drell-Yan inclusive cross section, except that the subprocess cross section is evaluated using QCD instead of QED. The factorization assumption is embodied in this equation. The integrand is a product of three separate factors: a subprocess cross section and two parton distributions, which are assumed to be universal, for each interacting hadron. The validity of factorization in $hN \to QX$ requires that m_Q be large[59]. The inclusive heavy-quark cross section is expected to behave as

$$\sigma(hN \to Q\overline{Q}X) \propto \frac{1}{m_Q^2} F_{hN}(m_Q/\sqrt{s}), \qquad (1.25)$$

where m_Q^2 is the mass of the heavy quark, and F_{hN} is a scaling function.

Due to the heavy mass of c and b quarks, a non-relativistic potential model[64] can provide a fair description of the quarkonium bound states. Thus, one can calculate the subprocess cross section[62] with their wave functions in combination with the amplitude of QCD hard scattering (the diagram in figure 1.11 with quarkonium's leg omitted). The dimuon decay of these quarkonia is through the annihilation of the heavy quark and antiquark inside the quarkonium.

A natural step to improve the production mechanism is to include the next order perturbative QCD calculation. To order α_s^3, there are more contributions to the subprocess cross section from different diagrams in which a parton recoils against the resonance in the final state, thus leading to a large transverse momentum. This is similar to the Drell-Yan case in which the higher order diagrams contribute to the large transverse momentum. Among these diagrams, only 1.11(g) provides the *direct* J/ψ or Υ production. The resonances pro-

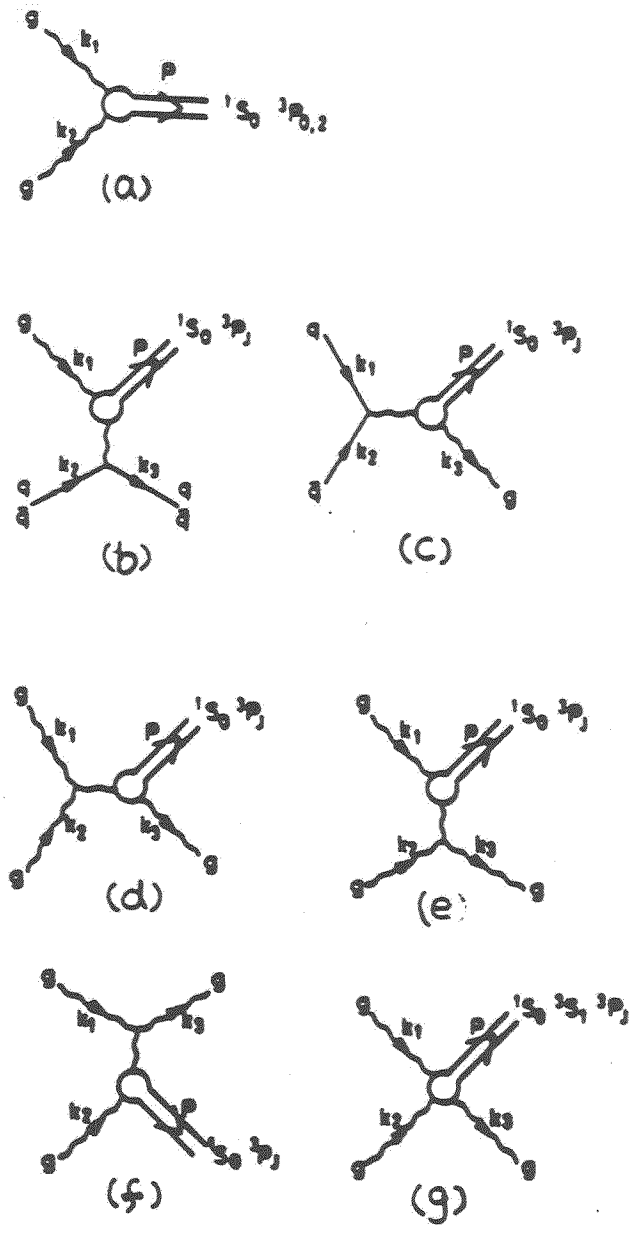

Figure 1.11: The heavy quarkonia production diagrams[74]. The spectroscopic notation for the quarkonium states (e.g., $c\bar{c}$ and $b\bar{b}$ eigenstates) is $^{2S+1}L_J$ where L=0, 1, ... corresponds to S, P, ... , respectively and where $J = L + 0$ or $J = L + 1$ for the singlet(S=0) and triplet(S=1) states, respectively.

duced in the other diagrams might contribute the the J/ψ and Υ production via radiative decay.

The cross section[62] calculated with the above α_s^2 and α_s^3 diagrams agrees reasonably well with the J/ψ and Υ data, within theoretical and experimental errors, in the absolute magnitudes of the cross sections, as well as in the transverse momentum and energy dependence.

1.6.1 Charm Quark Production

However, there are more challenging aspects of the charm data than that of bottom to theoretical calculation. First, the most serious problem is the overall normalization of the charm quark cross section. The LEBC-MPS collaboration measured 34.4±4.2μb for $\sigma(pp \rightarrow \overline{D}DX)$ at $\sqrt{s}$ =38.8 GeV. The perturbative QCD calculation of this cross section is highly sensitive to the choice of the charm quark mass m_c and is about a factor of 2 smaller than data for the choice of m_c=1.2 GeV. Yet, the theoretical confidence in the cross section calculation drops as m_c decreases.

Second, the nuclear dependence for the production of charm mesons and baryons indicates the value of α is about 0.75, which is similar to that for the production of light hadrons, such as pions and kaons.

Third, the hadrons containing a charm quark, such as $D^{\pm}$, Λ_c, and $\overline{\Lambda}_c$, are observed to be produced predominantly centrally in x_F or y. This is in agreement with theoretical expectations. However, there are significant leading charm effects in the distribution $d\sigma/dx_F$ observed in $\pi^- N \rightarrow (D^-, \overline{D}^0)X$ [88]. It is flatter and extending to larger values of x_F than that of $\pi^- N \rightarrow (D^+, D^0)X$. The interpretation of leading charm effects seems to require a model beyond the scope of QCD perturbation theory.

These problems encountered above seem to imply that non-perturbative

and higher-order effects may make big contributions to the hadroproduction of charm.

1.6.2 Bottom Quark Production

The mass of the bottom quark is approximately 5 GeV, comparable to the values $P_T \geq 5$ GeV at which hadron jet physics is known to be described reasonably successfully. Therefore, QCD perturbation theory is expected to be more reliable for bottom quark production. Indeed, it describes the data within a factor of two.

1.6.3 Other Possible Production Mechanisms

Some other mechanisms were introduced in attempts to describe the charm production data. While some or all of these may be relevant for charm, with mass $m_c \sim 1$ GeV, they are not justified to be relevant for the production of bottom quarks with mass $m_b \simeq 5$ GeV. For instance, the probability that there is an intrinsic heavy-quark component in the initial hadron state falls as m_Q^{-2}. This means that the intrinsic heavy quark provides a higher-twist contribution to $\sigma(hN \to bX)$, suppressed by m_b^{-2}. It is relevant for bottom quark production only in restricted parts of phase space. Likewise, diffractive[91], recombination?, and final state prebinding? contributions are either included in the perturbative expansion or belong to the higher-twist class.

1.7 Motivation for the Study of J/ψ , ψ' , and Υ Production in Nuclei

The hadroproduction mechanisms of quarkonium are generally believed to be quark or gluon fusion. The latter one becomes dominant when the beam energy is beyond the order of 100 GeV. This offers an opportunity to extract the

gluon distribution in the nucleon from quarkonium production cross sections and to observe the possible EMC-type effect on the gluon distribution[56] in nuclei. However, a recent experiment E537[57] at Fermilab reported an observation that the cross section per nucleon for J/ψ production is suppressed in tungsten interactions relative to the lighter targets, especially at large values of x_F . This is just opposite to the expectation from the various explanations of the EMC effect. Three-gluon fusion[107], nuclear shadowing[108], and rescattering models[109] were proposed to describe the feature of large x_F depletion.

In addition, heavy-ion collision experiments[58] also observed a similar J/ψ suppression phenomenon. It was shown that this attenuation is a natural feature of inclusive nuclear reactions, independent of the state of the nuclear matter [76]. Therefore, a full understanding of the mechanism of this suppression in the simpler proton-nucleus collision environment can provide basic information for a further search of the signature of the quark-gluon plasma in heavy-ion collision experiments.

The mass range of E772 data covers quarkonia J/ψ , ψ' , and $\Upsilon's$, and there were 5 nuclear targets used for A-dependence study. Therefore, our data can provide a more complete study of the nuclear effects on the production cross sections and possible new production mechanisms of quarkonia.

1.7.1 J/ψ Nuclear Dependence

As stated in the discussion of section 1.6.1, there is some evidences that the theoretical interpretation of charm results will not be simple, because m_c and $< P_T, c >$ are small, non-perturbative and higher-order perturbative effects are likely to be large. Several J/ψ experiments agree that if the A-dependence is parametrized as $A^{\alpha(x_F)}$, then $\alpha(x_F \geq 0.2)$ =0.7-0.9. This is significantly different from $\alpha \simeq 1$, which is expected for a hard scattering process. The anomalously

large open-charm (D mesons) cross sections at high x_F are also inconsistent with incoherent hard scattering. Because of limited statistics, these effects are not as firmly established as the A-dependence. Thus, a J/ψ nuclear-dependence study may provide a better way to examine the validity of intrinsic charm production mechanism[90], nuclear shadowing model[65], rescattering model[99], comover model[93,94], and final hadron size model[101].

1.7.2 Υ Nuclear Dependence

Bottom quark production appears to offer a valuable new process in which to test perturbative QCD in detail. Because m_b is large, theory is expected to be quantitatively reliable.

1.8 Experiment E772 at Fermilab

A precision A-dependence experiment E772[66] was performed in the Fermilab Meson-East Laboratory using an 800 GeV proton beam incident on five different nuclear targets. It was carried out from 1987 to 1988 by a collaboration group comprising physicists from Case Western Reserve University, Fermilab, Los Alamos National Laboratory, Northern Illinois University, State University of New York at Stony Brook, University of Illinois at Chicago, and University of Texas at Austin. First results on the A-dependence of the Drell-Yan cross sections have been published[79]. Results on the J/ψ and ψ' production have also been published[103]. Results on Υ production will be published shortly[104].

The principal goal of E772 was to measure the A-dependent behavior of dimuon production, i.e., to measure the ratio

$$Ratio = \frac{\sigma_A(\mu^+\mu^-)/A}{\sigma_D(\mu^+\mu^-)/2}, \tag{1.26}$$

where $\sigma_A(\mu^+\mu^-)/A$ is either the Drell-Yan or the heavy-quarkonium production

cross section per nucleon on a target of nucleon number A. Deviations from unity indicate the antiquark (or maybe gluon) structure functions are modified by the nuclear medium. Expected deviations from unity in this ratio are at the level of 5% ; thus, a significant measurement requires the determination of the ratio to an accuracy of about $1 - 2\%$.

To achieve an accuracy of 1-2 % error in the cross section ratio, this experiment required a *high incident beam flux* as well as an *accurate target-to-target relative normalization*, *high background rejection*, and *good mass resolution*. A high incident flux is needed because the Drell-Yan cross sections in the region of interest are 10^{-33} to 10^{-38} cm^2. The background rejection is required, because no tracking device can handle the charged particle fluxes near the target. The accurate target-to-target relative normalization was essential for an 1% experiment. Good mass resolution is important not only for separating the continuum from resonance dimuon production but also for resolving peaks from one another.

In order to obtain a high statistics sample of Drell-Yan events, we needed a total luminosity of the order of 10^{43}. This gives 10^5 dimuon events with a spectrometer of $\sim$ 5% acceptance. The intensity of the proton beam at Fermilab was between 10^{10} and 10^{11} protons per second. In a 6-month run, it would produce a total proton number of 10^{17}. Using targets of ~ 8 g/cm^2, this would give a luminosity of $\sim 10^{43}$, which just met our needs.

The E605 spectrometer at the Meson-East experimental area of Fermilab was designed to measure high-mass and forward-going lepton pairs in p-p center-of-mass frame; therefore, it is the right apparatus to use for selecting the desired type of annihilation, viz., beam quark annihilating with target antiquark. With a proton beam (2 up quarks and 1 down quark), harder quark distributions , and this kinematic condition (quark in the beam and antiquark in the target),

a study of $\overline{u}$ quark distributions in nuclear targets became achievable in this experiment.

This spectrometer was designed to have the capacity to handle the high beam flux of the ME beam line. An intelligent trigger system associated with this spectrometer rejects most of the background produced by the high-flux beam. From the E605 data (1984), we know that it has a mass resolution (FWHM) of about 85 MeV at the Υ mass, which is sufficient to separate resonance states in both J/ψ and Υ families. A modified E605 spectrometer implemented with a new target-motion device, allowed us to perform precise relative normalizations.

Chapter 2

Apparatus

The experiment E772 was performed at the Meson-East experimental area of Fermi National Accelerator Laboratory. The spectrometer employed was a modified version of the E605 spectrometer[1]. The major spectrometer elements are shown in figure 2.1. It has the capabilities to take *high beam flux*, to give *good mass resolution*, and to allow for *accurate target-to-target relative normalization*. It was used in E772 to meet the experimental requirements set by the physics goals described in chapter 1. This apparatus consisted of a target-interchange device, 3 dipole magnets, 7 hodoscope planes, 4 drift tube planes, 6 multi-wire proportional chamber planes, 12 drift chamber planes, and 6 proportional counter planes. It also has an electromagnetic and a hadronic calorimeter and a ring-imaging Cherenkov counter, which, however, were not used in this work.

2.1 Apparatus Overview

In this experiment, the coordinate system used is the following: the z axis follows the beam direction, the y axis points upward vertically, and the x axis is along the horizontal direction to form a right-handed coordinate system. The x and y coordinates were measured from the beam line and z = 0 was at the

[1] FNAL-605, in Major Detectors in Elementary Particle Physics, Particle Data Group, LBL-91 Supplement, revised (1985).

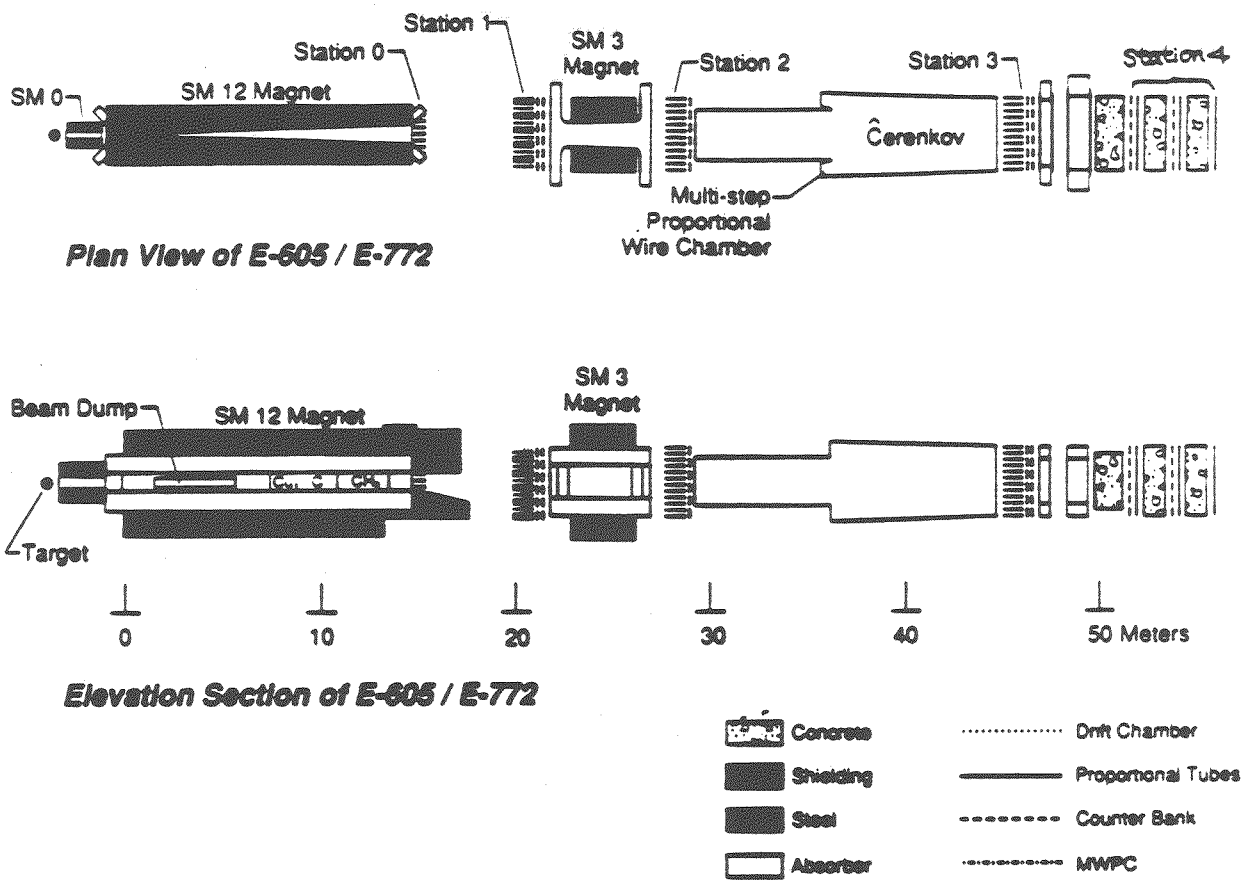

Figure 2.1: The E605/E772 spectrometer

upstream face of the SM12 dipole magnet.

The carefully tuned and monitored 800 GeV proton beam was sent to the experimental area, where it struck one of 5 nuclear targets. The targets were arranged into groups of 2 or 3 targets under the control of a target-interchange device, as discussed in the section 2.3.1. The high-momentum charged particles produced in the target were split according to the sign of their charges while going through the set of three magnets. The muons were focused onto the downstream detectors with magnet SM12, which swept away the low-momentum particles. Inside this magnet was a beam dump, which stopped the 800 GeV proton beam. It also stopped the large flux of low-P_T particles from the targets. Also inside SM12 was an absorber wall, which stopped most of the slow hadrons produced in the beam dump. It consisted of Cu, C, and CH_2 blocks, and gave a hadron attenuation factor of e^{-20}. With this absorber wall, this apparatus had a mass resolution of $\sim$ 200 MeV and $\sim$ 300 MeV (FWHM) for the J/ψ and Υ peaks, respectively. The muon momenta were accurately measured by the SM3 magnet and its upstream and downstream wire chamber sets. Positive identification of muons was achieved by requiring signals in the hodoscopes and the proportional tubes located in the downstream end of the calorimeter and between sections of the concrete walls. Electrons and any hadrons that leaked through the absorber wall were stopped in the calorimeter, whereas muons penetrated the calorimeter and the additional concrete blocks behind the calorimeter.

2.2 Proton Beam and Monitors

The 800 GeV proton beam[80] was produced in the Tevatron, which is a superconducting proton synchrotron. It then was extracted and split by the

switchyard, for sending 3 streams of proton beams to the Meson, Neutrino, and Proton beam lines for fixed-target experiments. Protons in a spill were bunched into RF *buckets* which were separated from one another by 19 ns, with bucket length of $\sim$ 1 ns. Each *spill* contained about 10^9 buckets and lasted 23 seconds. The spill repetition rate was 1/minute.

The proton beam was transported through the Meson-East beam line, as shown schematically in figure 2.2. The number of protons was measured by two monitors, SEM3 and SEM4 (Secondary Emission Monitors). They measured the total beam flux per spill independently. SEM3 was located further upstream than SEM4. When the proton beam went through the foils in these monitors, secondary electrons in nuclei were knocked out and collected at an anode. This anode current was integrated and digitized. The SEM4 circuit was set to give out one pulse per 0.8×10^8 protons. These pulses were counted with scalers in the E772 counting room. The SEM calibration data are summarized in an internal memo by C.N. Brown.

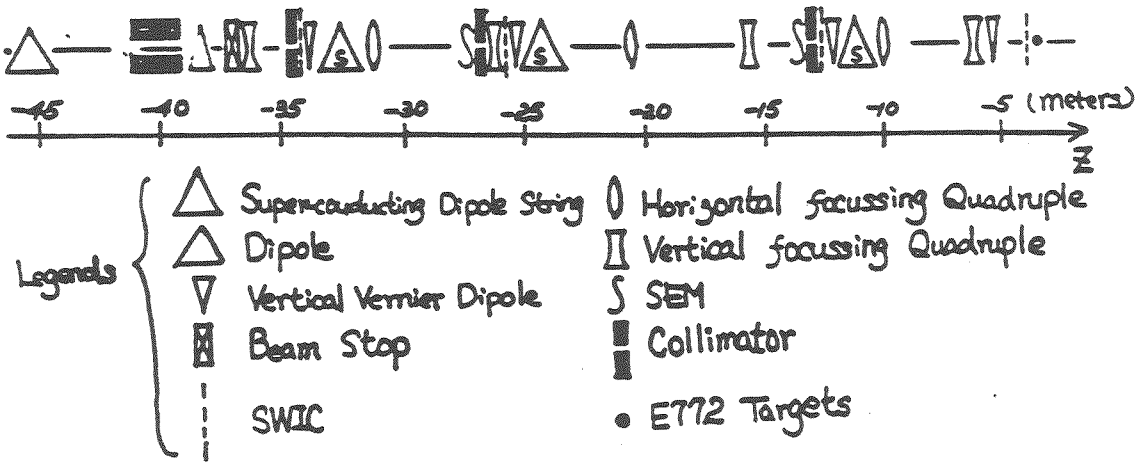

Figure 2.2: The Meson East beam line configuration.

This beam transport system consisted of magnets, monitors, collimators, and beam stop. The dipole magnets, which included superconducting dipole strings and vertical vernier dipole, were used to steer the beam horizontally and vertically. The protons were focused in both x and y by horizontal and vertical focusing quadruple magnets. The three Segmented Wire Ion Chambers (SWIC's) right after the collimators provided information on beam positions and profiles for beam tuning. A beam stop was available to stop the beam in the case of upstream beam-line tuning or emergency.

In total, there were 8 beam monitors that were used in E772 to record relative proton count, beam position, and beam profile. Table 2.1 shows the device names, scaler name and function of each monitor.

device name	name of scaler monitor	type of monitor
SEM3 SEM4	SEM3 SEM4	integrated proton count monitors
BPMX BPMY	BEAM-X,I_x BEAM-Y,I_y	intensity and position monitors
$\lambda/4$ cavity	LAM4	intensity monitor
90°-monitor	AMON WMON	luminosity monitors
ME6SWIC		beam profile in x and y

Table 2.1: Specifications of monitors.

The Beam Position Monitor (BPM) was located about 3 meters upstream of the target box. It was both a beam-position and intensity monitor. It consisted of two cylinder-like metal strips A and B attached to the opposite sides of its inner wall, having their axes aligned with the axis of this monitor. These two strips recorded image currents I_A and I_B, induced by the proton beam going

through the monitor along the direction of its axis. Knowing the values of these two currents, we could find out the beam position and intensity according to the relationships below,

$$\text{Beam position} \propto (I_A - I_B)$$
$$\text{Beam intensity} \propto (I_A + I_B)$$

This BPM had position resolution of about 0.2 mm and could be operated properly in the range between $\sim 10^{11}$ and 10^{13} protons/spill.

The $\lambda/4$ cavity monitor, which was located about 1m downstream of the BPM's, operated on a similar principle. It's output current was, to first order, independent of beam position.

The luminosity monitor AMON consisted of 4 scintillation counters (AMON1, AMON2, AMON3, and AMON4) located on the right-hand side of the target, while WMON was another set of similar counters. Their counting rates were proportional to the product of beam intensity and target thickness, and thus served as relative luminosity monitors. Because the detectors covered a small solid angle as viewed from the targets, the AMON and WMON counting rate per SEM were characteristic of each target. These counters were also used in the measurement of the electronic live time and spill duty factor.

The four removable SWIC's provided the information of beam position and profile along the proton beam line, right up to the target box. They provided a cross check with the measurement by BPM's spill by spill. During the data taking, ME3SWIC and ME4SWIC were moved out of the beam line in order to reduce background events generated from these possible upstream sources. The nearest one with respect to the target box was used to calibrate the measurements of BPM's in early runs.

With all these monitors in operation, we could closely monitor the beam characteristics in Meson-East beam line. The typical beam parameters are listed in table 2.2.

beam parameter	
flux	10^{10} - 10^{11} protons per sec.
dimensions(FWHM) at target	8×2 (x,y(mm))
positions stability(1 hour)	± 1 mm in both x and y
positions stability(several days)	± 3 mm in x and ± 1 mm in y

Table 2.2: Proton beam characteristics.

2.3 Targets and Target-Motion Device

A wide range of atomic weights (from 2 to 184) was covered by our A-dependence study. The targets used were: D, C, Ca, Fe, and W. The center of the target box was located at $(x, y, z) = (0., 0., -3.43)$ meters. Target areal densities were kept nearly equal in order to have the same trigger rate for different targets. Because of the ~ 7.62-cm diameters of all targets and 8×2 mm dimensions of the beam, the targeting efficiency was 100 % . The parameters of these targets and the target-interchange cycles will be described later in this section.

2.3.1 Target-Motion Device

The target array was moved by a motor with 4 sensors to latch the array into each target position. During the data taking period, there were 4 rotations of the 5 nuclear targets to group our 5 nuclear targets: 1) D and Ca; 2) D and Fe; 3) D, Ca, and Fe; 4) D, C, and W. A three-target assembly is shown in figure 2.3. The targets were moved by control from the counting room, up and

down relative to the beam line. The 37-second interval between spills was long enough to permit motion from one target position to the next.

In a typical three-target grouping, each of the three targets was exposed to 12 beam spills with a 36 minute 12-6-12-6 cycle and these cycles were repeated for 5 to 10 days. For the two-target grouping, each target was exposed to 16 spills with a 32 minute cycle. With this frequent target interchange, the uncertainties associated with the drifts in beam tuning, monitor gains, and detector efficiency were reduced to a minimum in the A-dependent ratios.

2.3.2 Liquid D_2 Cylinder Target

The liquid deuterium (D) target, made at Fermilab, consisted of a cylindrical target flask with a cryogenic D_2 liquefier. The flask, which was positioned in an aluminum box, was made of 2.54×10^{-3} cm stainless steel with a diameter of 7.62 cm and a length of 50.8 cm. The whole D target system was operated at a temperature of 24° K.

Over the course of data taking, there were three deuterium gas samples used. These samples were assayed and found to have the compositions shown in table 2.3. The pressure in the flask was monitored by a pressure gauge and its signal was converted to a voltage and then digitized. It was recorded in a monitoring scaler in the counting room. By knowing the D_2 gas pressure in the reservoir, the density of the liquid in the flask could be computed using thermodynamic $P - T - \rho$ data. This is given in an internal memo by H.W. Baer and G. Danner.

2.3.3 Solid-Target Disks

There were 6 sets of solid targets fabricated at Los Alamos National Laboratory: 2 different thicknesses of carbon and calcium targets, 1 thickness of

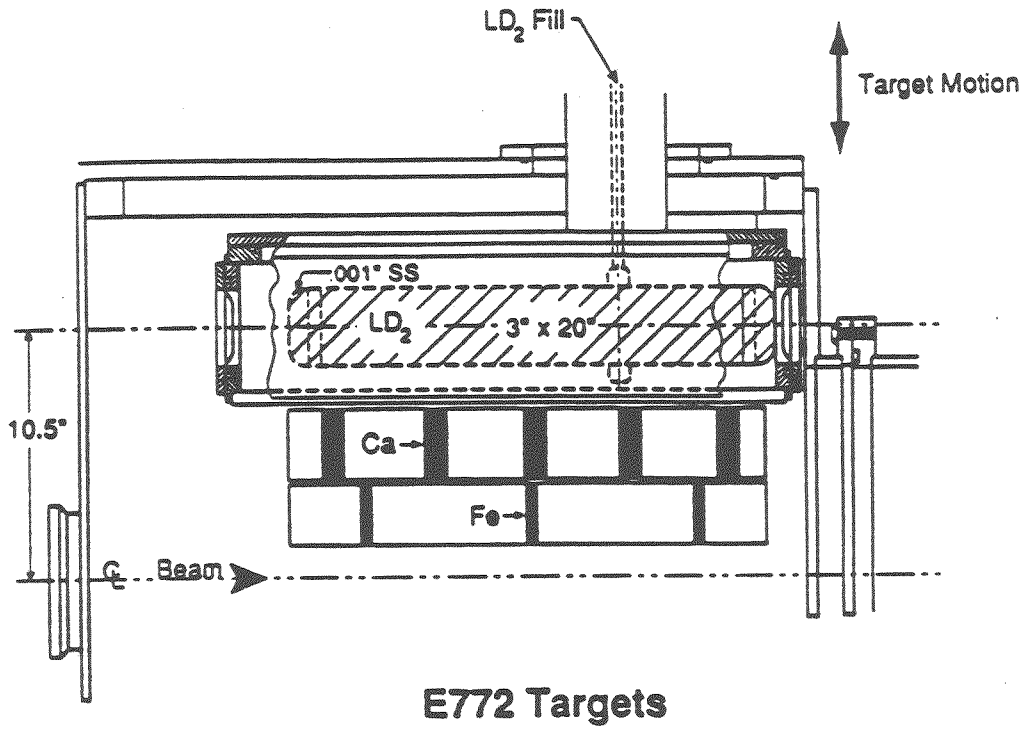

Figure 2.3: Target box array mounting arrangement of target disks.

targets	diameter (cm)	component percentage(%)				thickness (g/cm^2)	λ_I (g/cm^2)
		D_2	HD	H_2	T_2		
$^{2.01}$D	7.6200	98.6	0.80	0.09	0.08	8.293	$\sim$ 54.7
$^{2.01}$D	7.6200	97.0	2.52	0.13	0.09	8.251	$\sim$ 54.7
$^{2.01}$D	7.6200	94.6	5.10	0.20	0.10	8.186	$\sim$ 54.7

Table 2.3: Liquid D_2 target parameters.

stainless steel and tungsten targets. Target parameters are listed in table 2.4. Each set consisted of several disks (2, 3, 4 or 5) held in a cylindrical tube, as

targets	diameter (cm)	no. of disks	thickness (g/cm^2)	λ_I (g/cm^2)
^{12}C	7.2774	4	9.002	86.3
^{12}C	7.2774	5	11.251	86.3
$^{40.1}$Ca	6.9534	3	11.817	117.0
$^{40.1}$Ca	6.9534	5	19.698	117.0
$^{55.4}$SS	7.2800	3	12.079	131.9
$^{183.8}$W	7.2778	2	11.511	185.0

Table 2.4: Solid-target parameters.

shown in figure 2.3. The targets were contained within a large vacuum box directly open to the beam line vacuum system, which had a pressure of approximately 10^{-4} Pa. Two of theses tubes were mounted in alignment frames below the deuterium target.

2.4 Dimuon Spectrometer

This spectrometer, with three magnets and an internal beam dump, can measure equally well electron and muon pairs. The former must be measured without an absorber wall. Muon pairs was the choice in E772 because of the very large interaction rates available when an absorber wall is used. In this configuration, dimuon backgrounds were produced in the beam dump and by

semileptonic decays of D mesons produced in the target. The amount of material between the target and the detector was a compromise between the ability to accept a higher incident flux and the poorer resolution due to multiple scattering of the muons in penetrating the absorber wall.

2.4.1 Magnets

Three dipole magnets (SM0, SM12 and SM3)[80] were used in our experiment with a field configuration to select forward going dimuons ($x_F > 0.$) in the p-p center-of-mass frame, and to reject low-momentum particles ($P_{\mu\mu} <$ 100 GeV). With the direction of increasing z, SM0 was attached to the downstream face of the target box, SM12 was placed between SM0 and the drift tube planes, and SM3 was located between multi-wire proportional chamber and drift chamber planes. This is shown in figure 2.1.

Magnetic Field Configurations

The magnetic fields of these three magnets were oriented horizontally and with relative field directions that depended on different mass settings. The field strengths of these three dipole magnets could be configured to optimize acceptance for different regions of dimuon mass. In E772, three configurations (as shown in table 2.5) were chosen that maximized the yield at 4.5, 6 and 8.5 GeV (referred to as low-, intermediate- and high-mass settings) respectively, as shown in figure 2.1. SM0 served to open up the small opening angles between low-mass muon pairs in the low-mass setting. SM12 was used to focus high-p_t particles into downstream detectors. SM3 was used to measure their momenta. Most of the time, these three magnet currents were stable to one part in 10^3. Their values were monitored spill by spill by a set of scalers.

MASS SETTINGS	SM0 (amps)	SM12 (amps)	SM3 (amps)
LOW MASS	2000.	-2750.	4265.
INT. MASS	2000.	-2750.	-4265.
HIGH MASS	0.	-2750.	-4265.

Table 2.5: Magnet-current configurations.

2.4.2 Beam Dump

Approximately 5.5 meters downstream of the target the non-interacted beam was stopped in a water-cooled copper beam dump. It was located inside SM12 and had a length of 4.27 m. The distance between beam dump and target-center was 5.16 m. This was large enough so that the reconstructed z-vertex of target events would be clearly distinguished from beam-dump events in the off-line track reconstruction. The high x_F dimuon events that were important for the J/ψ and Υ A-dependence studies mostly had at least one track going through part of the beam dump; therefore, the information of beam dump geometry (as shown in figure 2.4) was essential for the muon energy-loss correction in the off-line analysis.

2.4.3 Absorber Walls

Beyond the beam dump, at the downstream end of the 15m dipole, there was a hadron absorber wall constructed of copper, graphite and borated polyethylene blocks. This wall almost fully blocked the SM12 aperture except for the small gaps[2] at the center. There were 1 section of Cu wall, 4 sections of C walls, and 3 sections of CH_2 walls. The absorber-wall parameters are shown in table 2.6.

[2]These gaps at the center of the absorber wall are for allowing the decayed leptons from possible Axion decays to go through.

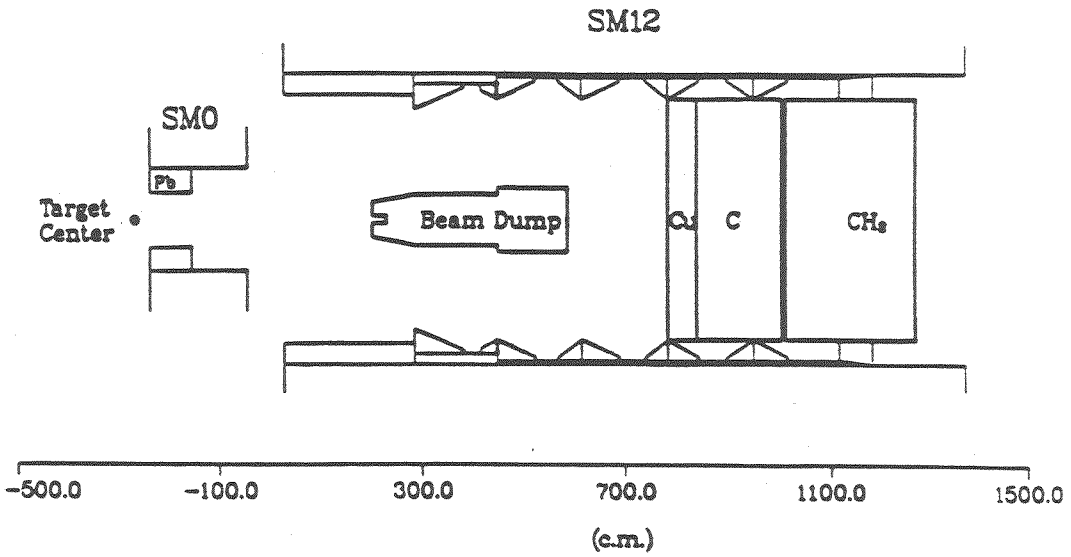

Figure 2.4: The geometry of beam dump and absorber wall inside the SM12.

Type of mat'l	Z coord. of the front face	Thick-ness	Gap		Remarks on the gap
			width	height	
Cu	320"	24"	2.00"	4.000"	lead on sides
C (1st)	344"	27"	3.00"	4.500"	lead on sides
C (2nd)	371"	27"	3.50"	4.000"	lead on sides
C (3rd)	398"	18"	3.75"	4.000"	lead on sides
C (4th)	419"	15"	4.00"	6.000"	all graphite
CH_2(1st)	434"	36"	8.00"	5.500"	wood on sides
CH_2(2nd)	470"	36"	12.00"	5.500"	wood on sides
CH_2(3rd)	506"	24"	7.50"	7.375"	wood on sides

Table 2.6: Absorber wall configurations.

2.5 Tracking Detectors

The tracking detectors were the key part of our apparatus to measure the values of kinematic variables of the lepton pairs. Several wire-chamber and scintillator planes were grouped together to form a detector STATION. There were five stations providing tracking information along the spectrometer, numbered from 0 to 4 in the order of increasing z. STATION 0 was attached to the downstream end of the SM12 yoke. STATION 1 and 2 were just upstream and downstream of SM3. A *Čerenkov* counter was located between STATION 2 and 3. Calorimeters were located behind STATION 3, followed by a hadron absorber wall and STATION 4. There were 8,112 channels of detector tracking data.

2.5.1 Hodoscopes

There were 7 hodoscope planes, which were named with the X- or Y- orientation and the station number: Y1, X1, Y2, X3, Y3, Y4, and X4. Their positions are shown in figure 2.1 and table 2.7. Hodoscope planes were included at each station, except for STATION 0. Each plane was divided into two halves: left(YL) and right(YR) for the Y plane; and up(XU) and down(XD) for the X plane. Each plane was made of plastic scintillator strips. The number of strips(or counters) for each station is displayed in table 2.7, where '*' indicates the end counter. The total number of channels was 194.

NA 110 plastic scintillator was the material of the hodoscopes. The light from each scintillator strip was collected onto a Hamamatsu R329 phototube via a plexiglas light guide. The phototube signals were sent into LeCroy discriminators in the counting room. The pulse height of each channel was carefully set with a Sr beta source in order to have 2 times the amplitude of the discriminator

detector name	Z position (m)	dimensions $x(m)\times y(m)$	thickness inch	channels $x\times y$	cell width (mm)
Y1	20.469	1.22 × 1.52	3/16	2×12	127
X1	20.507	1.22 × 1.52	3/16	12×2	102
Y2	28.319	1.63 × 1.73	2/16	2×17	102
X3	46.659	2.64 × 2.34	4/16	13×2	220(110)*
Y3	46.919	2.64 × 2.34	4/16	2×13	178(191)*
Y4	51.702	2.95 × 2.54	4/16	2×14	178(203)*
X4	54.130	3.20 × 2.90	8/16	16×2	203(181)*

Table 2.7: Hodoscope characteristics.

level.

The hodoscopes had the fastest time response of the various electronic detectors. They were used to select muon tracks and to eliminate *out-of-time* chamber hits, define the *fast trigger logic*, and, most important of all, form 'roads' back to the target, as is described in the next chapter.

2.5.2 Wire Chambers

There were four types of wire chambers used in our experiment: proportional drift tubes (PDT), multiwire proportional chambers (MWPC), drift chambers (DC) and proportional tube counters (PT).

STATION 0 had 4 planes of PDT chambers to measure the y position without any hodoscope plane. Each plane was 1.00 m × 1.22 m and had 120 cylindrical aluminum tubes with a diameter of 1cm. The chamber resolution was between 300 and 400 μm. Their track information was not used in the E772 off-line analysis, but was used in E605 to improve the precision of the momentum measurement.

MWPC and drift chambers were used to measure the track coordinate U, Y, and V at each plane z position for STATIONs 1, 2, and 3. The hodoscope

plane in these stations was located right behind the wire chambers. The U and V coordinates of the particle trajectories at each station, were defined as: 1) U was oriented clockwise along the z axis at an angle of arctan(1/4) with respect to the Y axis. 2) V was oriented counterclockwise at the same angle with respect to the Y axis. Each drift chamber pair with the same view had a plane shifted by half a cell with respect to the other one in order to resolve the drift-direction ambiguity. The hit patterns of MWPC's and drift chambers were the main information used to perform the off-line track reconstruction.

STATION 1 consisted of six MWPC's of 2 mm wire spacing and two hodoscope planes (Y1 and X1). Each U and V plane was 1.28 m × 1.51 m and had 896 channels of output, while the Y plane was 1.28 m × 1.50 m and had 736 channels. The chamber resolution was 635 μm.

STATION 2 had six planes of drift chambers with cell size of about 1 cm and one hodoscope plane Y2. Each U and V plane was 1.68 m × 1.83 m and had 208 channels of output, while the Y plane was 1.68 m × 1.79 m and had 176 channels. The chamber resolution was 254 μm.

STATION 3 had six planes of drift chambers with cell size of about 2 cm and two hodoscope plane X3, Y3. Each U and V plane was 2.69 m × 2.43 m and had 144 channels of output, while the Y plane was 2.69 m × 2.33 m and had 112 channels. The chamber resolution was 229 μm.

STATION 4 consisted of three planes of proportional tubes (PTY1, PTX, and PTY2), which measured the X and Y coordinates, and two hodoscope planes Y4, X4. They were arranged in the order of Y4, PTY1, X4, PTX1, and PTY2 with increasing z. Their track information was used to help the *muon identification* in off-line analysis. Each plane consisted of two layers of proportional tube cells with the size of $25mm \times 25mm$. The two layers of each plane were staggered by half a cell in order to cover the dead region between

cells. The summary of wire chamber characteristics is shown in table 2.8.

The gas mixture in each chamber was provided by a gas-mixture system. Four types of gas were used: ethane, argon, carbon dioxide, and freon. The gas used in the MWPC's was a mixture of 25 % (82.6 % Ar/ 17 % CO_2/ 0.4 % Freon) and 75 % (50 % Ar/ 50 % Ethane). The PDT's, DC's, and PT's used the same gas mixture of 50% Ar and 50% ethane.

detector name	type	Z position (m)	dimensions $x(m) \times y(m)$	channels	cell width (mm)	resolution μm
Y0A	**PDT**	14.694	1.00 × 1.22	120	10.16	406
Y0B	**PDT**	14.703	1.00 × 1.22	120	10.16	305
Y0C	**PDT**	14.713	1.00 × 1.22	120	10.16	356
Y0D	**PDT**	14.721	1.00 × 1.22	120	10.16	356
U1A	**MWPC**	18.967	1.28 × 1.51	896	1.97	635
Y1A	**MWPC**	19.218	1.28 × 1.50	736	2.03	635
V1A	**MWPC**	19.478	1.28 × 1.51	896	1.97	635
U1B	**MWPC**	19.733	1.28 × 1.51	896	1.97	635
Y1B	**MWPC**	19.982	1.28 × 1.50	736	2.03	635
V1B	**MWPC**	20.237	1.28 × 1.51	896	1.97	635
U2	**DC**	27.522	1.68 × 1.83	208	9.86	254
U2'	**DC**	27.576	1.68 × 1.83	208	9.86	254
Y2	**DC**	27.771	1.68 × 1.79	176	10.16	254
Y2'	**DC**	27.825	1.68 × 1.79	176	10.16	254
V2	**DC**	28.023	1.68 × 1.83	208	9.86	254
V2'	**DC**	28.077	1.68 × 1.83	208	9.86	254
U3	**DC**	45.755	2.69 × 2.43	144	20.21	229
U3'	**DC**	45.825	2.69 × 2.43	144	20.21	229
Y3	**DC**	46.008	2.69 × 2.33	112	20.83	229
Y3'	**DC**	46.078	2.69 × 2.33	112	20.83	229
V3	**DC**	46.260	2.69 × 2.43	144	20.21	229
V3'	**DC**	46.330	2.69 × 2.43	144	20.21	229
PTY1	**PT**	51.860	2.97 × 3.05	120	25.40	
PTX	**PT**	54.251	3.43 × 3.09	135	25.40	
PTY2	**PT**	55.899	3.59 × 3.64	143	25.42	

Table 2.8: Wire Chamber characteristics.

Chapter 3

Trigger and Data Acquisition System

A trigger and data acquisition system[80] developed for E605 were used in this experiment, E772. A schematic of this system is shown in figure 3.1. It consisted of a *Triggering System*, a *Readout System*, a *MegaMemory*, and an *On-line Computer*. Background rejection at the on-line stage was mainly carried out by this intelligent trigger system designed to select dimoun events originating in the target. This trigger rate was sufficiently low so that the Readout System could write out the event data to the megamemory without producing significant *dead time*. After every accelerator spill, data were recorded to the magnetic tapes under the control of an on-line computer for detailed off-line analysis.

3.1 Triggering Scheme

There were 2 levels of trigger systems employed to make the trigger decision for recording a set of interesting hit information from the detectors. The *first level trigger system* selected dimuon events and rejected muons associated with different RF buckets. It reduced the trigger rate to a level where the *second level trigger system* could make a further trigger decision, with a small dead

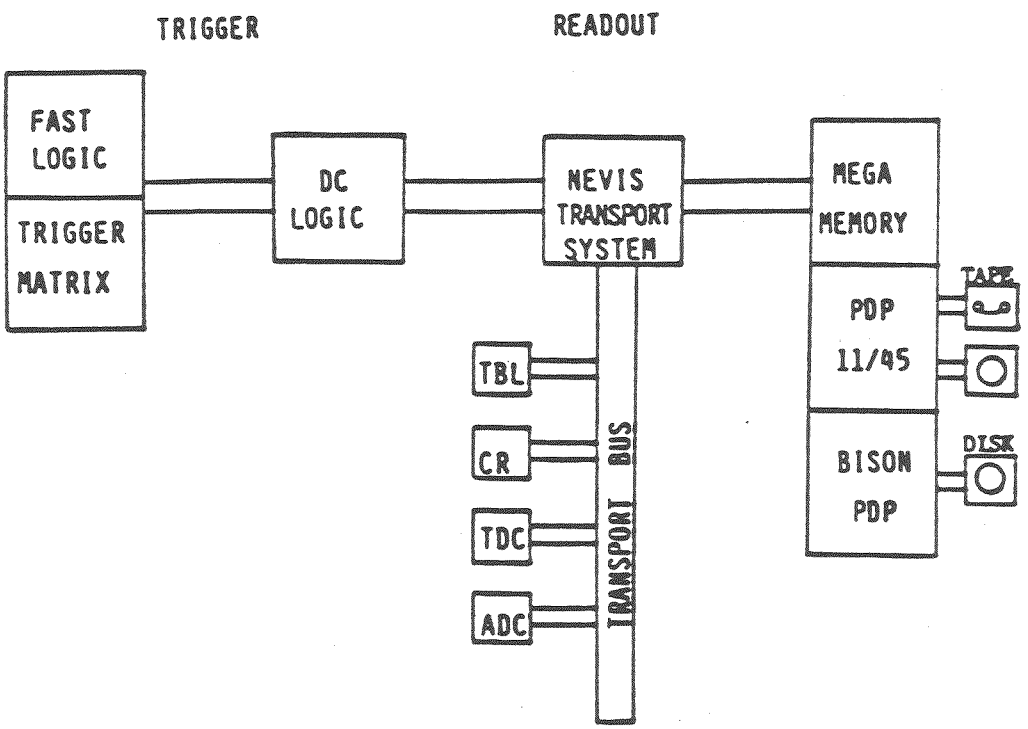

Figure 3.1: The Block diagram of the trigger and data acquisition systems.

time. The first-level triggers consisted of Fast Triggers from coincidence outputs of half-bank(Right and Left) hodoscope signals. The second-level triggers consisted of a set of 4 logically OR'ed outputs for hodoscope half banks(Up, Down, Right, and Left) from Trigger Matrix, and Multiplicity-Veto triggers from coincidence outputs of single-counter signals in each X hodoscope plane. The prescaled first-level triggers and the second-level triggers were the input to DC logic bus. The second level trigger system then made several coincidences out of these triggers on the bus, in order to generate final triggers that corresponded to $\mu^+\mu^-$ pairs (dimuon), $\mu^\pm\mu^\pm$ pairs (like sign), and single μ^+ or μ^- events.

The main trigger (dimuon) basically selected events with the topology of a $\mu^+\mu^-$ pair from the target. It reduced the primary background events, which were muon-pair events from the beam dump, by a factor of $\sim 10^3$.

3.2 First-level Trigger System

Scintillation counters were used to provide input signals for the *Fast Logic*, because of their fast response time (rise-time typically on the order of 1 $nsec$). Signals from the phototubes attached to the scintillation counters were brought into the counting room via coaxial cables to LeCroy 4416 16-channel discriminators. Each discriminator output was synchronized to the accelerator RF signal by the pulse stretchers [86] in order to prevent accidental coincidence between buckets, and then fanned out to several places mainly for making first-level triggers.

3.2.1 Fast Logic

The triggers produced at this Fast Logic were used to start the second-level trigger decision cycle. It roughly defined a trigger set that required muons

transversing the apparatus. In this sub-section, the arrangements and requirements of the Fast Logic are discussed.

The signals from each half-bank of counters(Left and Right halves of each plane) were sent to a hodoscope terminator module, where the logical OR over the half bank was performed. The OR signal was then fed into LeCroy 365AL Quad Logic Units, which generated the output signal $\frac{3}{4}\mu L$ and $\frac{3}{4}\mu R$ from the coincidence of any three out of the four (L or R) bank counters: X1, Y2, Y4, and X4. Finally, the signals $\frac{3}{4}\mu L$ and $\frac{3}{4}\mu R$ were further combined to produce the following Fast Triggers

$$\begin{aligned} \tfrac{3}{4}\mu LR &= \tfrac{3}{4}\mu L \odot \tfrac{3}{4}\mu R \\ \tfrac{3}{4}\mu LPS &= \tfrac{3}{4}\mu L \ /4\mathrm{K} \\ \tfrac{3}{4}\mu RPS &= \tfrac{3}{4}\mu R \ /4\mathrm{K} \end{aligned}$$

where the symbol /4K stands for prescaled by 4096, i.e., only one out of 2^{12} signals was considered as a trigger. The prescaling factor was high because the requirement $\frac{3}{4}\mu$ (L or R), corresponding to an apparent muon on either side of the apparatus, was very easily fulfilled. The Fast Triggers were then logically ORed by the *Trigger Fan In*(TFI) module to *start* the DC Logic cycle. Basically, $\frac{3}{4}\mu LR$ generated the 'go' signal for the second-level trigger system to look for target dimuons, because it roughly defined two muons transversing the apparatus. These triggers, $\frac{3}{4}\mu LR$, $\frac{3}{4}\mu LPS$, $\frac{3}{4}\mu RPS$, and TFI, were also sent to the DC Logic at the second-level trigger system.

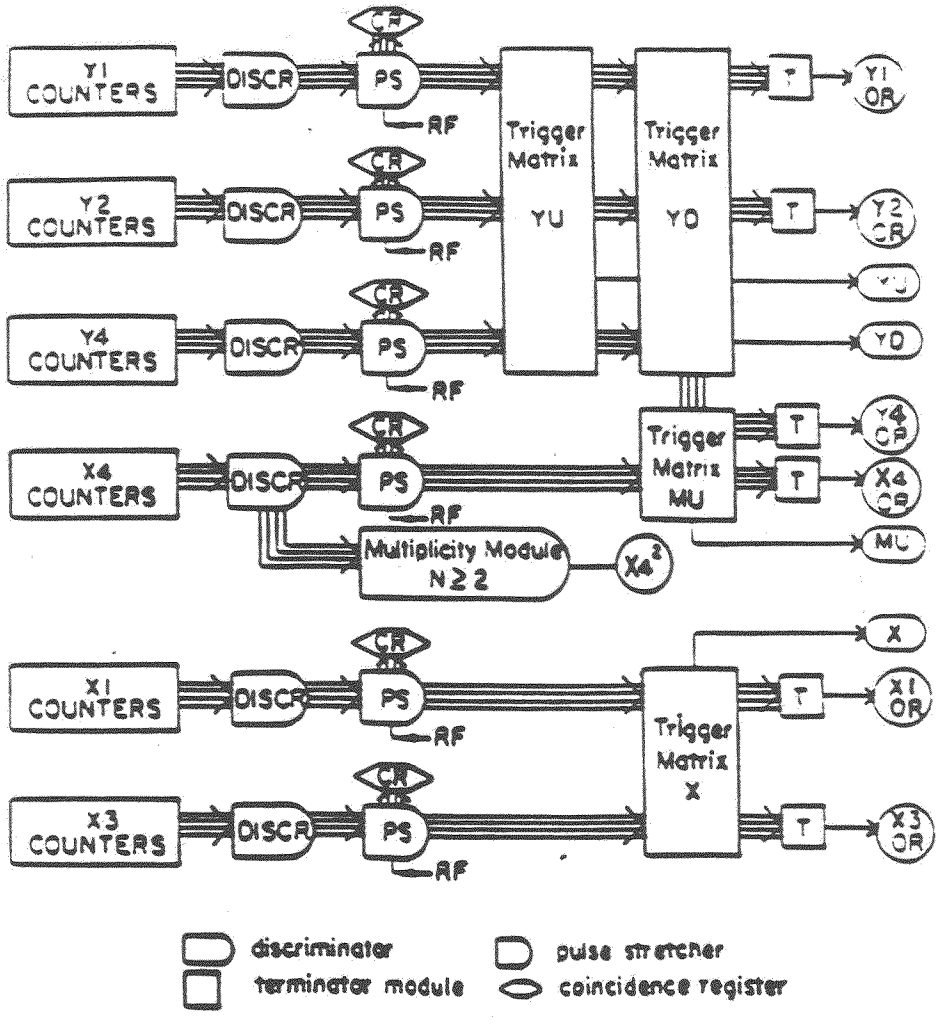

Figure 3.2: The Fast Logic and Trigger Matrix.

3.3 Second-level Trigger System

The final triggers formed at the second-level trigger system, mainly using a μ matrix from Trigger Matrix, largely reduced the first-level trigger set into a target dimuon trigger set. The final trigger decision was made by the *DC Logic* based on the information from the first-level triggers via DC logic bus inputs. Figure 3.3 illustrates the operational scheme of the second-level trigger system. The DC logic cycle was initiated by a TFI pulse entering the *Trigger Generator Input* (TGI) module. This module generated fast gates for the first-level triggers, MWPC's, and drift chambers. The first-level triggers on the DC logic bus were used by *Pin Logic* modules to form final triggers, which were fed into the *Trigger Generator Output* (TGO). This TGO then generated gates for CR's, TDC's, and ADC's, and initiated the read-out cycle.

3.3.1 Trigger Matrix

The triggers produced by this intelligent trigger matrix[83] were the *core* of the whole trigger system, but they were not used to start the second-level trigger decision cycle. The output signals produced by the trigger matrix were ANDed logically at the second level to form the E772 main triggers DIMU and SINK in order to select two muon events from the target.

The pulse stretcher outputs were grouped as a half bank(Left or Right) of Y1, Y2, and Y4 hodoscope planes. These groups were sent as inputs to the Trigger Matrix via a 16-channel ribbon cable for filtering out *target-muon events*. Only Y-view hodo-roads were employed, because events originating from different z coordinates had distinguishable hit patterns in the Y view under the deflection of the horizontal magnetic fields.

This Trigger Matrix was, conceptually, a lookup table incorporated into the

ECL random access memory(RAM) chips. It was configured to do a 3-fold coincidence on preset hodoscope counter combinations of Y1, Y2 and Y4. These combinations were identified using Monte Carlo apparatus simulations, for a muon track coming from the target. The allowed combinations were then written into a disk file, which was loaded into the RAMs by the on-line program before data taking. There were three trigger-matrix files, which were loaded into the trigger matrix for low-, intermediate-, and high-mass data taking, respectively. While taking data, the input address to each RAM was formed from the signals of 4 counters from one hodoscope bank, and 4 counters from a second bank. The output of each RAM (i.e., the stored value) corresponded to the allowed set of counters in the third bank that completed the correct matrix combinations. These output signals were then logically ANDed with the actual set of hodoscope hits in the third bank to form the matrix outputs. All matrix outputs in each quarter bank were logically ORed by hodoscope terminator modules to form 4 μ-matrix outputs called $\mu_R^U, \mu_R^D, \mu_L^U$, and μ_L^D.

These 4 large groups of hodoscope combinations roughly defined muons that originated at the target and that went above (U), or below (D), the beam dump and to the left(L), or right(R), side of the apparatus. Finally, the logic signals,

$$\mu^U = \mu_L^U \oplus \mu_R^U \qquad \mu^D = \mu_L^D \oplus \mu_R^D$$
$$\mu_L = \mu_L^U \oplus \mu_L^D \qquad \mu_R = \mu_R^U \oplus \mu_R^D$$

were formed and sent to the DC Logic via a DC logic bus for further processing.

3.3.2 Multiplicity Vetoes

The triggers produced by this multiplicity veto module were adopted to keep trigger rates low and deadtime small without losing good dimuon events They were prepared at the first level, then used in the DC Logic to form final triggers. A current sum of counter signals in each X hodoscope plane was fed into a LeCroy discriminator to form one multiplicity veto signal per plane at the first-level. Two veto signals, called $\overline{NX1}$ and $\overline{NX3}$, were generated if more than 10 counters had fired in the X1 hodoscope plane, or more than 9 had fired in the X3 hodoscope plane. These vetos were based on the assumption that good dimuon events should not fire many counters, and were checked by comparing multiplicity distributions for dimuon events with those of background events. A signal called 2X4 required at least two hits in X4, one of them being outside the two central counters.

3.3.3 Trigger Generator Input (TGI)

The TGI module received the TFI signal from the Fast Logic at the "TRIG" input while the DC logic bus contained signals from the Fast Logic, Trigger Matrix, and multiplicity modules. The main purpose of this TGI module was to generate a *start signal* for the DC Logic to process signals on the DC logic bus and *strobe* the DC logic bus, to generate *fast gates* for MWPC coincidence registers (CR's) and Station 2 drift chamber TDC's, and also to control the *DC logic dead time*. If the DC logic cycle had not been completed yet, the incoming trigger would be blocked and a logic busy signal was produced out of this TGI module. Meanwhile, it would also receive a "HOLD" signal from TGO to produce a readout-system busy signal if the readout system was busy for writing out data. These two busy signals were fanned in to form the system

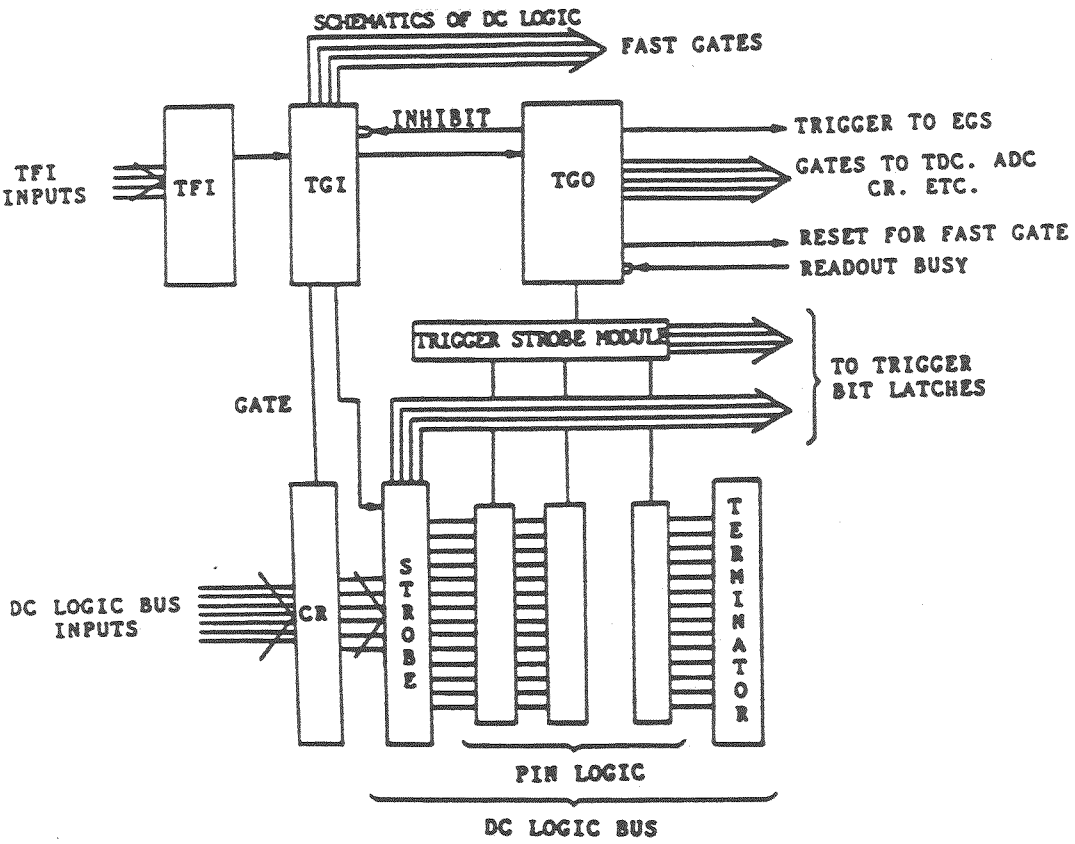

Figure 3.3: The schematic diagram of TGI, DC Logic, and TGO.

busy (SB) signal, which was used in the live-time monitoring. The purpose of this dual busy arrangement was to permit the DC Logic to continue to cycle in order to monitor the readout deadtime and to continue to drive the scalers (pulse counters) during the computer readout, but prevent the Pin Logic from generating new triggers during this period with the dead-time signal from the TGI module.

3.3.4 DC Logic

The DC Logic[81] was a flexible general-purpose triggering system capable of generating up to 16 different triggers. It mainly consisted of two 18-line buses with their associated drivers and terminators. The 16 *Pin Logic* modules in the lower bus provided us the flexibility to set up desired final triggers. They formed logical decisions from the 16 logic-bus lines according to the arrangement of internal pins(or jumpers). While a Pin Logic was true, a NIM pulse would come out at the "S" output of this Pin Logic module and be sent to a scaler. If the dead time was not on, a NIM pulse also emerged from the "SD" output and a positive going pulse would appeared at the "T" output. The former one was also used to drive a scaler and the latter one was the final trigger output. A negative going pulse, which was used for prescaling triggers, appeared at the "P" output.

During a DC Logic cycle, the input signals on the bus were latched, so that further processing could be done with DC levels without worrying about timing. Once the DC Logic bus had been strobed by a strobe module, Pin Logic modules plugged into this logic bus could form any logical combination of the signals on this bus. The final triggers set by the Pin Logic modules and employed for E772 were:

1. main data acquisition triggers:

$$\begin{aligned} \text{DIMU} &= \mu_L \odot \mu_R \odot \mu_U \odot \mu_D \\ \text{SINK} &= \mu_L \odot \mu_R \odot \mu_U \odot \mu_D \odot 2X4 \odot \overline{NX1} \odot \overline{NX3} \end{aligned}$$

2. four study triggers:

$$\begin{aligned} (1)\ \tfrac{3}{4}\mu LRPS &= (\tfrac{3}{4}\mu L \odot \tfrac{3}{4}\mu R)/2084 \\ (2)\ \tfrac{3}{4}\mu LPS &= (\tfrac{3}{4}\mu L)/32 \\ (3)\ \tfrac{3}{4}\mu RPS &= (\tfrac{3}{4}\mu R)/32 \\ (4)\ \text{LIKE} &= \mu L \odot \mu R \odot 2X4 \odot \overline{NX1} \odot \overline{NX3} \end{aligned}$$

In other words, SINK required, at least, two opposite-sign, left-right, low-background-multiplicity, high-P_T muons. The study triggers were prescaled by factors ranging from 32 to 2084. The requirements of LIKE trigger and same sign of charge, in the off-line analysis on muon-pair events, allows us to study the properties of accidental-coincidence dimuon events.

3.3.5 Trigger Generator Output (TGO)

If the criterion of any Pin-Logic module was satisfied, its trigger output was immediately strobed and transfered to the trigger bit latches (TBL's). Meanwhile, the trigger strobe module sent a signal to the TGO module, which, in turn, sent out various gates to the following places: 1) the CR's for latching hodoscope-counter hits; 2) the MWPC CR's and Station 2 TDC's for blocking the reset pulse and holding data in the TDC's; 3) the Station 3 TDC's for recording chamber hits; and 4) the ADC's for registering pulses from calorimeter

phototubes. In this way, data in TDC's and latches were available to the Trigger processor[82], which was designed for the E605 final trigger decision. It was not used to reject events on-line in this experiment, but to label the data stream with its decision.

Simultaneously, TGO started the readout cycle by sending a signal to the Event Generator Source(EGS) in the transport system. In turn, the TGO module would receive a readout busy signal to prevent it from generating additional TGO's during readout.

3.4 Readout System

The readout system consisted of a *Nevis data transport system* [85], and the *data latch systems* such as TBL's, CR's, TDC's, and ADC's, as indicated in figures 3.1 and 3.4. These data latch systems, which had *latched* the hit information, *translated* them into data words and *transfered* these data words to the transport system. It then received these *parallel* data streams and *organized* them into an output data stream of standard format in a time-efficient manner.

The Nevis transport system exploited the notion of data-driven processing, wherein data transfers were controlled by the presence of the data itself, rather than by a central controller. It served as the interface between the data latches and a megamemory[84], operating at a data transfer rate of 200 nsec/16-bit word. Up to two thousand events could be read out during the one-minute beam spill, with an event length of about 250 words.

Physically this transport system consisted of a crate that can hold up to 22 modules. These transport modules connected to the power bus and the *data bus* at the back of the crate. The *clock signal* was received by each module on

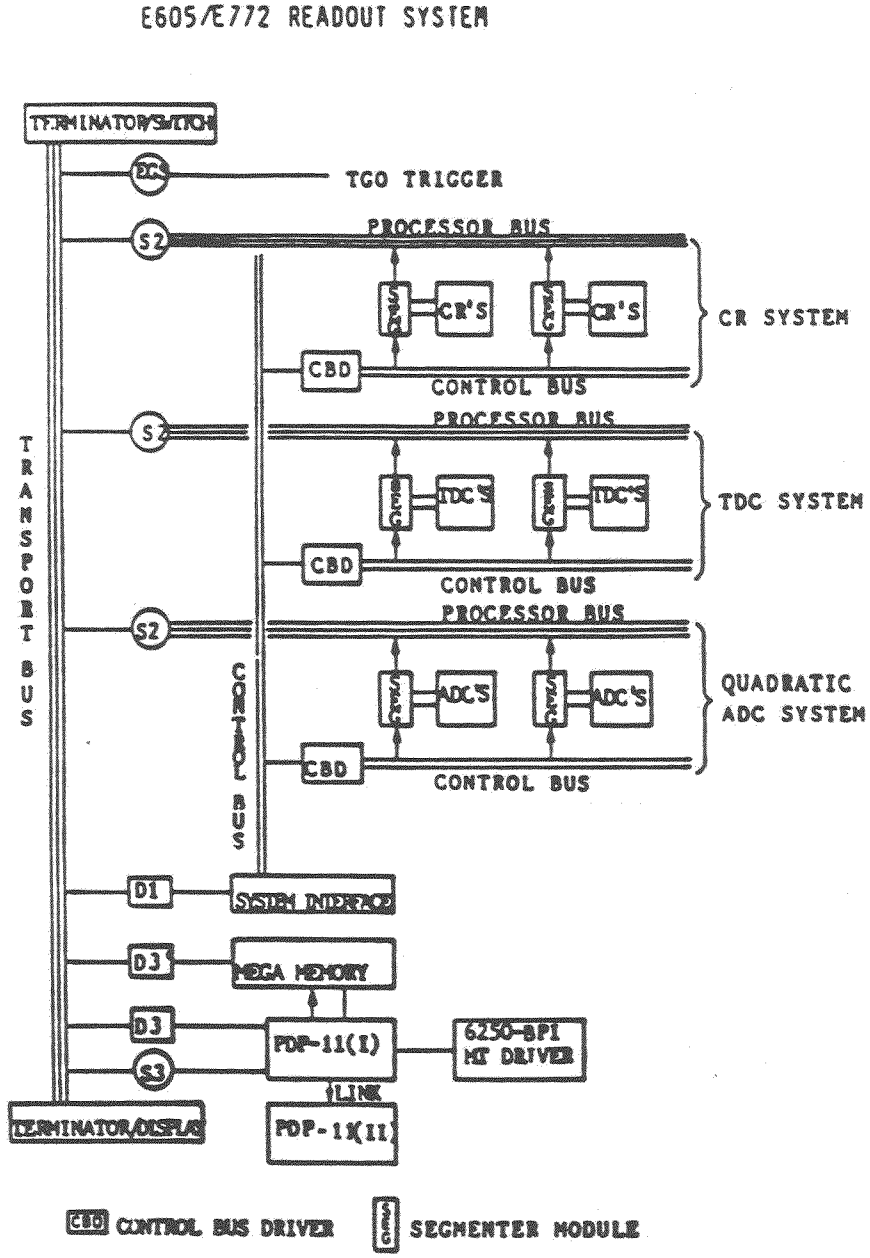

Figure 3.4: The Readout System.

its front panel through a lemo connection. The data bus was a sixty-conductor flat cable that carried thirty signals. Transport system modules served primarily as interfaces between the bus and external devices, such as: 1) the TDC segmenter module, through which data from up to eight 32-channel TDC's was transmitted; and 2) interface to the megamemory and the DR11-B interface to the PDP-11 Unibus.

In the 1987 run, experiment E772 collected data from a total of 8312 channels comprising 194 channels of hodoscope counters, 480 channels of drift tubes, 5056 channels[1] of MWPC's, 1984 channels of drift chamber's, about 200 channels of calorimeter phototubes, and 398 channels of proportional tubes. Information was passed from the ADC's, TDC's, and latches through the Nevis Transport System to a 4-megabyte memory. During the nine seconds after the beam gate, the data in this memory was written to 6250 BPI magnetic tapes by a PDP-11/45 computer.

3.5 Summary of Collected Raw Data

Typically, 1000 events per spill were written to tape. Of these events $\sim$ 20 were valid dimuon events from the target. The following table shows the summary of raw data:

[1]This was the reason to latch MWPC hit information with the fast gate sent by the TGI module in advance before starting the DC Logic cycle.

Magnet Setting	$<M_{\mu^+\mu^-}>$	Targets	Raw Events
Low Mass	5.4 GeV	Fe/Ca/D	$\approx$ 9.0 M
		W/C/D	$\approx$ 2.9 M
Medium Mass	7.0 GeV	Fe/Ca/D	$\approx$ 22.3 M
		W/C/D	$\approx$ 7.1 M
High Mass	9.5 GeV	Fe/Ca/D	$\approx$ 4.2 M
Total no. of mag. tapes=700; Total raw events $\approx$ 45.5 M			

Table 3.1: E772 raw data summary.

Chapter 4

Scaler-Based Run Monitoring Data

The scaler run monitoring data served two functions in E772. A large majority of the scaler data was used for monitoring the *beam conditions* and *apparatus performance*. In the final target-to-target relative cross section normalization, scaler data were used to determine the relative number of incident protons on the different targets and the relative electronic live time during beam spills. The way these quantities enter the final normalization calculation is given in chapter 6. During actual beam spills, accurate target-to-target relative normalizations of intensity and live time were achieved primarily by the use of cyclic target interchanges with the target motion mechanism described in chapter 2. Because of this arrangement, long-term drifts in the intensity and live-time monitors were largely cancelled in the A-dependent ratios. Short-term variations in these monitor signals were studied by taking separate run monitoring data which revealed the correlations between the incident beam characteristics and the monitor signals. These scaler data characterized the following beam spill parameters: integrated intensity, beam positions on target, spill duty factor, and spill uniformity. By carefully selecting spill parameters, the short-term fluctuations in monitor signal were reduced to a minimum. The uncertainty

of each normalization was determined by measurements of a set of redundant monitors. As shown in chapter 6, an uncertainty of less than 1% was achieved for these two relative normalizations.

These spill parameters were recorded by a set of 123 scalers, along with other run conditions, such as: system live time, magnet currents, megamemory overflows, and target positions. Physically, these 123 counting rates came from two main sources: 1) monitors - beam, target, spill, system live time, sag, RF bucket and phase, magnet NMR's and current monitors; and 2) fast trigger m.es - μ matrix, TFI components, multiplicity vetos, Pin Logic "S" outputs, and Pin Logic "SD" outputs (TGO triggers).

4.1 The Dual Role of Scaler Data

The scaler data was used for both *on-line monitoring* and *off-line spill rejection*. The on-line program SCAN, which read in the scaler data directly from on-line computer PDP-11/45 and calculated several values from the scaler data, provided a scan on the following quantities: beam horizontal and vertical positions, duty factor, system live times, D_2 target pressure, RF phase, and relative monitor gains. If any value went out of bounds that were set by the values under normal condition, this program wrote out a warning message on a screen together with an audible sound.

At the end of each spill, scaler data generated from CAMAC crates was written to magnetic tapes according to the spill format by the PDP-11/45 computer. These data were used in off-line analysis to provide information of normalization and to select good spills. Meanwhile, the same scaler data were also transferred by this computer to a peripheral micro-VAX as the *rasputin* files. The result reported in this chapter was obtained on the VAX machine by

analyzing scaler data in rasputin files.

The following sections will discuss how we set the criteria of a good spill for the purpose of accurate target-to-target relative normalization using the scaler data. The *scaler monitor* is defined here as a scaler data word that is obtained or calculated from one or several scaler data words using a certain algorithm. In this spill-quality study, there were two types of scaler monitors: beam and apparatus monitors. The former monitored the beam characteristics and gain stability of beam monitors, and the latter monitored the run condition of the apparatus.

4.2 Beam Monitors

This section will discuss beam scaler monitors that were used to monitor the beam positions, intensity, duty factor, and spill uniformity. They were also used to study the correlations between beam characteristics and the relative gain of SEM3/SEM4, LAM4/SEM4, I_x/SEM4, and I_y/SEM4. Performance data taken in actual data runs are shown in figures 4.1 and 4.2.

4.2.1 Beam Position and Intensity

The characteristics of beam position and intensity monitors were discussed in chapter 2. The scaler monitors associated with these monitors were (POSX, POSY) and (SEM4, SEM3, LAM4, I_x, I_y), where the first set recorded horizontal and vertical beam positions, and the second set measured the relative beam intensity.

4.2.2 Beam Duty Factor

This duty factor measures the uniformity of the number of protons per RF bucket in a spill. The chamber and hodoscope multiplicity became large above

normal when the beam duty factor dropped below the normal value. This kind of spill would cause an inefficiency or rate-dependence of the tracker in the off-line analysis program; therefore, it is an important spill parameter to describe the spill quality. There were two sets of duty-factor counters (AMON3,S3REF) and (X3L7,Y1R3). The scintillation counters in each set recorded the rates *independently*; therefore, the probability of finding a pair of pulses from individual counters of each set, occurring at the same time, is given by,

$$(\mathrm{AMON3}\times\mathrm{S3REF})/(\ \#\ \text{of buckets in each spill})^2$$

or

$$(\mathrm{X3L7}\times\mathrm{Y1R3})/(\ \#\ \text{of buckets in each spill})^2$$

The coincidence rate of each pair of signals is the product of the above joint probability and the number of effective buckets in a spill. According to this argument, with 1×10^9 buckets in each spill, the duty factor can be derived as below,

$$\mathrm{D.F.} = (\mathrm{AMON3}\times\mathrm{S3REF})/(\mathrm{AMON3}\odot\mathrm{S3REF}\times10^9)$$
$$\mathrm{D.F.} = (\mathrm{X3L7}\times\mathrm{Y1R3})/(\mathrm{X3L7}\odot\mathrm{Y1R3}\times10^9),$$

where AMON3 and S3REF were counting rates of the AMON3 counter and a reference counter at station 3; X3L7 was the counting rate of the 7th counter in the left bank of the X3 hodoscope plane, and Y1R3 was that of the 3rd counter in the right bank of the Y1 hodoscope plane; AMON$\odot$S3REF and X3L7$\odot$Y1R3 were the coincidence rates of each pair of signals.

4.2.3 Spill Uniformity

There were 3 sub-spill gates G1, G2, and G3 in the duration of a spill, with lengths of 2, 10, and 8 seconds. By monitoring the counting rates in these

3 gates, we could characterize some features of spill structure. During data taking, aborted and nonuniform spills can cause intensity and beam position monitors to not operate properly[1]; therefore, we adopted 3 scaler monitors AMON2LT, AMON2LTDEL, and FRACG3 to monitor the structure of a bad spill: 1) AMON2LT measured the live-time in each sub-spill gate G1, G2, and G3; 2) AMON2LTDEL indicated the difference of live-times in [G1,G2] or [G2,G3]; and 3) FRACG3 measured the percentage of AMON2 counting rate in G3. Because an aborted spill was usually aborted at the point where it was either in the second or third sub-spill gate [G2 or G3], the value of spill monitor FRACG3, defined below, would drop significantly for that spill.

$$\text{FRACG3} = \text{AMON2}\odot\text{G3} \;/\; (\text{AMON2}\odot\text{G1}+\text{AMON2}\odot\text{G2}+\text{AMON2}\odot\text{G3})$$

For a perfect uniform spill, the value of FRACG3 should be 0.40 but in the usual case it fluctuated between 0.3 and 0.5.

4.2.4 Representative Monitor Performance Data

The position-intensity correlations and the gain stability of our luminosity monitors were measured by analyzing several sets of data[2] where the beam position was swept horizontally and vertically across the targets, and normal data set 1B.

Position-Intensity Correlation Measurements

During this scanning, the beam had the size 7.0 mm × 0.5 mm, an intensity of 3.5×10^{11} protons/spill, and a steady duty factor between 45 and 65 % . The beam horizontal position was swept from -4.0 to +3.0 mm using the ME4ED

[1] Please refer to E772 internal communication, H.W. Baer and M.J. Wang, 4/18/88.

[2] This data set which contains RUN 6297 to 6318, was taken on 10/08/87.

magnet, and the vertical position was swept from -2.5 to -0.5 mm using the ME6V magnet. The vertical beam position was kept constant while the horizontal position was swept, and vice versa. Figure 4.1 shows the beam conditions *versus* the gains. Because SEM3/SEM4 remained constant during sweeps, we assumed that the individual gain of SEM was likely to stay constant.

From the correlations shown in figure 4.1, we obtained the following conclusions,

LAM4: no dependence on position was observed, but had $\sim$ 1 % drift over 1 hour.

I_x: there was 1.3 - 1.5 % increase in gain per mm in x-sweeping.

I_y: there was 0.6 - 0.7 % decrease in gain per mm in x-sweeping.

Monitor Gain Stability *versus* Beam Characteristics

Because the performance of the monitor and its electronic circuits depend on temperature, humidity, beam intensity, and beam structure, the stability of the monitor's gain must be carefully watched. The long-term (more than 1 hour) drift effects caused by the first 2 factors, as we stated at the beginning of this chapter, were cancelled largely in the ratios, but the short-term effects (at the time scale of a 23-second spill), caused by the last two factors, could not be ignored in the A-dependence study. By taking the ratios of scaler outputs, we were able to watch the relative gain stability spill by spill. The upper panel of figure 4.2 shows the beam characteristics and the lower panel presents the relative gains : SEM3 / SEM4, LAM4 / SEM4, I_x / SEM4, and I_y / SEM4 as functions of spill number for data set 1B. The correlation between relative gains and beam conditions is very clearly seen at the step-like and spike-like changes of ratios.

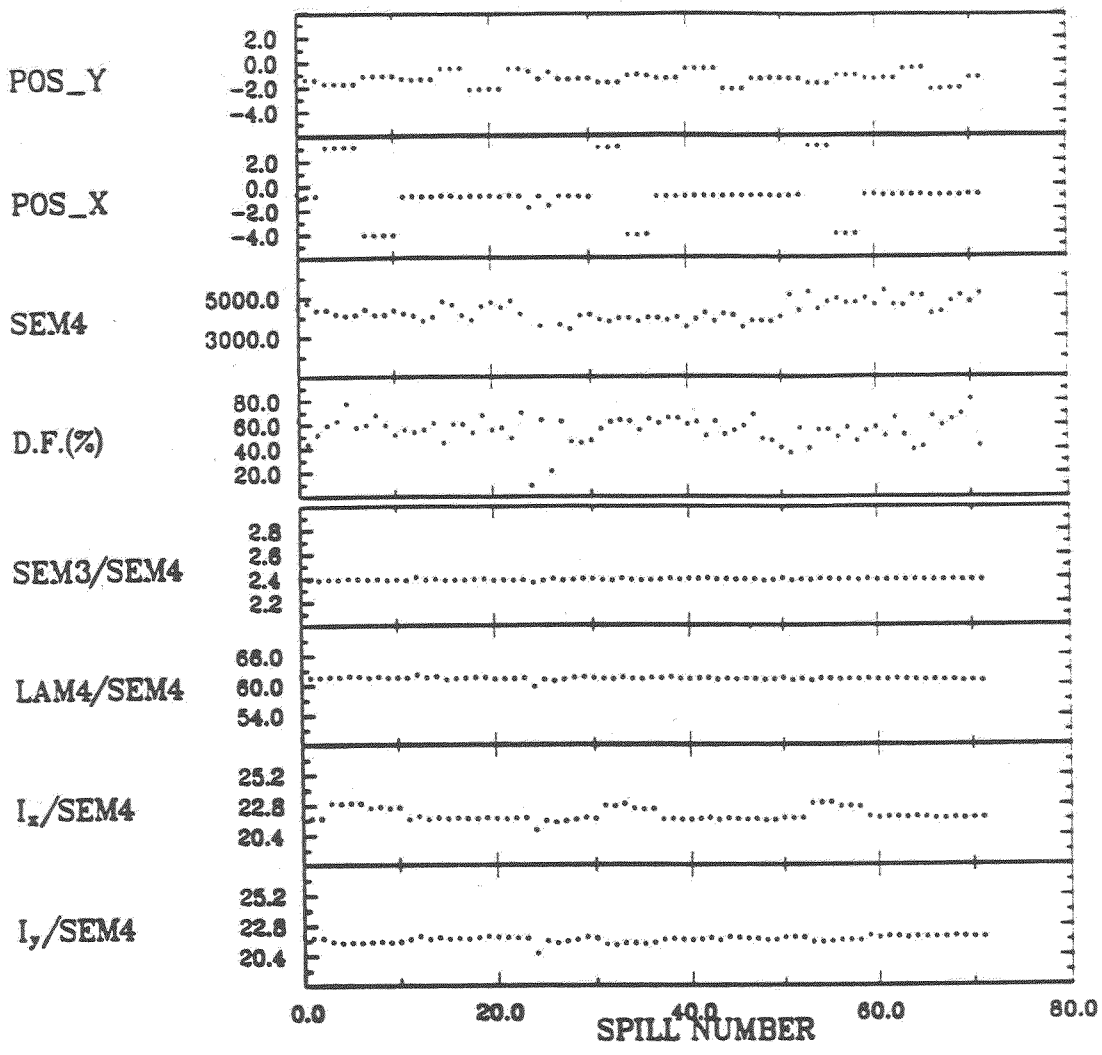

Figure 4.1: Position and Intensity Correlation *versus* spill number. The unit for both variables POSX and POSY is mm. These data were taken in a running period where the beam was moved up and down(POSY) and left and right(POSX) across the target using magnets ME4ED and ME6V. The ratio SEM3/SEM4 is seen to remain constant during these beam scans.

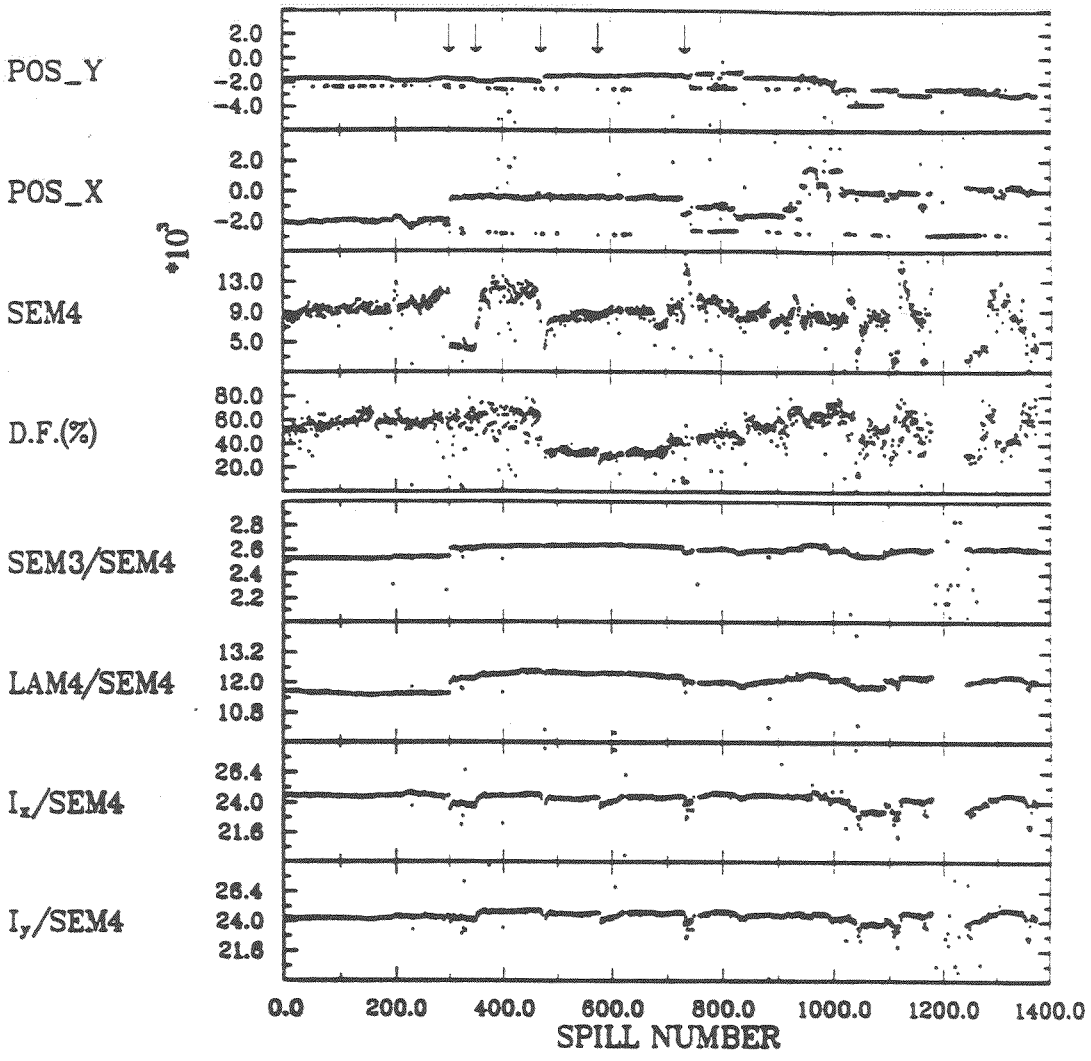

Figure 4.2: Beam characteristics and ratios of monitor counts *versus* spill number for data set 1B. The first arrow (from left to right) indicates an abrupt change in X-position and intensity(SEM4) of beam. The second arrow indicates an abrupt change in beam intensity, but with no changes in X- or Y-beam position. The third arrow marks a change in Y-beam position accompanied by a drop in beam intensity and duty factor. The last arrow marks a period of high intensity fluctuations.

There were 2 step-like changes, which are indicated by the first 2 arrows in figure, and 3 spike-like fluctuations, which are pointed out by the last 3 arrows. The beam was tuned in the accelerator after spill number 1000; therefore, all the features of the beam shown in this figure fluctuated more than those in the previous spills. The first step[3] shown in SEM3 / SEM4, LAM4 / SEM4, and I_x / SEM4 was caused by both beam position and intensity changes and the second step of I_x / SEM4 and I_y / SEM4 was due to intensity change only. The first spike[4] of I_x / SEM4 and I_y / SEM4 were clearly correlated with both drops in intensity and duty factor but the second spike was caused by low duty factor only. The last but the biggest spike of I_x / SEM4 and I_y / SEM4 was caused by the saturation of the voltage-frequency converter, which converted analog signals of I_x and I_y into pulse signals, in the situation of high intensity(above 17000) and low duty factor(below 20 %) .

The effect caused by step-like and spike-like jumps of monitor gains would be diluted or cancelled largely in the *integrated* A-dependent ratios, but those independent large fluctuations could make more contributions to the uncertainty of the intensity measurement. In order to reduce these short-term fluctuations as much as possible, constraints on beam positions, intensity, duty factor, and spill uniformity were demanded. The effect of these cuts will be shown in the last section.

The final normalizations of relative proton count measured by SEM3, SEM4, LAM4, I_x, and I_y are shown in chapter 6.

---

[3]It is indicated by the first arrow at spill number 300.

[4]It is indicated by the third arrow in the order of increasing spill number.

4.3 Apparatus Monitors

This section will present 4 sets of scaler monitors which monitored the system live time, megamemory overflows, stability of magnet currents, and target position.

4.3.1 System Live Time

Because live time was one of the normalization constants, its precision and accuracy were two important factors in designing the measurement. There was a certain cycle time in both the DC Logic and the Readout system; therefore, a high trigger rate beyond the frequency of these cycles would result in a loss of some good dimuon events. This could be corrected by a live-time normalization. It is shown below,

$$
\begin{aligned}
&(Yield)_{recorded}/(Yield)_{actual} \\
&\qquad = \int I(t) \cdot LT(t) \cdot \sigma \cdot \rho L \cdot \overline{N} dt / \int I(t) \cdot \sigma \cdot \rho L \cdot \overline{N} dt \\
&\qquad = \int I(t) \cdot LT(t) \cdot \rho L dt / \int I(t) \cdot \rho L dt \\
&\qquad = \int I(t) \cdot LT(t) dt / \int I(t) dt
\end{aligned}
$$

where $I(t)$ is the time dependence of the intensity, σ is the production cross section, ρL is the target areal density, $\overline{N}$ is the product of other normalization constants and $LT(t)$ is the multiple step function for describing live time, with value of 1 for accepting events and 0 for blocking events.

The beam intensity monitor SEM4 and the luminosity monitors AMON and WMON were used to measure the system live time by taking them in coincidence with the system busy signal. The signal of SEM4, which was an averaged response over thousands of buckets, was usually higher than 10^3 per spill; therefore, the precision, which was limited by the coincidence procedure

and counting rate of SEM4, could reach about 0.1 % per spill or per data set. The usual counting rates of bucket-response signals AMON and WMON were at least 10^4 per spill; thus, the precision of this measurement, which was dominated by statistical fluctuation, could be 1% per spill. The precision of these measurements would be improved to a level much less than 1% in a data set that consisted of 10^4 good spills.

The uncertainty of this measurement was determined by three redundant live-time monitors. The results will be shown in the chapter on normalization. These monitors, SEM4LT, AMONLT, and WMONLT, are defined below,

$$\begin{aligned} \text{SEM4LT} &= \text{SEM4}\odot\text{SB} \;/\; \text{SEM4} \\ \text{AMONLT} &= \text{AMON}\odot\text{SB} \;/\; \text{AMON} \\ \text{WMONLT} &= \text{WMON}\odot\text{SB} \;/\; \text{WMON} \end{aligned}$$

where SEM4⊙SB, AMON⊙SB, and WMON⊙SB are coincidence rates of SEM4, AMON, and WMON with system busy which was the logically ORed output of DC-Logic busy and Readout system busy.

The final normalizations of relative live time measured by SEM4LT, AMONLT, and WMONLT are shown in chapter 6.

4.3.2 Megamemory Overflow

The RF scaler was adopted as an indicator of a *partial* spill caused by megamemory overflow[5]. The central control room at the accelerator sent out a RF signal with frequency of 53 MHz that determined the bucket structure of spills. For a 23-second spill, the constant counting rate of this beam-gated RF signal was 9.46×10^6 per spill [6] (presacle factor = 128). Because of its

[5] A data length longer than 4 megabytes is beyond the capability of our megamemory.

[6] The actual count was 9.54×10^6 per spill.

constant rate, it was used to indicate the length of the beam gate. In the case of megamemory overflow, this memory unit would send out a signal to gate off the RF scaler and stop data acquisition. A smaller counting rate of this RF monitor became a signature of megamemory overflow status.

4.3.3 Stability of Magnet Currents

The stability of magnetic fields depended mainly on the stability of the electric currents going through the coils. These values of currents were measured by power supply shunt voltages, which were converted to scaler pulses. The current stabilities of SM0, SM12, and SM3 magnets were monitored by three scaler monitors SM0ERR, SM12ERR, and SM3ERR, which are defined below

$$\begin{aligned} \text{SM0ERR} &= |\text{SM0AI-SM0AI}_{set}| \\ \text{SM12ERR} &= |\text{SM12AI-SM12AI}_{set}| \\ \text{SM3ERR} &= |\text{SM3AI-SM3AI}_{set}| \end{aligned}$$

where (SM0AI_{set},SM12AI_{set},SM3AI_{set}) is the current configuration[7] of mass setting; SM0AI, SM12AI, and SM3AI are scaler monitors, which indicate the actual values of currents in those three magnets.

4.3.4 Target Selection

Various targets in a group (either 2 or 3 targets) were cycled alternatively into the beam during each run. A dependable way to determine the target position was very crucial for an A-dependence experiment. We used AMON/SEM4 or the target-position scaler monitor to select the target. The counting rate of AMON was proportional to the beam intensity and the thickness and type of

[7] Please refer to table 2.5.

target; therefore, the ratio AMON/SEM4, which is only sensitive to the thickness of target, can be used to indicate the target positions. This capability is clearly shown in figure 4.3, where the data in data set 6A is presented. In this data, the high(~20), intermediate(~15), and low(~8) values of AMON/SEM4 corresponded to Fe, Ca, and D targets, respectively. Target-selection can also be carried out using target-position scaler or target-trigger bit. In the off-line analysis, we used either target bit or target-position scaler to select data for each target, spill by spill.

4.4 Spill-Selection Criteria

Beside the scaler monitors mentioned above, there were still two other checks for the spill quality. The status of megamemory and the readout system, which were not recorded by scalers but kept in the data streams, were also examined at the data-reduction stage in order to make sure the data of a spill was properly read out from the data acquisition system. All the spill requirements were decided in a compromising way in which we took both statistics of data and effect of bad spills into consideration. Table 4.1 shows all the requirements of those scaler monitors for selecting good spills in low-, intermediate-, and high-mass data analysis.

The effect of these scaler cuts is demonstrated in figure 4.4 which shows the gain-stability plot imposed with the following scaler cuts: -3.0 < POSX < 2.0 and -4.0 < POSY < 2.0, SEM4 > 1500, D.F. > 0.20, FRACR3 > 0.20, RF > 9.46×10^6. The short-term fluctuations are clearly much less than those of the same study without cuts (figure 4.4). Generally speaking, all relative gains were stable to a 2 % level throughout most intervals in the time scale of a target-interchange cycle, except for the steps and spikes. This stability enabled us to

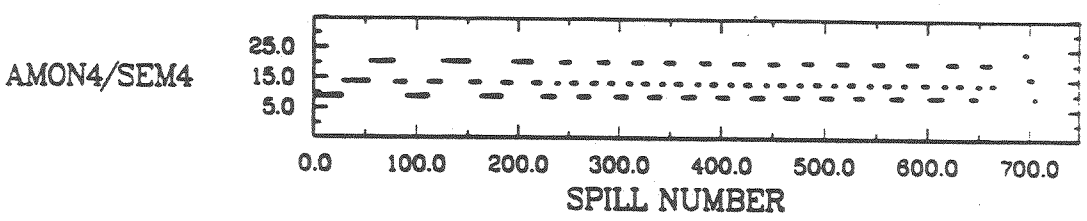

Figure 4.3: AMON/SEM4 *versus* spill number.

spill cut	requirement		
	low mass	int. mass	high mass
beam pos x	-3<POSX<2 (mm)	-	-
beam pos y	-4<POSY<2 (mm)	-	-
SEM4 and taps	1500<SEM4< 15000	1500<-<25000	1500<-<40000
	10<TAPS<4000	-	-
duty factor	D.F.>0.20	-	-
bad spill	AMON2LT<0.90	-	-
structure	AMON2LTDEL>0.10	-	-
	FRACG3<0.20	-	-
SEM4 live time	SEM4LT>0.90	-	-
AMON live time	AMONLT>0.90	-	-
RF count	RFCNT>9.4×10^6	-	-
SM0 current	SM0ERR<50 (amps)	-	-
SM12 current	SM12ERR<50 (amps)	-	-
SM3 current	SM3ERR<50 (amps)	-	-

Table 4.1: Definitions of spill cuts, where taps is the number of events per spill transferred by the Nevis transport system.

have less than 1 % uncertainty in the target-to-target relative proton counts. Detail analysis and results will be shown in the chapter on normalization.

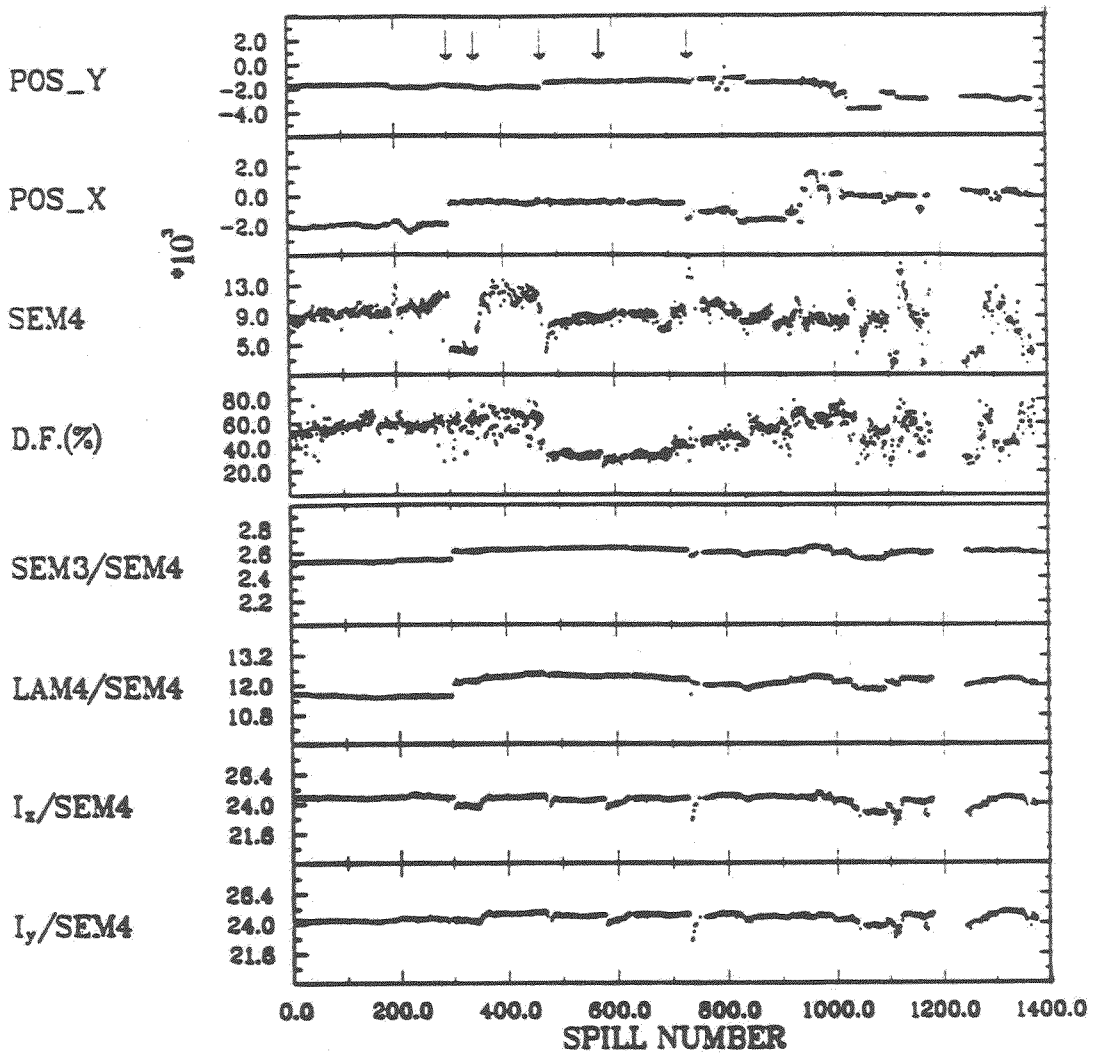

Figure 4.4: Gain stability *versus* beam characteristics, with spill cuts imposed. In the top panel, the first two arrows indicate step-like changes, and the others indicate spike-like changes.

Chapter 5

Muon Track Reconstruction and Data Reduction

E772 data was divided into 10 data sets according to different magnetic field configurations, ways of target grouping and different run conditions. We had carefully excluded bad runs from each data set, with the information recorded in four log books. At the first two passes of data analysis performed on Cyber at Fermilab and ACP in Los Alamos, the following ratios of each run were examined: number of events written out to that read in; number of events written out to number of relative proton counts recorded by SEM4; and the error messages, in order to keep only good runs in each data set. There were 61 bad runs in total that were rejected. The quality of data in each run was examined spill by spill with scaler monitors, which recorded the apparatus performance at one minute cycle during data taking. Those scaler cuts that we adopted to get rid of bad spills were listed in table 4.1 of the previous chapter. Events in each spill were reconstructed by the track reconstruction procedure. Background and bad events were rejected by various cuts, which will be explained in detail in the following sections. This data was processed once on CDC-Cyber machines at Fermilab through three passes. During this analysis, we had learned the proper way to set the values of cuts in the analysis program, to correct the correlation

between kinematic variables, to correct the rate-dependence problem, and to select good spills before starting the final analysis on an ACP machine. With all the criteria specified for run, spill, and event, first two passes of data analysis were performed on a 43-node ACP machine for eight months. The final pass was completed on a VAX machine.

This chapter will present the data analysis in the following sequence: basic principle of *track reconstruction*, *ACP analysis*, and *summary* of good dimuon data.

5.1 Track Reconstruction

This section will outline the general principle of track reconstruction used for both Cyber and ACP analysis. There were two major parts in the analysis of each event. First, the tracking program used the information of hits from the drift chambers and MWPC's to find tracks and identified the muon tracks with the hits in the proportional chambers, which were placed in downstream of the concrete blocks. Second, the trace-back procedure traced the particle trajectory back through the SM12 and SM0 analysis magnets to the target position.

5.1.1 Muon Track Finding and Fitting

First the drift-chamber hits and drift times of station 2 and 3 were read from the raw data. In each view, associated pairs(yy' or uu' or vv'), called *doublets*, of drift chamber hits were chosen by picking up two hits with separation less than the dimension of a cell. The staggered arrangement of the primed and unprimed drift chamber planes, allowed us to resolve some left-right ambiguities with respect to the fired anode wire and figure out the resolved hit position by

converting drift time into drift distance with space-time relation,

$$D = v * t + g * t^2 \tag{5.1}$$

where D is drift distance, t is drift time, v is drift velocity, and g is a deceleration constant [1]. These reconstructed hit-positions then were used for track *finding* and *fitting*.

Track Finding

The tracking program, JACTRACK[67] then searched for sets of y-u-v *triplets* that consisted of at least 4 crossed hits whose cross intersections were very close to a space point in station 2 and 3 drift chambers. After all triplets were found, this program searched for doublets that were not subsets of the previously found triplets. If no triplets were found or the number of triplet combinations between station 2 and 3 exceeded 10000, the event was discarded.

Track Fitting

The subroutine DCTRAX in tracker then performed a 6-point fit to all combinations of station 2 and 3 doublets and triplets, and constructed a list of all track segments(called *DC track segments*) with good χ^2. All DC track segments were required to satisfy the following criteria, otherwise were thrown out[2]: 1) their non-bend plane views were consistent with a track coming from the target, with the requirement that $x - x_{target} < 7$ inches; 2) these tracks were emerging from the SM3 aperture; and 3) the number of DC track segments of each event must be greater than 0 but less than 250.

[1] g=0 for station 2 chambers and g<0 for station 3 chambers.

[2] Some ghost tracks were removed at this stage.

Next, subroutine WCTRAX required each of the DC track segments to be lined up with a track segment[3] of the station 1 MWPC's in the non-bend plane in order to form a track candidate emerging from the SM12 aperture. A single-bend-plane approximation for the SM3 magnet was used to associate DC track segments with track segments in the MWPCs. Finally, the hits along each of the track candidates were fitted into two straight-line segments joined at the bend plane of SM3 in order to determine the trajectory parameters and momentum and clarify the unresolved left-right ambiguities by choosing the track with good χ^2. All track candidates were required to satisfy the following criteria in the fitting procedure: 1) a minimum of three out of six chamber hits at station 1; and 2) a minimum of four out of six chamber hits in each of stations 2 and 3 were required for each track. In total, there was a minimum of 12 out of 18 chamber hits per track.

For each track found, at least three out of five hits at station 4 were needed for *muon identification*. Any event with at least two opposite sign muons was considered for traceback, otherwise the event was rejected. Each one of the muon's trajectories was then traced back to the beam dump using a crude SM12 magnetic field map. The only purpose of such a traceback was to provide a means of rejecting muons that had clearly originated in the beam dump or scattered off the SM12 interior walls. Finally, a muon multiplicity cut was used to select events with more than one, but less than five, muon tracks, which were then written on an output file to be analyzed in the next stage.

[3]It required at least 1 hodoscope overlapping MWPC hits, the number of MWPC hits per plane less than 20.

5.1.2 Trace-Back Algorithm

The object of this algorithm is to get the muon's vector momentum at the target by tracing the muon back from the SM3 bend plane where the initial momentum and position of the muon were given from the previous track reconstruction procedure. The momentum of the muon at the target can be reconstructed in the traceback procedure, given the following quantities: SM0 and SM12 magnetic fields, the dimensions and locations of the absorber walls and beam dump, and the constraint of the target center as the production point.

There were three major ingredients in the traceback algorithm: *tracing* through magnetic fields, *energy loss* due to the absorber walls and beam dump, and *multiple scattering* due to the absorber walls and beam dump.

Tracing

TRACER is the subroutine that calculated the emerging momentum (P_x^o, P_y^o, P_z^o) and transverse position (x^o, y^o) at plane z^o of a particle with charge q emerging from a magnetic field with given initial momentum(P_x^i, P_y^i, P_z^i) and position (x^i, y^i, z^i). The algorithm is given below,

$$
\begin{aligned}
x^o &= x^i + \textstyle\int_{z^i}^{z^o}(P_x/P_z)dz \approx x^i + (P_x^i/P_z^i)(z^o - z^i) \\
y^o &= y^i + \textstyle\int_{z^i}^{z^o}(P_y/P_z)dz \approx y^i + (P_y^i/P_z^i)(z^o - z^i) + (qc/P_z^i)\int_{z^i}^{z^o} dz' \int_{z^i}^{z'} B_x dz'' \\
P_x^o &= P_x^i \\
P_y^o &= P_y^i + \tfrac{q}{c}\textstyle\int_{z^i}^{z^o} B_x dz \\
P_z^o &= \sqrt{(P_y^i)^2 + (P_z^i)^2 - (P_y^o)^2}
\end{aligned}
$$

where the approximation is valid for small $P_{x,y}/P_z$ and c is the speed of light.

Energy Loss

Highly relativistic muons lose energy through ionization, bremsstrahlung, and pair production processes. Because energy loss is a random process, what is usually known is their average values for a given muon momentum and material thickness. Energy loss distributions were calculated by integrating the differential energy loss distributions in an infinitesimal piece of material. The median values of those distributions were fitted as a function of the incident muon energy to obtain the energy loss correction due to the absorbers. It gave,

$$
\begin{aligned}
ELOSS_{CH_2} &= (2.427 + 0.001067 * P) * 0.19 * (0.986/1.032) \\
ELOSS_{C} &= (2.427 + 0.001067 * P) * 0.38 * (1.790/2.265) \\
ELOSS_{Cu} &= (2.427 + 0.001067 * P) * 0.43 \\
ELOSS_{dump} &= 7.54 + 0.0116 * P \\
ELOSS_{Pb} &= 4.25 + 0.0194 * P
\end{aligned}
$$

where the total thickness of CH_2, C, Cu, copper beam dump, and Pb are 96. 87, 24, 168, and 96 inches respectively.

Multiple Scattering

Multiple scattering is also a random process, which is caused mostly by Coulomb scattering from nuclei in the absorber. It was corrected by directing the muon's momentum to the target center from a computed multiple scattering bend plane.

TRACER was called by the traceback program PBSWIM to trace the track back to the center in z of each section of absorber wall with the starting point in the SM3 bend plane. There were 3 sections of CH_2, 4 sections of C, and one section of Cu walls[4]. At the center in z of each wall, the energy loss correction

[4]Please refer to table 2.6 for detailed configurations.

was applied to the muon's momentum according to the thickness and material of wall. Then the track was traced through the aperture where the beam dump was placed. In this procedure, the muon track was traced back with 17 steps in which the energy loss correction was applied while going through the dump. In the last two steps, the track was traced back to the downstream face of SM0, then to the target. Finally, an iteration process was used in order to correct effects of multiple scattering with a target constraint ($\delta y = y - y_{target} \leq 0.001$ inch) at the target. This program iterates the whole traceback process from the z position of a multiple scattering plane with the momentum vector pointing to the target center, until the target constraint was satisfied or the number of iterations exceeded 10. Any track that went outside the aperture was discarded in this process.

5.2 ACP Analysis

The track reconstruction analysis on Cyber at Fermilab took about 8 hours to finish one 6250 BPI tape; thus, it took about 8 months to finish all 700 tapes. With the improved tracker, it would take more than 16 months to finish all the analysis, and would require a memory size of 2 megabytes. Because both conditions were not met satisfactorily by the Cyber machines at Fermilab, we assembled in Los Alamos an ACP (Advanced Computing Project) machine[5], which has 43 nodes and 6 megabytes per node to accomplish the E772 analysis in a resonable time scale. The ACP hardware construction took about 6 months and the software conversion of tracker took one-man year to finish at Los Alamos National Laboratory.

[5]The ACP system was designed at Fermilab as a parallel computing system. This 43-node machine is more powerful than a Cray-1 machine for non-vector codes.

5.2.1 E772 Data Reduction

Data was reduced in 3 stages: first pass, second pass, and third pass. At each stage, all raw information on the data tape was passed together with software information to an output disk file called DST, which had the same format as that of the raw data file. This enabled the same analysis programs to work with either raw data tapes or DSTs.

5.2.2 The First Pass

The main task of the first pass was to carry out the first part of *track reconstruction*, which was explained in the previous section. An event with an incorrect format[6] was discarded. Long events that were generated with very high chamber and hodoscope multiplicities were cut by a maximum event length of 1776 words for DSTs. Before starting the track finding procedure, event data was unpacked block by block. There were EGS(Event Generator Source), RF scaler, trigger bits, coincidence registers, TDC's, Kaplan ADC's, and trigger processor blocks.

Stages of data analysis involved converting the hodoscope and wire chamber data into spatial positions and performing *track finding* and *fitting* procedures for each event with several requirements. The data reduction and the requirements in this pass are illustrated in table 5.1 for RUN 6275, which is the first run of low-mass data set 6. The key words in the name of each subroutine and the corresponding cut requirement are italicized in this table. At the end of this pass, only 7.2 % of the analyzed events satisfied all of the requirements in this pass, and these were written to a DST output file for the next-stage analysis (2nd pass).

[6]Please refer to the internal communication - 'The Last Word' for correct event format.

name of subroutine	requirement of cut	passed	failed	survival percentage
*FORM*CHK:	discards those of bad event *format*	62283	0	100.0
TPORAP:	checks the hodo hit pattern (1 < nkroad < maxroad)	61290	993	98.4
DC*TRIPS*:	no room for *triplet*	61290	0	100.0
	no entries in *triplet* bank	60670	620	99.0
	too many *triplet* combination	60031	639	98.9
*DC*TRAX:	no room for track bank	60031	0	100.0
	no *drift chamber* track	59244	787	98.7
	track bank overflow	54617	4627	92.2
*WC*TRAX:	no room for track bank	54617	0	100.0
	no *wire chamber* tracks	47308	7309	86.6
	workspace overflow	47292	16	~ 100.0
	reached track limit	47248	44	99.9
*SORT*RK:	1st pass: > 1 track	37036	10212	78.4
(sorting	> 1 muon tracks	36522	514	98.6
tracks)	2nd pass: > 1 track	27487	9035	75.3
	(P_T at dump).lt.1.5 GeV	4751	22736	17.3
	number of tracks < 5	4482	269	94.3
ALL CUTs		4482	57801	7.2

Table 5.1: First pass cuts summary of RUN 6275.

5.2.3 The Second Pass

The trigger and event format were checked again the same way as in the first pass. An event whose length was longer than 1919 words was discarded. The muon track was identified in this pass. Two-target muon events were selected and the z-vertex cut was imposed in order to get rid of events from the beam dump and upstream apparatus. At the end of this pass for RUN

name of subroutine	requirement of cut	passed	failed	survival percentage
DIMUSE:	two target muons	3170	1291	71.1
	z-vertex cut(+140,-140in)	2583	587	81.5
ALL CUTs		2583	1878	**57.9**

Table 5.2: Second pass cuts summary of RUN 6275.

6275 (table 5.2), 57.9 % of analyzed events satisfied all the requirements in this pass, and these were written to a DST output file for the next-stage analysis (3rd pass). Before starting the third pass, the DST outputs of each run were combined into 10 files according to the division of the data set.

5.2.4 The Third Pass

This was the pass which did the *traceback* procedure. It was regarded as the final pass which generated relevant histograms of physics interests, for event reconstruction. The quality of each spill was required by a set of scaler cuts which were carefully set in the analysis of previous chapter. Table 5.3 shows the spill selection for data set 6 in which most unqualified spills were discarded by the intensity cut. In total, 69.4 % of analyzed spills which satisfied all the requirements of the spill cuts, were analyzed further at the event level.

name of cut	passed	failed	passed percentage
SM0 OK	16020	15	99.9
SM12 OK	16016	4	~100.0
SM3 OK	16012	4	~100.0
SEM and TAPS OK	12059	3953	75.3
RF CLK CNT OK	11653	406	96.6
SEM4 LT OK	11649	4	~100.0
AMON LT OK	11644	5	~100.0
BAD STRUCTURE	11318	326	97.2
DUTY FACTOR OK	11160	158	98.6
POS X OK	11138	22	99.8
POS Y OK	11138	0	100.0
MEGAMEMORY OK	11138	0	100.0
READOUT OK	11136	2	~100.0
ALL CUTs	11136	4899	**69.4**

Table 5.3: Third pass spill-quality cuts summary of data set 6.

More stringent event cuts: muon pair with opposite sign, xy target cut, z-vertex cut, and dump cut; at target and dump positions were adopted to keep only good dimuon events. The first cut kept the dimuon event only. The xy target cut required the distances between the x, y coordinates of reconstructed vertex and x, y coordinates of beam-target axis to be greater than 5 inches. z-vertex cut demanded that the z coordinate of vertex must lie between -50 and +70 inches[7] from the z coordinate of target center. The dump cut required the absolute values of y coordinates for both muon tracks at z =176", where it was in the middle of beam dump, to be less than 2.5 inches for all data.

More analysis were proceeded on the third-pass DST data files using the same program for booking different kinds of histogram that were not performed in the third pass. Because all of the information on the muon pair at target

[7]The negative sign means downstream from target center.

name of cut	passed	failed	survival percentage
SINK trigger	224491	48219	82.3
two target muons	224488	3	~ 100.0
opposite sign pair	217382	7106	96.8
xy-target cut (±2.5 in.)	200410	16972	92.2
z-vertex cut (+50,-70 in.)	168969	31441	84.3
y dump cut (|y|>2.5 in. at z = 176 in.)	148812	20157	88.1
ALL CUTs	148812	123898	**54.6**

Table 5.4: Third pass event cuts summary of data set 6.

was stored in the third pass DST, a time-consuming traceback procedure was not necessary for this pass, which would have different histograms or event cuts set up for some special purposes. For example, J/ψ and ψ' are located in the low-mass region, where the low-mass, *accidental-coincidence* background events are populated. In order to optimize the function of cuts, we adopted a different set of event cuts than those shown in table 5.4 for Drell-Yan data analysis; thus, eliminating of as many accidental events as possible, but keeping as many good events as possible, especially in the regions of large x_F and P_T , where the A-dependence behavior was important in this study. After the cut study, we found that only the ±100-inch z-vertex cut met the above requirements for this J/ψ and ψ' A-dependence study.

5.3 Summary of Analyzed Data

Good dimuon data were separated into three sets according to three magnetic field configurations. The low-mass data contains data set 6 and 10. Intermediate-mass data contains data set 1, 2, and 9. High-mass data contains data set 8. There were a total of 6.23×10^3 good dimuon events reconstructed

in this analysis. The following table shows the data summary:

magnet setting	$<M_{\mu^+\mu^-}>$	targets	proton flux	total dimuon events
Low Mass	5.4 GeV	Fe/Ca/D	$5.0*10^{15}$	148k
		W/C/D	$2.5*10^{15}$	68k
Medium Mass	7.0 GeV	Fe/Ca/D	$2.5*10^{16}$	263k
		W/C/D	$0.9*10^{16}$	109k
High Mass	9.5 GeV	Fe/Ca/D	$1.7*10^{16}$	35k

Table 5.5: E772 data summary.

Chapter 6

Normalization of Absolute and Relative Cross Sections

Absolute normalization is indispensable for extracting the scattering *cross section* from the *yield*. The relationship between these two quantities for our experiment is listed below,

$$Y(\mu\mu) = N_0 T(\xi) \cdot [\sigma^A_{\mu\mu}/n] \cdot n n_A L \cdot lt \cdot \varepsilon \cdot \overline{\Omega} \cdot \epsilon$$

It is useful to define the normalized yield Y_{NZ} as,

$$Y_{NZ} = Y(\mu\mu)/N_0 T(\xi) \cdot \rho L \cdot lt \cdot \epsilon \cdot \overline{\Omega}$$

where N_0 is the number of incident protons, T is the target transmission factor, n is the number of nucleons in the nucleus, n_A is the number of nuclei per unit volume, L is the target thickness, $\rho(= n n_A)$ is the number of nucleons per unit volume, lt is the system live time, ε is the detection efficiency, $\overline{\Omega}$ is the acceptance of the spectrometer, and ϵ is the off-line track reconstruction efficiency. The cross section per nucleon is obtained by dividing the normalized yield by the detection efficiency. This chapter will show how we achieved a 2% target-to-target relative normalization from the determination of *beam intensity, target thickness, live-time, tracker efficiency*, and *acceptance*. Information on beam intensity and live time were obtained from scaler data. Target transmission

factors and target thickness were calculated from accurate target data. Tracker efficiency was extracted from histograms ($Yield/SEM4$ *versus* $SEM4$) and was checked by a Monte Carlo rate-dependence study. Acceptance was calculated with a Monte Carlo simulation. Sources of random $\mu^+\mu^-$ background for this experiment were studied and subtracted from the data.

6.1 Relative Target-to-Target Normalizations

In this study of $\sigma^A_{\mu\mu}$ A-dependence, the values and uncertainties of relative target-to-target normalizations are crucial. The A-dependent ratio of nuclear target to deuterium is given by,

$$R = [\sigma^A_{\mu\mu}/\sigma^D_{\mu\mu}] \cdot (2/n) = N_{A/D} \cdot [Y^A/Y^D]$$

Each item in the normalization is listed below,

$$N_{A/D} = \underline{N_0^D/N_0^A} \cdot \underline{T^D(\xi)/T^A(\xi)} \cdot \underline{n_D L^D/n_A L^A} \cdot \underline{lt^D/lt^A} \cdot \underline{\varepsilon^D/\varepsilon^A} \cdot \underline{\overline{\Omega}^D/\overline{\Omega}^A} \cdot \underline{\epsilon^D/\epsilon^A}$$

Each normalization and uncertainty is discussed in detail in the following sections.

6.1.1 Beam Intensity Ratio N_0^D/N_0^A

As the last chapter has shown, there were 5 intensity monitors, SEM3, SEM4, L_4, I_x, and I_y, for recording the number of protons incident on each target. By integrating these 5 scaler monitors, good spill by good spill for every target in each data set and then taking ratios of D's proton counts to those of other targets, we obtain the intensity-normalized constants N_0^D/N_0^A. The discrepancy between different measurements of N_0^D/N_0^A is less than 1% ; therefore, the uncertainty in this normalization is negligible. This is illustrated with scaler data in table 6.1 for data set 10. The N_0 shown in this table is the scaler-monitor count, which is not the absolute proton count and (M) represents $\times 10^6$. We adopted the value of SEM4 as our intensity normalization constant because this monitor had been calibrated several times to actual proton count. We then could derive not only the ratio of normalized cross sections but also the normalized cross section itself for each target.

$N_0, N_0^D/N_0^A$	SEM4(M)	SEM3(M)	$L_4(M)$	$I_x(M)$	$I_y(M)$	mean	DEV
N_0^D	9.826	22.99	1803	1018	1012		
N_0^C	8.396	19.65	1538	867.0	862.1		
N_0^W	8.310	19.45	1527	861.8	856.9		
N_0^D/N_0^C	1.170	1.170	1.172	1.174	1.174	1.172	0.002
N_0^D/N_0^W	1.182	1.182	1.181	1.181	1.181	1.181	0.001

Table 6.1: Normalization and uncertainty of relative incident proton measurements for data set 10.

6.1.2 Target Areal Density Ratios $n_D L^D/n_A L^A$

There were 5 nuclear targets for this A-dependence study. The nucleons in D nucleus are viewed as quasi-free particles; therefore, they provide a free isoscalar nucleon reference in this study. The liquid D_2 target was built and maintained by the Fermilab cryogenic group, and solid-target disks of C, Ca, Fe, and W [68] were fabricated in Los Alamos.

The 7 items under consideration for the areal density, ρL, of the cryogenic deuterium target are: 1) beam-heating effect on target density; 2) mass transport in the target cell due to the heat load; 3) bubble formation due to beam heating; 4) D_2 composition; 5) target thickness (including the thickness of containers); 6) D_2 vapor pressure; and 7) target-beam centering. The temperature rise caused by beam heating was calculated to be less than 0.3 °K; therefore, the effects due to items 1, 2, and 3 were negligible. The information on target thickness was obtained from item 5 and the density was calculated from item 4 and 6. The total uncertainty of ρL for the deuterium target was dominated by uncertainties of the measurements associated with items 4 to 7 and is shown in table 6.2[1]. This 0.40% uncertainty is the largest one among all our targets.

For solid targets, it is more straightforward to calculate the areal density

[1] Please refer to target analysis by G. Danner and H.W. Baer, 8/11/88.

source of uncertainty		contribution to ρL
in target thickness:	flask length	0.01%
	beam-target misalignment	0.1%
in density ρ:	pressure regulation	0.12%
	sample composition	0.063%
	pressure-temperature data	0.12%
	density-temperature data	0.34%
total(quadrature)		0.40%

Table 6.2: Contributions to ρL uncertainty of D target.

ρL and estimate the uncertainty. All weights and measurements are averages of at least three independent measurements [68]. The uncertainty of ρL was

target	source of uncertainty	contribution to ρL
W	measurement of mass	.0.0015%
	measurement of area	0.10%
	non-parallelism of disk faces	0.030%
	beam target misalignment	0.011%
	beam heating	0.019%
	total(quadrature)	0.11%

Table 6.3: Contributions to ρL uncertainty of solid targets.

calculated from uncertainties in the individual measurement according to,

$$\begin{aligned} \rho L &= W/(\pi D^2/4), \\ \delta(\rho L)/(\rho L) &= [(\delta W/W)^2 + (2\delta D/D)^2]^{1/2} \end{aligned}$$

where ρ is the density, W is the weight, D is the diameter, and L is the target thickness. The total uncertainty of the W target is the largest one among the solid targets. It is shown in table 6.3.

6.1.3 Beam Attenuation Ratios $T^D(\xi)/T^A(\xi)$

The proton beam was attenuated inside each target by inelastic scattering: therefore, the previous luminosity normalization should be corrected. This effect is illustrated in figure 6.1 in which N_0 is the number of protons incident on target, dN is number of protons attenuated inside the target slice of width dz, and L is the total length of the target. The intensity attenuation function, $N(z)$, is given by

$$N(z) = N_0 e^{-n_A \sigma_i z} = N_0 e^{-z/\lambda}$$

where $\lambda = \frac{1}{n_A \sigma_i}$; σ_i is the inelastic scattering cross section[2]. The total effective number of protons for muon-pair production is simply the integration of $N(z)$ from 0 to L, divided by the target thickness L, and is expressed as

$$N_{eff} = N_0[(1 - e^{-\xi})/\xi] = N_0 T(\xi)$$

where $\xi = L/\lambda$. The normalizations of the transmission factor, T^D/T^A, are summarized in summary table 6.8.

6.1.4 Electronic Live Times and Their Target Dependence

In the last chapter, there were 3 monitors, SEM4, AMON, and WMON, used to record the live time for each target. The ratios SEM4·SB / SEM4, AMON·SB / AMON , and WMON·SB / WMON measured the live times of our trigger and transport system. The discrepancy between different measurements is much

[2]The solid-target inelastic cross sections were calculated by A. Klein, using the model of C.Y. Wong[69] for 400 GeV protons, which is a very good approximation for the 800 GeV case. The D-target inelastic cross section was taken from the measurement by Roberts et al.[70].

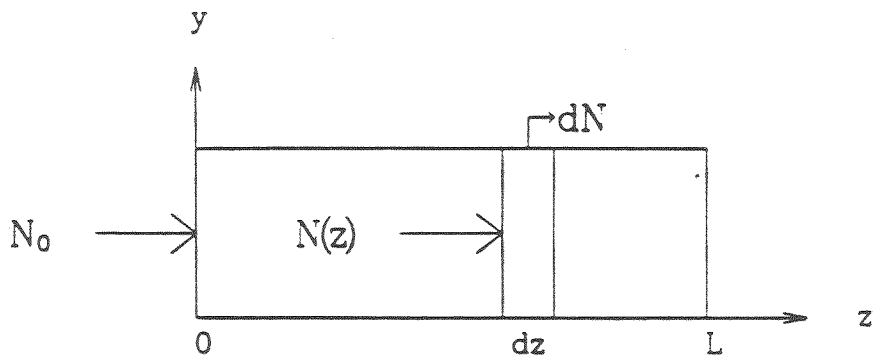

Figure 6.1: Beam attenuation diagram.

less than 1% . This is illustrated with scaler data of data set 10 in table 6.4. These high live times($> 98\%$) were the result of effective rejection of beam-

$lt, lt^D/lt^A$	SEM4LT	AMONLT	WMONLT	mean	DEV
lt^D	0.9933	0.9864	0.9861	0.9886	0.0047
lt^C	0.9939	0.9878	0.9874	0.9897	0.0042
lt^W	0.9948	0.9899	0.9896	0.9914	0.0034
lt^D/lt^C	0.9994	0.9986	0.9987	0.9989	0.0005
lt^D/lt^W	0.9985	0.9965	0.9965	0.9972	0.0013

Table 6.4: Normalization and uncertainty of live-time measurements.

dump events by the *trigger matrix*, which was a set of trigger roads for events originating from the target.

6.1.5 Detection Efficiency

Because the total number of tracks that fired detectors was dominated by events generated from the 168" copper beam dump, the difference in areal density between targets had a negligible effect on absolute detection efficiency. Meanwhile, the long-term drift in the detector system largely cancels out in the ratio of detection efficiencies, due to the frequent change of target position. Therefore, it was justified to assume that there was no A-dependence caused by the difference in target and time dependence of the detection efficiency, i.e., $\epsilon^D/\epsilon^A = 1$.

6.1.6 Rate-Dependence of Tracker

If the software reconstruction efficiency is a constant under different kinds of environments, then the ratio of yield to luminosity per spill should be independent of luminosity. The *rate-dependence* histogram (Yield / SEM4 *versus*

SEM4) of our data revealed that there was a decrease of the tracker efficiency at large target areal density with the same value of SEM4 or at high instantaneous luminosity for the same target. Even though we had adjusted all target thicknesses to be as close as possible and interchanged targets through short-term cycles to minimize the discrepancy of run conditions between targets, the existing differences in areal density and instantaneous luminosity between targets could still introduce an A-dependence to the ratio of normalized yields if the rate-dependence effect was not corrected. Meanwhile, its uncertainty was the biggest one among all systematic errors; therefore, we studied this effect from both our data and rate-dependence MC simulations.

The loss of reconstructed events due to tracker inefficiency was found to be directly proportional to both the instantaneous beam intensity[3], I, and the target areal density, ρL, and this dependence was also observed in Monte Carlo studies. The tracker efficiency can be formulated as

$$< \epsilon > = 1 - \alpha \times \rho L \times < I > \tag{6.1}$$

$$< \epsilon > \approx 1 - \alpha \times [\Sigma_{i=1}^{N} (\rho L)_i] \times < I > \tag{6.2}$$

where ϵ is the tracking efficiency and α is the rate-dependence coefficient, which is obtained from a fit to the data for each data set; the symbol $< I, \epsilon >$ represents the average values of instantaneous intensity and tracker efficiency over all the spills in one data set; N is the number of target in each data set. The averaged tracking inefficiency was calculated by dividing the difference between averaged yield per SEM4, $< Yield/SEM4 >$, and yield per SEM4 at zero intensity, $(Yield/SEM4)^0$, by $(Yield/SEM4)^0$. The tracking efficiency is calculated by the following equation

[3]This could be represented by the counts of SEM4 per spill.

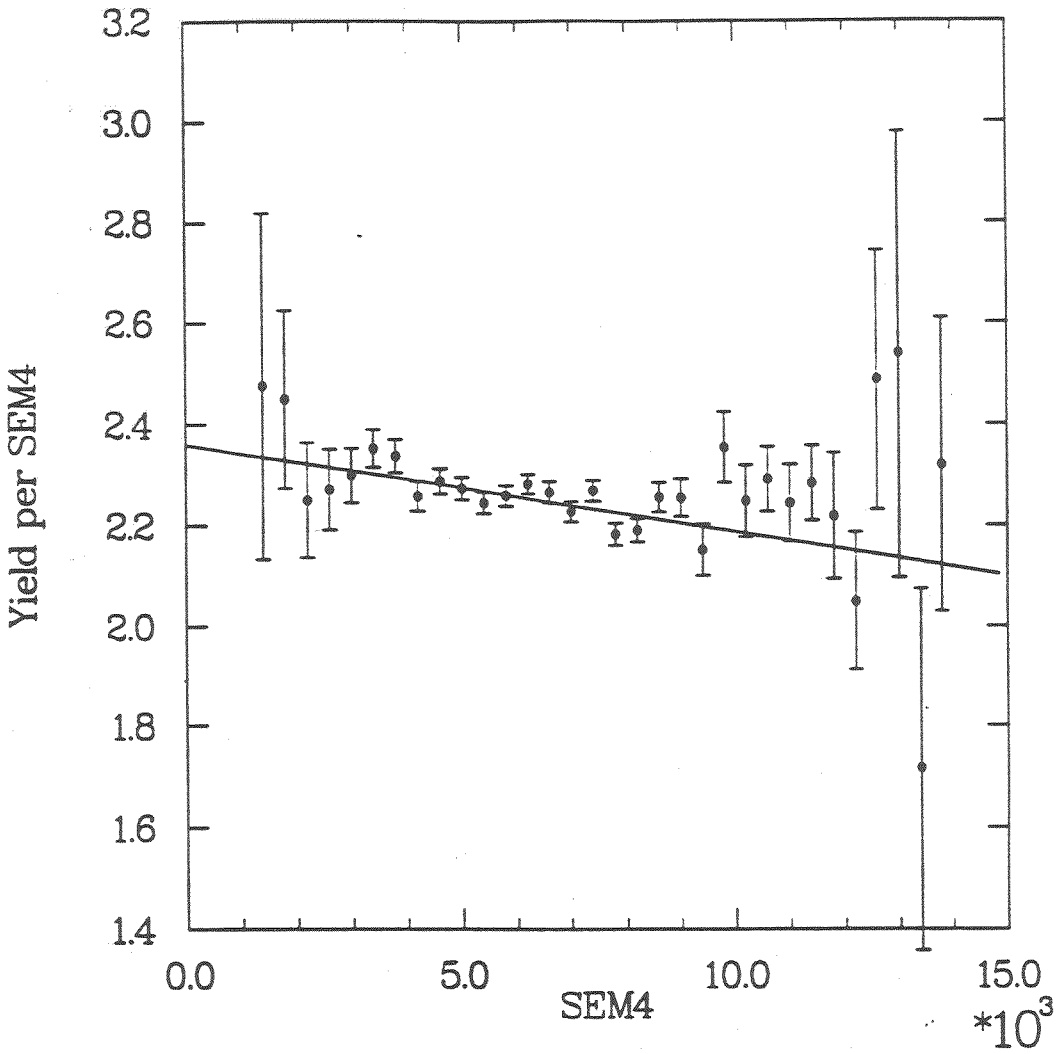

Figure 6.2: Rate-dependence study for data set 6.

$$< \epsilon > \quad = 1 - [(Yield/SEM4)^0 - < Yield/SEM4 >]/(Yield/SEM4)^0.$$

A straight line was fitted to the rate-dependence histogram, which included all target data in each data set in order to get a precise fit. The offset of this line at SEM4 = 0 is the yield per SEM4 with assumed 100% tracker efficiency. Knowing the averaged instantaneous luminosity and areal density of a data set, the rate-dependence coefficient α can be deduced from equation 6.2. Figure 6.2 shows the straight-line fit on rate-dependence histogram for getting the coefficient α of data set 6. Once we get the value of α for each data set, then the calculation of tracker inefficiencies for each target is straightforward by equation 6.1. Table 6.5 shows all of the corrections, which are the inverse of tracker efficiencies, for targets in each main data set.

The correction of target-to-target differences in the reconstruction efficiency was calculated simply by taking the ratio of rate-dependence corrections of targets.

6.2 Absolute Acceptance Calculations

The acceptance as a function of any kinematic variable x is defined as below

$$A(x) \quad = \lim_{N\to\infty} Y_{accepted}(x)/Y_{thrown}(x); N \equiv \int Y_{thrown}(x)dx$$

$$= \int \sigma(x, y_1, \cdots, y_n) A(x, y_1, \cdots, y_n) \prod_{i=1}^{n} dy_i / \int \sigma(x, y_1, \cdots, y_n) \prod_{i=1}^{n} dy_i$$

$$\Rightarrow \int \sigma(y_1, \cdots, y_n) A(x, y_1, \cdots, y_n) \prod_{i=1}^{n} dy_i / \int \sigma(y_1, \cdots, y_n) \prod_{i=1}^{n} dy_i$$

data set	rate dep. coefficient	<I>	tracking efficiency	<duty factor>	correction factor
1	0.00114±0.00009	14.1	90.0±0.8	60%	D (1.084±0.010) Ca(1.129±0.010)
2	0.00124±0.00013	13.1	89.7±1.1	60%	D (1.088±0.013) Fe(1.134±0.014)
6	0.00213±0.00024	6.31	91.2±1.0	43%	D (1.071±0.012) Ca(1.106±0.012) Fe(1.108±0.012)
8	0.000290±0.000097	19.0	96.4±1.2	43%	D (1.028±0.013) Ca(1.041±0.013) Fe(1.042±0.013)
9	0.00150±0.00017	9.55	91.1±1.0	43%	D (1.075±0.012) C (1.108±0.012) W (1.110±0.012)
10	0.00227±0.00061	4.76	93.7±1.7	50%	D (1.056±0.019) C (1.062±0.019) W (1.081±0.020)

Table 6.5: Rate dependence study.

where "$\Rightarrow$" is valid provided that $\sigma(x, y_1, \cdots, y_n) = \sigma(x)\sigma(y_1, \cdots, y_n)$; A is the true acceptance[4] as a function of all kinematic variables. Each event was simulated by the Monte Carlo technique, which generated the value of every variable by sampling over the distribution of that variable with a random number generator. The assumed distributions for continuum and resonance dimuon are summarized in table 6.6, where $\upsilon = \sqrt{4\tau + x_F^2}$, $P_T^{max} = (\sqrt{s}/2)\sqrt{(1-\tau)^2 - x_F^2}$.

Variable	Range	Drell-Yan	J/ψ ,ψ' ,Υ
M,x_F	M(6. ,16.)	2-D cross section table	$\delta(m - m_{resonance})$
(high mass)	x_F (-.2 ,.8)	calculated with Duke-Owen	$(1+\tau-\upsilon)^2/\upsilon$
M,x_F	M(3.5,16.)	2-D cross section table	$\delta(m - m_{resonance})$
(int. mass)	x_F (-.2 ,.8)	calculated with Duke-Owen	$(1+\tau-\upsilon)^2/\upsilon$
M,x_F	M(4. ,16.)	2-D cross section table	$\delta(m - m_{resonance})$
(low mass)	x_F (-.2 ,.8)	calculated with Duke-Owen	$(1+\tau-\upsilon)^2/\upsilon$
P_T	(0.,P_T ^{max})	P_T /(1+(P_T /p_0)^2)^6	same as the left
ϕ_γ	(0.,2π)	uniform	uniform
$cos\theta_{\mu^+\mu^-}$	(-1.,1.)	1 + $cos^2\theta_{\mu^+\mu^-}$	uniform
$\phi_{\mu^+\mu^-}$	(0.,π)	uniform	uniform

Table 6.6: Distributions used for Drell-Yan and resonances event simulation

This simulation included all multiple scattering and energy loss that occurs in the passage of muons through materials, as well as an accurate geometrical survey of the apparatus. Muon pairs were generated over all of the phase space defined in table 6.6 according to the hypothetical distributions. Those pairs that traced through the spectrometer successfully were recorded and written to a raw data file with the same format as that of the real data file. This fake data was then analyzed as if it were real data. Later, the number of Monte Carlo events that passed the analysis chain was divided by *twice* the number

[4]This means that the acceptance depends only on the the apparatus, not on any distribution of kinematic variables.

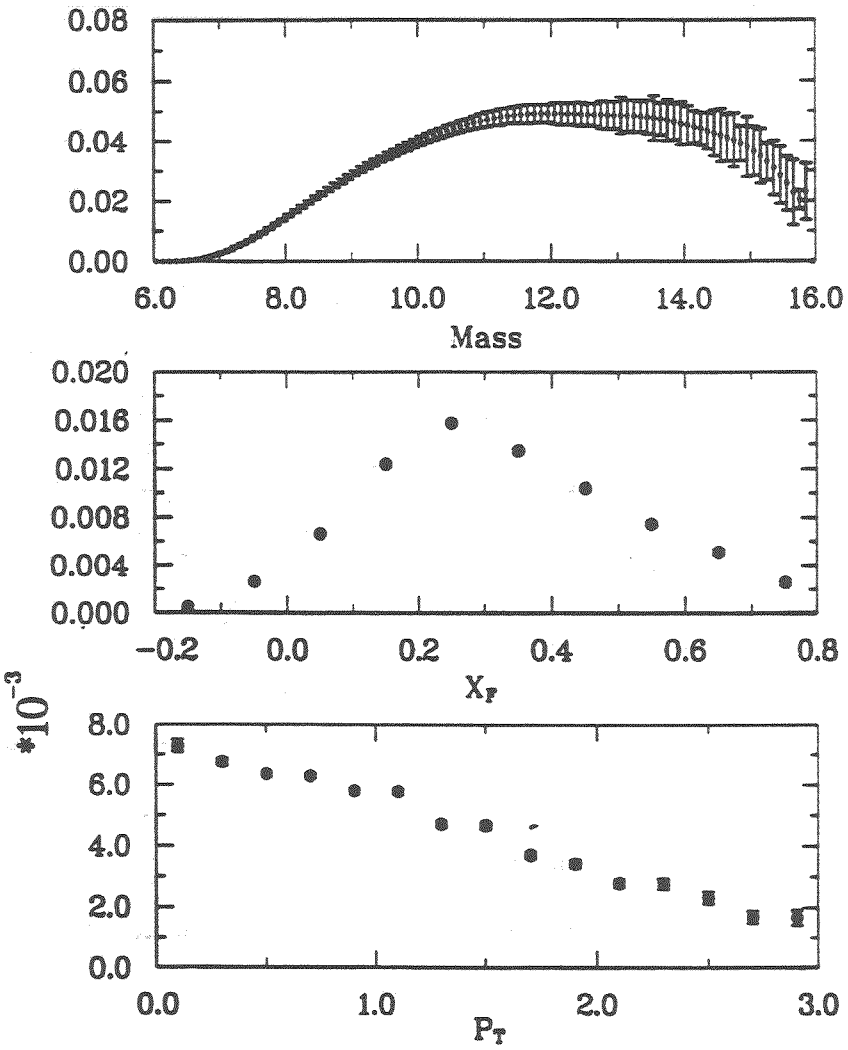

Figure 6.3: Drell-Yan acceptance functions for high mass setting as calculated by the Monte Carlo simulation.

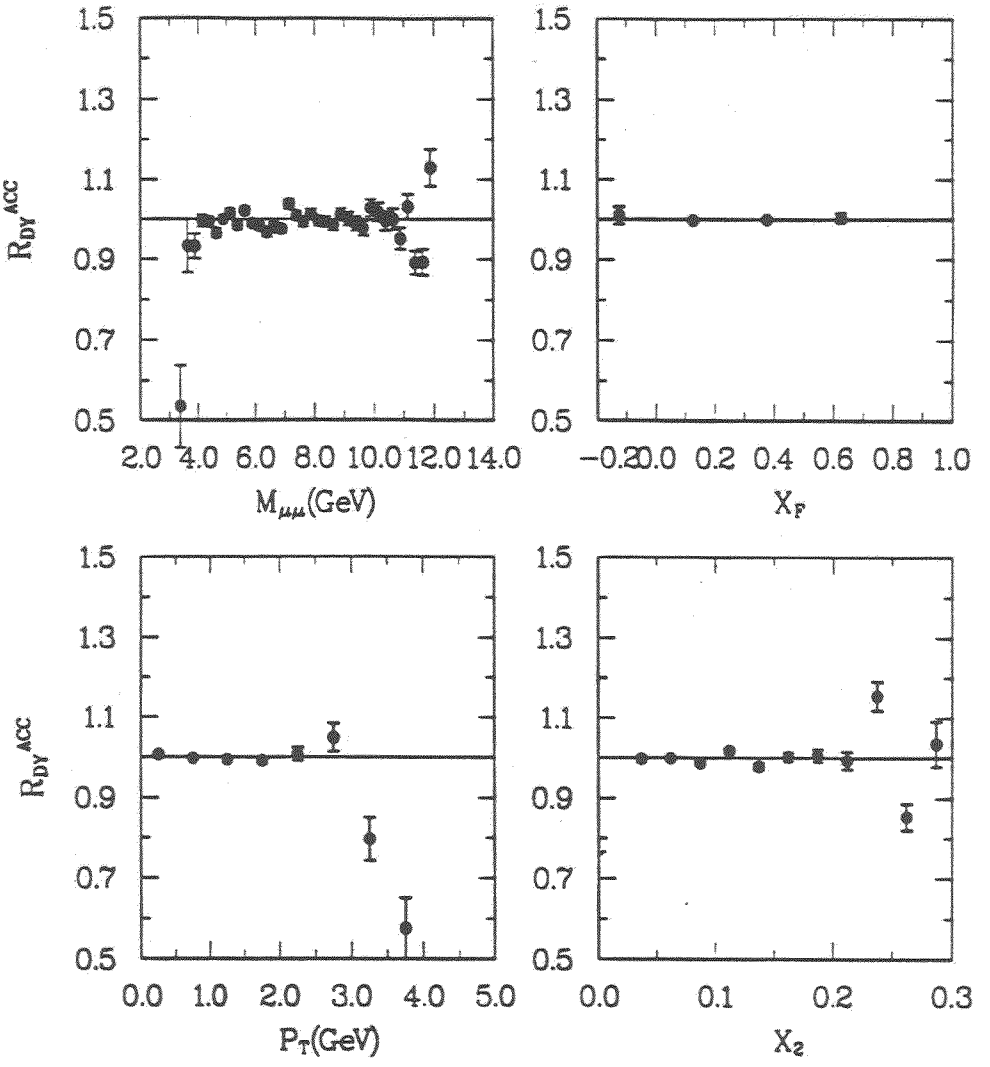

Figure 6.4: Relative Drell-Yan acceptance as functions of $M_{\mu^+\mu^-}$, x_F , P_T , and x_2 .

of generated events because we didn't throw events in the range of $(\pi, 2\pi)$ for $\phi_{\mu^+\mu^-}$ where no event could possibly be accepted due to the signs of the muon charges.

Over one million Drell-Yan pairs were tracked through a complete simulation of the spectrometer, including firing the experimental trigger. Figure 6.3 shows the Drell-Yan acceptance as functions of $M_{\mu^+\mu^-}$, x_F , and P_T . Because MC simulation was a powerful technique to understand the behavior of our apparatus, we carried out several studies using this simulation program on absolute acceptance, resolutions[5], relative acceptance, accidental coincidence background, and rate-dependence. The target-to-target acceptance correction, which is one of the relative normalizations, was calculated to 1 % level.

6.3 Target-to-Target Relative Acceptance Corrections

The target dependence of the acceptance was studied by taking ratios of solid-target acceptance to that of D against different variables $M_{\mu^+\mu^-}$, x_2 , x_F , and P_T . In the following kinematic regions: 4< $M_{\mu^+\mu^-}$<11, 0< x_2 <0.25, -0.2< x_F <0.6, and 0< P_T <2.5, ratios are kept constant as seen in figure 6.4. This means that this correction does not depend on kinematic variables in the region of interest, and only an overall correction constant is needed for each ratio. The acceptances of solid targets were calculated by MC to be 1.009 larger than that for the liquid deuterium. This correction was then applied to the data.

[5]Such as $M_{\mu^+\mu^-}$, z-vertex, x-tgt, y-tgt, and momentum resolution.

6.4 Dimuon Backgrounds

The background of this experiment comes from three possible sources: 1) interaction of secondary pions with the targets; 2) dimuon events generated from upstream sources; and 3)the accidental coincidence muon-pair event. The contributions from the first two sources are found to be negligible. The last one has a visible effect on our data, especially in the low-mass and intermediate-mass data sets.

6.4.1 Dimuons from Secondary Pion Flux

Because the secondary pion flux produced in the front part of a target could interact with nuclei in the passage through the rest of the target, the contribution of dimuon yield from this source was studied. First, the Monte Carlo acceptance for pions at 7 different energies [6], starting from 280 GeV to 760 GeV in steps of 80 GeV, was calculated. Then the pion flux and cross section were folded with the acceptance in order to obtain the yield. In conclusion, there was less than 0.5 % dimuon produced from this secondary pion beam. This was a negligible uncertainty compared to that of rate dependence, and was not included in our correction factors.

6.4.2 Dimuons from Other Sources

During data taking, we took some target-out data in order to study the background events generated from the possible upstream sources for each mass setting. After processing these data through all passes, there were about 8, 5, 0.4 muon-pair events per 10^6 SEM for low, intermediate, and high mass, and were negligible compared to the event rate from the D target.

[6] Please refer to E772 internal communication by A. Klein, 4/6/88.

6.4.3 Subtraction of Accidental $\mu^+\mu^-$ Pairs

Accidental coincidence of single-muon events (or equivalently called $\mu^\pm\mu^\pm$) that populated the region 2.0<$M_{\mu^+\mu^-}$<6.0 GeV, 0.0<x_F < 0.35, and 0.0<P_T < 2.5 GeV, were the main source of our background. Because of the non-zero acceptance at mass near 4 GeV, low- and intermediate-mass data were contaminated by these events, but not the high-mass data. These accidental events could be estimated from observed like-sign pairs with the assumptions that the apparatus was symmetric about the horizontal plane at $y = 0$ and the same production rate for single μ^+ and μ^- events.

A like-sign pair was selected by the LIKE trigger, which demanded at least one muon in the left part of the apparatus and the other in the right part and the software requirement of a muon pair with the same sign of charge. The probabilities of producing single μ^+ or μ^- events with the same momentum vector are the same; therefore, in a large enough sample, each $\mu^+\mu^-$ accidental coincidence event corresponds to either a $\mu^+\mu^+$ or $\mu^-\mu^-$ coincidence event. With this relation, we can reconstruct the kinematics of opposite-sign accidental coincidence events from like-sign events by reflecting either muon momentum vector about the horizontal plane, $y = 0$, to the other part of the apparatus, and calculate kinematic variables of this muon pair with one reflected momentum. The $M_{\mu^+\mu^-}$, x_F , and P_T distributions of this like-sign event are shown in figure 6.5. The LIKE trigger was prescaled by a factor of four; therefore, this factor was applied to the like-sign histograms before these like-sign histograms were subtracted from the reconstructed dimuon histograms for correcting the contamination from accidental coincidence events.

In the intermediate-mass data, the DIMU trigger, which didn't contain two veto triggers $\overline{NX1}$ and $\overline{NX3}$ in itself, was the only available trigger for opposite-

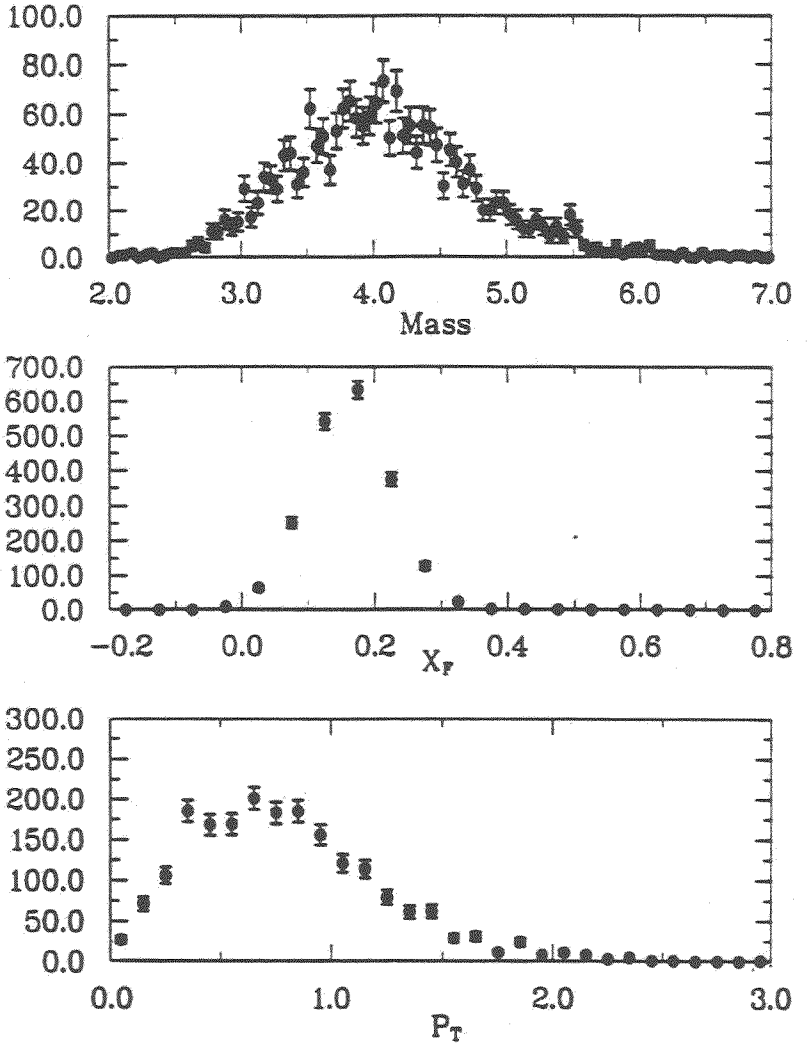

Figure 6.5: Measured like-sign dimuon distributions for low mass data set 6.

sign dimuon event; therefore, the correction for veto effect in this data set was studied and added to the like-sign corrections. Table 6.7 shows the summary of like-sign corrections for low- and intermediate-mass data.

data set	N($\mu^+\mu^-$)	observed $\mu^\pm\mu^\pm$	correction factor	actual $\mu^\pm\mu^\pm$	N($\mu^\pm\mu^\pm$)/N($\mu^+\mu^-$)
1	138512	412	6±1	2472±412	0.018±0.003
2	123980	388	6±1	2328±388	0.019±0.003
6	148812	2026	4±0	8104±180	0.054±0.001
9	109125	340	5±1	1700±340	0.016±0.003
10	68429	487	4±0	1948±88	0.028±0.001

Table 6.7: Summary of accidental coincidence events.

6.5 Summary of Normalization and Systematic Errors

The systematic error in the ratio of the yield from the solid targets *versus* deuterium is dominated by the error in the rate dependence (1.5 %), acceptance (0.4 %), deuterium areal density (0.4 %) and beam attenuation (0.3 %) as listed in table 6.9. All other contributions are negligible. The results in a total estimated systematic error in the ratios of less than 2 % .

This section summarizes all the normalizations used in data set 6, 10; 1, 2, 9; and 8 in the order of low-mass, intermediate-mass, and high-mass data. They include proton count (N_0), target transmission factor ($T(\xi)$), number of nucleons per unit area (nn_AL), live time (lt), and rate-dependence correction (ϵ). Table 6.8 shows the summary of all normalizations.

data set	target	N_0	$T(\xi)$	nn_AL (10^{24})	lt	ϵ	N	$N_{A/D}$
1	D	79.49	0.927	4.959	0.9834	1.084	0.003017	
1	Ca	79.69	0.951	7.123	0.9824	1.129	0.002129	0.706±0.010
2	D	65.60	0.927	4.959	0.9839	1.088	0.003667	
2	Fe	64.27	0.954	7.282	0.9841	1.134	0.002581	0.704±0.013
6	D	24.42	0.928	4.935	0.9865	1.071	0.009708	
6	Ca	21.15	0.951	7.123	0.9856	1.106	0.007833	0.807±0.014
6	Fe	20.39	0.954	7.282	0.9865	1.108	0.007929	0.817±0.014
8	D	72.21	0.928	4.896	0.9924	1.028	0.003157	
8	Ca	60.66	0.951	7.123	0.9918	1.041	0.002554	0.809±0.015
8	Fe	59.66	0.954	7.282	0.9919	1.042	0.002535	0.803±0.015
9	D	41.80	0.928	4.896	0.9871	1.075	0.005734	
9	C	34.21	0.936	6.775	0.9847	1.108	0.005187	0.905±0.016
9	W	35.12	0.969	6.937	0.9908	1.110	0.004746	0.828±0.015
10	D	9.826	0.928	4.896	0.9864	1.056	0.02398	
10	C	8.396	0.949	5.421	0.9878	1.062	0.02489	1.038±0.028
10	W	8.310	0.969	6.934	0.9899	1.081	0.01956	0.816±0.022

Table 6.8: Summary of normalizations.

sources of systematic errors	estimated uncertainty
luminosity and position of proton beam	$\ll 1$ %
targets	0.4 %
live time(kept above 98 %)	$\ll 1$ %
tracker efficiency	1.5 %
relative acceptance	0.4 %
total systematic error	**1.6 %**

Table 6.9: Summary of systematic errors

Chapter 7

Presentation of Results

This chapter presents E772 data in the following three stages. First, the event distributions *versus* $P_{\mu^+\mu^-}$, $M_{\mu^+\mu^-}$, x_F , P_T , x_1 , x_2 , and cosθ are shown. The absolute cross sections and K-factors for high mass settings are presented. Second, the A-dependence study of the Drell-Yan process is reported. Third, the peak-fitting procedure for the J/ψ , ψ' , and Υ resonances and the A-dependent study are presented. Most of the A-dependent results have been published or submitted to Physical Review Letter [79,103,104]. All the A-dependent numbers are tabulated in the appendix.

7.1 Event Distributions

Event distributions show how the data are distributed *versus* various kinematic variables. They reflect the acceptance of the apparatus. Using the measured momentum vectors at the vertex of two-muon tracks, the invariant mass $M_{\mu^+\mu^-}$, x_F , and transverse momemtum P_T of dimuons were calculated with the formulas:

$$M_{\mu^+\mu^-} = \sqrt{E^2_{\mu^+\mu^-} - P^2_{\mu^+\mu^-}} \tag{7.1}$$

$$x_F = \frac{p^z_{\mu^+} + p^z_{\mu^-}}{\sqrt{s}/2(1 - M^2_{\mu^+\mu^-}/s)} \tag{7.2}$$

$$P_T = \sqrt{(p^x_{\mu^+} + p^x_{\mu^-})^2 + (p^y_{\mu^+} + p^y_{\mu^-})^2} \tag{7.3}$$

where $E_{\mu^+\mu^-}$ and $P_{\mu^+\mu^-}$ are the energy and momentum of the dimuon. $p^{x,y,z}_{\mu}$ are momentum components in x, y, z direction in the p-p center-of-mass frame. The parton variables x_1 and x_2 were obtained by equations

$$x_1 = \frac{1}{2}x_F + \sqrt{\tau + \frac{1}{4}x_F^2}, \tag{7.4}$$

and

$$x_2 = -\frac{1}{2}x_F + \sqrt{\tau + \frac{1}{4}x_F^2}. \tag{7.5}$$

Figure 7.1 shows the mass distributions for three magnet settings labelled low-mass setting, intermediate-mass setting, and high-mass setting. The Drell-Yan yields peak at 4.5, 6, and 8.5 GeV for low-, int.-, and high-mass settings, respectively. In the low mass case, the two peaks at masses 3.11 GeV and 3.70 GeV correspond to the J/ψ and ψ' . They are well separated and have experimental widths (FWHM) of 230 MeV and 200 MeV. Because most of the lower mass muon pairs that pass the 2.5 inch dump cut have at least one muon going through the beam dump, the mass resolutions at lower mass (J/ψ) are worse than those at higher mass (ψ'). The intermediate mass data contains most of the Drell-Yan data which lie between the ψ' and $\Upsilon(1s)$. The $\Upsilon(1s)$, $\Upsilon(2s)$, and $\Upsilon(3s)$ at masses 9.40 GeV, 9.95 GeV, and 10.26 GeV, respectively, are evident in the high mass data. The experimental widths (FWHM) of the $\Upsilon(1s)$ is 280 MeV.

Figure 7.2 shows the event distributions of muon-pair kinematic quantities $P_{\mu^+\mu^-}$-(in lab. frame), $M_{\mu^+\mu^-}$, x_F , and P_T . Figure 7.3 shows the event distributions of quark variables x_1 , x_2 , and decay angle cosθ of μ^+. The massive muon pairs with $M_{\mu^+\mu^-}$-> 3 GeV accepted by the E772 spectrometer, are forward moving($x_F > 0$) with the longitudinal momentum above 90 GeV in the

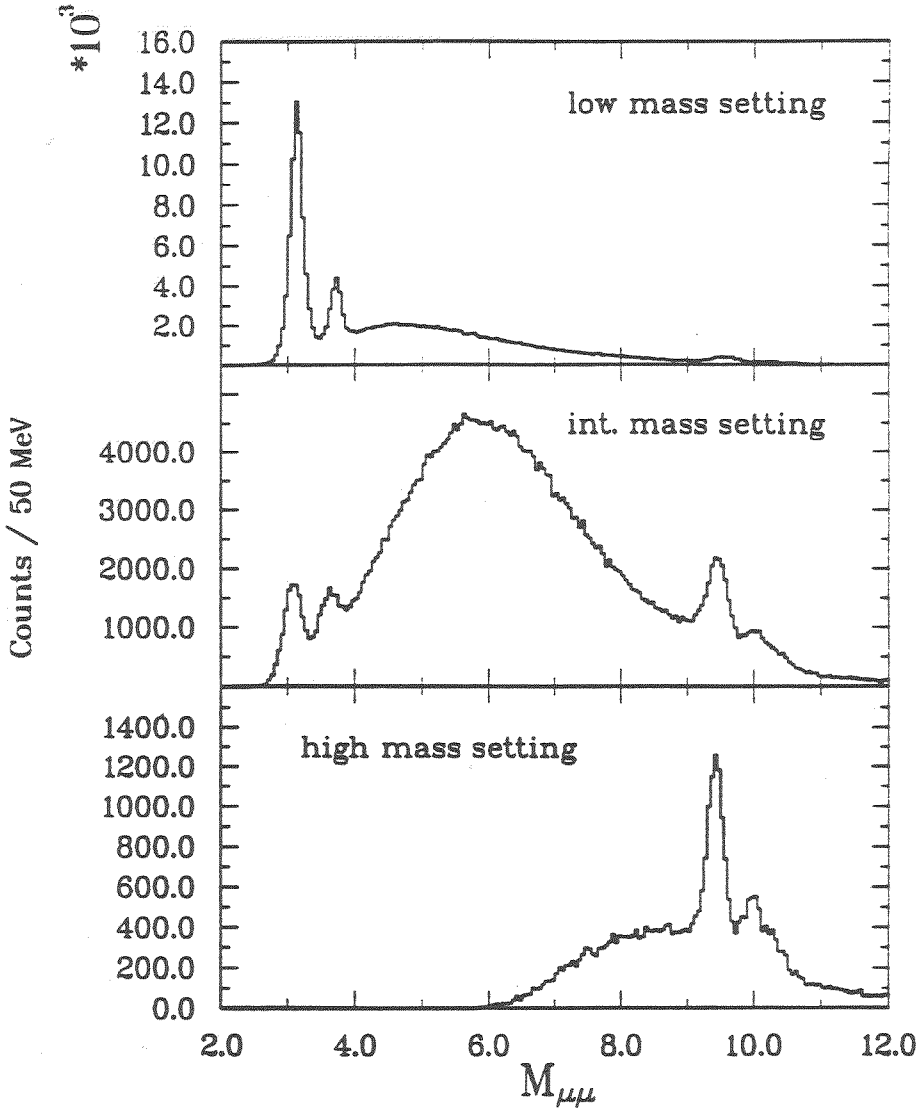

Figure 7.1: The measured mass spectra at the three spectrometer settings.

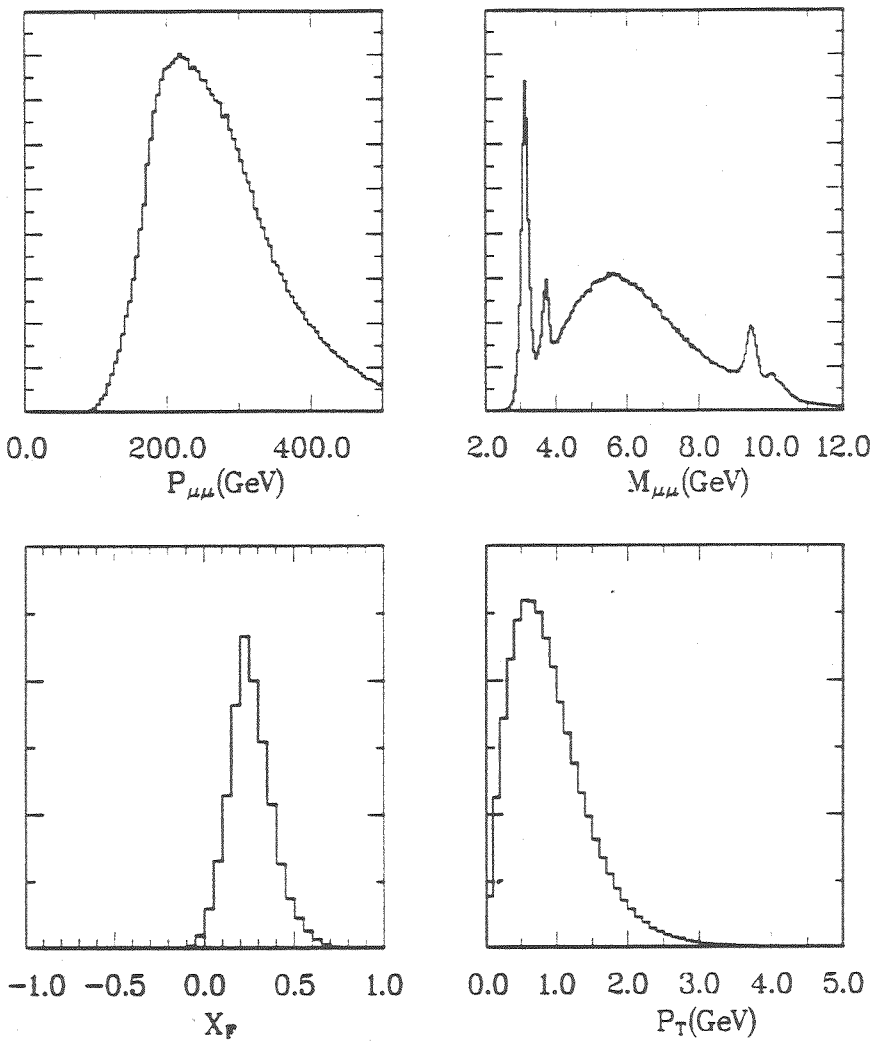

Figure 7.2: The event distributions of all data *versus* muon-pair variables. $P_{\mu\mu}$ is the sum of the laboratory momenta of the μ^+ and μ^-. Mean values for these distributions are given in table 7.1.

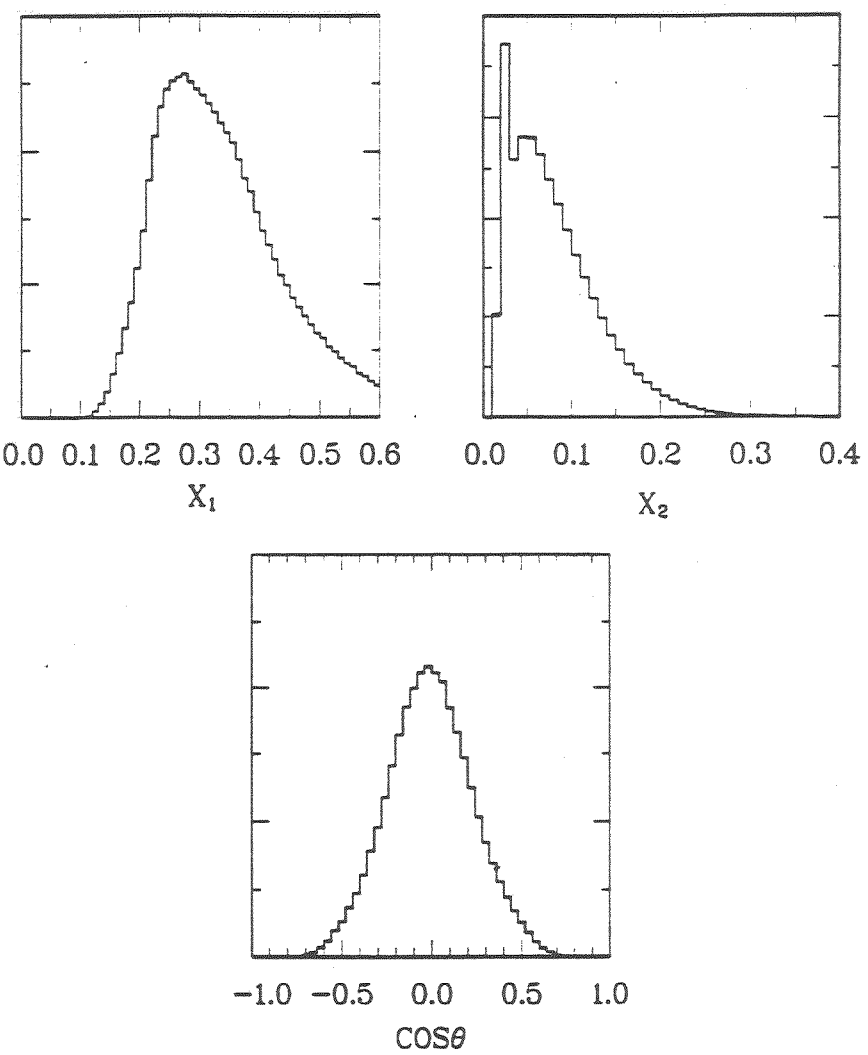

Figure 7.3: The event distributions of all data *versus* parton variables x_1 and x_2 , and as the μ^+ decay angle. Mean values for these distributions are given in table 7.1.

lab. frame and having a P_T kick up to 4 GeV. Those beam partons which formed muon pairs via Drell-Yan process or vector-meson production, are very stiff in longitudinal momentum with average value $<x_1> = 0.369$ and ranging up to $x_1 = 0.8$. The average values and ranges of each kinematic variable are listed in table 7.1.

variable	$P_{\mu^+\mu^-}$-(GeV)	$M_{\mu^+\mu^-}$-(GeV)	x_F	P_T (GeV)
<variable>	267	5.99	0.257	0.908
range	90 - 500	2 - 12	-0.1 - 0.75	0 - 4

variable	x_1	x_2	$\cos\theta$
<variable>	0.329	0.081	-0.009
range	0.1 - 0.8	0.01 - 0.35	-0.75 - 0.75

Table 7.1: Average values and ranges of kinematic variables in the measured event distributions using all data.

7.2 Absolute Cross Sections

We have determined absolute cross sections for two purposes. First, we can check both the data analysis and MC simulations by comparing our results to other existing experimental cross sections. Second, we wish to determine the K-factor for the Drell-Yan process. This is done by comparing our experimental cross sections with Drell-Yan cross sections calculated with quark distribution functions in LLA (Leading Log Approximation), as discussed in section 1.4.3.

7.2.1 Differential Cross Sections *versus* $M_{\mu^+\mu^-}$-and x_F

The differential cross sections *versus* $M_{\mu^+\mu^-}$-and x_F were obtained by normalizing the $M_{\mu^+\mu^-}$-and x_F spectra with proton count (N_0), transmission factor

$(T(\xi))$ [1], number of nucleons per unit area (ρL), live time (lt), acceptances ($\overline{\Omega}(M_{\mu^+\mu^-}$-or x_F)), and a rate-dependence correction (ϵ). It can be expressed in the following equation

$$\frac{d\sigma}{dx} = \frac{\lim_{\Delta x \to 0} \Delta Y / \Delta x}{N_0 \times T(\xi) \times \rho L \times lt \times \overline{\Omega}(x) \times \epsilon} \tag{7.6}$$

where x can be either $M_{\mu^+\mu^-}$-or x_F ; ΔY is the yield in kinematic interval Δx; the numerical values of these normalization constants are given in the table 6.8 and figure 6.3. The total systematic error is estimated as 12% in which uncertainties of absolute proton count and trigger efficiency dominate. The uncertainty on the absolute incident proton flux measurements is estimated to be 5% , and the uncertainty on the trigger efficiency is estimated to be 10% .

Figure 7.4 shows the measured differential cross section in $M_{\mu^+\mu^-}$. The data are for the D target. One sees that the cross sections are quite small. ranging from 1.2×10^{-5} to 2.6×10^{-2} nbarn / (GeV×nucleon) in the mass region of $2 < M_{\mu^+\mu^-} < 15$ (GeV). Figure 7.5 shows the Drell-Yan[2] differential cross section in x_F measured with the D target. There, cross sections range from 3.3×10^{-4} to 5.3×10^{-2} nbarn / (GeV×nucleon) in the region of $-0.2 < x_F < 0.8$. Solid curves shown in both figures are calculations of the Drell-Yan cross sections, normalized to the acceptance-corrected $M_{\mu^+\mu^-}$-and x_F spectra, using the structure functions of Eichten et al.[73].

7.2.2 Extracted K-Factor

The K-factor is extracted by taking the ratio of experimental cross section to the cross section calculated with quark distribution functions in LLA. The LLA cross sections were calculated using Q^2-dependent parton distribution functions

[1] It deals with the target-attenuation effect on incident beam flux.

[2] With cuts of $4 < M_{\mu^+\mu^-} < 9$ and $M_{\mu^+\mu^-} > 11$ (GeV).

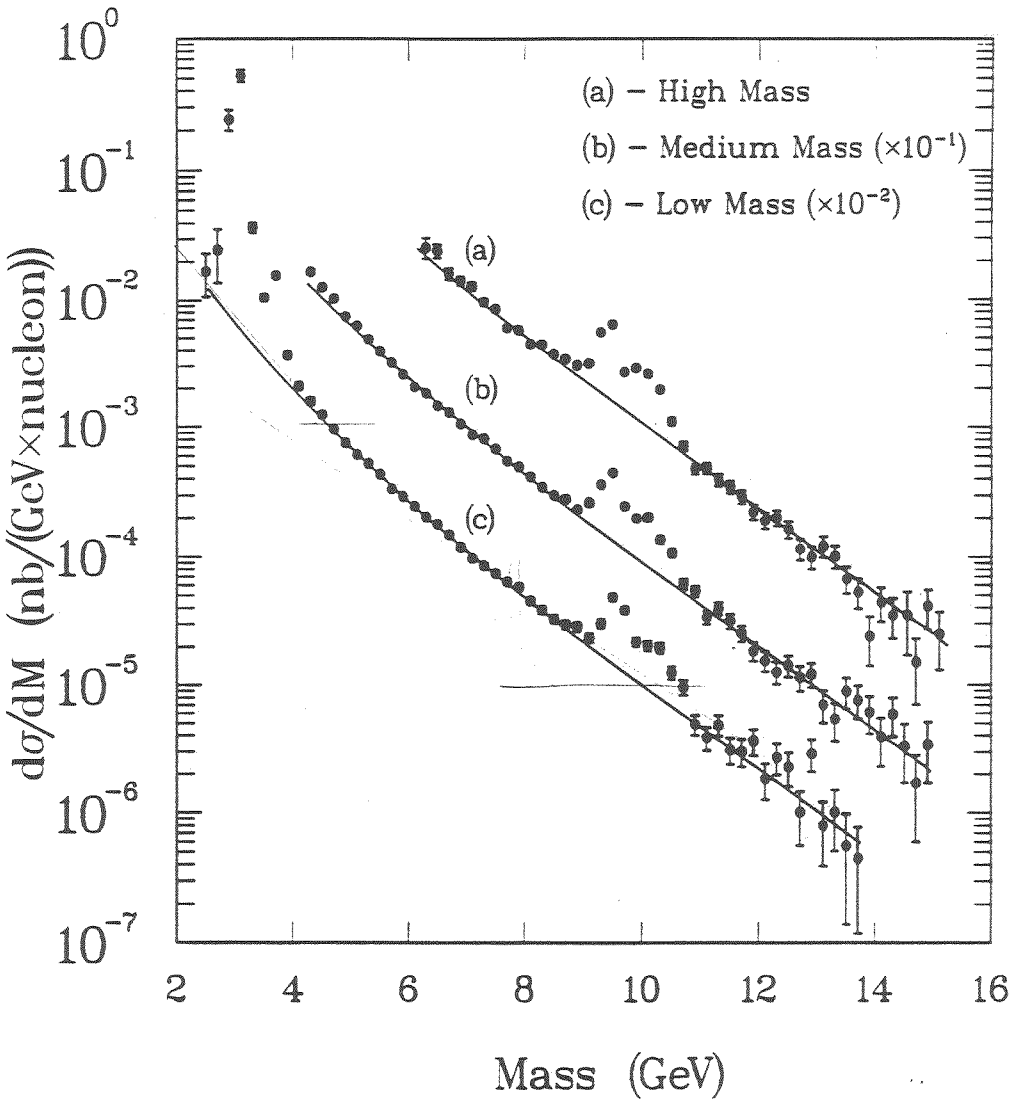

Figure 7.4: Acceptance-corrected mass spectra at the three spectrometer settings for the D target measured in the work. The solid curve is the Drell-Yan cross section, normalized to the data, using the EHLQ parametrization for parton distributions[73].

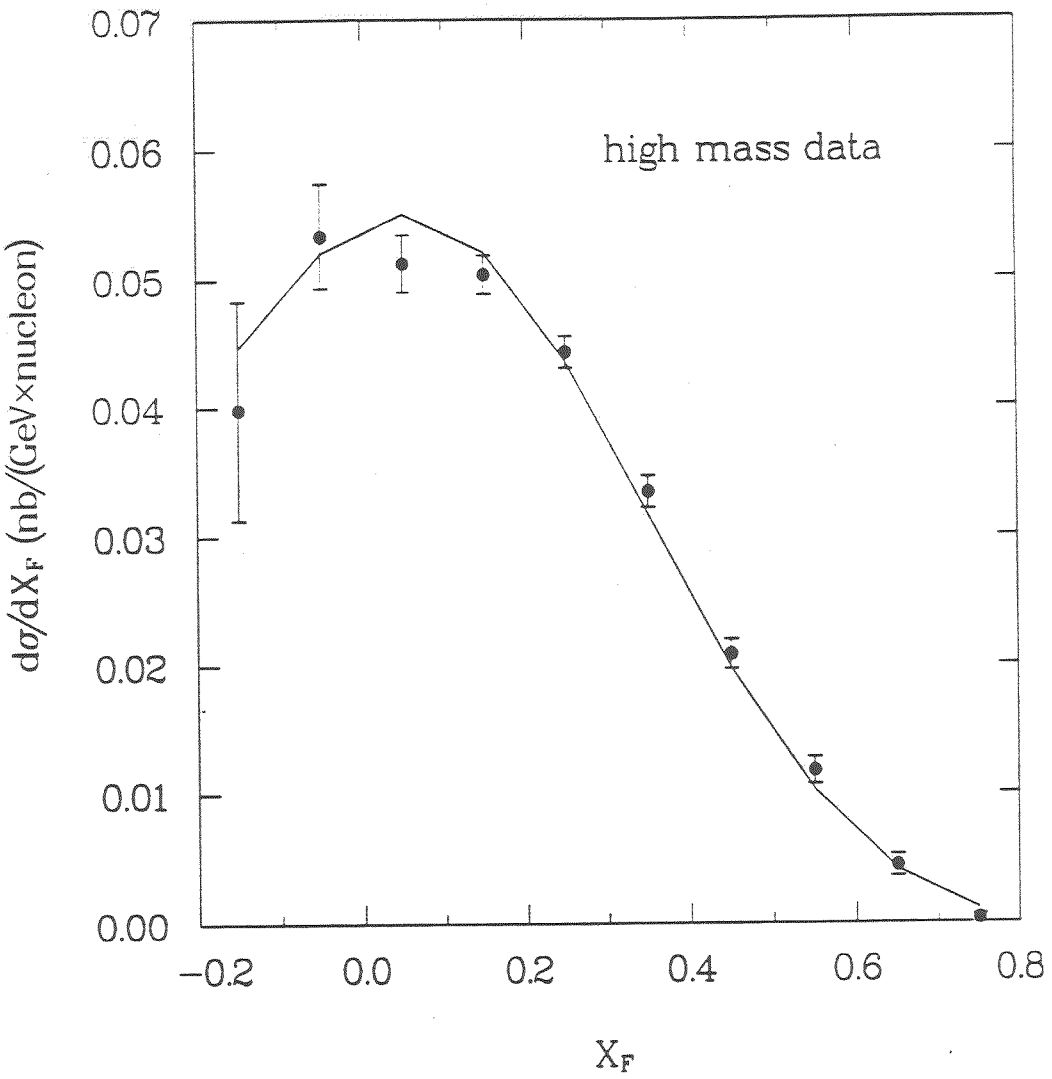

Figure 7.5: The measured acceptance-corrected x_F spectrum for the D target. The solid curve is the Drell-Yan cross section, normalized to the data, using the EHLQ parametrization for parton distributions[73].

that were obtained from EHLQ parametrization[73]. It can be expressed in the following equation

$$K(x) = \frac{d\sigma/dx_{(exp.)}}{d\sigma/dx_{(LLA)}} \qquad (7.7)$$

where x is either $M_{\mu^+\mu^-}$ or x_F . The normalization constants obtained in a fit to the $M_{\mu^+\mu^-}$ and x_F spectra in figure 7.4 and 7.5 are 2.35 and 2.26, respectively. If the assumption of constant K-factor is valid, these two values are the measured K-factors.

7.3 A-dependence of the Drell-Yan Process

The Drell-Yan data shown in this section were obtained with the mass cut of $4<M_{\mu^+\mu^-}<9$ and $M_{\mu^+\mu^-}>11$ (GeV). With these cuts, the resonances are excluded. There are a total 450k Drell-Yan events out of 623k dimuon events. The average values of the event distributions for each variable are listed in table 7.2

variable	$M_{\mu^+\mu^-}$(GeV)	x_F	P_T (GeV)	x_1	x_2
<variable>	6.21	0.257	0.950	$\sim$ 0.369	0.085

Table 7.2: Average values of variables for the Drell-Yan data.

The ratio R_{DY} is defined in the following equation

$$R_{A/D} = \frac{Y^A}{Y^D} \times N_{A/D} \tag{7.8}$$

where A represents a nuclear target of atomic weight A, and D represents the deuterium target; $N_{A/D}$ is the relative target-to-target normalization given in table 6.8.

Our results are presented in the following order. First, we show the ratios of integrated cross sections *versus* A. Second, the ratios *versus* dimuon variables $M_{\mu^+\mu^-}$, x_F , and P_T are presented. Third, the ratios *versus* quark variables x_1 , x_2 are shown.

7.3.1 A-Dependence of integrated Drell-Yan Cross Section

Figure 7.6 shows the measured ratio of integrated Drell-Yan cross section, R_{DY}, *versus* A. For C, Ca, Fe, and W, the atomic weights are 12.01, 40.08.

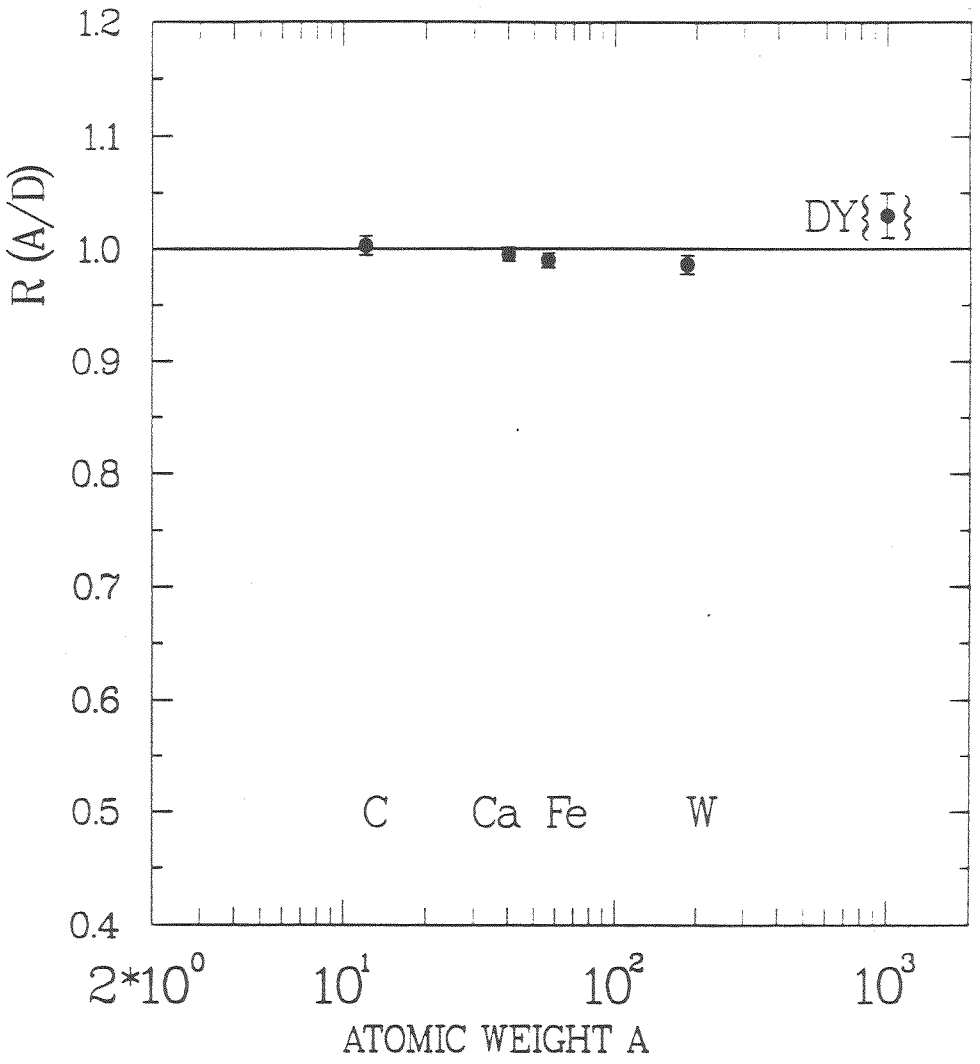

Figure 7.6: A-dependence of the integrated Drell-Yan cross-section, R_{DY}. The error bars reflect the statistical error. The systematic error for each point is estimated to be 2% .

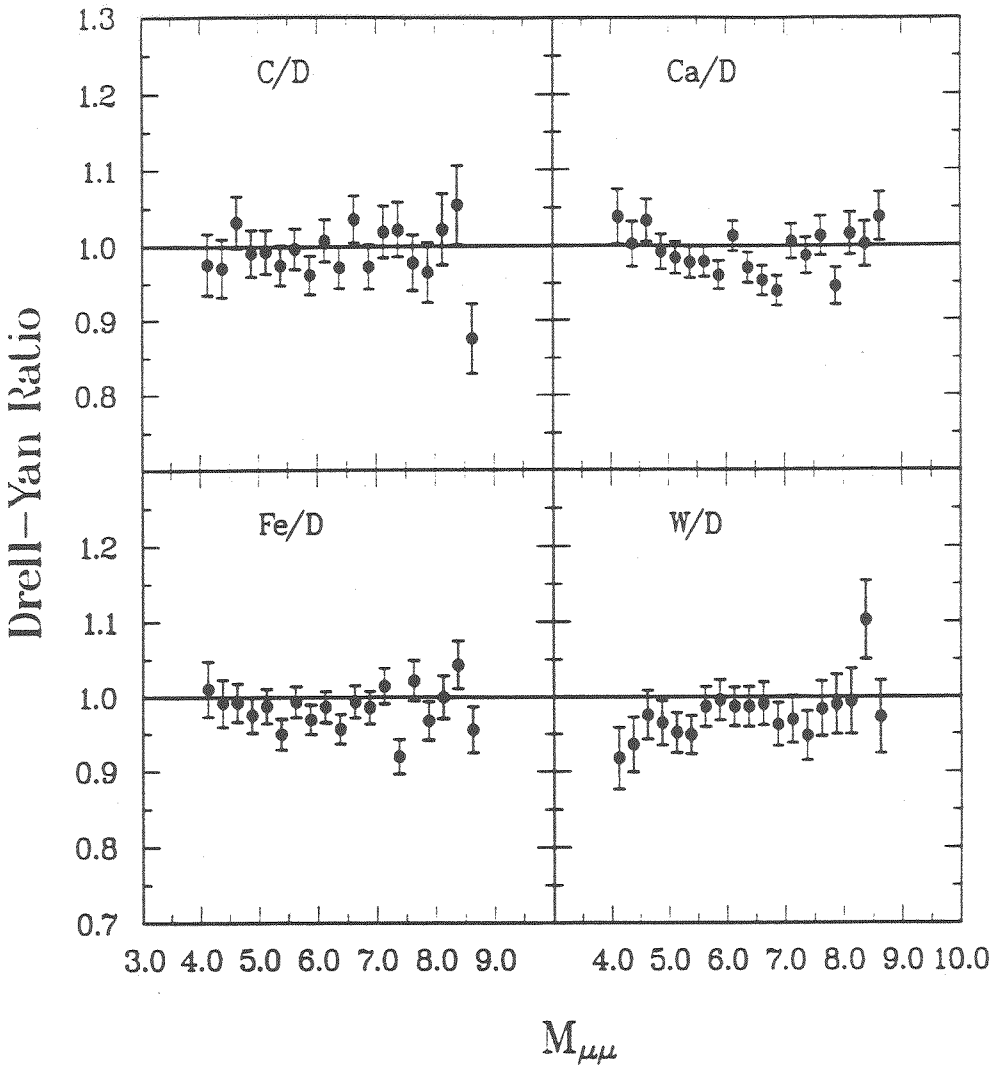

Figure 7.7: The measured values of the ratios $R_{DY}(M_{\mu^+\mu^-})$ for the Drell-Yan production; only the statistical error is shown.

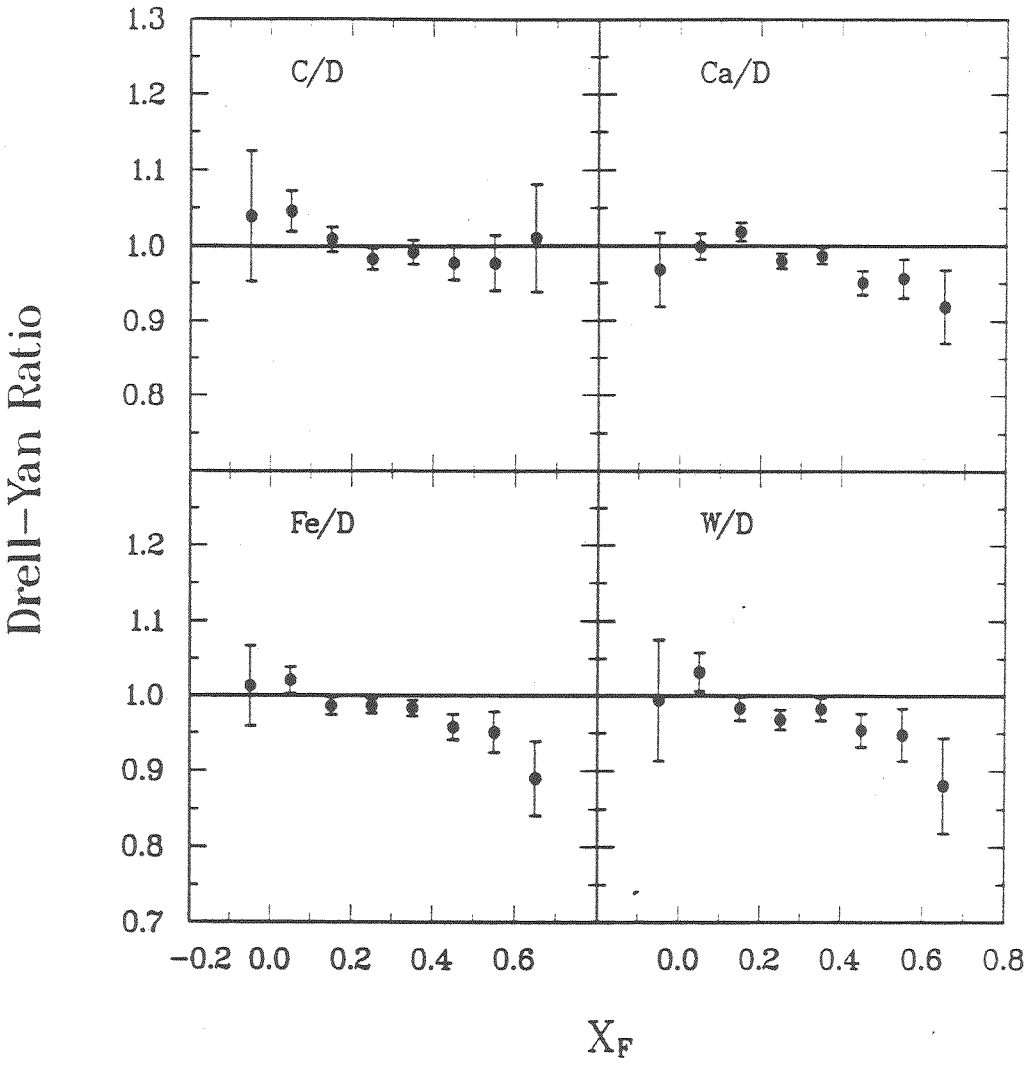

Figure 7.8: The measured values of the ratios $R_{DY}(x_F)$ for the Drell-Yan production; only the statistical error is shown.

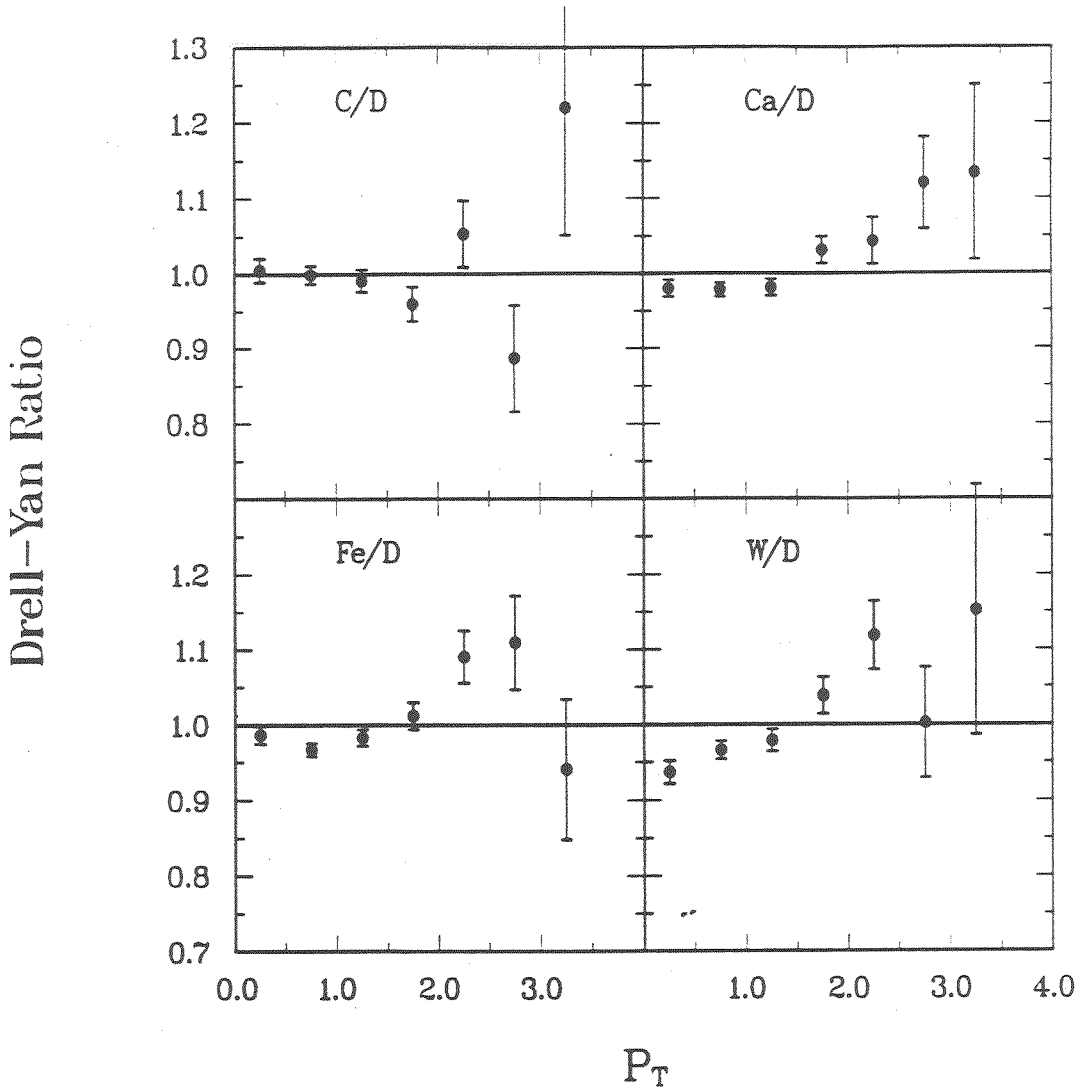

Figure 7.9: The measured values of the ratios $R_{DY}(P_T)$ for the Drell-Yan production; only the statistical error is shown.

55.85, and 183.85, respectively. The statistical error of each ratio is about 1% and the systematic error is estimated as 2% . The four measured values of R_{DY}(A/D) are consistent with unity to within the uncertainty.

7.3.2 $M_{\mu^+\mu^-}$, x_F , and P_T Dependence

Figure 7.7 shows the measured A-dependences of the ratio, $R_{DY}(M_{\mu^+\mu^-})$, as a function of $M_{\mu^+\mu^-}$in the interval from 4 GeV to 9 GeV. Figure 7.8 shows the measured A-dependences of the ratio $R_{DY}(x_F)$ as a function of the variable x_F between -0.20 and 0.65. This ratio shows a nuclear depletion at x_F >0.4 . Figure 7.9 shows the measured A-dependence of the ratio $R_{DY}(P_T)$ as a function of P_T . This ratio shows depletion in region of P_T < 1.5 GeV and enhancement in region of P_T >1.5 GeV.

7.3.3 x_1 and x_2 Dependence

The quark variables, x_1 and x_2 were calculated with equations 1.3 and 1.4 using the measured quantities $M_{\mu^+\mu^-}$and x_F . x_1 and x_2 are the momentum fractions of beam and target nucleon carried by the active quark or antiquark. Figure 7.10 shows the ratio $R_{DY}(x_1)$ as a function of x_1 for the four targets. Figure 7.11 shows the ratio $R_{DY}(x_2)$ as a function of x_2 for the four targets. One sees that, in the region of 0.1<x_2 <0.3, there is no enhancement in $R_{DY}(x_2)$, but there is clear depletion at x_2 =0.05. The magnitude of this depletion becomes larger at the heavier target. For the W target, there is 7.6 ± 1.7 % depletion at $x_2 = 0.05$.

In figure 7.12, the ratio $R_{DY}(x_2)$ is shown for two Q^2 intervals, corresponding to 4 ≤ $M_{\mu^+\mu^-}$< 6 GeV and 6 ≤ $M_{\mu^+\mu^-}$< 9 GeV. Although, there is some indications that the 6 to 9 GeV data show greater small-x_2 depletion, the two data sets are not statistically incompatible.

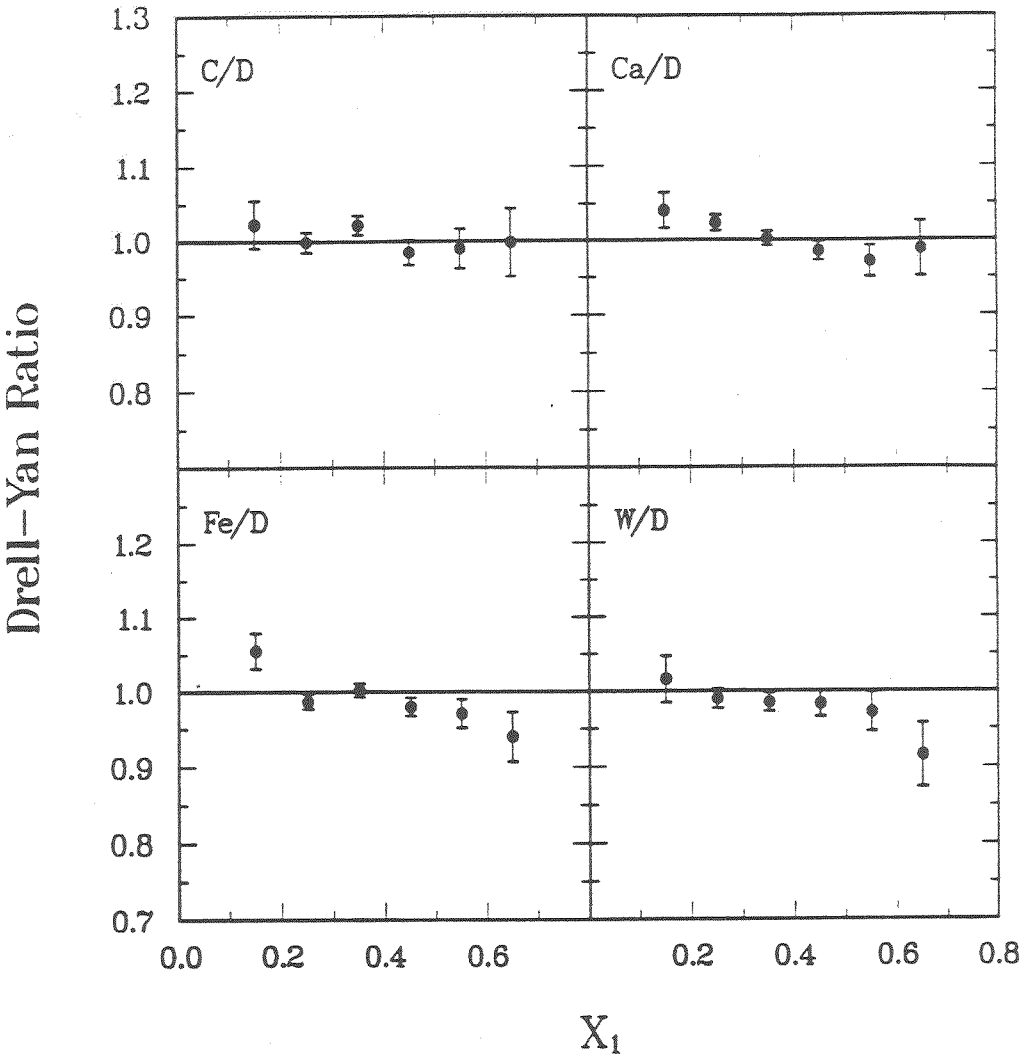

Figure 7.10: The measured values of the ratios $R_{DY}(x_1)$ for the Drell-Yan production; only the statistical error is shown.

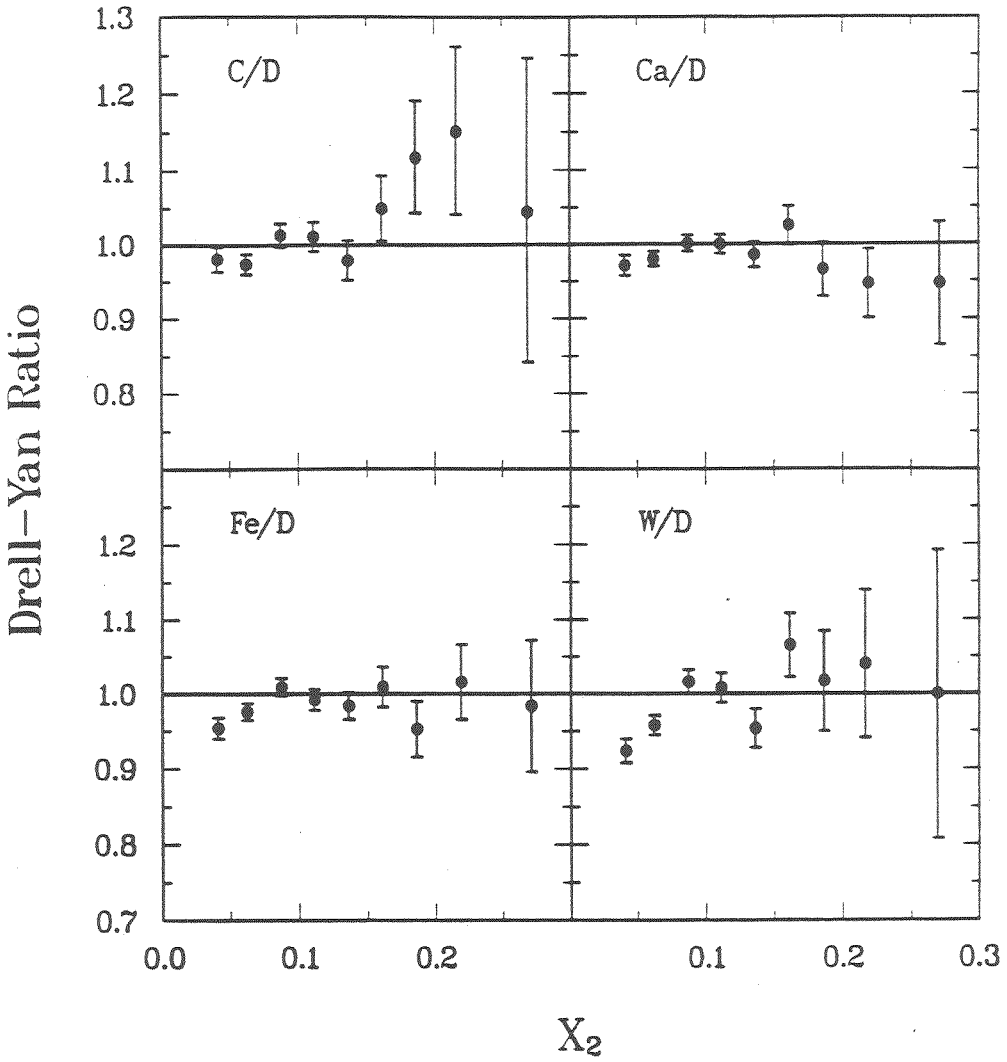

Figure 7.11: The measured values of the ratios $R_{DY}(x_2)$ for the Drell-Yan production; only the statistical error is shown.

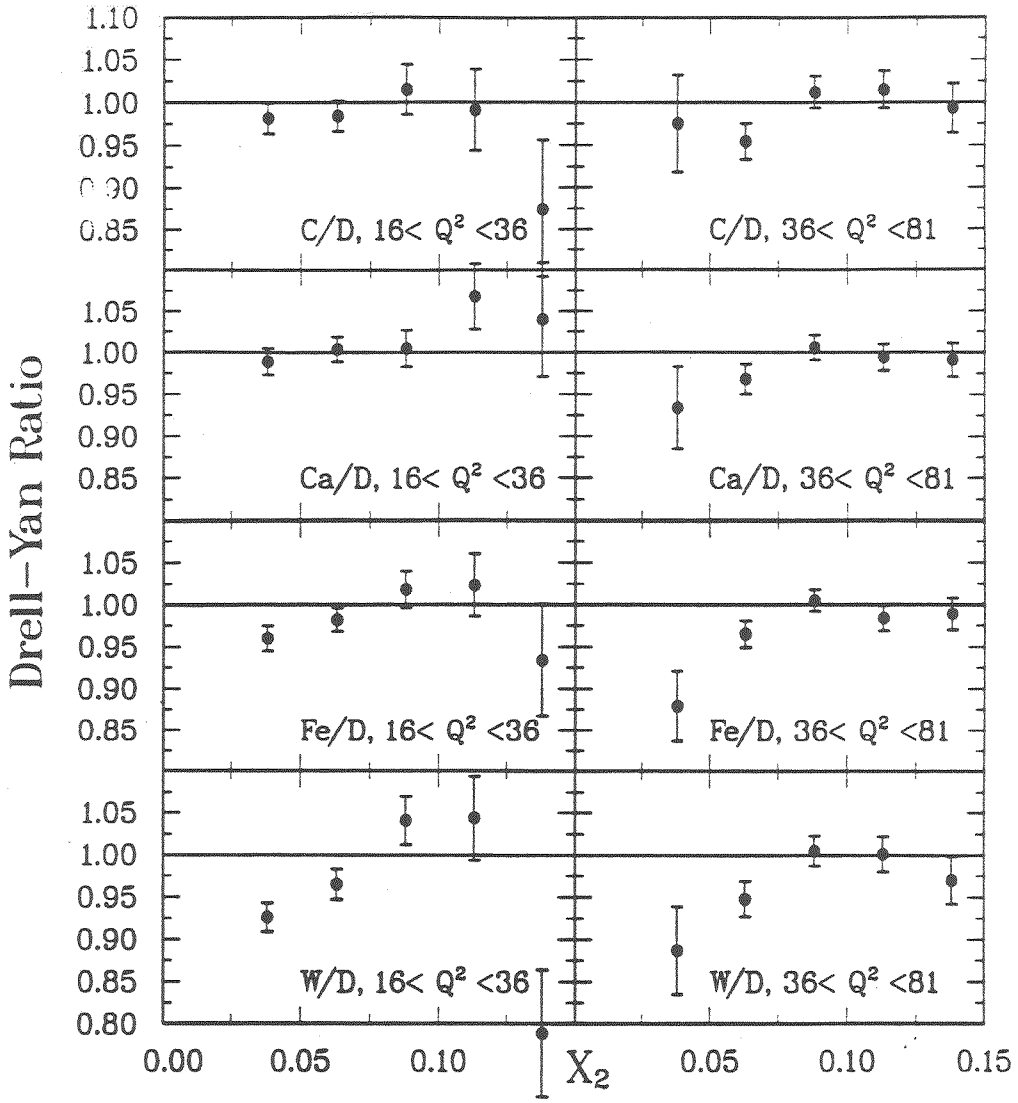

Figure 7.12: The Q^2 dependence of low-x_2 depletion on the ratios $R_{DY}(x_2)$ for the Drell-Yan production; only the statistical error is shown.

7.4 Extraction of Quarkonium Yields

The fitting program used for J/ψ , ψ' , and Υ peak-area extraction is called NEWFIT[3]. It was developed at LAMPF and is based on the CERN program MINUIT. It has a wide range of options for user's special purpose. Spectra can be fit with the following options:

(1) For peak shapes, one can choose input line shapes given as a histogram, or as functional forms of Lorenzian, Gaussian, Gaussian folded with two exponential tails, Gaussian with three exponential tails, asymmetric Gaussian, and Lorenzian + Gaussian.

(2) Energy of peak is either fixed or floating.

(3) Width(s) of one peak can be tied to that of another peak.

(4) Polynomial up to 8th order or simple exponential functions can be used for background fitting.

(5) One can fix the shape of polynomial background and use it for fitting an overall normalization constant.

Extraction of J/ψ and ψ' Peak Areas

Clean peak-extraction from the Drell-Yan continuum is necessary to determine the quarkonium A-dependence, because the Drell-Yan continua which lie under the peaks have very different A-dependence behavior than that of the resonances. Most of the data on the resonances were recorded in the intermediate-

[3]C.L. Morris at LAMPF is the original author.

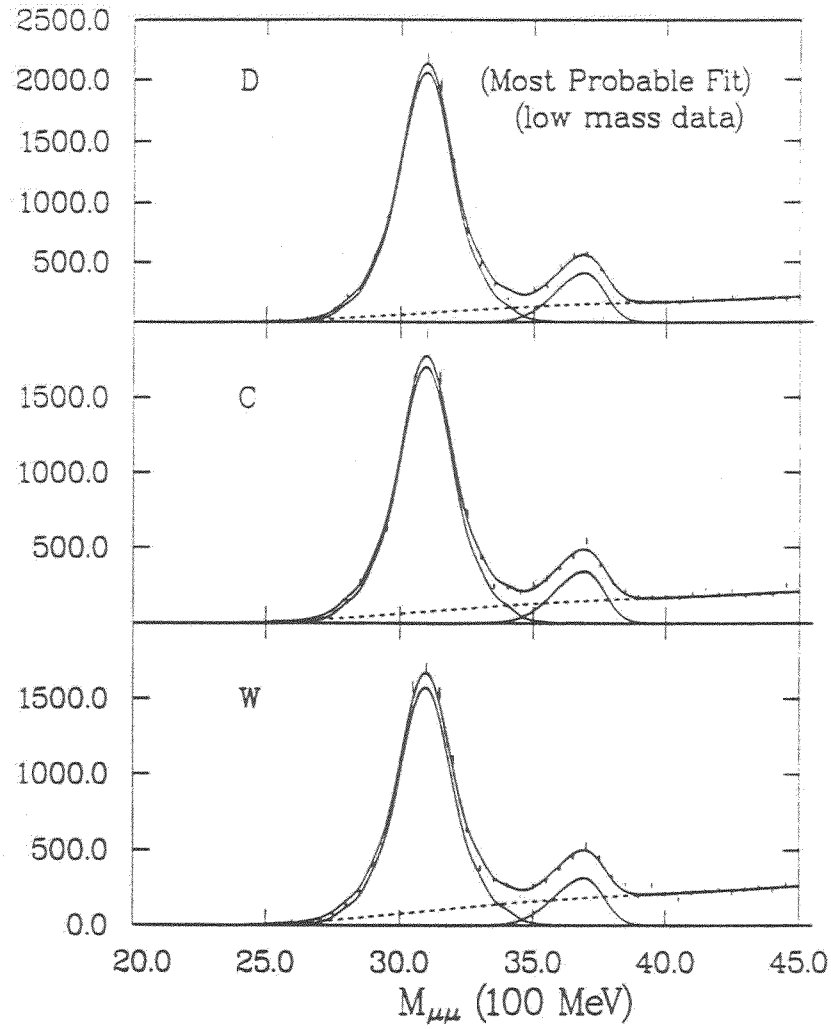

Figure 7.13: The peak-area extraction in the mass spectra of data set 10 for D, C, and W targets.

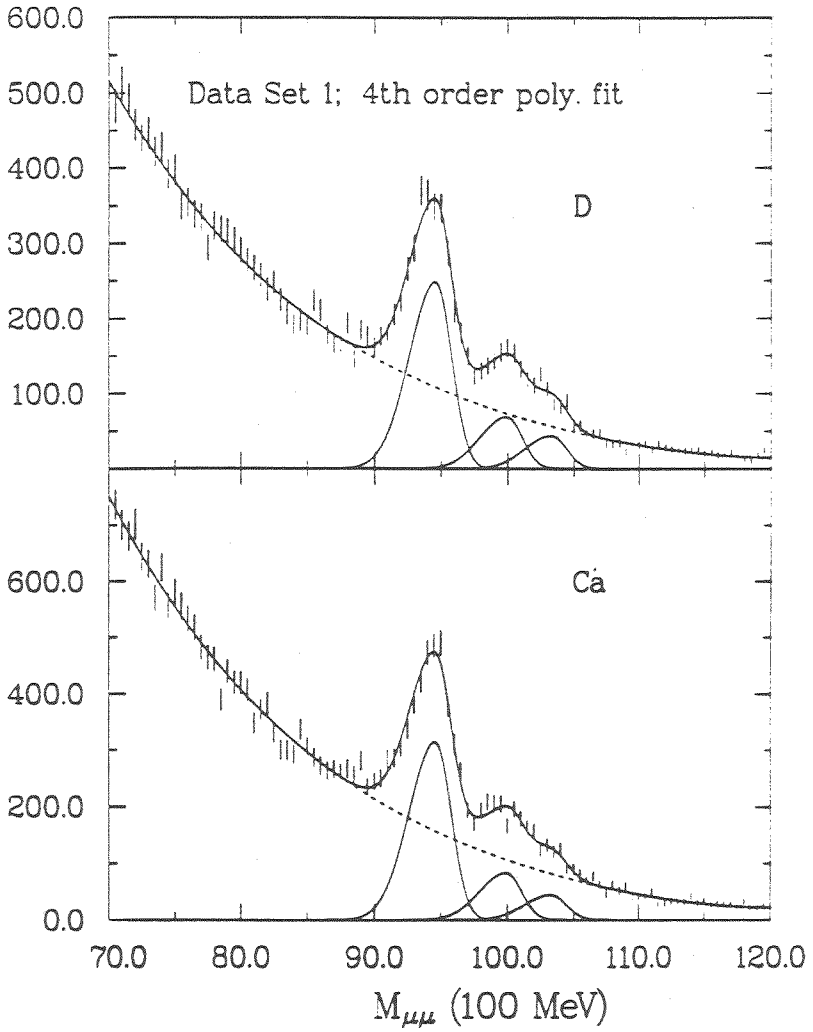

Figure 7.14: The peak-area extractions for the Υ peaks from D and Ca targets. The line shapes are asymmetric Gaussian functions.

and low-mass settings. For these two settings, the small SM0 magnet immediately downstream of the targets was turned on. The field map for SM0 was not accurately known and, thus, it was not possible to simulate the low-mass end of acceptance. Therefore, a good simulation of the Drell-Yan continuum in the J/ψ and ψ' region was not achieved. The only possible method to determine the shape of the continuum was to use polynomial functions with constraints from the continuum outside the peak region. Because the J/ψ rides on the edge of spectrometer acceptance, the usual peak shapes, such as Gaussian, could not fit the observed J/ψ peak shape very well. The J/ψ peak shape for each target was taken as the empirical peak shape or as an asymmetric Gaussian shape that was determined in a fit on the all-target spectrum. The ψ' was always fit using an asymmetric Gaussian peak shape. In order to study the fluctuation in peak areas caused by the uncertainty of continuum shape under the peaks, we adopted three different polynomial fits with two extreme continuum levels (high and low) as limits and the optimum one as the continuum line shape for the most probable fit. The largest deviation from the most probable ratio was assigned as the fitting error. Figure 7.13 shows the most probable fits of J/ψ and ψ' to D, C, and W mass spectra. The ratios $R_{J/\psi}$ and $R_{\psi'}$ were computed using equation 7.8.

Extraction of Υ Peak Areas

In the Υ analysis, we used skewed Gaussian peak shapes and polynomial function to fit the all-target [4] integrated mass spectrum in order to get the values of the $\Upsilon(1s)$ mass and the peak width. The masses of the $\Upsilon(2s)$ and $\Upsilon(3s)$ were then fixed by the known energy spacings. The peak widths were assumed to be the same as that of $\Upsilon(1s)$. The mass spectrum of each target was

[4](Ca+Fe+D) and (C+W+D).

then fit using a 4-parameter fit (areas of $\Upsilon(1s)$, $\Upsilon(2s)$, and $\Upsilon(3s)$ and a scale factor for the background). The peak masses, peak widths, and background shape were fixed. Figure 7.14 shows the most probable fits for the intermediate mass data for Ca and D targets. The ratios R_Υ for each nuclear target were computed using equation 7.8.

7.5 A-dependence of J/ψ and ψ' Cross Sections

Our J/ψ and ψ' data are presented in the following order. First, we show the ratios of integrated cross sections *versus* A. Second, the ratios *versus* dimuon variables x_F and P_T are presented. Third, the ratios *versus* quark variables x_2 are presented.

7.5.1 A-Dependence of Integrated J/ψ and ψ' Cross Sections

Figure 7.15 shows the integrated ratios $R_{J/\psi}$ and $R_{J/\psi'}$ for all targets. For comparison, the Drell-Yan ratio R_{DY} is also shown. Clearly, the nuclear dependence of the Drell-Yan cross section is very different from that of J/ψ and ψ' production.

7.5.2 x_F and P_T Dependence of J/ψ and ψ' Production

Mass-spectra binned according to x_F and P_T were obtained from the final analysis. The x_F and P_T bin sizes are 0.1 and 0.50 GeV, respectively. Because the J/ψ and ψ' are sitting on the edge of acceptance, the mass spectra between 3 and 4 GeV have very strong x_F and P_T dependence. In addition, the mass resolution becomes worse at the larger values of x_F and P_T . Due to these two factors, some subtlties of fitting had to be treated carefully. Basically, we followed the same procedure as discussed in the previous section, but the peak

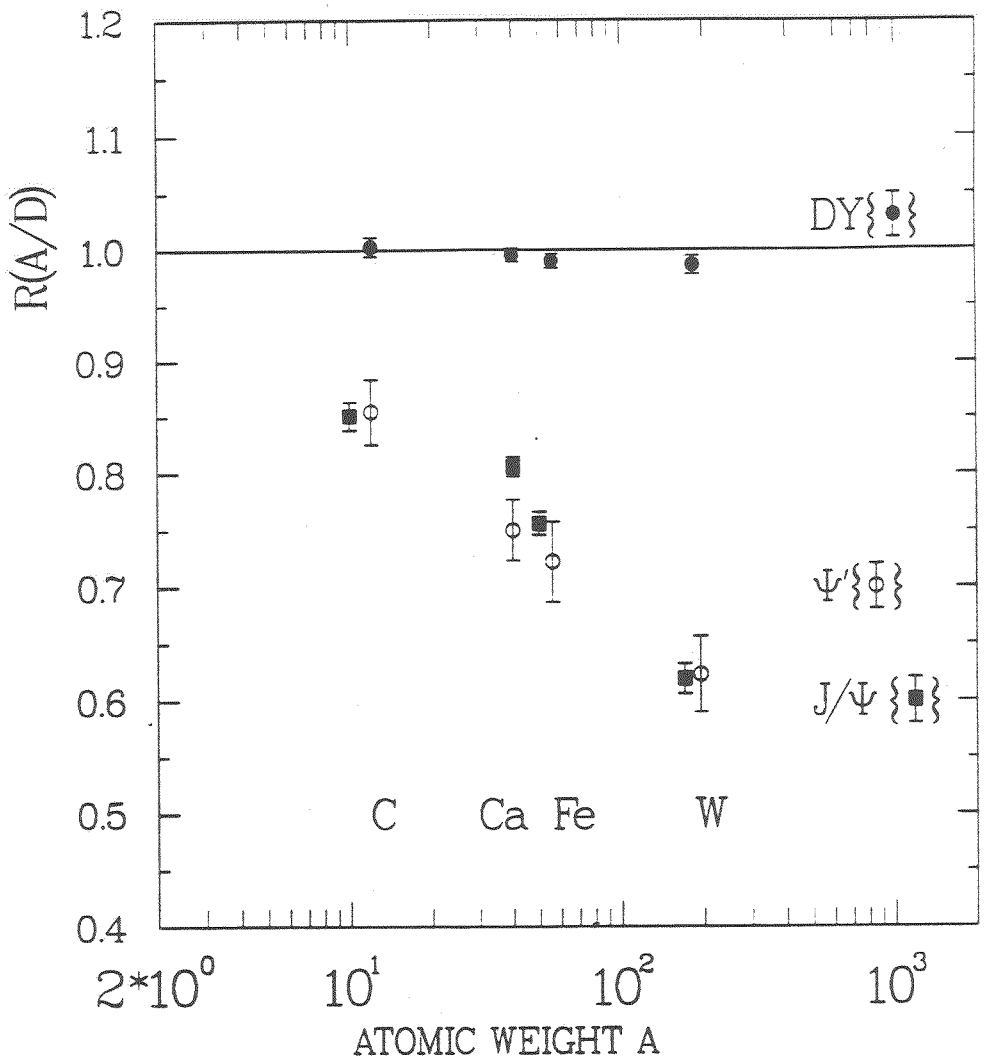

Figure 7.15: The measured R_{DY}(integrated), $R_{J/\psi}$(integrated), and $R_{\psi'}$(integrated) *versus* A; the errors shown for the J/ψ and ψ' represent the statistical and peak-fitting error. For R_{DY}, only the statistical error is shown.

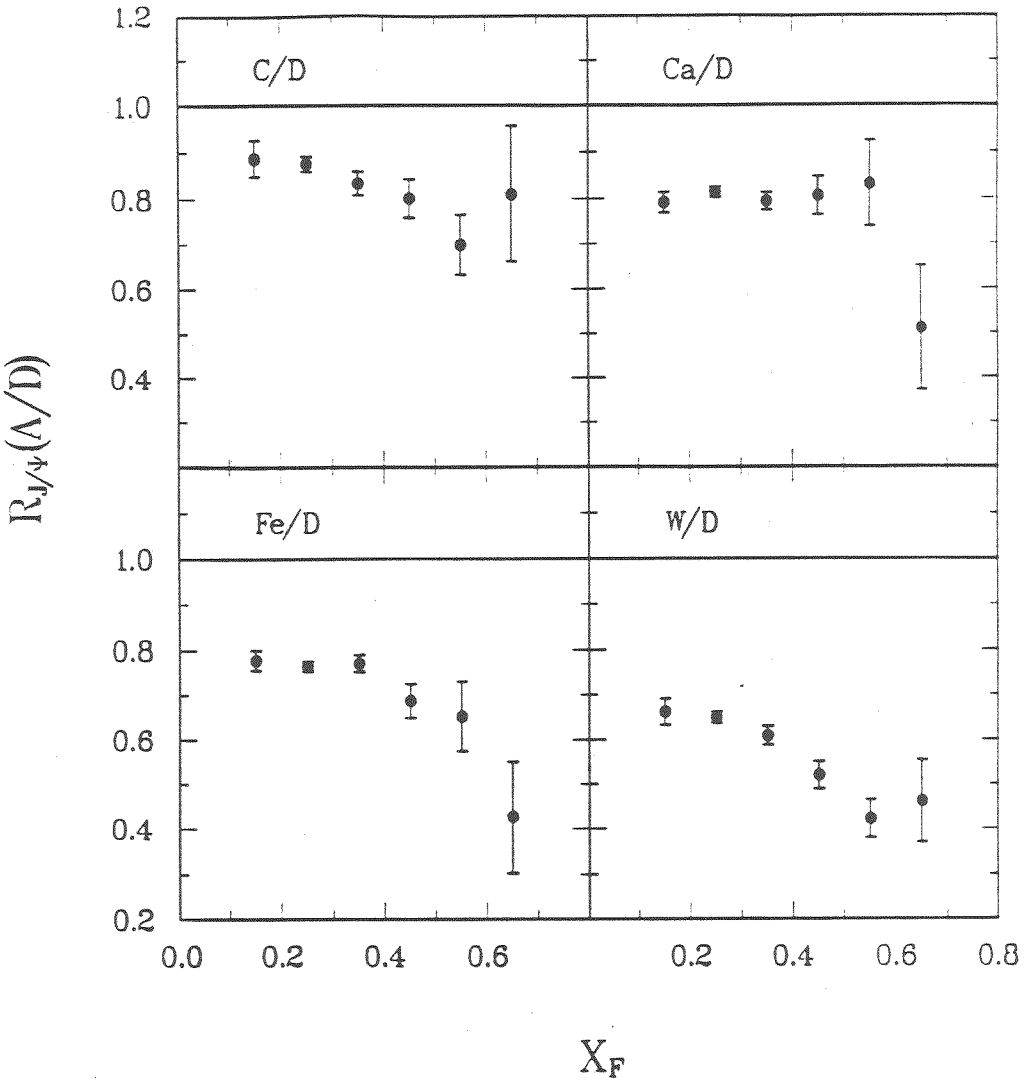

Figure 7.16: The measured values of the ratios $R_{J/\psi}(x_F)$ for the J/ψ production; the error shown for the J/ψ represents the statistical and peak-fitting error. The nuclear attenuation of the J/ψ cross sections are seen to increase with increasing x_F.

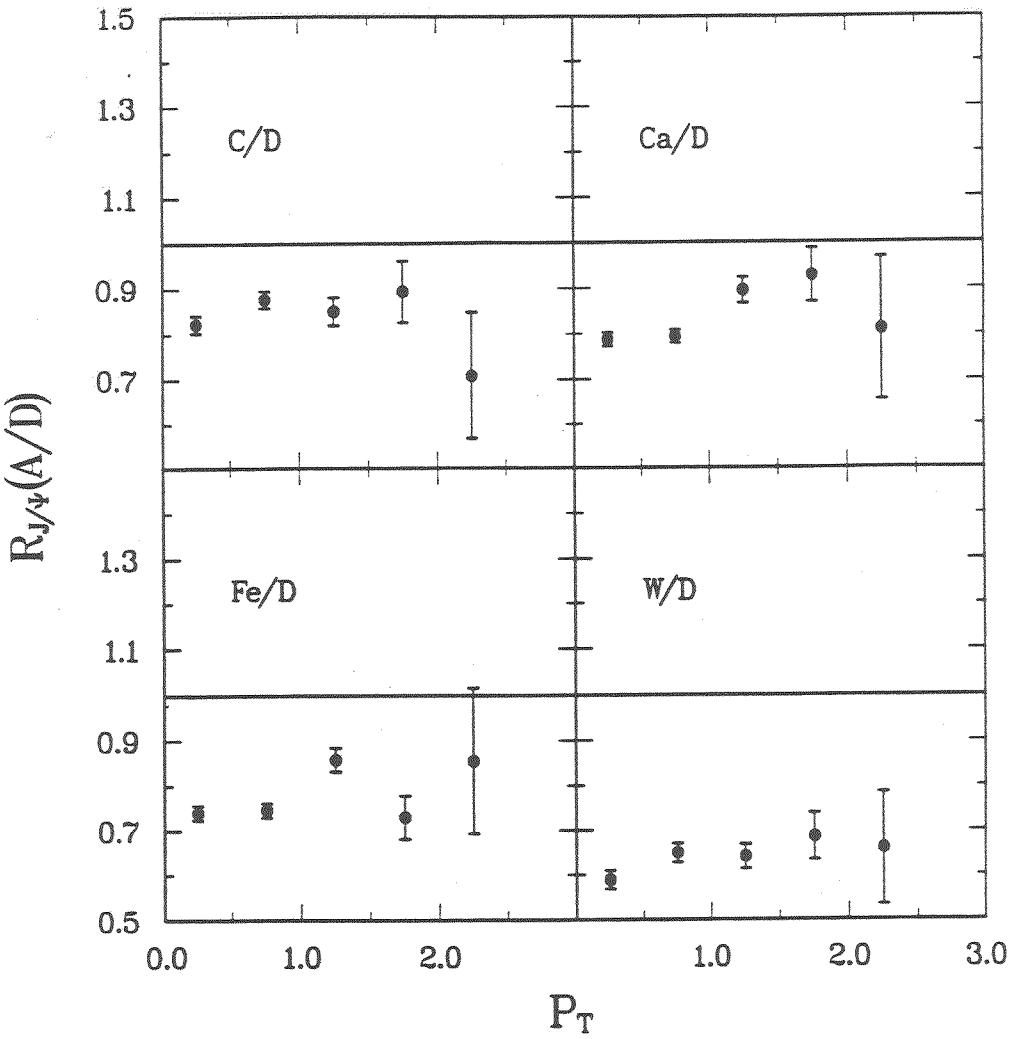

Figure 7.17: The measured values of the ratios $R_{J/\psi}(P_T)$ for the J/ψ production; the error shown for the J/ψ represents the statistical and peak-fitting error.

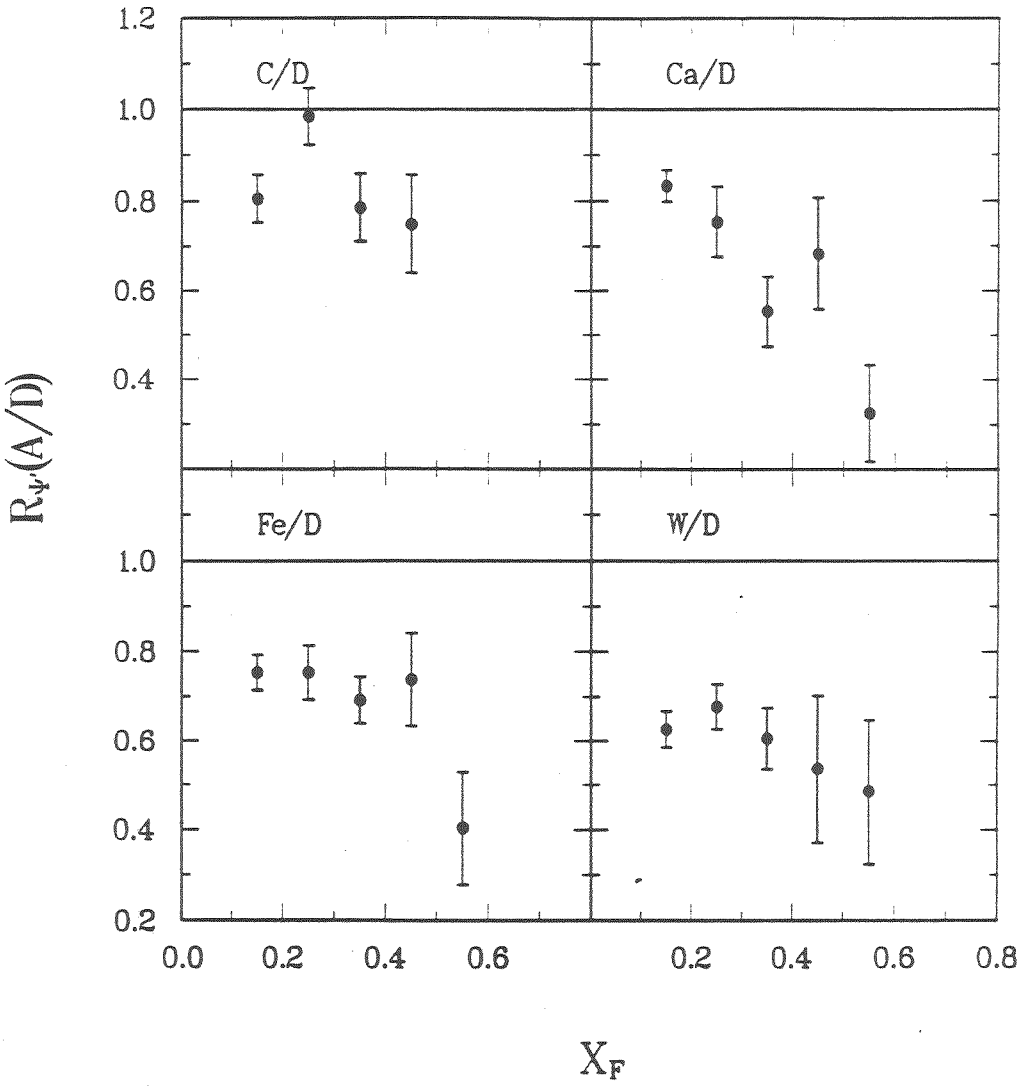

Figure 7.18: The measured values of the ratios $R_\psi(x_F)$ for the ψ' production: the error shown for the ψ' represents the statistical and peak-fitting error.

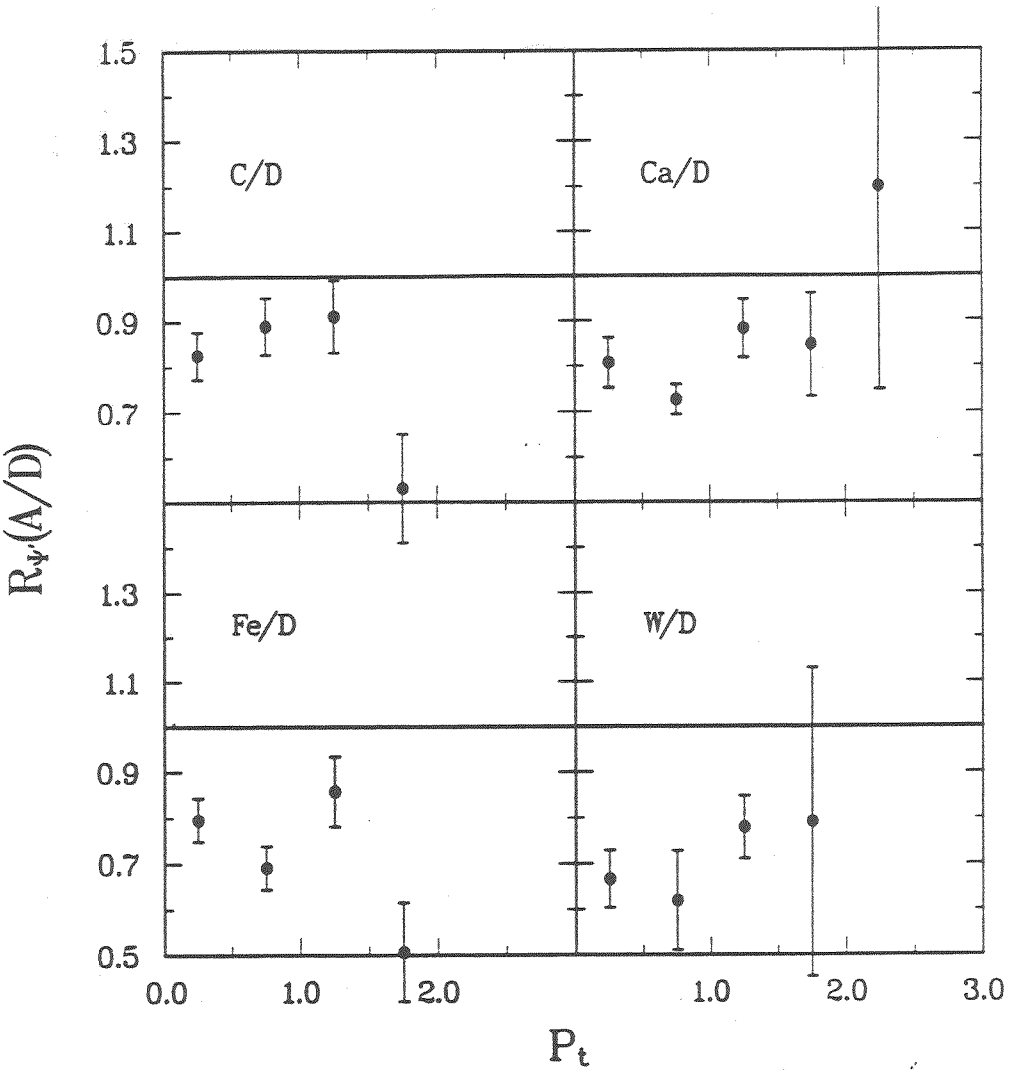

Figure 7.19: The measured values of the ratios $R_\psi(P_T)$ for the ψ' production: the error shown for the ψ' represents the statistical and peak-fitting error.

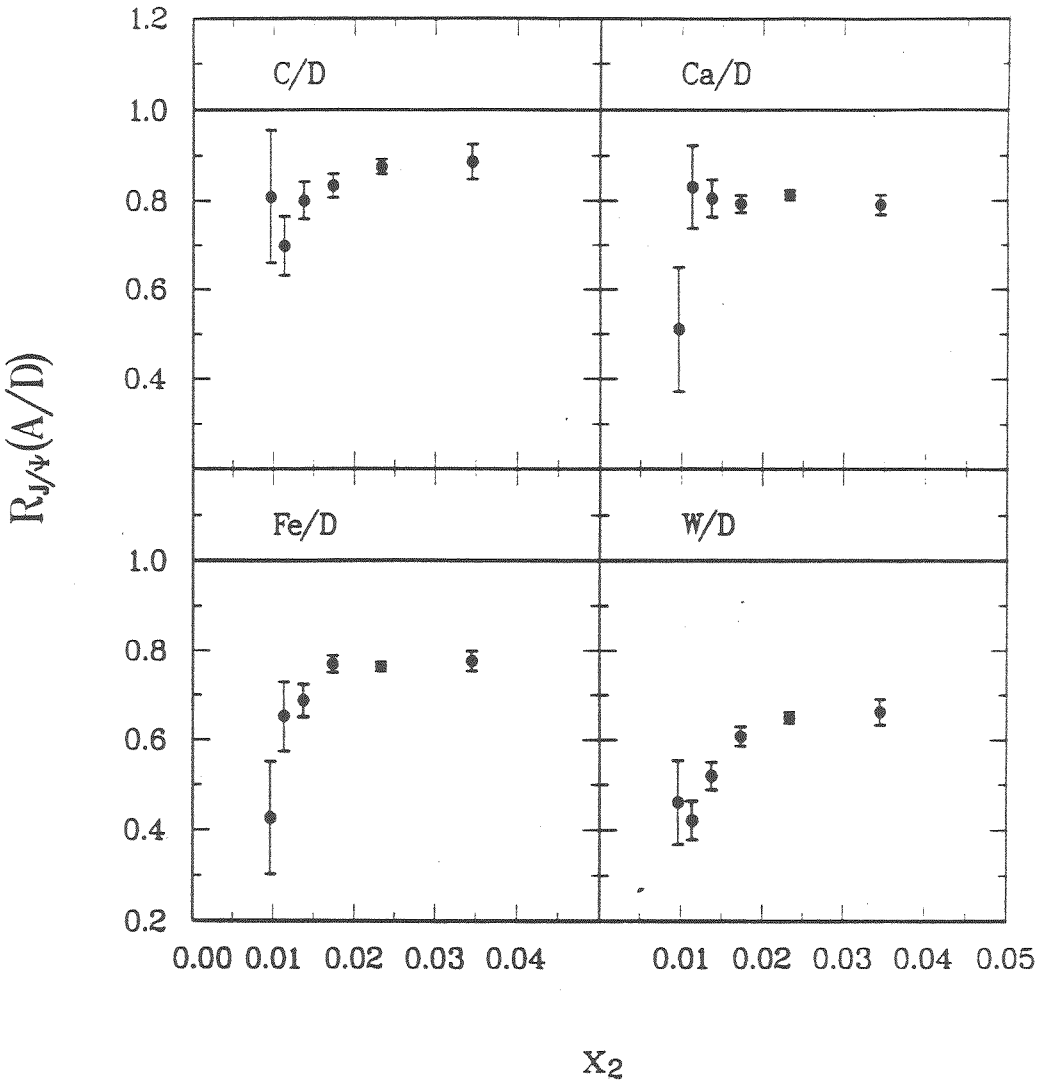

Figure 7.20: The measured values of the ratios $R_{J/\psi}(x_2)$ for the J/ψ production: the error shown for the J/ψ represents the statistical and peak-fitting error.

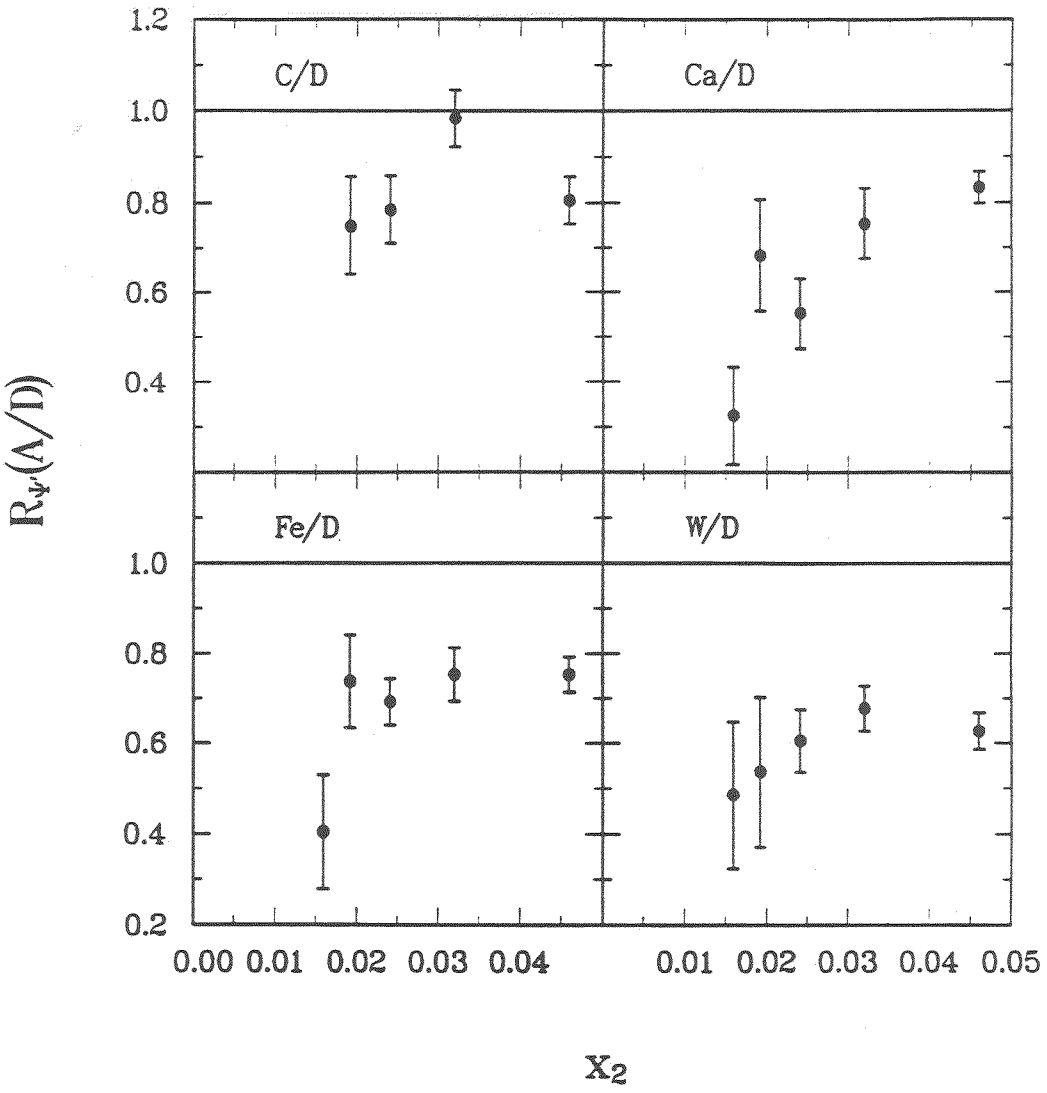

Figure 7.21: The measured values of the ratios $R_{\psi'}(x_2)$ for the ψ' production; the error shown for the ψ' represents the statistical and peak-fitting error.

shape for the J/ψ was taken to be an asymmetrical Gaussian function instead of an empirical one. Also, the widths of the ψ' was tied to the J/ψ width for the data with x_F >0.2 or P_T >1.5 GeV. Figure 7.16 to 7.19 show the results on x_F and P_T A-dependence for the J/ψ and ψ' . The average values of x_F and P_T for both J/ψ and ψ' are reported in table 7.3.

resonances	tgt	data set	$<x_F>$	$<P_T>$
J/ψ	D	6	0.264	0.636
	Ca	6	0.264	0.654
	Fe	6	0.263	0.651
	D	10	0.285	0.676
	C	10	0.282	0.687
	W	10	0.279	0.697
ψ'	D	6	0.232	0.676
	Ca	6	0.221	0.684
	Fe	6	0.229	0.671
	D	10	0.248	0.671
	C	10	0.256	0.666
	W	10	0.245	0.689

Table 7.3: Average values of the observed x_F and P_T for J/ψ and ψ' for data set 6 and data set 10. These values are not corrected for acceptances.

7.5.3 x_2 Dependence of J/ψ and ψ' Production

Figures 7.20 and 7.21 display the J/ψ and ψ' cross section as a function of x_2 . These were computed using equation 7.5 with $\tau = (m(c\bar{c})/38.8)^2$, where $m(c\bar{c}) = 3.1$ and 3.7 GeV for the J/ψ and ψ' , respectively. This assumes that the parton fusion process $gg \rightarrow J/\psi$ diminates the production mechanism (see discussion in section 8.5). One can see that the large x_F depletion, as seen in figures 7.16 and 7.18, is mapped into a small x_2 depletion by this assumption. Also, the range of x_2 is very small, from $x_2 = 0.01$ to 0.04, as seen in figures 7.20

and 7.21. These results are discussed in section 8.5.

7.6 A-dependence of Υ (1s)

Our $\Upsilon(1s)$ data are presented in the following order. First, we show the ratios of integrated cross sections *versus* A. Second, the ratios *versus* dimuon variables x_F and P_T are presented. Third, the ratios *versus* quark variables x_2 are presented.

7.6.1 A-Dependence of Integrated $\Upsilon(1s)$ Cross Sections

Figure 7.22 shows the integrated ratio $R_{\Upsilon(1s)}$ for all targets. The error bars shown for the $\Upsilon(1s)$ represent the statistical and fitting errors added in quadrature. One sees that the depletion of the $\Upsilon(1s)$ cross section increased with A. There is 13.2% depletion of $R_{\Upsilon(1s)}$ for W.

7.6.2 x_F and P_T Dependence of $\Upsilon(1s)$ Production

Figure 7.23 shows the measured ratio $R_\Upsilon(x_F)$ for Ca and Fe. These ratios show enhanced nuclear depletion at negative x_F. At x_F = -0.1, R_Υ(Ca/D) is 0.753±0.082 and R_Υ(FE/D) is 0.658±0.075. These depletions are significantly less than the ratios at x_F = 0.1 and 0.3. Figure 7.24 shows the measured $R_{\Upsilon(1s)}(P_T)$ for Ca and Fe. The P_T smearing of the $\Upsilon(1s)$ is similar to that of Drell-Yan, but the ratio shows significant nuclear depletion, which is not present in the Drell-Yan data.

7.6.3 x_2 Dependence of $\Upsilon(1s)$ Production

Figure 7.25 displays the Υ cross-section ratio as a function of x_2. This was computed using equation 7.5 with $\tau = (m(b\bar{b})/38.8)^2$, where $m(b\bar{b}) = 9.46$ GeV for the Υ.

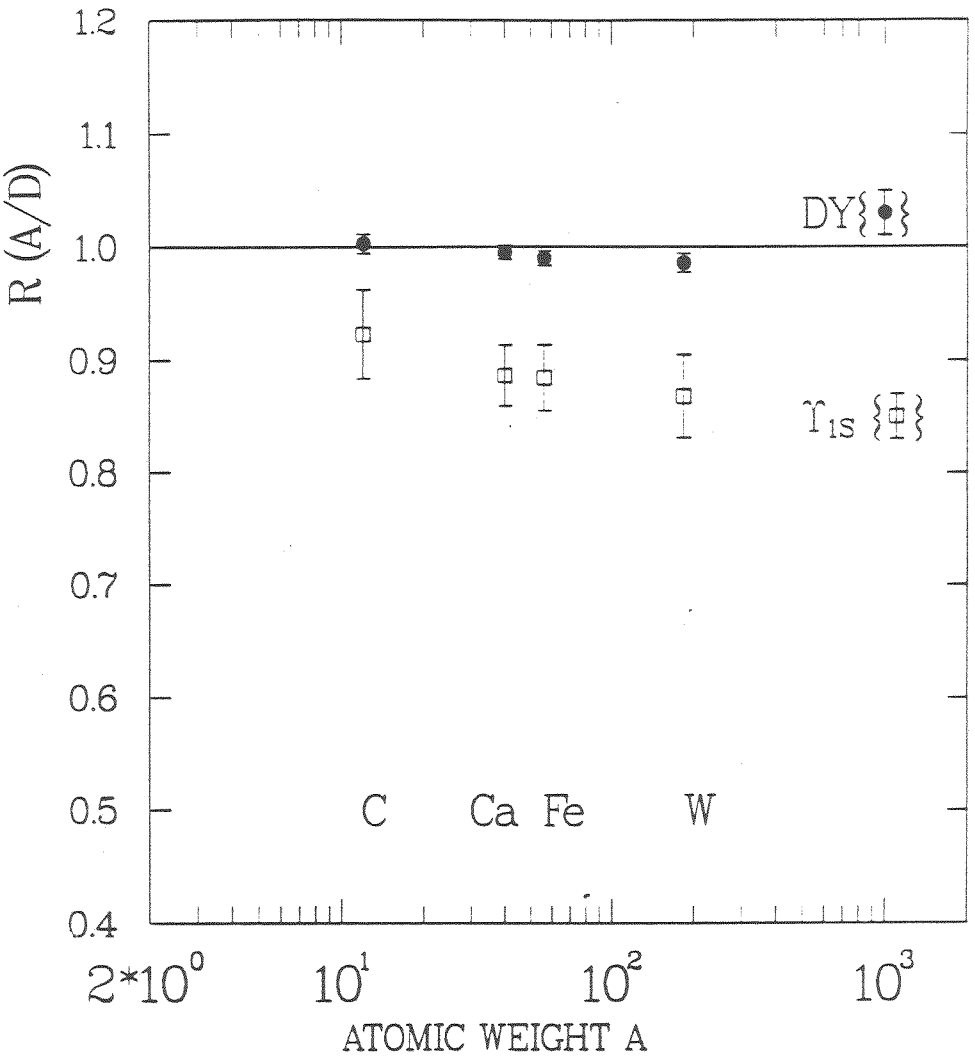

Figure 7.22: The measured integrated ratios R_{DY} and R_{Υ} *versus* A; the error shown for the $\Upsilon(1s)$ represents the statistical and peak-fitting error. For R_{DY}, only the statistical error is shown.

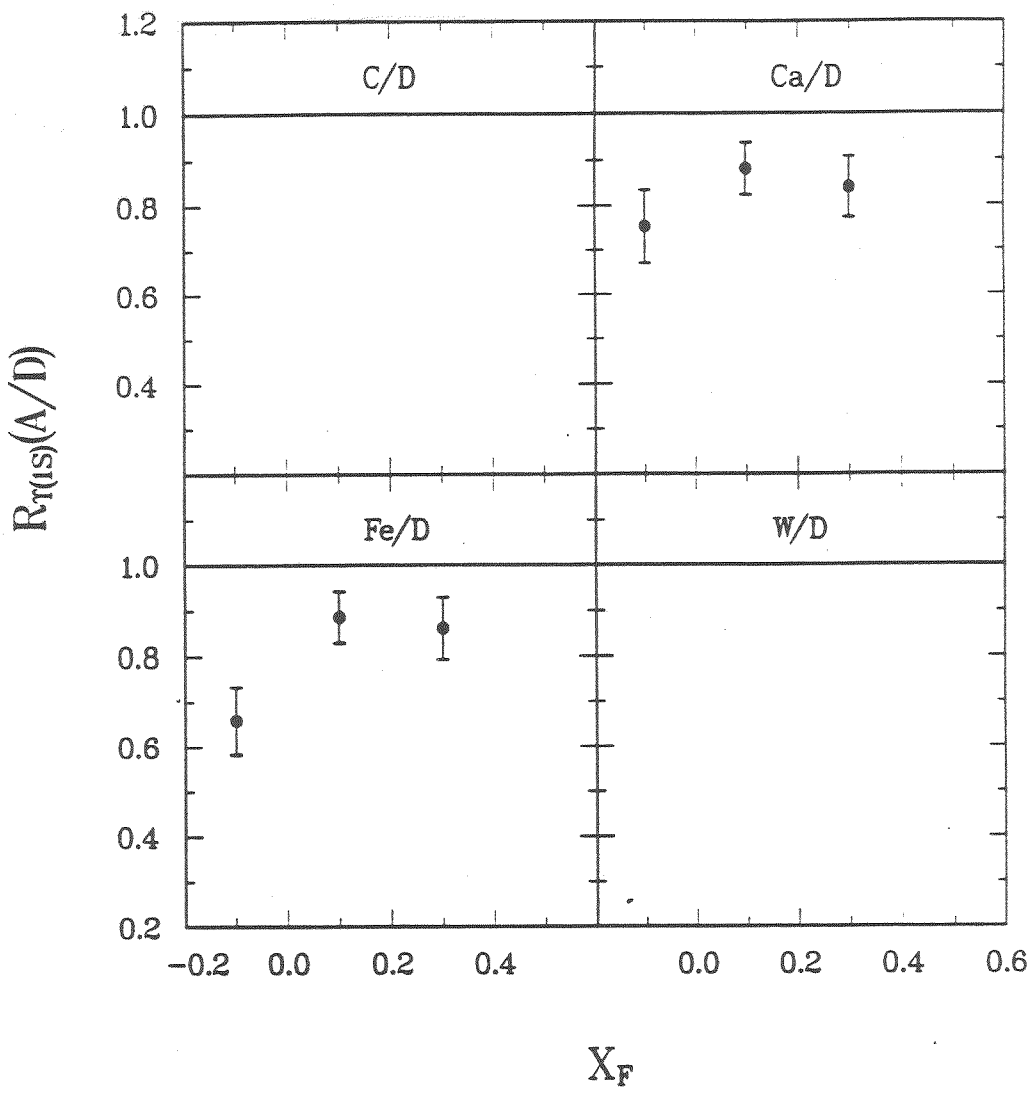

Figure 7.23: The measured values of the ratios $R_\Upsilon(x_F)$ for $\Upsilon(1s)$ production: the error shown for the $\Upsilon(1s)$ represents the statistical and peak-fitting error. Sizeable nuclear depletion is seen for $\Upsilon(1s)$ events produced with negative x_F.

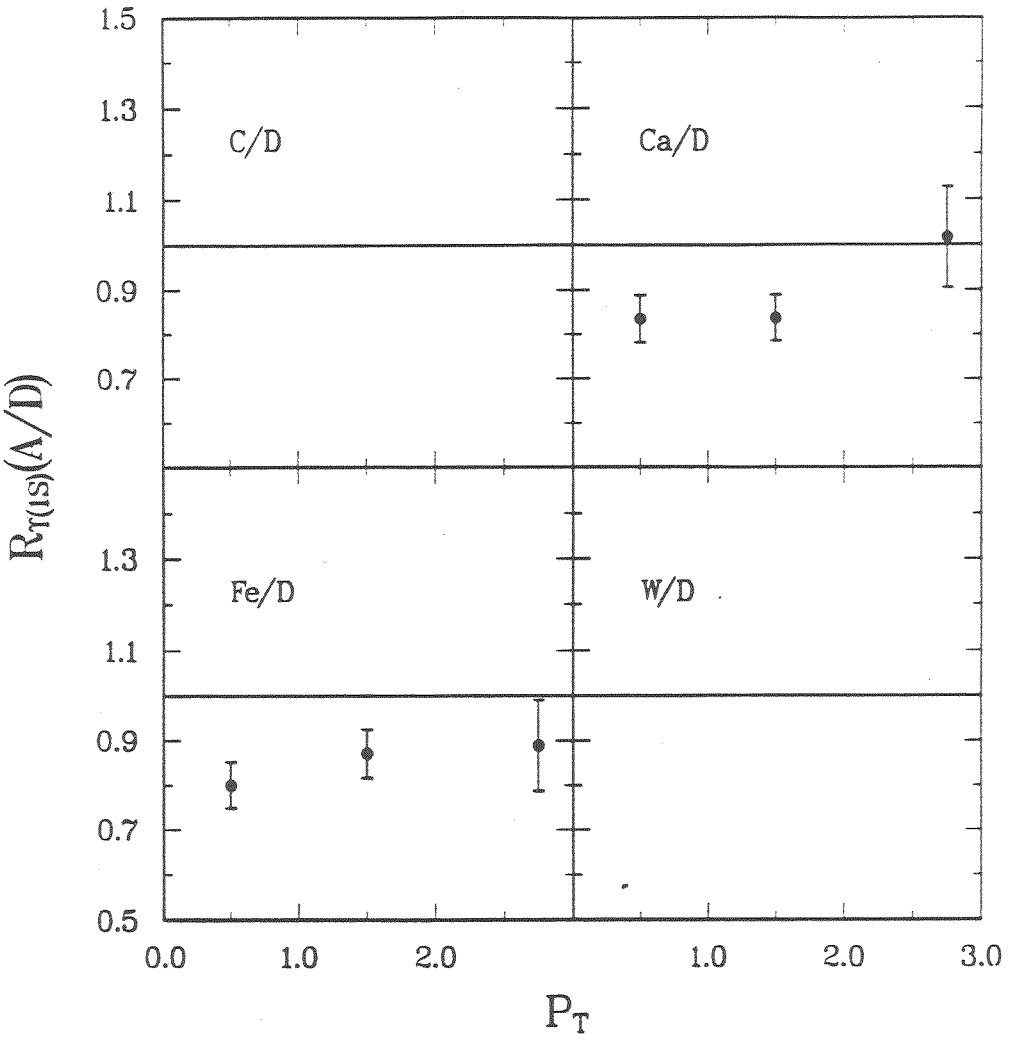

Figure 7.24: The measured values of the ratios $R_\Upsilon(P_T)$ for the Υ production: the error shown for the $\Upsilon(1s)$ represents the statistical and peak-fitting error.

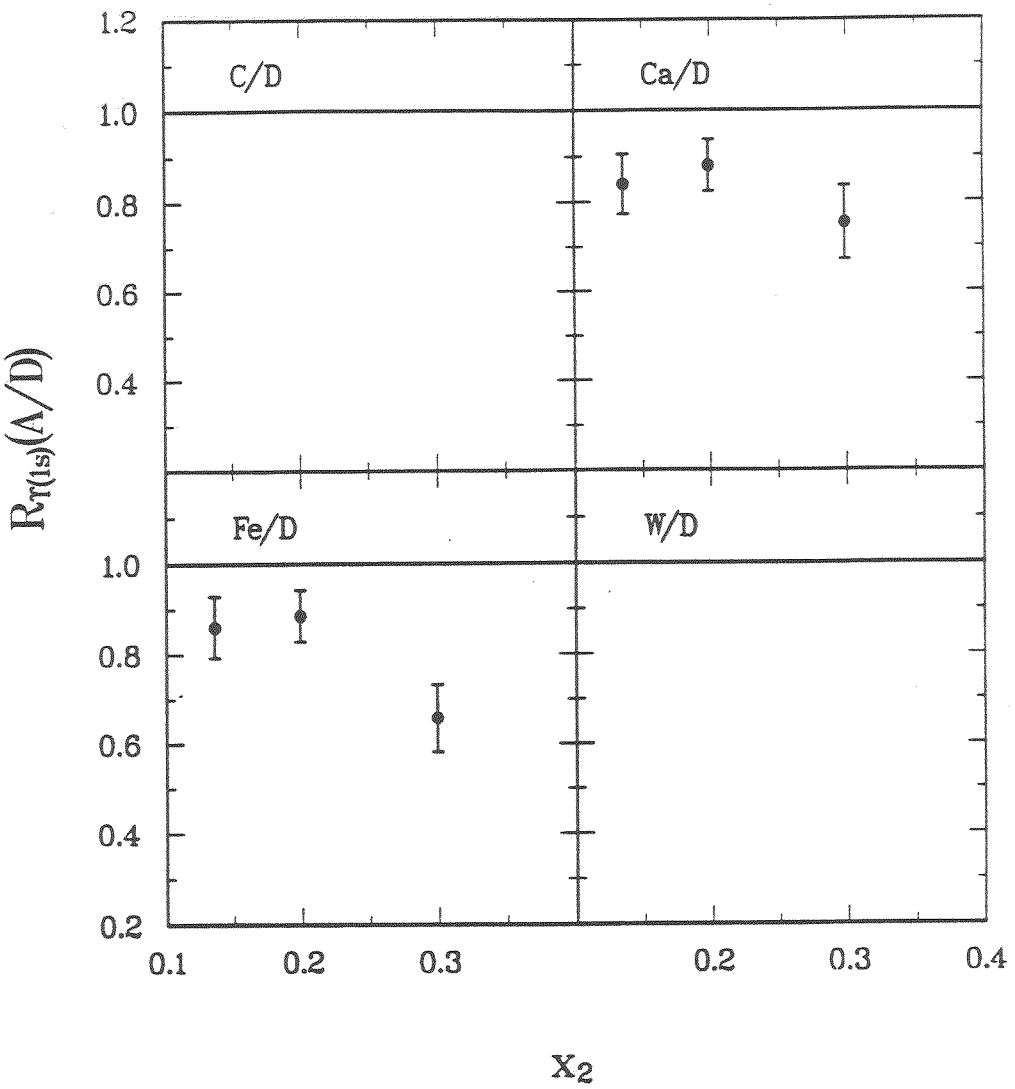

Figure 7.25: The measured values of the ratios $R_\Upsilon(x_2)$ for the Υ production; the error shown for the $\Upsilon(1s)$ represents the statistical and peak-fitting error.

7.7 A-dependent Ratios Expressed in Terms of Alpha(α)

We can express the A-dependence of the Drell-Yan cross sections and of the J/ψ , ψ' , and Υ cross sections in terms of α defined by the equation

$$\sigma_A = A^\alpha \sigma_N, \tag{7.9}$$

or by

$$\alpha = \frac{\ln \frac{\sigma_A}{\sigma_N}}{\ln A}. \tag{7.10}$$

In the previous presentation of our data, the A-dependence was expressed in terms of the ratio R of nuclear cross sections divided by the D cross section. The relation between ratio R(A/D) and α is

$$\alpha = 1 + \frac{\ln R}{\ln(A/2)} \tag{7.11}$$

or

$$R = (\frac{A}{2})^{\alpha-1} \tag{7.12}$$

Figure 7.26 shows the integrated cross section ratio $R(A/D)$ for all our data. A fit to these data with the function $R = (A/2)^{1-\alpha}$ gives $\alpha_{DY} = 0.998 \pm 0.001$, $\alpha_{\Upsilon(1s)} = 0.964 \pm 0.006$, and $\alpha_{\psi'} = 0.902 \pm 0.007$. Figures 7.27 and 7.28 show α *versus* x_F and P_T for the Drell-Yan cross-section ratios and for the J/ψ , ψ' , and $\Upsilon(1s)$ cross-section ratios. Figure 7.29 shows α *versus* x_2 for the Drell-Yan data in the Q^2 intervals 16 to 36 GeV^2 and 36 to 81 GeV^2.

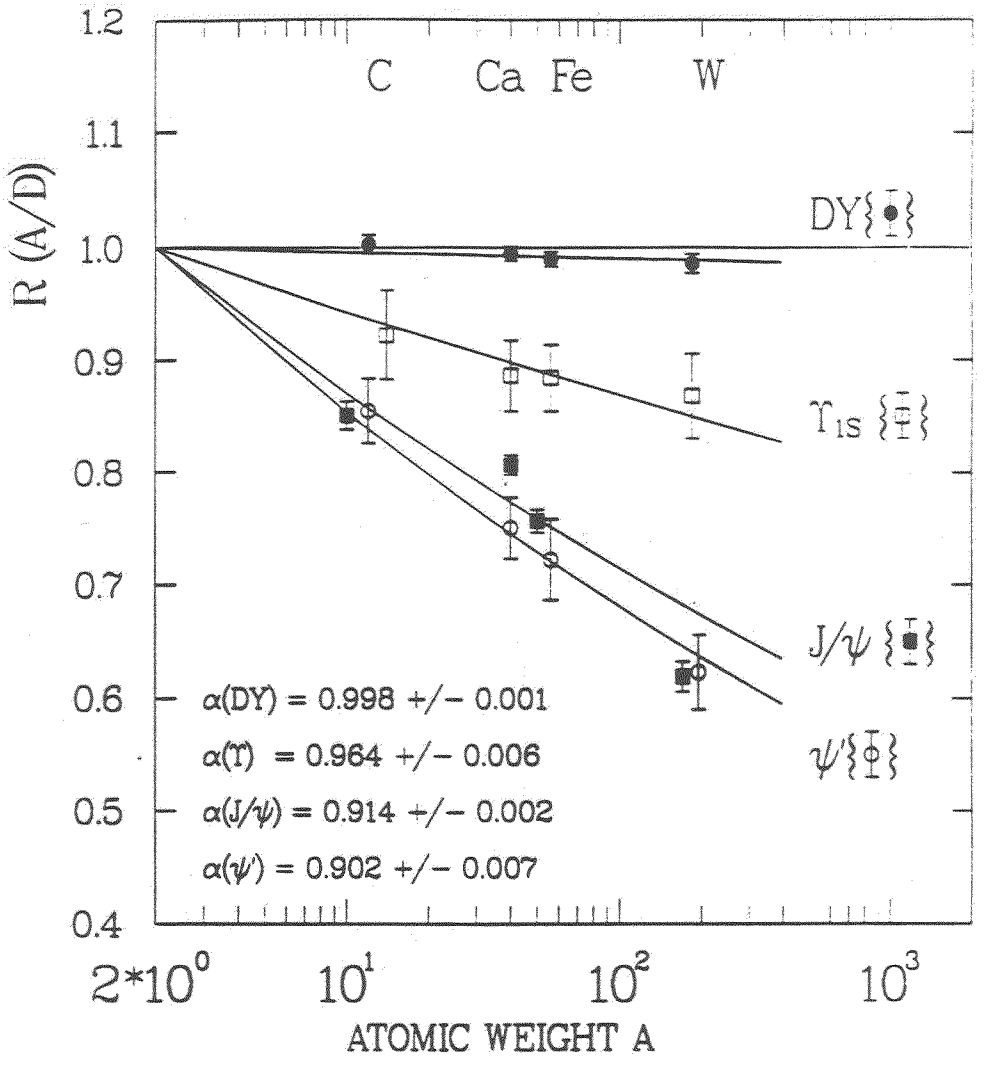

Figure 7.26: The measured R_{DY}(integrated), R_{Υ}(integrated), $R_{J/\psi}$(integrated), and $R_{\psi'}$(integrated) *versus* A; the curves are the function $R = (A/2)^{1-\alpha}$ fit to the data; the errors shown for the resonances represent the statistical and peak-fitting error. For R_{DY}, only the statistical error is shown.

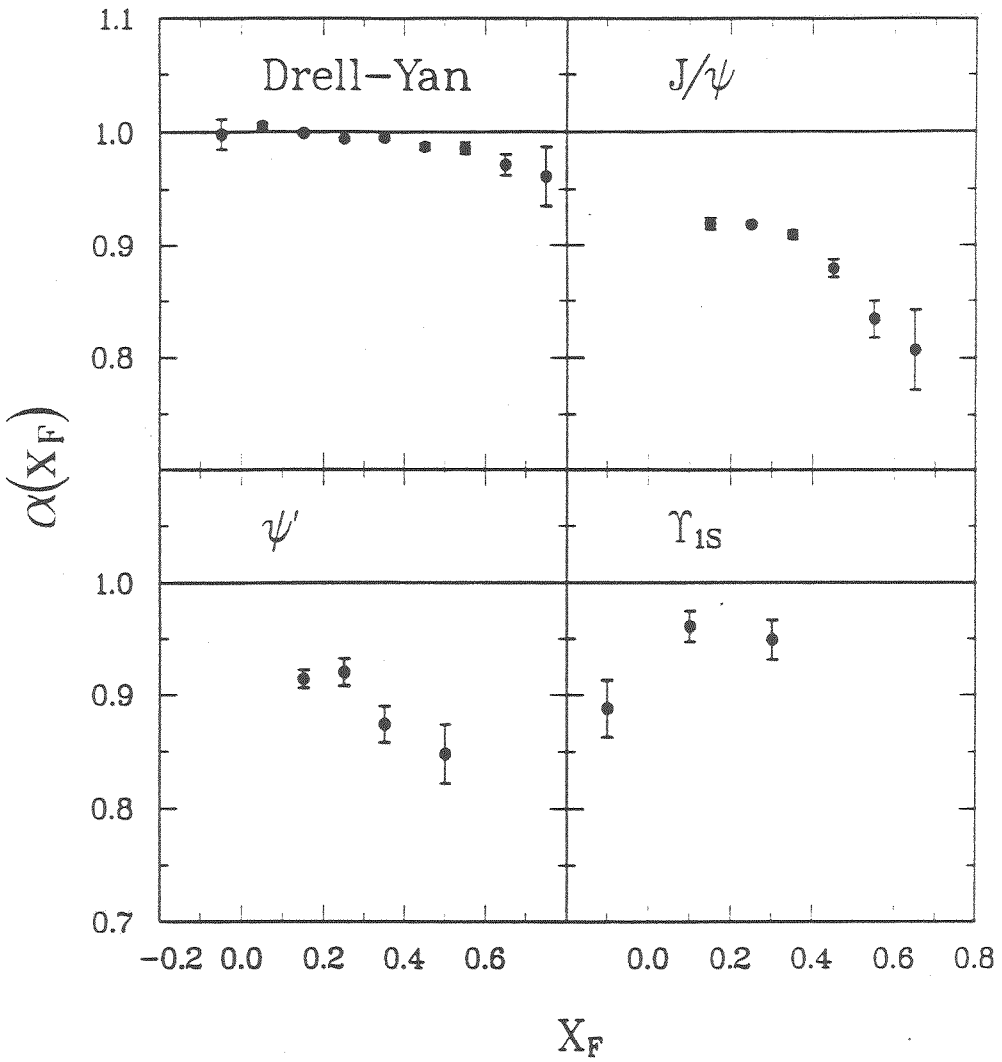

Figure 7.27: Extracted values of α *versus* x_F for all data; the errors shown for the resonances represent the statistical and peak-fitting error. For α_{DY}, only the statistical error is shown.

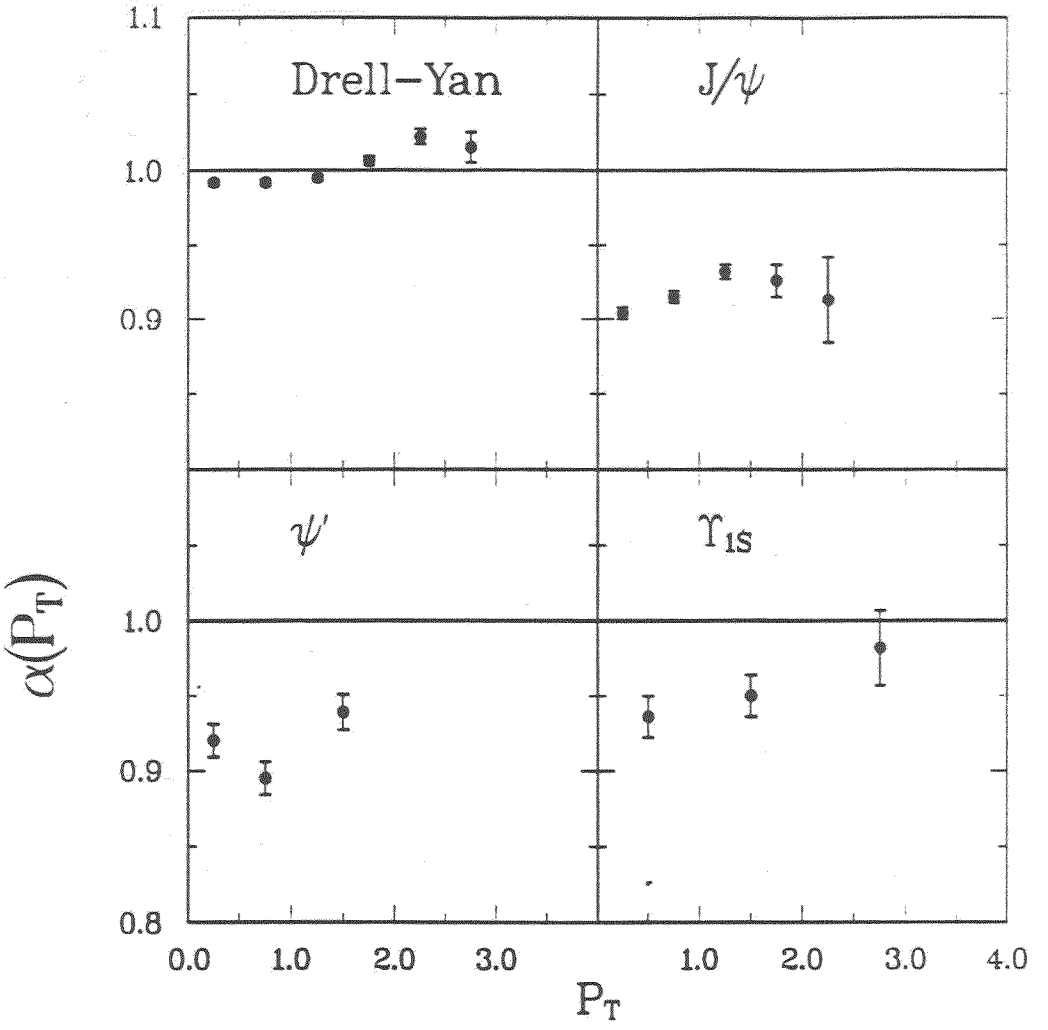

Figure 7.28: Extracted values of α *versus* P_T for all data; the errors shown for the resonances represent the statistical and peak-fitting error. For α_{DY}, only the statistical error is shown.

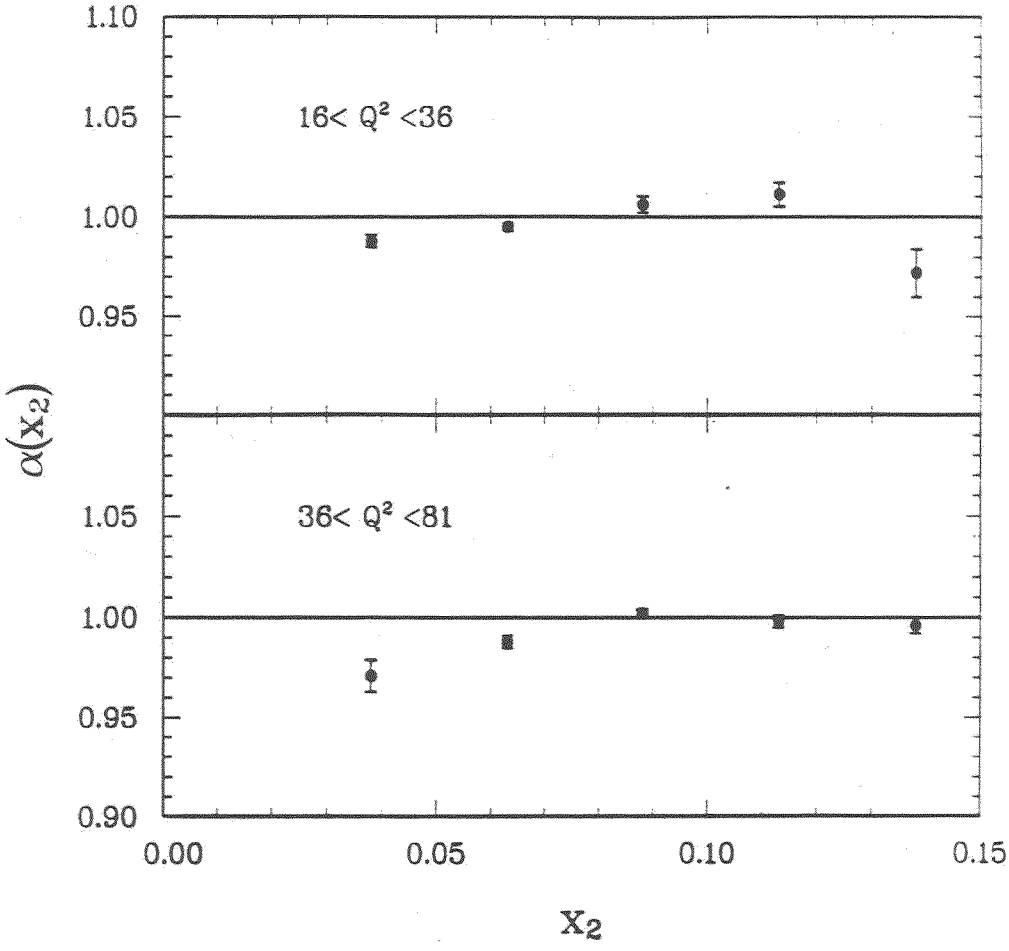

Figure 7.29: Extracted values of α *versus* x_2 for the Drell-Yan data, as shown in figure 7.12; the error reflects the statistical error on the measured $R_{DY}(x_2)$.

Chapter 8

Discussion of Results

The Drell-Yan ratio R_{DY}(integrated) was determined to be consistent with unity for all targets to within 2 % . The implications of this new result and comparison with other data are discussed in section 8.1. Even though the Drell-Yan ratio is very close to unity, there are some interesting A-dependent behaviors revealed by ratios as functions of $M_{\mu^+\mu^-}$, x_F , and P_T . This topic is discussed in section 8.2 in conjunction with initial-state-interaction effects. A further understanding of the A-dependent behavior of $M_{\mu^+\mu^-}$and x_F requires us to study the data in terms of quark variables x_1 and x_2 . This is discussed in section 8.4 with comparison to low-x depletion phenomenon observed in DIS experiments[30] and predictions of EMC models on antiquark distributions.

A-dependent behavior for charmonium states J/ψ and ψ' as functions of x_F and P_T were observed. These are discussed in section 8.5. Our experiment is the first to measure the A-dependence of Υ production. Interesting phenomena are revealed in this study in the region of negative x_F . Discussion and comparison with previously measured J/ψ and ψ' data are given in section 8.6.

8.1 Nuclear Transparency for the Drell-Yan Process

Figure 7.15 shows that the A-dependence of the integrated Drell-Yan ratio R_{DY}(A/D) is very different from those for J/ψ and ψ' production. The Drell-Yan nuclear cross sections are almost exactly proportional to the atomic number A. Previous experiments E288[77] and NA10[55] showed this at a much lower level of accuracy. The results are compared in table 8.1. The nearly unity value

group	beam type and energy (GeV)	range in $\sqrt{\tau}$	$\sigma(A_1)/\sigma(A_2)$
E288	p, 400	$0.18 < \sqrt{\tau} < 0.37$	1.022±0.057±0.088
NA10	π, 140	$0.27 < \sqrt{\tau} < 0.37$	0.912±0.021±0.053
	π, 286	$0.27 < \sqrt{\tau} < 0.37$	0.992±0.027±0.059
E772	p, 800	$0.10 < \sqrt{\tau} < 0.28$	0.986±0.008±0.020

Table 8.1: Ratio $\sigma(Pt)/\sigma(Be)$ of the Drell-Yan total cross sections (per nucleon) for E288; Ratio $\sigma(W)/\sigma(D)$ of the total cross sections for NA10 and E772.

of R_{DY} supports the incoherence picture of the Drell-Yan total cross section as discussed in section 1.5. It also implies that the Drell-Yan process occurs with equal probability any where in the nucleus, i.e., the nucleus is transparent to the Drell-Yan process at 800 GeV and at x_F >0. In contrast, the inelastic hadronic scattering cross sections grow with $A^{2/3}$, indicating that a beam hadron does not penetrate very far into the nucleus and does not see the nucleons in the back side of the nucleus. These two very different A-dependent behaviors are discussed in section 8.3.

8.2 Role of Initial-State-Interaction Effects in E772 Drell-Yan Data

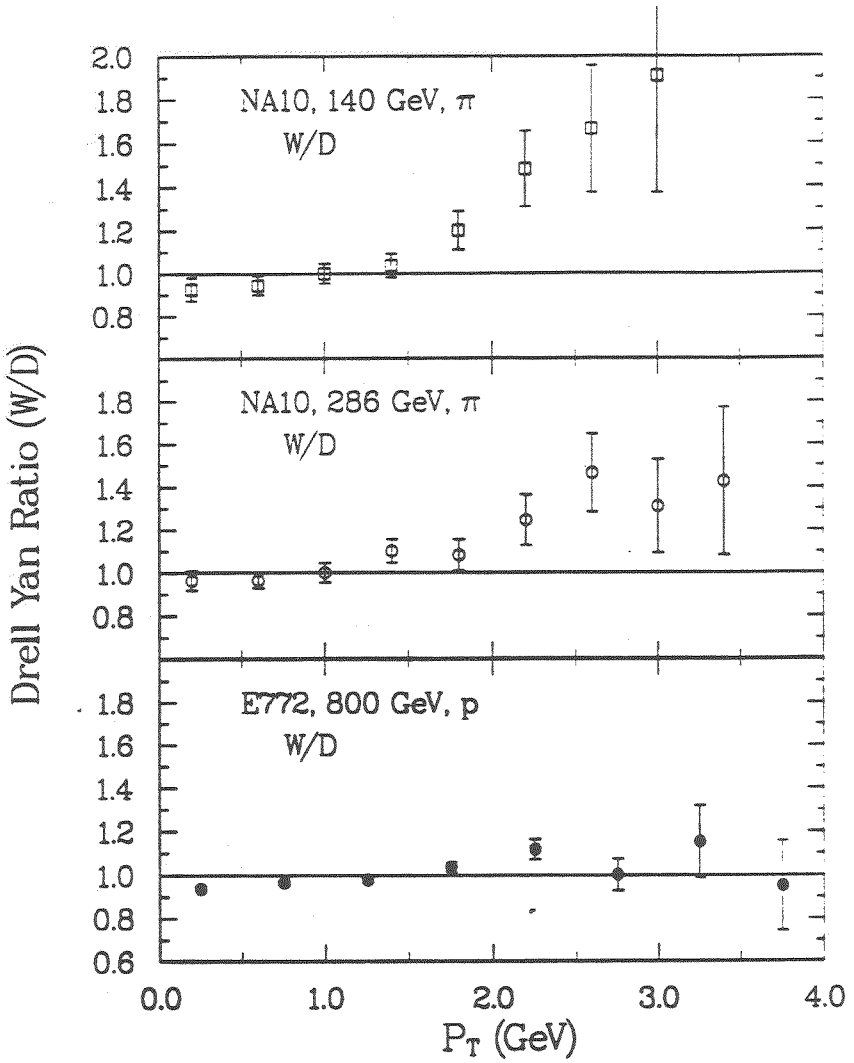

Figure 8.1: Comparison of NA10 data[55] with our data on $R_{DY}(P_T)$. The P_T -smearing effect is evident in all three experiments.

Beyond the integrated cross sections, some interesting A-dependent behaviors show up as functions of P_T , $M_{\mu^+\mu^-}$, and x_F (as shown in figure 7.9, 7.7, and 7.8). According to the theoretical arguments[27] discussed in section 1.5.5, P_T smearing is the main manifestation of initial-state interactions. Our data shown in figure 7.9 exhibit the expected P_T smearing effects. For Ca, Fe, and W, the ratio $R_{DY}(P_T)$ is below unity in the region of $P_T < 1$ GeV and above unity in the region of $P_T > 1$ GeV. For the lightest nucleus ^{12}C, no depletion is seen. For the heaviest target $^{183.85}$W, the depletion is 0.937±0.015 at P_T = 0.25 GeV. Thus, the low-P_T depletion is seen to increase with increasing A. However, there is no observed A-dependence of the point P_T^c where the ratio equals unity (at $P_T \simeq$1.5 GeV). These observations qualitatively agree with the P_T smearing effect described by Michael and Bodwin [54,29,27]. In figure 8.1, we compare our results on P_T smearing with those of E288[77] and NA10[55]. Figure 8.1 shows qualitatively that $R_{DY}(P_T)$ has similar behavior in all three experiments.

Figure 8.2(a) shows our measured A-dependence in the $M_{\mu^+\mu^-}$-distributions $R_{DY}(M_{\mu^+\mu^-})$ compared to those measured in E288. In the region 5 $< M_{\mu^+\mu^-} <$ 8 GeV, both data are consistent with unity. The deviations from unity in our data for $M_{\mu^+\mu^-}$>9 GeV are due to the A-dependent behavior of Υ quarkonium states.

Figure 8.2(b) shows our measured A-dependence in the x_F distributions $R_{DY}(x_F)$ compared to those measured in NA10. Within uncertainties, in the region 0.05 $< x_F <$ 0.55, the data are in agreement with each other and give a value close to unity. However, our higher statistics data reveal a consistent trend of depletion in $R_{DY}(x_F)$ at large x_F .

The near unity value of $R_{DY}(M_{\mu^+\mu^-})$ and $R_{DY}(x_F)$ in most kinematic regions agrees with the theoretical expectation that initial-state interactions do

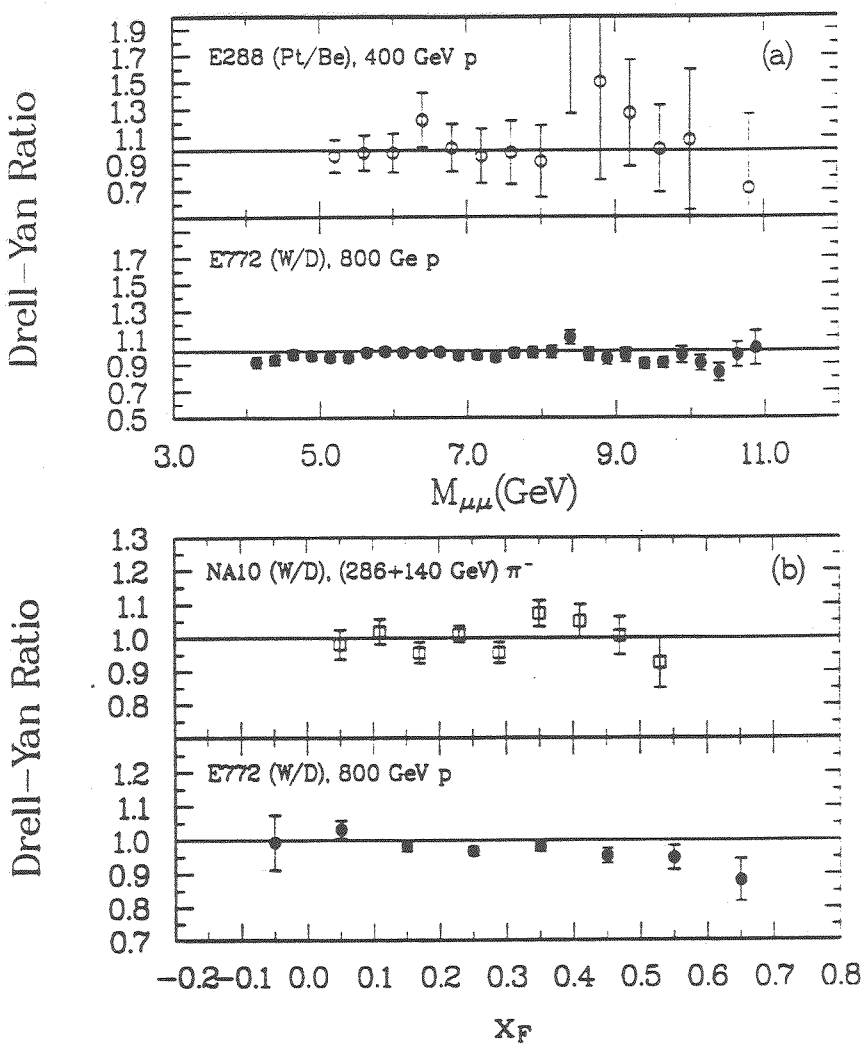

Figure 8.2: Comparison of E288[77] and NA10[55] data with E772 data (all data) on $M_{\mu^+\mu^-}$-and x_F A-dependence. The depletion in $R_{DY}(x_F)$ at large x_F is clearly seen for the first time in E772.

not invalidate factorization. However, the large-x_F depletion as shown in figures 7.8 and 8.2 raises the question - "to what level of accuracy does factorization hold in the region of large x_F ?".

According to the discussion in section 1.4.5 we should not see any effects on $R_{DY}(\ M_{\mu^+\mu^-})$ and $R_{DY}(\ x_F\ )$ due to initial-state interactions because the target-length condition is always satisfied in E772. Thus, we must ask whether the observed large x_F depletion is due to modification of parton distributions by the nuclear medium. To answer this, we must look at the A-dependent behaviors in terms of quark variables x_1 and x_2 , i.e., we must look at $R_{DY}(x_1$) and $R_{DY}(x_2$).

8.3 Transparency of the Nucleus to High-Energy Partons in the Beam

As discussed in section 8.1, the A^1 behavior of the integrated σ_{DY} confirms the incoherence picture of $p+A$ Drell-Yan cross sections. One may ask further "what is the A-dependence of the cross section in the beam quark variable x_1 involved in the nuclear Drell-Yan reaction?". This is given by $R_{DY}(x_1$). Figure 7.10 shows that the measured $R_{DY}(x_1$) are close to unity for all targets. Figure 8.3 shows the comparison between NA10[55] and E772 W/D data of $R_{DY}(x_1$). These data are consistent with each other. At first look, the near unity value of $R_{DY}(x_1$) is trivial because the parton distributions in the beam should not depend on the nuclear environment of targets. However, a closer look at the passage of a beam parton transversing nuclear medium before annihilating with an antiparton, raises a question about the role of soft-gluon interactions with the nuclear medium on the incoming parton. The data on $p+A$ interactions can be understood in the following physics picture.

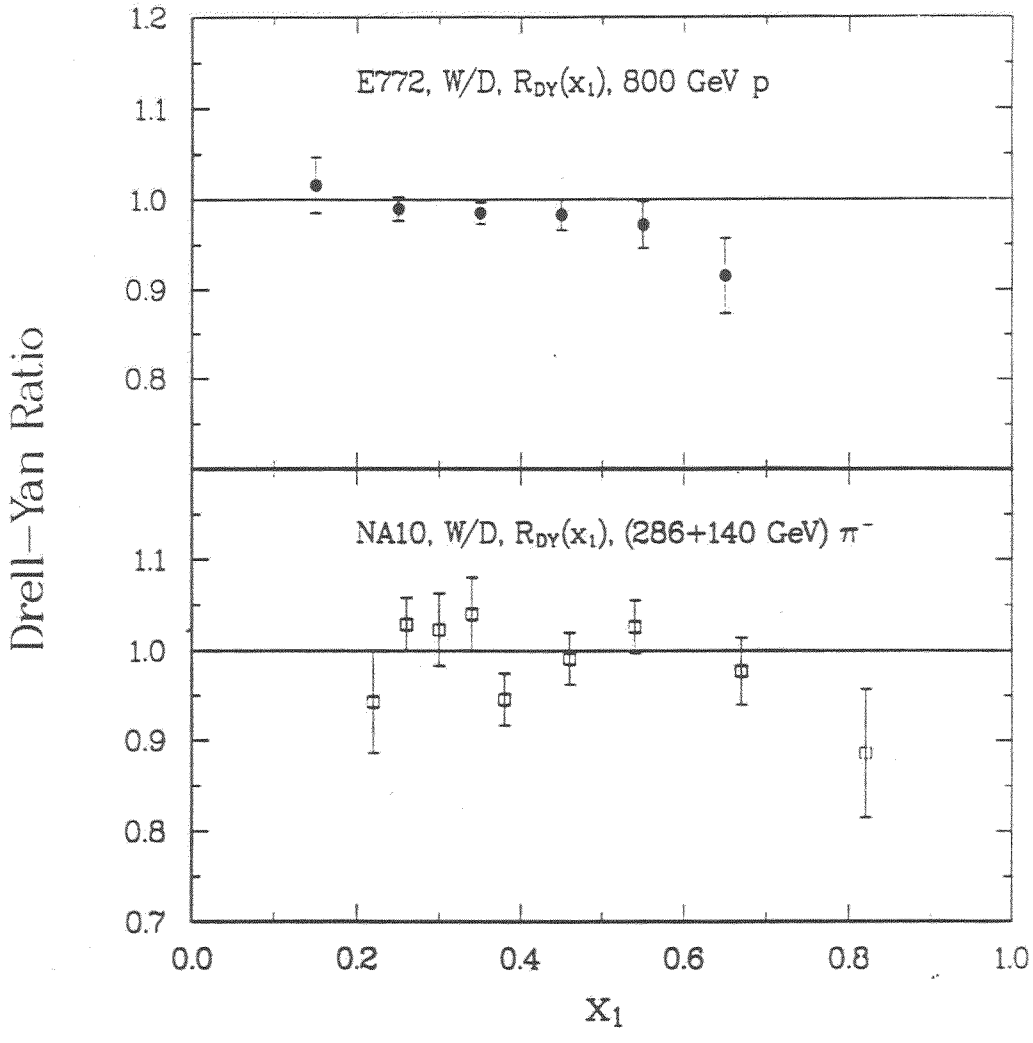

Figure 8.3: Comparison of NA10[55] with E772 W/D data.

In proton-nucleus collision, the proton breaks up at the surface of the nucleus and thus gives the inelastic cross section an $A^{2/3}$ behavior. However, the fast partons in the proton travel all way through the nucleus. While these stiff quarks traverse the nuclear medium, they undergo soft-gluon interactions with other partons before producing the Drell-Yan annihilation process. Because of the destructive interference of induced soft-gluon radiation, as proved by Bodwin et al. [25,26], the parton's longitudinal momentum is not degraded while transversing nuclear medium. In our experiment, with $x_F > 0$, it is these stiff partons that annihilate with antipartons in the nucleus. Thus, we observe the Drell-Yan cross section to exhibit an A^1 behavior. Because the cancellation of the soft color force applies equally to stiff partons and to stiff antipartons, we would expect an A^1 behavior for pion induced Drell-Yan cross sections at $x_F > 0$. Indeed, this is verified by the NA10 data of figure 8.2, which shows $R_{DY}(x_F) = 1$ for $x_F > 0$. This is the reason that we see similar effects in $R_{DY}(x_F)$ and $R_{DY}(P_T)$ in $p + A$ and $\pi + A$ Drell-Yan data.

8.4 A-dependence of $R_{DY}(x_2)$

Even though the A-dependent cross section ratios are consistent with unity (figure 7.6), an α parameter fit to the ratios in figure 7.6 gives a value of 0.998 ± 0.001. Also, the ratios in the region of large x_F show depletion as discussed in section 8.3. Actually these two observations just reflect an A-dependent depletion of parton distribution functions in the region of $x_2 < 0.1$. This depletion is seen in $R_{DY}(x_2)$ as shown in figures 7.11 and 7.12. All targets show depletion at $x_2 < 0.1$ and show no enhancement at $0.1 < x_2 < 0.3$. A horizontal-straight-line fit to the Ca and Fe data in the region $0.1 < x_2 < 0.3$ gives $R_{DY}(x_2) = 0.992 \pm 0.007$. Figures 7.11, 7.12, and 7.29 show three

features of this low-x_2 depletion: 1) a weak Q^2 dependence of this depletion; 2) the magnitude of depletion increases when A increases; and 3) no observed A-dependence of the depletion on-set x_2^c where the ratio equals unity (at $x_2^c \simeq 0.085$).

8.4.1 Comparison of $R_{DY}(x_2)$ with Neutrino DIS Data and EMC Data

In figure 8.4, we compare our measurement of $R_{DY}(x_2)$ for Fe/D with the measurement of $R_{\overline{q}}(x_2)$ performed by CDHS[102] using deep inelastic ν and $\overline{\nu}$ scattering on Fe and H_2 targets. The ratio $R_{\overline{q}}(x_2)$ is given by

$$\begin{aligned} R_{\overline{q}} &= \overline{q}_{Fe}/\overline{q}_{H_2} \\ &= (\overline{u}+\overline{d}+2\overline{s})_{Fe}/(\overline{u}+\overline{d}+2\overline{s})_{H_2} \end{aligned}$$

However, our ratio is $R_{DY} \simeq (\overline{u})_{Fe}/(\overline{u})_D$ as discussed in section 1.5.3. With the assumption of an SU(3) symmetric sea, where $\overline{u} = \overline{d} = \overline{s}$, these ratios are identical. Both quantities are a measure of nuclear effects on the sea antiquark. Clearly, our data place much tighter constraints on the nuclear medium effects in antiquark distributions, and they show that there is no enhancement of the nuclear antiquark sea in the region of x_2 between 0.08 and 0.28.

In figure 8.5 and 8.6, we compare our $R_{DY}(x_2)$ for Fe/D and W/D with R_{EMC} for Cu/D and Sn/D[30]. For the mid-A nuclei Fe and Cu, the two experiments show nearly the same amount of depletion at small x. For the ratios of heavier targets W/D and Sn/D, the small x depletion is less in our data of W/D. It should be noted that our Drell-Yan data probes mostly the $\overline{u}$ distribution whereas the DIS of EMC experiment probes a weighted linear combination of $q + \overline{q}$ distributions as given by F_2 (see section 1.2.3). The

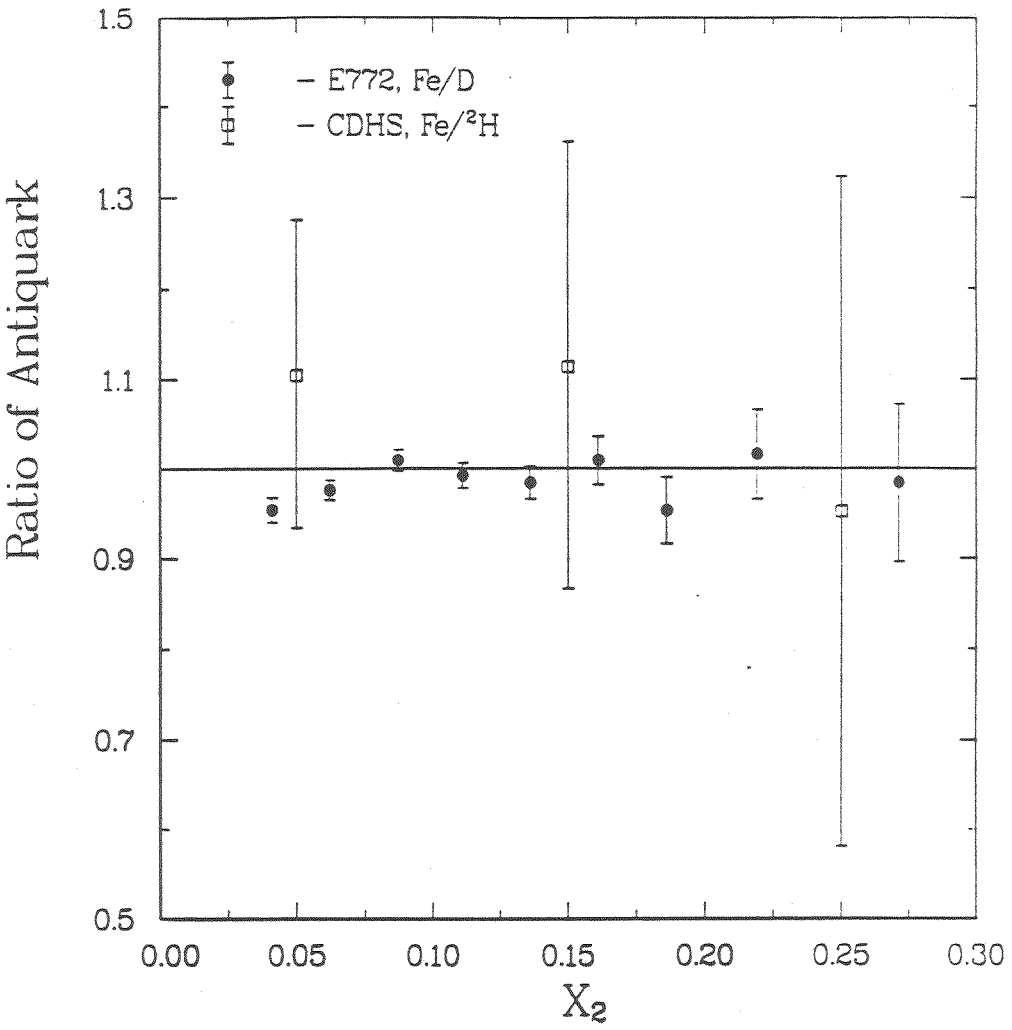

Figure 8.4: Comparison of CDHS Fe/^{2}H data[102] with E772 Fe/D data. Both experiments are sensitive to the nuclear medium effects on antiquark distributions. Our data provide much tighter constraints on these effects than previously available.

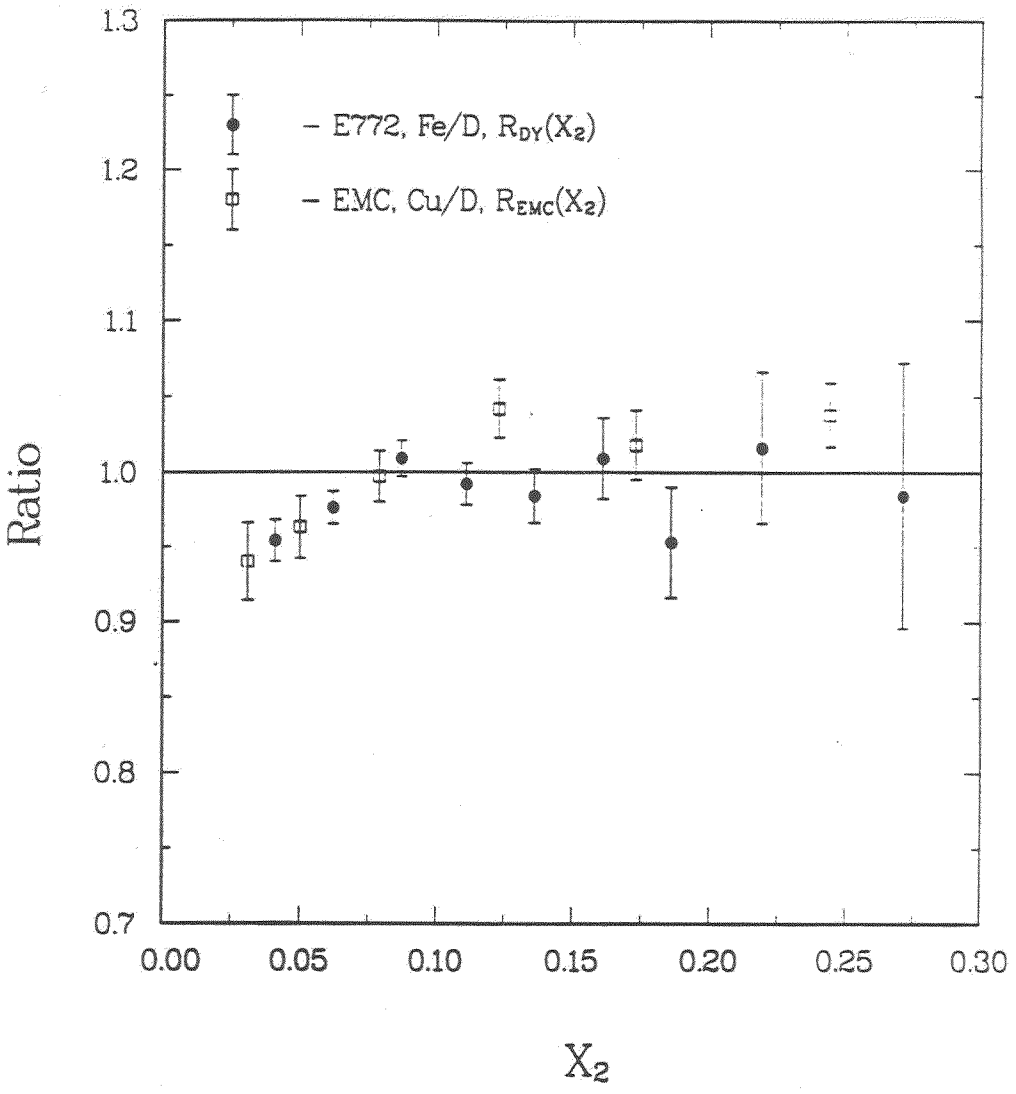

Figure 8.5: Comparison of EMC Cu data[30] with E772 Fe data in the low x region.

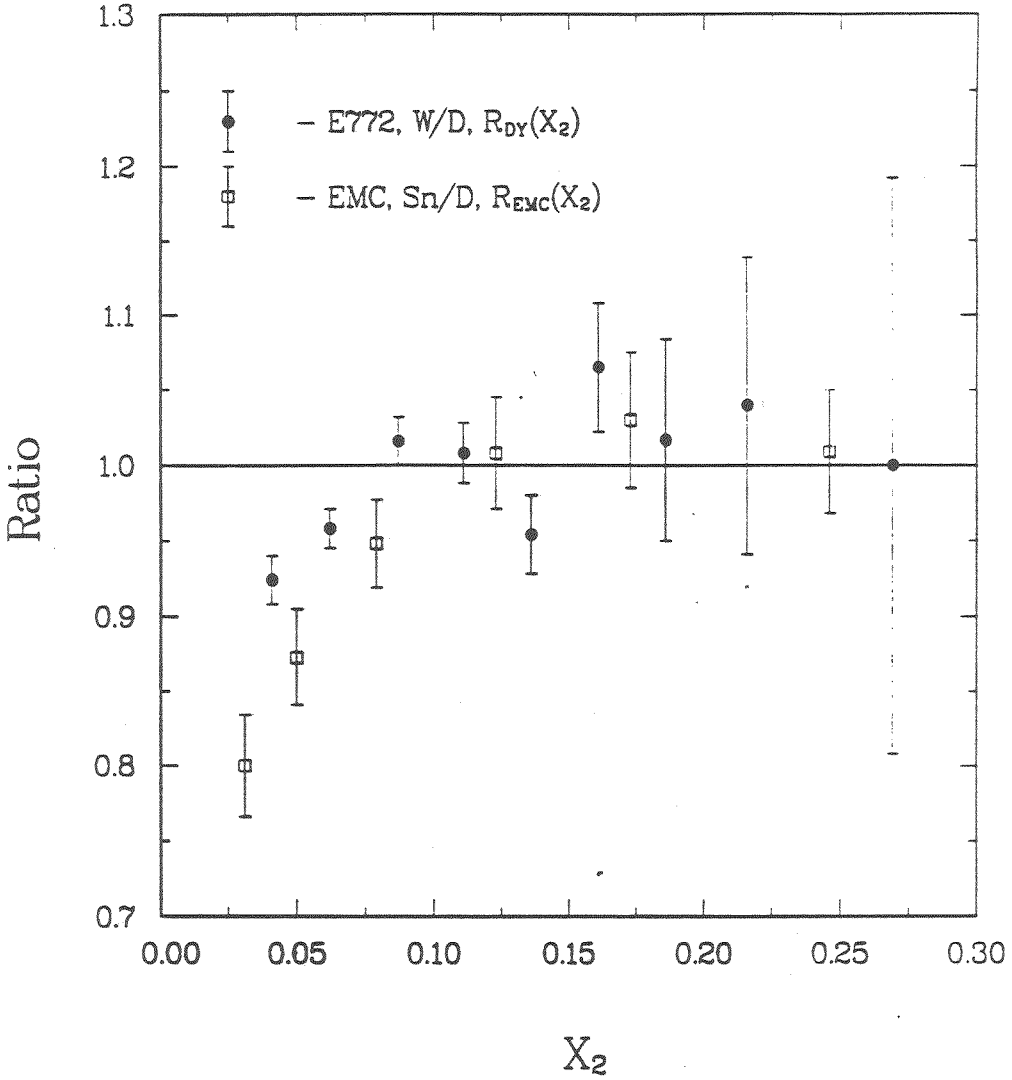

Figure 8.6: Comparison of EMC Sn data[30] with E772 W data in the low x region.

difference in $R_{DY}(x_2)$ and $R_{EMC}(x_2)$ at small x_2 for W/D and Sn/D, suggests that the small-x_2 depletion phenomenon is parton-dependent.

At the present time, nearly all the theoretical works on low-x_2 depletion are focused on DIS data. Because of the different features of Drell-Yan data, an understanding based on parton-recombination model is needed to describe our observations. Very recently Frankfurt and Strikman[105] have suggested that the sea antiquarks are less depleted at x=0.05 than are the valence quarks. This is in agreement with our W/D results compared to the EMC Sn/D data.

8.4.2 Predictions and Implications of EMC Models for Drell-Yan Data

The theoretical attempts to calculate the EMC effect fall into three general categories: pion-excess models, rescaling models, and quark cluster models, as discussed in section 1.5.2. We used these models to predict the nuclear dependence of Drell-Yan dimuon production. Figure 8.7 compares E772 data with the results of calculation[56] in which the EHLQ parametrization[73] of parton distributions was used. The force parameter of pion excess model[43,44] is chosen as $g_0' = 0.6$. Clearly, the E772 data are inconsistent with the predictions of these two models. Both models predict a sizeable enhancement in the antiquark content of nuclei, in disagreement with our data. The acceptance of the E772 spectrometer was taken into account in each of the calculations.

Our Drell-Yan data are also compared with a version of the rescaling model [42]. In this model, the scale of the antiquark distribution functions changes such that $\overline{q}(x_2, Q^2) \rightarrow \overline{q}(x_2, \xi Q^2)$, where $\xi \sim 2$ over the Q^2 range of our data. The theoretical prediction is shown in figure 8.7. In the region x_2 >0.1, it approximately describes the Drell-Yan data. In the region $x_2 < 0.1$, this model is not applicable because it does not treat the shadowing phenomenon.

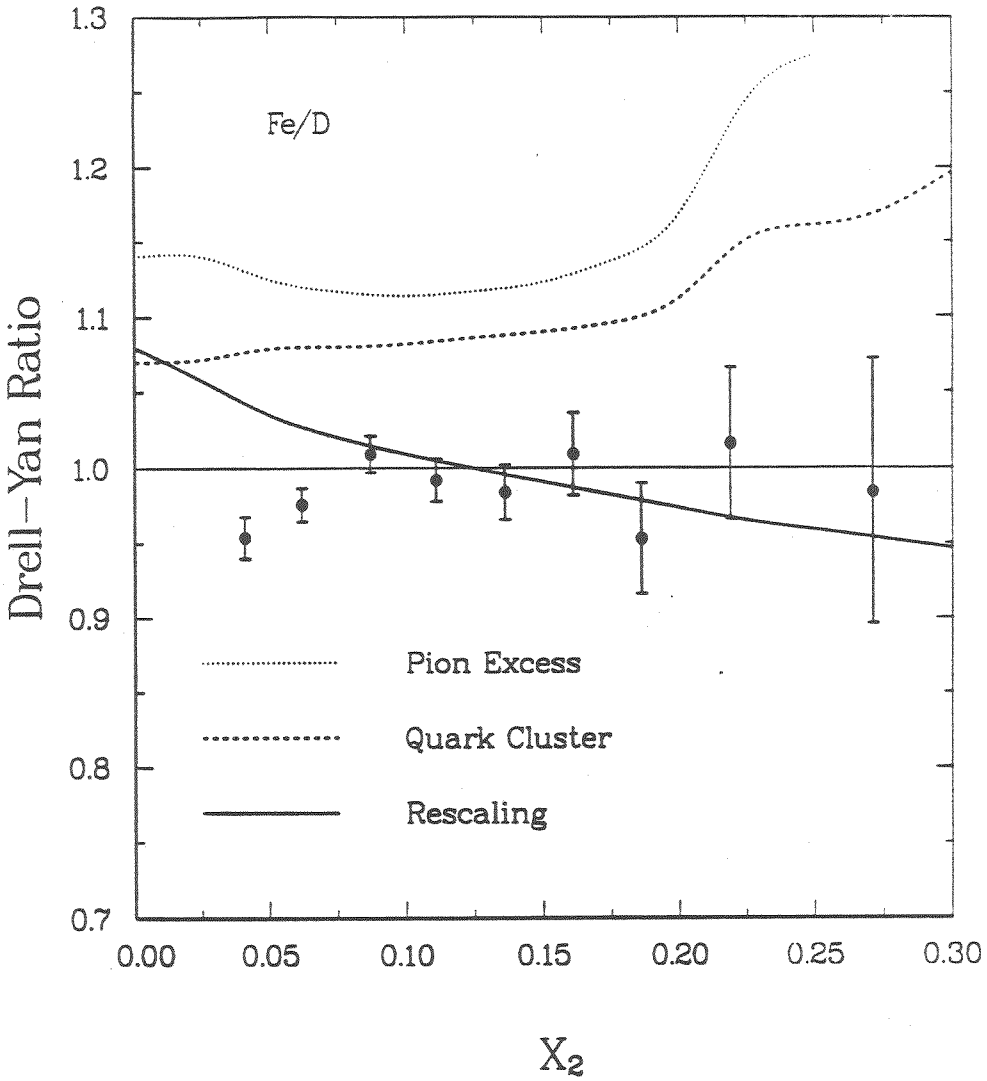

Figure 8.7: Comparison of predictions of EMC models with E772 data on *Fe* target[79]. The models are discussed in the text. The pion-excess and quark-cluster models are seen to predict too much nuclear enhancement of the Drell-Yan cross section.

Because of the success of the rescaling model in both DIS and Drell-Yan processes, the assumption of this model seems to suggest that a detailed study of hadron confinement is needed in order to understand the underlying mechanism responsible for the change of the QCD parameter in nuclear environments. Without this prior study, a further understanding on the origin of EMC effect seems to be unreachable.

The failure of the pion excess model to predict our Drell-Yan data seems to imply two possible deficiencies of this model. First the mechanism to describe the nuclear effect on the pion distribution may not be complete. Second the validity of the convolution picture may break down for Drell-Yan process. This is a more serious problem since it is the common assumptions for most the conventional nuclear physics models. The breakdown of this picture would imply the potential problem of extending the nuclear physics description to the parton degree of freedoms.

8.5 Implications of the Observed A-dependence in J/ψ $(c\bar{c})$ Production

Our data on the A-dependence of J/ψ and ψ' production are shown in figure 7.15 to 7.19. These data show sizeable nuclear attenuation of production cross sections for both the J/ψ and ψ' . In figure 7.15, we see that the overall nuclear-attenuation is nearly the same for both the J/ψ and ψ' . The result implies that the final hadron size might be irrelevant to the A-dependent behavior of J/ψ and ψ' production. The final Bohr radius of the $\psi'(2s)$ is four time that of the $J/\psi(1s)$.

To compare the A-dependence of our J/ψ data measured with D, C, Ca, Fe, and W targets with the E537 data[57] measured with Be and W targets, we

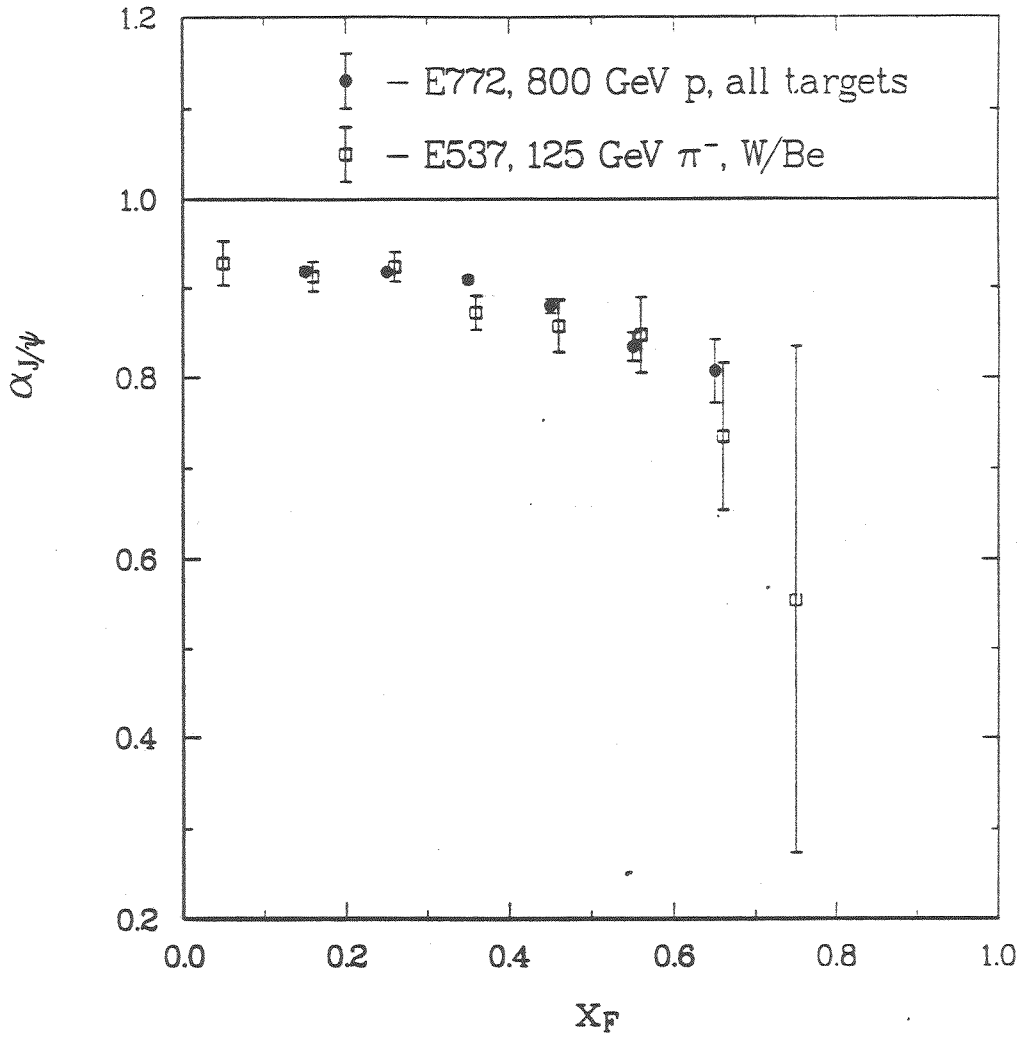

Figure 8.8: Comparison of E537[57] with E772 data on the x_F A-dependent ratio of J/ψ production cross sections.

use the A^{α} parametrization of cross sections. This allows for direct comparison of results. The two data sets are compared in figure 8.8 and are found to be in essential agreement on the shape and magnitude of the $\alpha(x_F)$ behavior.

What is the source of nuclear attenuation of J/ψ production cross sections? J/ψ production can be suppressed by secondary scattering in the nucleus, which breaks up the $c\bar{c}$ pair. This has been regarded as a possible explanation of the suppression of the J/ψ cross section at small x_F that was observed in central nucleus-nucleus collisions. At high energies and large x_F , the formation time for the $c\bar{c}$ pair to turn into a J/ψ is long due to time dilation, and the J/ψ forms well outside the nucleus[76]. Hence secondary-scattering effects should be small, and can not be the reason for the suppression at large x_F [57]. On the contrary, it would predict less suppression with increasing x_F .

Recently, the so-called co-mover model has been developed to describe the J/ψ production in nuclei. It takes into account the attenuation of $c\bar{c}$ states by secondary reactions of the J/ψ with some combination of the remaining nucleons of the target plus hadronic debris formed in the collision (co-movers)[76,92,93,94]. It is clear that these models predict a smaller A-dependence at large x_F for two reasons. First, the more energetic the J/ψ , the longer it stays in its (presumed) spatially small, color-singlet state. Second, for the most energetic J/ψs, the density of co-movers decreases. The observation of a significant suppression in the yield of the J/ψ at large x_F implies that attenuation cannot be the complete explanation of the A-dependence of hadronic J/ψ production. Additional evidence against the co-mover picture is found in beam-dump measurements of the A-dependence of inclusive charm production[96,97]. There, it is found that α is substantially less than unity. Presumably open-charm channels should not suffer attenuating reactions in the same way as $c\bar{c}$ states.

Another attempt to describe this large x_F suppression is the nuclear shad-

owing model. Here it is assumed that gluon distribution functions are modified by the nuclear medium[65]. This interpretation has two potential problems. On one hand, the common formula used to reconstruct parton variables x_1 and x_2 from dimuon variables,

$$x_1 = \frac{1}{2}(x_F + \sqrt{x_F^2 + 4m_{q\bar{q}}^2/s})$$
$$x_2 = \frac{1}{2}(-x_F + \sqrt{x_F^2 + 4m_{q\bar{q}}^2/s})$$

only hold for the direct fusion process $gg \rightarrow J/\psi$, which apparently is not allowed by the conservation of quantum number. All the production diagrams shown in figure 1.11 require detailed information about the particles which are produced associated with J/ψ , in order to reconstruct precise values of parton variables x_1 and x_2 . This is simply impossible for an inclusive process. $p + A \rightarrow \mu^+\mu^- + X$.

On the other hand, if we assume the formula mentioned above can provide a good approximation for parton variables, there is an another indication to show this picture is not adequate to explain this large x_F suppression phenomenon. Figure 8.9 shows the comparison of our data with that of NA3 and E537 data, where the x_2 variable is computed with the above formulas with $M_{q\bar{q}} = 3.097$ GeV. These data sets give three different curves. This shows that these depletion phenomena do not scale with x_2 , even though they scale with x_F . Hence, the nuclear dependence can not be ascribed to the target parton distribution function alone. If QCD factorization is valid but target structure function effects are present, then the ratio would depend on x_2 alone but not on $\sqrt{s}$.

Hoyer and Vänttinen[100] indicate that since the data of figure 8.9 show a marked dependence on $\sqrt{s}$, one is forced to conclude that the factorized cross

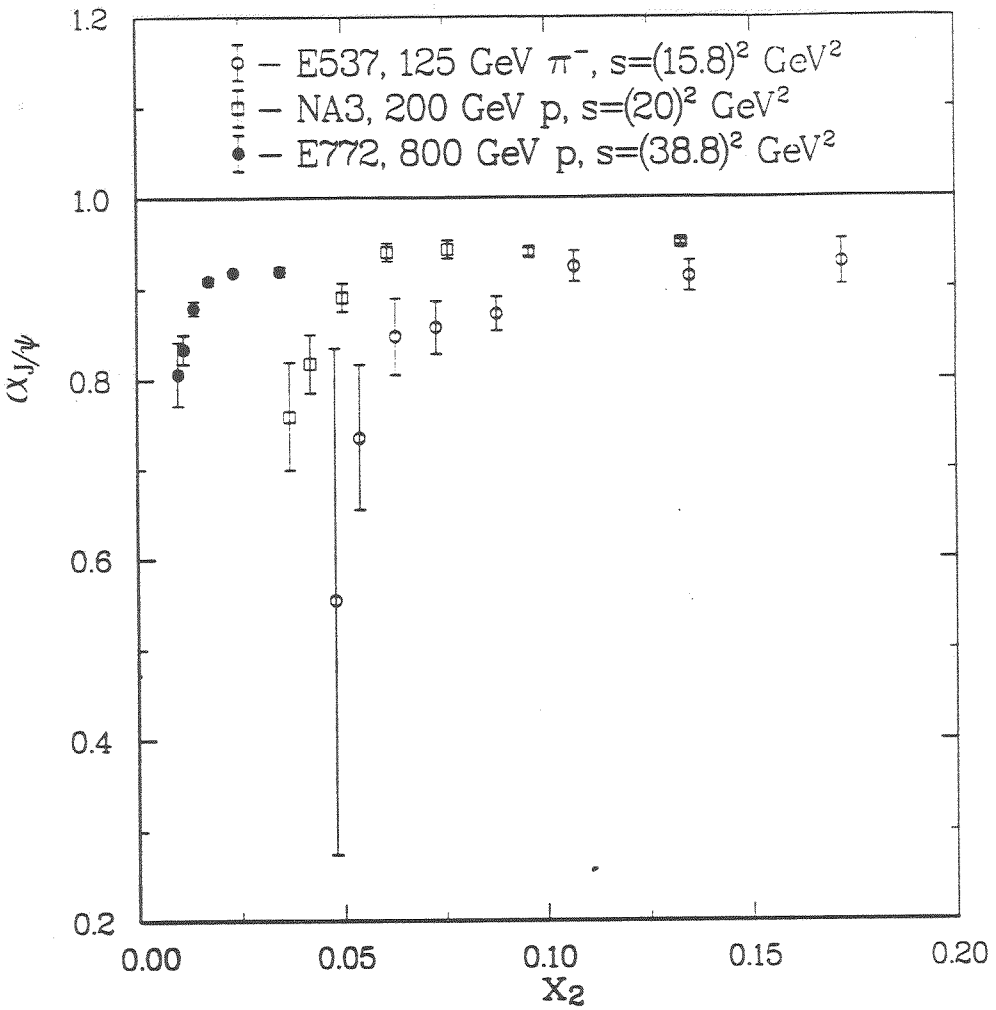

Figure 8.9: Comparison of NA3 data[74] and E537 data[57] with E772 data on the x_2 A-dependent ratio of J/ψ production cross sections.

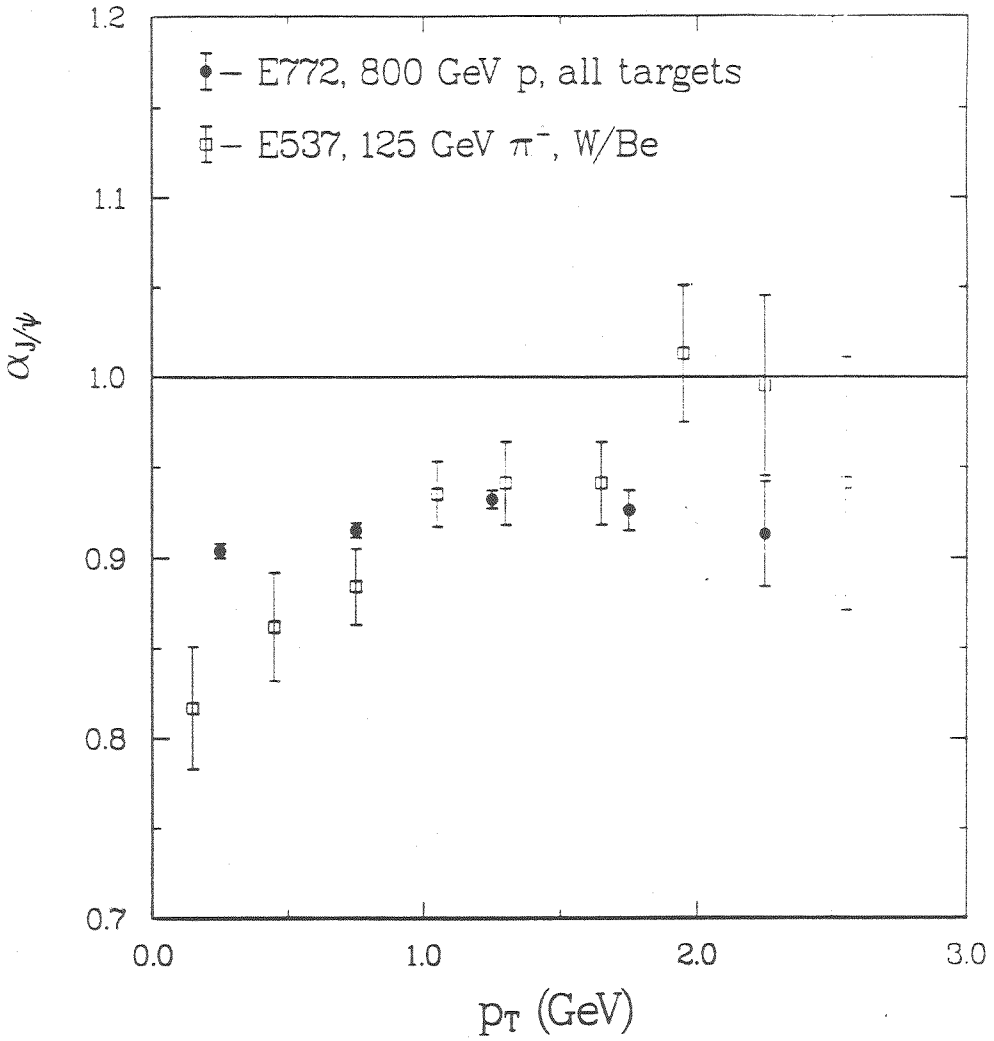

Figure 8.10: Comparison of E537 data[57] with E772 data on the P_T A-dependent ratio of J/ψ production cross sections.

section formula is not valid in the context of J/ψ production. If the ratio is instead compared at the same value of x_2 , clear energy dependence is seen. This contradicts the prediction which follows from factorization assumption.

Further Hoyer and Vänttinen indicate that the large-x_F nuclear effects observed in J/ψ production which are scaled with x_F over a very wide energy range (40 to 800GeV/c) *suggests* that the *higher-twist effects* are related to the fragmentation of the beam hadrons and associated with the breakdown of the factorization assumption. This feature is natural in models where the beam hadrons have intrinsic charm[90]. Also according to the discussion in chapter 1, the magnitude of the J/ψ cross section at large x_F seems to require a new contribution like intrinsic charm. More important is that it has been shown that the A-dependence of the intrinsic charm contribution should behave as A^α, with $\alpha \simeq 2/3$. Hence, the decrease of the effective value of α with x_F can be understood as due to the increasing importance of the intrinsic charm component.

8.6 Implications of the Observed A-dependence in Υ $(b\bar{b})$ Production

Our measurement of the A-dependence of $\Upsilon(1s)$ production is shown in figure 7.22 to 7.26. Figure 7.26 shows that the nuclear attenuation of the $\Upsilon(1s)$ cross section is considerable less than for J/ψ and ψ' production. The $\Upsilon(1s)$ data on all targets is well described by $A^{0.964\pm0.006}$. The data on $R_{\Upsilon(1s)}(P_T$) is somewhat sparse (figure 7.24), but does show the trend of P_T smearing. For Ca at P_T = 2.75 GeV, the measured ratio $R_{\Upsilon(1s)}(P_T$) = 1.00 $\pm$ 0.13; at P_T = 0.25 GeV, $R_{\Upsilon(1s)}(P_T$) = 0.83 $\pm$ 0.08. The measured $R_{\Upsilon(1s)}(x_F$) shown in figure 7.23 reveal the interesting new phenomenon of sizeable nuclear depletion of the production cross section at negative x_F . This is seen for both the Ca

and Fe targets.

A decisive test on the higher twist nature of large x_F heavy quark production would be a comparison of the Υ and J/ψ cross sections, for which the relative higher twist contribution should scale like m_c^2/m_b^2. The A-dependence in Υ production at 800 GeV, which is shown in figure 7.27 reveals less depletion in large x_F .

Chapter 9

Summary of Principal Results and Conclusions

In this experiment, the A-dependences of the Drell-Yan process and of J/ψ, ψ', and Υs vector meson production in $p-A$ collisions at 800 GeV ($\sqrt{s} = 38.8$ GeV) were measured. The principal results and physics implications are listed below.

For the Drell-Yan ratios R_{DY} we find:

(1) *Very little nuclear medium dependence of* $R_{DY}(integrated)$ [1]. The Drell-Yan nuclear cross sections with 800 GeV protons, and in the kinematic region $x_F > 0$ and $M_{\mu^+\mu^-} = 4 - 9$ GeV, are described by the equation $\sigma_A^{DY} = \sigma_N A^{0.998 \pm 0.001}$. This implies that the $q\bar{q}$ annihilation process occurs with very nearly equal probability anywhere within nucleus.

(2) *No nuclear enhancement of the antiquark sea distribution in the kinematic region of* $0.1 < x_2 < 0.3$ [2]. *The data in this* x_2

[1] Refer to figure 7.6 on page 153 for more details.

[2] Refer to figure 7.11 on page 159 for more details.

interval for Ca and Fe give $R_{DY}(x_2) = 0.992 \pm 0.007$. The standard models of the pion-excess and quark-cluster that give $R(x_2) \simeq 1.1$ in this interval, are therefore ruled out by this result. Predictions of the rescaling model for antiquark distributions are consistent with this observation.

(3) *There are 4-7% depletions in antiquark distributions in a heavy target at* $x_2 = 0.05$. Thus the "Shadowing effect" of antiquark distributions is observed for the first time. More theoretical effort is needed to understand this depletion. Our results have raised the question: "Are the Shadowing effects for quark and antiquark distributions the same?".

(4) *No nuclear enhancement and very little depletion in* $R_{DY}(x_1)$ *was observed in the region of* $0.1 < x_1 < 0.6$ [3]. This implies that fast beam quarks go through the nuclear medium with little change in the longitudinal momentum.

(5) *Weak nuclear enhancement of* P_T *distributions are observed in the kinematic region of* $P_T > 1.5\ GeV$ [4]. Initial state interactions were observed to produce more P_T smearing in heavier targets than that in the lighter targets. The observed P_T smearing indicates that beam quarks pick up P_T kicks via

[3] Refer to figure 7.10 on page 158 for more details.

[4] Refer to figure 7.9 on page 156 for more details.

soft gluon interactions while going through nuclear medium.

(6) *The measured K-factor is 2.30 as extracted from the $M_{\mu^+\mu^-}$ and x_F spectra.* The systematic error is estimated to be $\sim 12\%$ and the statistical error is negligible compared to the systematic uncertainty. This value falls well within the range of previous measurements.

In conclusion, our experiment using the Drell-Yan process has given the first accurate probe of nuclear modifications of antiquark distributions.

For the production of quarkonium states J/ψ , ψ' , and $\Upsilon(1s)$ we find:

(1) *The nuclear production cross sections (per nucleon) are depleted relative to the free nucleon cross section (as approximated with a deterium cross section). They can be described with an A^α power law with $\alpha = 0.914 \pm 0.002$ and $\alpha = 0.902 \pm 0.007$ for the J/ψ and ψ' , and $\alpha = 0.964 \pm 0.006$ for the $\Upsilon(1s)$* [5].

(2) *α is found to be a function of x_F for both J/ψ and ψ' production. For the J/ψ , its value goes from 0.919 ± 0.005 at $x_F = 0.15$ to 0.807 ± 0.035 at $x_F = 0.65$* [6]. *A similar behavior is observed in the ψ' .*

(3) *For the $\Upsilon(1s)$, α is also found to be a function of x_F . At $x_F = -0.1$, α is 0.888 ± 0.025, which is significantly less than*

[5] Refer to figure 7.26 on page 180 for more details.

[6] Refer to figure 7.27 on page 181 for more details.

the $\alpha = 0.961 \pm 0.014$ at $x_F = 0.1$ and the $\alpha = 0.949 \pm 0.018$ at $x_F = 0.3$ [7]. This enhanced depletion at negative x_F is here observed for the first time. It has become one of the motivations to study A-dependence in negative x_F for measurements at Fermilab in E789.

(4) *P_T smearing is observed for all three quarkonium states. The slope of the α versus P_T curve is similar to that of Drell-Yan. However, the quarkonium states exhibit significant nuclear depletion, which is not present in the Drell-Yan data* [8].

In conclusion, our experiment has given the first precise determination of the A-dependence of $p - A$ production cross sections for these quarkonium states. J/ψ , ψ' , and $\Upsilon(1s)$.

[7] Refer to figure 7.27 on page 181 for more details.

[8] Refer to figure 7.28 on page 182 for more details.

Appendix A

Numerical Tables of Data

A.1 Drell-Yan Data

R_{DY}(C/D)	R_{DY}(Ca/D)	R_{DY}(Fe/D)	R_{DY}(W/D)
1.003±0.0085	0.995±0.0061	0.990±0.0065	0.986±0.0083

Table A.1: Numerical table for figure 7.6.

$M_{\mu^+\mu^-}$(GeV)	R_{DY}(C/D)	R_{DY}(Ca/D)	R_{DY}(Fe/D)	R_{DY}(W/D)
4.125	0.976±0.041	1.038±0.036	1.011±0.037	0.918±0.041
4.375	0.971±0.039	1.002±0.030	0.992±0.032	0.936±0.037
4.625	1.032±0.034	1.033±0.028	0.993±0.026	0.976±0.033
4.875	0.991±0.031	0.992±0.023	0.976±0.024	0.965±0.030
5.125	0.993±0.029	0.984±0.021	0.988±0.023	0.952±0.027
5.375	0.975±0.027	0.978±0.021	0.950±0.021	0.949±0.026
5.625	0.997±0.027	0.979±0.020	0.994±0.021	0.987±0.027
5.875	0.962±0.026	0.961±0.019	0.970±0.020	0.996±0.027
6.125	1.008±0.028	1.013±0.020	0.987±0.021	0.987±0.026
6.375	0.972±0.028	0.971±0.020	0.957±0.020	0.987±0.027
6.625	1.036±0.031	0.954±0.020	0.994±0.022	0.991±0.029
6.875	0.973±0.030	0.940±0.020	0.986±0.022	0.963±0.029
7.125	1.019±0.034	1.006±0.023	1.015±0.024	0.970±0.032
7.375	1.022±0.036	0.987±0.024	0.920±0.023	0.948±0.033
7.625	0.978±0.037	1.013±0.026	1.022±0.027	0.984±0.037
7.875	0.965±0.040	0.946±0.025	0.968±0.026	0.990±0.040
8.125	1.022±0.047	1.016±0.028	1.000±0.029	0.994±0.044
8.375	1.054±0.052	1.002±0.030	1.043±0.032	1.102±0.052
8.625	0.876±0.047	1.038±0.032	0.956±0.031	0.973±0.049
8.875	1.007±0.056	0.963±0.032	0.964±0.033	0.947±0.052
9.125	0.965±0.053	0.984±0.031	0.940±0.030	0.966±0.052

Table A.2: Numerical table for figure 7.7.

x_F	R_{DY}(C/D)	R_{DY}(Ca/D)	R_{DY}(Fe/D)	R_{DY}(W/D)
-0.050	1.039±0.086	0.968±0.049	1.013±0.054	0.994±0.081
0.050	1.046±0.027	0.999±0.017	1.021±0.018	1.032±0.026
0.150	1.009±0.016	1.018±0.012	0.986±0.012	0.983±0.016
0.250	0.983±0.014	0.980±0.010	0.986±0.010	0.968±0.013
0.350	0.992±0.016	0.987±0.011	0.983±0.011	0.982±0.015
0.450	0.978±0.023	0.951±0.016	0.958±0.017	0.954±0.022
0.550	0.977±0.037	0.957±0.026	0.951±0.027	0.948±0.035
0.650	1.010±0.072	0.919±0.049	0.890±0.049	0.881±0.063
0.750	0.748±0.144	0.739±0.110	1.244±0.173	0.918±0.159
0.850	2.466±1.440	1.163±0.564	0.465±0.245	1.026±0.688

Table A.3: Numerical table for figure 7.8.

P_T (GeV)	R_{DY}(C/D)	R_{DY}(Ca/D)	R_{DY}(Fe/D)	R_{DY}(W/D)
0.250	1.005±0.016	0.980±0.011	0.987±0.012	0.937±0.015
0.750	0.999±0.012	0.978±0.009	0.967±0.009	0.966±0.012
1.250	0.991±0.015	0.981±0.011	0.983±0.011	0.979±0.015
1.750	0.960±0.023	1.031±0.018	1.012±0.018	1.038±0.024
2.250	1.053±0.044	1.043±0.031	1.090±0.035	1.118±0.046
2.750	0.887±0.071	1.120±0.061	1.109±0.063	1.002±0.073
3.250	1.221±0.170	1.134±0.116	0.941±0.093	1.152±0.166
3.750	0.741±0.180	0.788±0.142	0.871±0.168	0.951±0.207
4.250	1.108±0.461	0.767±0.240	1.233±0.398	1.331±0.515
4.750	0.448±0.554	0.362±0.300	1.473±0.824	1.229±1.132

Table A.4: Numerical table for figure 7.9.

x_1	R_{DY}(C/D)	R_{DY}(Ca/D)	R_{DY}(Fe/D)	R_{DY}(W/D)
0.150	1.023±0.032	1.040±0.024	1.055±0.024	1.016±0.031
0.250	0.999±0.014	1.023±0.011	0.987±0.010	0.990±0.013
0.350	1.022±0.013	1.002±0.010	1.002±0.009	0.985±0.012
0.450	0.985±0.017	0.985±0.013	0.980±0.012	0.983±0.017
0.550	0.990±0.027	0.971±0.021	0.971±0.019	0.972±0.026
0.650	0.998±0.046	0.988±0.037	0.940±0.033	0.915±0.042
0.750	0.897±0.093	0.934±0.077	0.997±0.076	0.812±0.084
0.850	0.881±0.270	0.916±0.215	1.207±0.257	0.881±0.267

Table A.5: Numerical table for figure 7.10.

x_2	R_{DY}(C/D)	R_{DY}(Ca/D)	R_{DY}(Fe/D)	R_{DY}(W/D)
0.041	0.981±0.017	0.971±0.014	0.954±0.014	0.924±0.016
0.062	0.974±0.014	0.980±0.010	0.976±0.011	0.958±0.013
0.087	1.013±0.016	1.001±0.011	1.009±0.012	1.016±0.016
0.111	1.011±0.020	1.000±0.013	0.992±0.014	1.008±0.020
0.136	0.979±0.027	0.986±0.017	0.984±0.018	0.954±0.026
0.161	1.049±0.044	1.025±0.026	1.009±0.027	1.065±0.043
0.186	1.117±0.074	0.966±0.036	0.953±0.037	1.017±0.067
0.216	1.151±0.110	0.947±0.046	1.016±0.050	1.040±0.099
0.269	1.044±0.202	0.947±0.082	0.984±0.088	1.000±0.192

Table A.6: Numerical table for figure 7.11.

x_2 ($16< Q^2 <36$)	R_{DY}(C/D)	R_{DY}(Ca/D)	R_{DY}(Fe/D)	R_{DY}(W/D)
0.038	0.981±0.018	0.989±0.016	0.960±0.015	0.926±0.017
0.063	0.984±0.018	1.004±0.015	0.982±0.014	0.965±0.018
0.088	1.015±0.029	1.005±0.022	1.018±0.022	1.041±0.029
0.113	0.991±0.048	1.068±0.040	1.023±0.037	1.044±0.050
0.138	0.874±0.082	1.040±0.069	0.934±0.067	0.789±0.075

Table A.7: Numerical table for figure 7.12.

x_2 (36< Q^2 <81)	R_{DY}(C/D)	R_{DY}(Ca/D)	R_{DY}(Fe/D)	R_{DY}(W/D)
0.038	0.975±0.057	0.934±0.049	0.879±0.042	0.887±0.052
0.063	0.954±0.021	0.968±0.018	0.965±0.016	0.948±0.021
0.088	1.012±0.019	1.006±0.015	1.005±0.013	1.005±0.018
0.113	1.015±0.022	0.994±0.016	0.984±0.015	1.001±0.021
0.138	0.993±0.029	0.991±0.020	0.989±0.019	0.970±0.028

Table A.8: Numerical table for figure 7.12.

A.2 J/ψ and ψ' Data

Integrated	R(C/D)	R(Ca/D)	R(Fe/D)	R(W/D)
Drell-Yan	1.003±0.0085	0.995±0.0061	0.990±0.0065	0.986±0.0083
J/ψ	0.851±0.012	0.806±0.009	0.756±0.010	0.619±0.013
ψ'	0.855±0.029	0.750±0.027	0.722±0.036	0.623±0.033

Table A.9: Numerical table for figure 7.15.

x_F	$R_{J/\psi}$(C/D)	$R_{J/\psi}$(Ca/D)	$R_{J/\psi}$(Fe/D)	$R_{J/\psi}$(W/D)
0.15	0.887±0.039	0.791±0.023	0.777±0.022	0.662±0.029
0.25	0.876±0.016	0.813±0.011	0.764±0.011	0.649±0.013
0.35	0.834±0.026	0.793±0.020	0.770±0.019	0.608±0.021
0.45	0.801±0.042	0.805±0.042	0.687±0.037	0.520±0.031
0.55	0.699±0.067	0.830±0.093	0.652±0.077	0.422±0.043
0.65	0.809±0.148	0.511±0.139	0.427±0.124	0.462±0.092

Table A.10: Numerical table for figure 7.16.

P_T (GeV)	$R_{J/\psi}$(C/D)	$R_{J/\psi}$(Ca/D)	$R_{J/\psi}$(Fe/D)	$R_{J/\psi}$(W/D)
0.25	0.823±0.019	0.788±0.015	0.740±0.017	0.589±0.020
0.75	0.877±0.019	0.794±0.015	0.746±0.016	0.649±0.021
1.25	0.851±0.031	0.895±0.028	0.858±0.026	0.641±0.027
1.75	0.894±0.068	0.928±0.058	0.730±0.048	0.686±0.053
2.25	0.708±0.140	0.811±0.157	0.855±0.161	0.660±0.125

Table A.11: Numerical table for figure 7.17.

x_F	$R_{\psi'}$(C/D)	$R_{\psi'}$(Ca/D)	$R_{\psi'}$(Fe/D)	$R_{\psi'}$(W/D)
0.15	0.805±0.052	0.832±0.035	0.753±0.039	0.627±0.042
0.25	0.984±0.062	0.753±0.078	0.753±0.060	0.678±0.050
0.35	0.785±0.074	0.553±0.079	0.692±0.052	0.606±0.070
0.45	0.749±0.108	0.682±0.125	0.738±0.103	0.537±0.166
0.55		0.325±0.108	0.404±0.125	0.486±0.162
0.65		0.255±0.205	0.319±0.280	

Table A.12: Numerical table for figure 7.18.

P_T (GeV)	$R_{\psi'}$(C/D)	$R_{\psi'}$(Ca/D)	$R_{\psi'}$(Fe/D)	$R_{\psi'}$(W/D)
0.25	0.825±0.052	0.807±0.055	0.795±0.048	0.666±0.062
0.75	0.889±0.063	0.726±0.033	0.691±0.046	0.619±0.108
1.25	0.911±0.081	0.882±0.065	0.858±0.077	0.779±0.069
1.75	0.531±0.120	0.847±0.114	0.507±0.108	0.791±0.338
2.25		1.199±0.451	1.889±0.785	

Table A.13: Numerical table for figure 7.19.

x_2	$R_{J/\psi}$(C/D)	$R_{J/\psi}$(Ca/D)	$R_{J/\psi}$(Fe/D)	$R_{J/\psi}$(W/D)
0.0345	0.887±0.039	0.791±0.023	0.777±0.022	0.662±0.029
0.0233	0.876±0.016	0.813±0.011	0.764±0.011	0.649±0.013
0.0173	0.834±0.026	0.793±0.020	0.770±0.019	0.608±0.021
0.0137	0.801±0.042	0.805±0.042	0.687±0.037	0.520±0.031
0.0113	0.699±0.067	0.830±0.093	0.652±0.077	0.422±0.043
0.0096	0.809±0.148	0.511±0.139	0.427±0.124	0.462±0.092

Table A.14: Numerical table for figure 7.20.

x_2	$R_{\psi'}$(C/D)	$R_{\psi'}$(Ca/D)	$R_{\psi'}$(Fe/D)	$R_{\psi'}$(W/D)
0.0460	0.805±0.052	0.832±0.035	0.753±0.039	0.627±0.042
0.0320	0.984±0.062	0.753±0.078	0.753±0.060	0.678±0.050
0.0241	0.785±0.074	0.553±0.079	0.692±0.052	0.606±0.070
0.0192	0.749±0.108	0.682±0.125	0.738±0.103	0.537±0.166
0.0159		0.325±0.108	0.404±0.125	0.486±0.162

Table A.15: Numerical table for figure 7.21.

A.3 $\Upsilon(1s)$ Data

Integrated	R(C/D)	R(Ca/D)	R(Fe/D)	R(W/D)
Drell-Yan	1.003±0.0085	0.995±0.0061	0.990±0.0065	0.986±0.0083
Υ (1s)	0.923±0.040	0.886±0.027	0.884±0.029	0.868±0.037

Table A.16: Numerical table for figure 7.22.

x_F	$R_{\Upsilon(1s)}$(Ca/D)	$R_{\Upsilon(1s)}$(Fe/D)
-0.10	0.753±0.082	0.658±0.075
0.10	0.880±0.056	0.886±0.057
0.30	0.839±0.067	0.861±0.068

Table A.17: Numerical table for figure 7.23.

P_T (GeV)	$R_{\Upsilon(1s)}$(Ca/D)	$R_{\Upsilon(1s)}$(Fe/D)
0.50	0.835±0.054	0.800±0.052
1.50	0.837±0.052	0.871±0.054
2.75	1.016±0.112	0.889±0.101

Table A.18: Numerical table for figure 7.24.

x_2	$R_{\Upsilon(1s)}$(Ca/D)	$R_{\Upsilon(1s)}$(Fe/D)
0.299	0.753±0.082	0.658±0.075
0.199	0.880±0.056	0.886±0.057
0.136	0.839±0.067	0.861±0.068

Table A.19: Numerical table for figure 7.25.

A.4 All Data in α representation

Integrated	R(C/D)	R(Ca/D)	R(Fe/D)	R(W/D)
Drell-Yan	1.003±0.0085	0.995±0.0061	0.990±0.0065	0.986±0.0083
Υ (1s)	0.923±0.040	0.886±0.032	0.884±0.030	0.868±0.038
J/ψ	0.851±0.012	0.806±0.009	0.756±0.010	0.619±0.013
ψ'	0.855±0.029	0.750±0.027	0.722±0.036	0.623±0.033

Table A.20: Numerical table for figure 7.26.

x_F	α_{DY}	$\alpha_{J/\psi}$	$\alpha_{\psi'}$	$\alpha_{\Upsilon(1s)}$
-0.10				0.888±0.025
-0.05	0.998±0.013			
0.05	1.005±0.003			
0.10				0.961±0.014
0.15	0.999±0.002	0.919±0.005	0.914±0.008	
0.25	0.994±0.002	0.918±0.002	0.920±0.012	
0.30				0.949±0.018
0.35	0.995±0.002	0.909±0.004	0.874±0.016	
0.45	0.987±0.003	0.879±0.008		
0.50			0.848±0.026	
0.55	0.986±0.005	0.834±0.016		
0.65	0.971±0.009	0.807±0.035		
0.75	0.961±0.026			

Table A.21: Numerical table for figure 7.27.

P_T (GeV)	α_{DY}	$\alpha_{J/\psi}$	$\alpha_{\psi'}$	$\alpha_{\Upsilon(1s)}$
0.25	0.992±0.002	0.904±0.004	0.920±0.011	
0.50				0.936±0.014
0.75	0.992±0.002	0.915±0.004	0.895±0.011	
1.25	0.995±0.002	0.932±0.005		
1.50			0.939±0.012	0.950±0.014
1.75	1.006±0.003	0.926±0.011		
2.25	1.022±0.005	0.913±0.029		
2.75	1.015±0.010			0.982±0.025

Table A.22: Numerical table for figure 7.28.

x_2	α_{DY} $(16< Q^2 <36)$	α_{DY} $(36< Q^2 <81)$
0.038	0.988±0.003	0.971±0.008
0.063	0.995±0.002	0.988±0.003
0.088	1.006±0.004	1.002±0.002
0.113	1.011±0.006	0.998±0.003
0.138	0.972±0.012	0.996±0.004

Table A.23: Numerical table for figure 7.29.

Bibliography

[1] S.D. Drell, T.M. Yan, Phys. Rev. Lett. **25**, 316 (1970); S.D. Drell, D.J. Levy and T.M. Yan, Phys. Rev. **187**, 2159 (1969); Phy. Rev. D **1**, 1035 (1969); and Phy. Rev. D **1**, 1617 (1969).

[2] J.P. Rutherfoord, "What Can We Learn About Parton Distribution Functions from the Drell-Yan process?" in Proceedings of the Workshop on Hadron Structure Functions and Parton Distributions, Fermilab 26-28 April, 1990 (to be published).

[3] C. Grosso-Pilcher and M.J. Shochet, "High Mass Dilepton Production in Hadron Collisions" in Annual Review of Nuclear and Particle Science, **36**, 1 (1986).

[4] J.P. Rutherfoord, "Real Photon and Drell-Yan Processes" in Proceedings of the International Symposium on Lepton and Photon Interactions at High Energies, Kyoto, 1985.

[5] I.R. Kenyon, Rep. Prog. Phys., **45**, 1261 (1982).

[6] E.L. Berger, "Hadronic Production of Massive Lepton Pairs" in Proceeding of the Drell-Yan Workshop, Fermilab, 1 (1982).

[7] C. Albajar *et al.*, Phys. Lett. **186B**, 237 (1987).

[8] A.J. Buras, Rev. of Modern Phys., **52**, 199 (1980).

[9] F.E. Close, An Introduction to Quarks and Partons, 217 (1979); H.D. Politzer, Phys. Rev. Lett. **30**, 1346 (1973).

[10] H.D. Politzer, Nucl. Phys. **B129**, 301 (1977).

[11] T. Sloan, G. Smadja, and R. Voss, Phys. Reports, **162**, 47 (1988).

[12] P.N. Harriman, A.D. Martin and W.J. Stirling, Phys. Rev. **D42**, 798 (1990).

[13] J.C. Collins and D.E. Soper, Phys. Rev. **D16**, 2219 (1977).

[14] J.S. Conway *et al.*, Phys. Rev. **D39**, 92 (1989); K.J. Anderson *et al.*, Phys. Rev. Lett., **43**, 1219 (1979).

[15] E.L. Berger, Z. Phys., **C4**, 289 (1980); E.L. Berger and S. J. Brodsky, Phys. Rev. Lett., **42**, 940 (1979).

[16] G.E. Hogan *et al.*, Pys. Rev. Lett. **42**, 948 (1979); M.J. Corden *et al.*, Phys. Lett. *76B*, 226 (1978).

[17] H.B. Greenlee *et al.*, Phs. Rev. Lett. **55**, 1555 (1985).

[18] B. Betev *et al.*, Z. Phys. **C28**, 15 (1985).

[19] A.C. Benvenuti *et al.*, Phys. Lett. **195B**, 91 (1987); J.J. Aubert *et al.*, Nucl. Phys. **B272**, 158 (1986); J.J. Aubert *et al.*, Nucl. Phys. **B259**, 189 (1985); A. Bodek *et al.*, Phys. Rev. **D20**, 1471 (1979).

[20] F. Halzen and A. D. Martin, *Quarks& Leptons*, (John Wiley & Sons, Inc., 1984); G. Altarelli, Phys. Rep. **81c**, 1 (1982).

[21] G. Altarelli and G. Parisi, Nucl. Phys., **B126**, 298 (1977).

[22] W.J. Stirling, "The K-Factor : A Theoretical Review" of Proceeding of the Drell-Yan Workshop, Fermilab, 1 (1982).

[23] T. Matsuura, S.C. Van der Marck, and W.L. Van Neerven, Phys. Lett. **211B**, 171 (1988).

[24] P. Aurenche, R. Baier, and M. Fontannaz, Fermilab-PUB-90/27-T, January (1990).

[25] J.C. Collins, D.E. Soper, and G. Sterman, Nucl. Phys. **B261**, 104 (1985).

[26] G.T. Bodwin, Phys. Rev. **D31** 2616 (1985).

[27] G.T. Bodwin, S.J. Brodsky, and G.P. Lepage, Phys. Rev. **D39**, 3287 (1989).

[28] A.H. Mueller, Phys. Lett. **108B**, 355 (1982).

[29] G.T. Bodwin, S.J. Brodsky, and G.P. Lepage, Phys. Rev. Lett. **47**, 1799 (1981).

[30] J. Ashman *et al.*, Phys. Lett. **202B**, 603 (1988).

[31] M. Arneodo *et al.*, Phys. Lett. **211B**, 493 (1988).

[32] A.C. Benvenuti *et al.*, Phys. Lett. **163B**, 282 (1985).

[33] G. Bari *et al.*, Phys. Lett. **163B**, 282 (1985).

[34] R.G. Arnold *et al.*, Phys. Rev. Lett. **52**, 727 (1984).

[35] A. Bodek *et al.*, Phys Rev. Lett. **50**, 1431 (1983); **51**, 534 (1983);

[36] J.J. Aubert *et al.*, Phys. Lett. **123B**, 275 (1983).

[37] E.L. Berger, "The EMC Effect" in Proceedings of the XXIII International Conference on High Energy Physics, Berkeley, July, (1986).

[38] E.L. Berger, Nucl. Phys. **B267**, 231 (1986).

[39] R.P. Bickerstaff, *et al.*, Phys. Rev. Lett. **53**, 2531 (1984).

[40] C. E. Carlson and T.J. Havens, Phys. Rev. Lett. **51**, 261 (1983).

[41] H.J. Pirner and J.P. Vary, Phys. Rev. Lett. **46**, 1376 (1981).

[42] F.E. Close, R.L. Jaffe, R.G. Roberts, and G.G. Ross, Phys. Rev. D**31**, 1004 (1985).

[43] E.L. Berger and F. Coester, Phys. Rev. **D32**, 1071 (1985).

[44] E.L. Berger, F. Coester, and R.B. Wiringa, Phys. Rev. **D29**, 398 (1984).

[45] M. Ericson and A.W. Thomas, Phys. Lett. **148B**, 191 (1984).

[46] C.H. Llewellyn-Smith, Phys. Lett. **128B**, 107 (1983).

[47] M. Ericson and A.W. Thomas, Phys. Lett. **128B**, 112 (1983).

[48] L.V. Gribov, E.M. Levin, and M.G. Ryskin, Phys. Rep. **100**, 1 (1983).

[49] N.N. Nicolaev and V.I. Zakharov, Phys. Lett. **55B**, 397 (1975).

[50] A.H. Mueller and J. Qiu, Nucl. Phys. **B268**, 427 (1986).

[51] E.L. Berger and J. Qiu, Phys. Lett. **206B**, 141 (1988).

[52] J. Qiu, ANL-HEP-PR-88-10, submitted to Nucl. Phys. B.

[53] S.J. Brodsky and H.J. Lu, Phys. Rev. Lett. **64**, 1342 (1990).

[54] C. Michael and G. Wilk, Z. Phys., **C10**, 169-173 (1981).

[55] P. Bordalo, *et al.*, Phys. Lett. **193B**, 373 (1988); **193B**, 368 (1987).

[56] W-Y.P. Hwang, J.M. Moss, and J.C. Peng, Phys. Rev. D**38**, 2785 (1988).

[57] S. Katsanevas *et al.*, Phys. Rev. Lett. **60**, 2121 (1988).

[58] A. Bussiere *et al.*, Z. Phys. **C38**, 117 (1988).

[59] J.C. Collins, D.E. Soper, and G. Sterman, Nucl. Phys. **B263** 37 (1986).

[60] S.W. Herb *et al.*, Phys. Rev. Lett. **39**, 252 (1977).

[61] J.J. Aubert *et al.*, Phys. Rev. Lett. **33**, 1404 (1974).

[62] R. Baier and R. Rückl, Z. Phys. **C19**, 251 (1983).

[63] V. Barger, W. Y. Keung and R. J. N. Phillips, Z. Phys. **C6**, 169-174 (1980).

[64] J.L. Rosner, "Heavy Flavor Theory" in Proceeding of the Banff Summer Institute (World Scientific, Singapore, 1989); W. Kwong, J.L. Rosner, and C. Quigg, Ann. Rev. Nucl. Part. Sci. **37**, 325 (1987); K. Berkelman, Rep. Prog. Phys. **49**, 1 (1986).

[65] F. E. Close, J. Qiu and R. G. Roberts, ANL-HEP-PR-89-22 (1989), unpublished.

[66] Fermilab E772 proposal, spokesman: J.M. Moss (1986).

[67] J.A. Crittenden, JACTRACK, E605 Internal Report of March 25, 1983 ; H.D. Glass, Ph. D. Thesis, SUNY at Stony Brook, 1985.

[68] J.C. Gursky, H.W. Baer, F.F. Flick, and D. Gallegos, Nucl. Inst. and Meth. **A282**, 62 (1989).

[69] C.Y. Wong, Phys. Rev. **D30**, 961 (1984).

[70] T.J. Roberts *et al.*, Nucl. Phys. **B159**, 56 (1979).

[71] J.T.T. Van, Proceedings of the First Moriond Workshop (1981).

[72] A. Bodek and J.L. Ritchie, Phys. Rev. **D23**, 1070 (1981); **D24**, 1400 (1981).

[73] E. Eichten, I. Hinchliffe, K. Lane, and C. Quigg, Rev. Mod. Phys. **56**, 57! (1984); **58**, 1065 (1986).

[74] J. Badier *et al.*, Z. Phys. **C20**, 101 (1983).

[75] A. D. Martin, R. G. Roberts and W. J. Stirling, Phys. Rev. **D37**, 11((1988).

[76] S.J. Brodsky and A.H. Mueller, Phys. Lett. **206B**, 685 (1988).

[77] A. Ito *et al.*, Phys. Rev. **D23**, 604 (1981).

[78] C.N. Brown, *et al.*, Phys. Rev. Lett. **63**, 2637 (1989).

[79] D. M. Alde *et al.*, Phys. Rev. Lett. **64**, 2479, (1990).

[80] M.L. Gerardo, University of Mexico, Ph. D. Thesis, 1989.

[81] Y.B. Hsiung, Ph. D. Thesis, Columbia University, 1986.

[82] Y.B. Hsiung *et al.*, "Use of a parallel pipelined, event processor in a massive-dimuon experiment", FSU-HEP-851001, 1985.

[83] H.D. Glass, Ph. D. Thesis, SUNY at Stony Brook, 1985.

[84] R.E. Plaag, Ph. D. Thesis, University of Washington, 1986; R.E. Plaag and J.P. Rutherfoord, Nucl. Instr. and Meth. **A273**, 177 (1988).

[85] J.A. Crittenden *et al.*, IEEE Trans. Nucl. Sci. **Ns 31**, 1028 (1984).

[86] R. Gray and J.P. Rutherfoord, Nucl. Instr. and Meth. **A244**, 440 (1986).

[87] L. Frankfurt and M. Strickman, Phys. Rep., **160**, 235 (1988); L.V. Gribov, E.M. Levin, and M.G. Ryskin, Nucl. Phys. **B188**, 555 (1981);
G. Altarelli,

[88] M. Aguilar-Benitez *et al.*, Phys. Lett. **161B**, 400 (1985).

[89] C. Baglin *et al.*, Phys. Lett. **220B**, 471 (1989).

[90] S. J. Brodsky and P. Hoyer, Phys. Rev. Lett. **63**, 1566 (1989).

[91] E.L. Berger, J.C. Collins, D. Soper, and G. Sterman, Nucl. Phys. **B286**, 704 (1987).

[92] J. P. Blaizot and J. Y. Ollitrault, Phys. Lett. **217B**, 386 (1989).

[93] S. Gavin, M. Gyulassy, Phys. Lett. **207B**, 257 (1988).

[94] S. Gavin and R. Vogt, to be published.
(1978).

[95] G. Bertsch *et al.*, Phys. Rev. Lett. **47**, 297 (1981).

[96] H. Cobbaert, *et al.*, Phys. Lett. **191B**, 456 (1987).

[97] M.E. Duffy *et al.*, Phys. Rev. Lett. **55**, 1816 (1985).

[98] S. Gavin and M. Gyulassy, Phys. Lett. **214B**, 241 (1988).

[99] J. Hüfner, Y. Krihara, and H.J. Pirner, Phys. Lett. **215B**, 218 (1988).

[100] P. Hoyer, M. Vänttinen, and U. Sukhatme, Phys. Lett. **246B**, 217 (1990).

[101] J. Hüfner, B. Povh, and S. Gardner; preprint, Max Plank Institute. Heidelberg, MPI H-1989-V32.

[102] H. Abramowicz *et al.*, Z. Phys., **C25**, 29 (1984).

[103] D. M. Alde *et al.*, Phys. Rev. Lett., **66**, 133 (1991).

[104] Nuclear Dependence of the Production of Υ Resonances at 800 GeV: D. M. Alde *et al.*, (to be published).

[105] L.L. Frankfurt, M.I. Strikman, and S. Liuti, Phys. Rev. Lett., **65**, 1725 (1990).

[106] S.J. Brodsky, F.E. Close, and J.F. Gunion, Phys. Rev. **D6**, 177 (1972).

[107] L. Clavelli, P. H. Cox, B. Harms, and S. Jones, Phys. Rev. **D32**, 612 (1985).

[108] J. Qiu, Nucl. Phys. **B291**, 746 (1987).

[109] B. Z. Kopeliovich and F. Niedermayer, Joint Institute for Nuclear Research Report No. E2-84-834, Dubna, U.S.S.R., 1984 (unpublished).